Adsorption-Induced Deformation of Nanoporous Materials — in-situ Dilatometry and Modeling

Dissertation zur Erlangung des
naturwissenschaftlichen Doktorgrades
der Julius-Maximilians-Universität Würzburg

vorgelegt von

Christian Balzer

aus Fulda

Würzburg 2017

Eingereicht am: 12. Juli 2017
bei der Fakultät für Physik und Astronomie

1. Gutachter: Prof. Dr. Vladimir Dyakonov
2. Gutachter: Prof. Dr. Oskar Paris
3. Gutachter: -
der Dissertation

Vorsitzender: Prof. Dr. Karl Mannheim

1. Prüfer: Prof. Dr. Vladimir Dyakonov
2. Prüfer: Prof. Dr. Oskar Paris
3. Prüfer: Prof. Dr. Haye Hinrichsen
im Promotionskolloquium

Tag des Promotionskolloquiums: 27. Oktober 2017

Doktorurkunde ausgehändigt am:

Summary

The goal of this work is to improve the understanding of adsorption-induced deformation in nanoporous (and in particular microporous) materials in order to explore its potential for material characterization and provide guidelines for related technical applications such as adsorption-driven actuation. For this purpose this work combines in-situ dilatometry measurements with in-depth modeling of the obtained adsorption-induced strains. A major advantage with respect to previous studies is the combination of the dilatometric setup and a commercial sorption instrument resulting in high quality adsorption and strain isotherms. The considered model materials are (activated and thermally annealed) carbon xerogels, a sintered silica aerogel, a sintered hierarchical structured porous silica and binderless zeolites of type LTA and FAU; this selection covers micro-, meso- and macroporous as well as ordered and disordered model materials.

All sample materials were characterized by scanning electron microscopy, gas adsorption and sound velocity measurements. In-situ dilatometry measurements on mesoporous model materials were performed for the adsorption of N_2 at 77 K, while microporous model materials were also investigated for CO_2 adsorption at 273 K, Ar adsorption at 77 K and H_2O adsorption at 298 K. Within this work the available in-situ dilatometry setup was revised to improve resolution and reproducibility of measurements of small strains at low relative pressures, which are of particular relevance for microporous materials.

The obtained experimental adsorption and strain isotherms of the hierarchical structured porous silica and a micro-macroporous carbon xerogel were quantitatively analyzed based on the adsorption stress model; this approach, originally proposed by Ravikovitch and Neimark, was extended for anisotropic pore geometries within this work. While the adsorption in silica mesopores could be well described by the classical and analytical theory of Derjaguin, Broekhoff and de Boer, the adsorption in carbon micropores required for comprehensive nonlocal density functional theory calculations. To connect adsorption-induced stresses and strains, furthermore mechanical models for the respective model materials were derived. The resulting theoretical framework of adsorption, adsorption stress and mechanical model was applied to the experimental data yielding structural and mechanical information about the model materials investigated, i.e., pore size or pore size distribution, respectively, and mechanical moduli of the porous matrix and the nonporous solid skeleton. The derived structural and mechanical properties of the model materials were found to be consistent with independent measurements and/or literature values. Noteworthy, the proposed extension of the adsorption stress model proved to be crucial for the correct description of the

experimental data.

Furthermore, it could be shown that the adsorption-induced deformation of disordered mesoporous aero-/xerogel structures follows qualitatively the same mechanisms obtained for the ordered hierarchical structured porous silica. However, respective quantitative modeling proved to be challenging due to the ill-shaped pore geometry of aero-/xerogels; good agreement between model and experiment could only be achieved for the filled pore regime of the adsorption isotherm and the relative pressure range of monolayer formation. In the intermediate regime of multilayer formation a more complex model than the one proposed here is required to correctly describe stress related to the curved adsorbate-adsorptive interface. Notably, for micro-mesoporous carbon xerogels it could be shown that micro- and mesopore related strain mechanisms superimpose one another.

The strain isotherms of the zeolites were only qualitatively evaluated. The result for the FAU type zeolite is in good agreement with other experiments reported in literature and the theoretical understanding derived from the adsorption stress model. On the contrary, the strain isotherm of the LTA type zeolite is rather exceptional as it shows monotonic expansion over the whole relative pressure range. Qualitatively this type of strain isotherm can also be explained by the adsorption stress model, but a respective quantitative analysis is beyond the scope of this work.

In summary, the analysis of the model materials' adsorption-induced strains proved to be a suitable tool to obtain information on their structural and mechanical properties including the stiffness of the nonporous solid skeleton. Investigations on the carbon xerogels modified by activation and thermal annealing revealed that adsorption-induced deformation is particularly suited to analyze even small changes of carbon micropore structures.

Zusammenfassung

Ziel dieser Arbeit ist es, dass Verständnis der adsorptionsinduzierter Deformation von nanoporösen (insbesondere mikroporösen) Materialien zu erweitern, um ihr Potenzial für die Materialcharakterisierung zu erforschen. Zusätzlich sollen Orientierungshilfen für technische Anwendungen, wie z.B. adsorptionsgetriebene Aktuatoren, bereitgestellt werden. Hierfür kombiniert diese Arbeit in-situ Dilatometriemessungen und detaillierte Modellierung der gemessenen adsorptionsinduzierten Dehnungen. Der wesentliche Vorteil dieser Arbeit gegenüber vorherigen Studien ist die Kombination des dilatometrischen Messaufbaus mit einer kommerziellen Gasadsorptionsanlage, was die Messung qualitativ hochwertiger Adsorptions- und Dehnungsisothermen erlaubt. Die betrachteten Materialsysteme sind (aktivierte und geglühte) Kohlenstoffxerogele, ein gesintertes Silica-Aerogel, ein gesintertes, hierarchisch strukturiertes, poröses Silica und binderlose Zeolithe der Typen LTA und FAU. Diese Auswahl umfasst mikro-, meso- und makroporöse ebenso wie geordnete und ungeordnete Modellmaterialien.

Alle Modellmaterialien wurden mit Rasterelektronenmikroskopie, Gasadsorption und Schallgeschwindigkeitsmessungen charakterisiert. In-situ Dilatometriemessungen an mesoporösen Modellsystemen wurden für N_2-Adsorption bei 77 K durchgeführt, während alle mikroporösen Modellsysteme zusätzlich bei CO_2-Adsorption (273 K), Ar-Adsorption (77 K) und H_2O-Adsorption (298 K) untersucht wurden. Der verfügbare Messaufbau für in-situ Dilatometrie wurde im Rahmen dieser Arbeit weiterentwickelt, um Auflösung und Reproduzierbarkeit der Messungen von kleinen Dehnungen zu verbessern, was insbesondere für mikroporöse Materialien von Bedeutung ist.

Die experimentellen Adsorptions- und Dehnungsisothermen des hierarchisch strukturierten, porösen Silicas und des mikro-makroporösen Kohlenstoff-Xerogels wurden mit dem *adsorption-stress*-Modell quantitativ ausgewertet. Hierfür wurde das *adsorption-stress*-Modell, ursprünglich eingeführt von Ravikovitch et al., für die Verwendung von anisotropen Porengeometrien erweitert. Während die der Deformation zu Grunde liegende Adsorption im Fall des mesoporösen Silicas gut mit der klassischen und analytischen Theorie von Derjaguin, Broekhoff und de Boer beschrieben werden konnte, erforderte die Adsorption in den Kohlenstoffmikroporen umfassende Berechnungen mittels nichtlokaler Dichtefunktionaltheorie. Um die adsorptionsinduzierten Spannungen mit entsprechenden Dehnungen zu korrelieren, wurden zusätzlich mechanische Modelle für die untersuchten Materialien entworfen. Das resultierende theoretische Konstrukt aus Adsorptions-, *adsorption-stress*- und mechanischem Modell wurde auf die ermittelten experimentellen Daten angewandt und strukturelle und mechanische Eigenschaften der Modellmaterialien bestimmt,

d.h. Porengröße bzw. Porengrößenverteilung sowie die mechanischen Module der porösen Matrix und des unporösen Festkörperskeletts. Es konnte gezeigt werden, dass die ermittelten Materialeigenschaften konsistent mit unabhängigen Messungen und/oder Literaturwerten sind. Hierbei ist zu beachten, dass sich die Erweiterung des *adsorption-stress*-Modells für eine korrekte Auswertung der experimentellen Daten als zwingend erforderlich erwies.

Des Weiteren konnte gezeigt werden, dass die adsorptionsinduzierte Deformation von ungeordneten mesoporösen Aero-/Xerogelstrukturen qualitativ denselben Mechanismen folgt, die für das geordnete, hierarchisch strukturierte, poröse Silica identifiziert wurden. Die entsprechende quantitative Modellierung erwies sich allerdings als schwierig, da die Poren in Aero-/Xerogelstrukturen geometrisch schlecht zu fassen sind. Gute Übereinstimmung zwischen Modell und Experiment konnte nur für das Stadium gefüllter Poren und den relativen Druckbereich der Monolagenbildung erzielt werden. Der Zwischenbereich der Multilagenadsorption erfordert ein komplexeres Modell, um die Spannung quantitativ korrekt zu beschreiben, die sich auf Grund der gekrümmten Adsorbat-Adsorptiv-Grenzfläche im Material ausbildet. Mit Hinblick auf mikro-mesoporöse Kohlenstoffxerogele konnte gezeigt werden, dass sich dort Deformationsmechanismen von Mikro- und Mesoporen überlagern.

Die Dehnungsisothermen der Zeolithe wurden nur qualitativ ausgewertet. Das Ergebnis für den Zeolithen vom Typ FAU stimmt gut mit anderen in der Literatur beschriebenen Experimenten und dem theoretischen Verständnis überein, das sich aus dem *adsorption-stress*-Modell ergibt. Im Gegensatz dazu ist die gemessene Dehnungsisotherme des Zeolithen vom Typ LTA eher ungewöhnlich, da sie monotone Expansion des LTA-Zeolithen über den gesamten Druckbereich zeigt. Qualitativ kann dieses Ergebnis ebenfals mit dem *adsorption-stress*-Modell erklärt werden, aber eine detaillierte, quantitative Analyse übersteigt den Rahmen dieser Arbeit.

Insgesamt erweist sich die Analyse der adsorptionsinduzierten Dehnungen der Modellmaterialien als geeignetes Mittel, um Informationen über deren strukturelle und mechanische Eigenschaften zu erlangen, was auch die Steifigkeit des unporösen Festkörperskeletts miteinschließt. Desweiteren zeigen Untersuchungen an aktivierten und geglühten Kohlenstoffxerogelen, dass adsorptionsinduzierte Deformation insbesondere geeignet ist, um kleine Änderungen an Mikroporenstrukturen zu analysieren.

Contents

1. Introduction **1**

2. Theoretical Background **5**
2.1. The Porous Solid . . . 5
2.1.1. Structure . . . 5
2.1.2. Mechanical Properties . . . 6
2.2. Adsorption . . . 8
2.2.1. Fundamentals and Terminology . . . 8
2.2.2. Micropores . . . 9
2.2.3. Meso- and Macropores . . . 12
2.3. Adsorption-Induced Deformation . . . 14
2.3.1. Adsorption-Induced Stress in Nanopores . . . 15
2.3.2. Cylindrical Meso- and Macropores . . . 18
2.3.3. Aero- and Xerogels . . . 20
2.3.4. Disordered Microporous Carbon . . . 22

3. Model Materials and Experimental Methods **27**
3.1. Model Materials . . . 27
3.1.1. Carbon Xerogels . . . 28
3.1.2. Zeolites . . . 31
3.1.3. Silica Aerogel . . . 32
3.1.4. Hierarchical Structured Porous Silica . . . 33
3.2. Characterization Techniques . . . 34
3.2.1. Determination of Bulk Density . . . 34
3.2.2. Gas Adsorption Measurements . . . 35
3.2.3. Sound Velocity Measurements . . . 38
3.2.4. Scanning Electron Microscopy (SEM) . . . 39
3.3. Gas Adsorption Measurements with in-situ Dilatometry . . . 39
3.3.1. Experimental Setup . . . 39
3.3.2. Measurement Procedure . . . 40
3.3.3. Dilatometric Artifacts, Countermeasures and Accuracy . . . 43

4. Results **45**
4.1. Nonlocal Density Functional Theory . . . 45
4.2. Sample Characterization . . . 51
4.2.1. SEM Images . . . 51
4.2.2. Monolithic Density and Sound Velocity Measurements . . . 51
4.2.3. Gas Adsorption . . . 53
4.2.4. Derived Structural Quantities . . . 57
4.3. in-situ Dilatometry . . . 59

5. Discussion **65**
5.1. Hierarchical Structured Porous Silica - Ordered Mesoporosity 65
5.2. Silica Aerogel - Disordered Mesoporosity 72
5.3. Carbon Xerogel I - Disordered Microporosity 78
5.4. Carbon Xerogel II - Disordered Micro- and Mesoporosity 87
5.5. Carbon Xerogel III - Activation, Thermal Annealing and Mechanical Properties 97
5.5.1. Activation 97
5.5.2. Thermal Annealing 101
5.5.3. Mechanical Properties of Carbon Xerogels 106
5.6. Zeolites - Ordered Microporosity 111

6. Conclusions **115**

7. Appendix **119**
A. Molecular Models of NLDFT Calculations 119
B. Disjoining Pressure Reference Isotherms 120
C. Connection between ASAP2020 and Dilatometer 122
D. in-situ Dilatometry Measurement on a Glass Rod 123
E. PSDs from N2 and CO2 Adsorption for Annealed Carbon Xerogels . 123
F. Estimate for Increase of Micropore Volume by Activation 125

Acknowledgements **127**

Symbols and Abbrevations **129**

References **133**

1. Introduction

The process denoted as *adsorption* describes the enrichment of fluid matter in the vicinity of a solid surface and is particularly pronounced for nanoporous materials, since they typically provide specific solid-fluid interfaces above 100 m^2/g. Nowadays, nanoporous materials and their adsorption properties are intensively applied in various technological fields such as desiccation, gas separation, liquid purification, pollution control and respiratory protection. Beyond these direct applications of adsorption, gas adsorption measurements are still one of the technically and scientifically most wide spread and established methods for the structural characterization of nanoporous materials. Comprehensive information on adsorption and its applications is found in various textbooks, e.g. [1–3].

An effect intrinsically connected to adsorption is *adsorption-induced deformation*, which denotes structural changes of a porous solid caused by the adsorption process. Adsorption-induced deformation has been reported for essentially any nanoporous material commonly used including synthetic carbons [4–15], coals [16–24], porous glasses/silica [25–33], zeolites [34–37], vermiculites [38], porous silicon [39–41] and metal organic frameworks (MOFs) [42, 43]. With the exception of MOFs, the observed volumetric strain of the nanoporous material was mostly found to be on the scale of per mill to percent and therefore adsorption-induced deformation is currently neglected in most theoretical considerations and technical applications. A comprehensive review about adsorption-induced deformation was recently given by Gor et al. [44].

Historically, the first scientific reports of adsorption-induced deformation date back nearly a century: in 1921 Whipple investigated the functionality of a hair hygrometer based on capillary effects [45] and in 1927 Meehan performed seminal measurements of the deformation of coal caused by CO_2 adsorption [16]. Meehan's results inspired Bangham and co-workers [46] to launch into comprehensive studies of coal deformation induced by various gases and vapors [17, 47–50]. As Meehan before, Bangham investigated adsorption-induced deformation dilatometrically on monolithic coal pieces. Furthermore, Bangham derived a very fundamental explanation for the observed coal deformations nowadays often referred to as *Bangham's law*, i.e., the reduction of the coal's surface energy by the adsorption [51]. Following Bangham's law adsorption should always cause the adsorbing material to expand. However, in the late 1940s and 1950s this concept was challenged by more refined dilatometric studies on coal [18, 19, 52] and porous glass [25], which exhibited stages of contraction during the adsorption process. Based on the available understanding of nanoporosity, qualitative explanations for the apparent failure of Bangham's law were suggested: in coal the pore size of the majority of

pore volume is similar to the size of the adsorbing molecules, which therefore can form contracting "bridges" between opposing pore walls [20]. In porous glass on the other hand, the pores are significantly larger, but here the adsorbed molecules may form menisci resulting in capillary stress [25]. At this point the scientific activity in the field of adsorption-induced deformation receded. In the 1970s dilatometric measurements on zeolites during the adsorption of water and noble gases [34–37] complemented the already existing experimental data by another class of materials, but no significant progress in understanding the available data was made.

The interest in adsorption-induced deformation reignited around the year 2000 and was fueled by various - in some cases still ongoing - developments, which can be roughly grouped into three categories:

(i) Firstly, nanoporous materials and applications emerged, where adsorption-induced deformation had an acute impact. One of the first examples for this category are silica aerogels, which advanced to a technologically relevant class of nanoporous materials in the 1980s and 1990s [53]. Soon it became evident that gas adsorption measurements failed severely in characterizing the structure of low density aerogels [54] and different attempts were made in order to explain the contradicting results (see e.g. ref [55]). In 2000 Reichenauer and Scherer elucidated this issue by means of in-situ dilatometry measurements during N_2 adsorption at 77 K: here the silica aerogel underwent massive reversible adsorption-induced strain exceeding 40 vol% and thus the obtained adsorption isotherm was superimposed by significant deformational artifacts [27, 56, 57]. The results of Reichenauer and Scherer were later reproduced for He and Ne adsorption [29].

Another class of materials, which became popular in recent years and revealed significant adsorption-induced deformation, are metal organic frameworks (MOFs) [58]. Similar to silica aerogels the adsorption-induced strains of MOFs are larger than for most other nanoporous materials; X-ray diffraction patterns of dried and humidity conditioned MOFs revealed changes of pore sizes of nearly 100% [42]. Thus adsorption isotherms of MOFs may be significantly affected by continuous or steplike structural changes [59]; very recently adsorption-induced deformation in MOFs was even suggested to be capable of causing *negative gas adsorption* [43].

Apart from the development of new nanoporous materials also long known materials and their adsorption-induced deformation returned to the focus of interest. E.g. within the context of climate change, the underground geological storage of CO_2 was discussed [60]. Here the options considered include the injection of CO_2 into coal beds unsuitable for mining in order to store it there and potentially extract CH_4 bound within the coal bed. However, during the CO_2 injection the permeability of the coal reduces significantly hampering the overall process [61]. Lab experiments with coal cores by Pini et al. [24] and Mazumder et al. [22, 23] suggested that adsorption-induced contraction of the transport pores

within coal is the origin of this issue.

Another rather new scientific field is the development of adsorption-driven actuators and sensors [62–64]. Since the adsorption-induced strains of most nanoporous materials are below 1 vol% the reported prototypes utilize bilayer and cantilever arrangements to amplify the displacement. The nanoporous materials used in the above given references were porous silica in form of thin films.

(ii) The second category of developments are experimental approaches beyond the traditional dilatometry to access adsorption-induced deformation: in 1996 Dolino et al. applied X-ray diffraction to access the adsorption-induced deformation of porous silicon interpreting shifts of diffraction peaks during the adsorption process as adsorption-induced strains [39]. The same concept was applied a few years later to MOFs [42]. Noteworthy, only materials with a significant degree of order exhibit diffraction peaks of sufficient sharpness to resolve the typically small adsorption-induced strains. Thus adsorption-induced deformation of the rather disordered nanoporous materials most commonly used can only be analyzed by diffraction or scattering techniques, if their respective strains are rather large (as e.g. for silica aerogels [65]). However, X-ray diffraction allows for investigations of adsorption-induced deformation on the microscopic scale of atomic lattices and pores and thereby provides information complementary to the dilatometric technique. Furthermore, many newly developed nanoporous materials are not naturally available as monolithic samples as required for dilatometric measurements but only in form of powder. Prominent examples for this are MCM-41 [66] and SBA-15 [67], which were developed in the 1990s and became stimulating nanoporous model systems due to their well-defined pore structure and ordered porosity. The adsorption-induced deformation of MCM-41 and SBA-15 was studied extensively by angle X-ray scattering by Paris and co-workers during the adsorption process in analogy to the previous work of Dolino et al. [30–32, 68].

In 2002 another experimental approach to adsorption-induced deformation was reported by Mogilnikov and Baklanov via ellipsometric porosimetry [28]. Similar to dilatometry this method measures adsorption-induced deformation on the macroscopic scale of the nanoporous material, however, it can be applied to very thin films. On the other hand, due to its optical nature ellipsometric porosimetry requires for transparent materials thereby limiting its applicability.

(iii) The last but not least category is the advancement of theoretical and computational methods and their application to adsorption-induced deformation. After the year 2000 a considerable number of theoretical studies investigated adsorption-induced stress in nanopores and the consecutive adsorption-induced strain of nanoporous solids [32, 40, 41, 69–98]. The majority of these studies focused on carbon micropores and silica mesopores. One of the most significant contributions to the field was presented in 2006 by Ravikovitch and Neimark [70], who suggested a thermodynamic approach nowadays known as *adsorption stress*

model. In following years the adsorption stress model was applied to explore the adsorption-induced deformation of various types of materials including zeolites [70], carbons [75], mesoporous silica [79, 84] and MOFs [81]. The advantages of the adsorption stress model over other approaches were its universal character and its compatibility with atomistic computational based methods such as density functional theory calculations and Monte Carlo simulations, which by now advanced to the state of the art adsorption models.

Against the background outlined above, the work at hand aims to complement the current understanding of adsorption-induced deformation in two ways: the first part is the preparation of a solid experimental foundation for studies on adsorption-induced deformation. For this purpose combined measurements of adsorption and in-situ dilatometry were performed on model materials, i.e., synthetic microporous carbons and mesoporous silica. A major advantage of the experimental setup refined and used in this work is its capability to simultaneously measure a sample's adsorption-induced strain and adsorption isotherm. In particular the instruments resolution of gas pressure surpasses other dilatometers reported in literature for studies of adsorption-induced deformation. The second part of this work is the application of the currently available models for adsorption-induced deformation to the obtained experimental data. The goals of this part are the validation or revision, respectively, of the most accepted concepts for adsorption-induced deformation and the exploration of its potential for a refined characterization of nanoporous materials. Given the success of the adsorption stress model by Ravikovitch and Neimark special focus was put on this approach.

2. Theoretical Background

This section gives a brief summary of the physical concepts forming the foundation of this work. Of particular importance are the porous solid with respect to its internal structure and mechanical properties as well as the phenomena of adsorption and adsorption-induced deformation including quantitative models for their respective description.

Since this work deals exclusively with gas adsorption, the terminology used follows the recommendations of the *International Union of Pure and Applied Chemistry* (IUPAC) for physisorption of gases [99].

2.1. The Porous Solid

2.1.1. Structure

A porous solid of specific bulk volume $V_b = 1/\rho_b$ consists of a nonporous solid phase, often denoted as skeleton or backbone, of specific volume $V_s = 1/\rho_s$ and a specific pore volume V_p. Here ρ_b and ρ_s are the bulk (or apparent) density of the porous solid and the density of its nonporous skeleton, respectively. The specific volumes and densities are related by

$$V_b = \frac{1}{\rho_b} = V_p + V_s = V_p + \frac{1}{\rho_s}. \tag{2.1}$$

The ratio of specific pore volume to specific bulk volume is the porosity ϕ [3]:

$$\phi = \frac{V_p}{V_b} = 1 - \frac{\rho_b}{\rho_s}. \tag{2.2}$$

Other quantities typically used to define a porous solid are its specific surface area $S = A_s/m_s$, i.e., the area of the skeleton-pore interface A_s per skeleton mass m_s, and the pore size (either as an average value or as a volumetric distribution). For given pore volume, specific surface area and pore size are related by the geometry of the pores within the porous solid. The most commonly used pore geometries are the slit-shaped pore, the cylindrical pore and the spherical pore. The slit-shaped pore is defined by its pore width w, while the cylindrical and the spherical pore are defined by their respective diameter d_p leading to [3]

$$V_p = S/2 \cdot w \qquad \text{for slit-shaped pore,} \tag{2.3a}$$
$$V_p = S/4 \cdot d_p \qquad \text{for cylindrical pore,} \tag{2.3b}$$
$$V_p = S/6 \cdot d_p \qquad \text{for spherical pore.} \tag{2.3c}$$

The IUPAC classifies pores with respect to their size [99] into *micropores* (w, $d_p < 2$ nm), *mesopores* (2 nm $< w$, $d_p < 50$ nm) and *macropores* (w, $d_p > 50$ nm). Furthermore micropores are subdivided into *ultramicropores* (w, $d_p < 0.7$ nm) and *super micropores* (0.7 nm $< w$, $d_p < 2$ nm), while all pores smaller than 100 nm are denoted as *nanopores*. The total pore volume of many real porous solids exhibits contributions of several pore classes, which are often related to different, structurally distinguishable levels of the porous solid. In these cases the total pore volume and the total specific surface area can be subdivided into micro-, meso- and macropore volume (V_{mic}, V_{meso} , V_{mac}) and respective specific surface areas (S_{mic}, S_{meso}, S_{mac}):

$$V_p = V_{mic} + V_{meso} + V_{mac}, \tag{2.4}$$

$$S = S_{mic} + S_{meso} + S_{mac}. \tag{2.5}$$

In analogy to Eq. 2.3 the specific surface area may also be related to structural entities forming the related porous phase (assuming structural entities can be clearly defined). In this work the relevant structures are spherical particles of diameter d_{part} and density ρ_{part} as well as long cylindrical rods of diameter d_{rod} and density ρ_{rod} [1]. The characteristic size of these structures is related to specific surface area and density by

$$d_{part} = \frac{6}{S \cdot \rho_{part}} \qquad \text{for spherical particle,} \tag{2.6a}$$

$$d_{rod} = \frac{4}{S \cdot \rho_{rod}} \qquad \text{for cylindrical rod.} \tag{2.6b}$$

Eq. 2.6b implies that the area of the rod's front sides is negligible.

2.1.2. Mechanical Properties

The mechanical properties of an isotropic and homogenous solid (porous or non-porous) are fully defined by two independent parameters [100]. In this work the mechanical parameters used are the Young's modulus E, the Poisson's ratio ν and the bulk modulus K, where [100]

$$E = 3K\left(1 - 2\nu\right). \tag{2.7}$$

The mechanical properties of a porous solid are also related to its internal structure and the mechanical properties of its nonporous backbone. In this context the model by Gibson and Ashby originally proposed for open-celled foams in the regime of linear elasticity is often used [101]:

$$\frac{E_b}{E_s} = C_{GA}\left(\frac{\rho_b}{\rho_s}\right)^2 = C_{GA}\left(1 - \phi\right)^2. \tag{2.8}$$

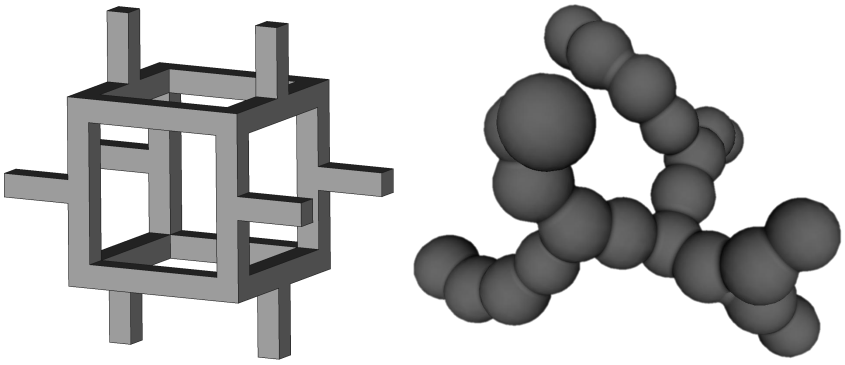

Figure 2.1.: 3D schematics of the Gibson-Ashby model (left) and an aero-/xerogel structure (right).

Here E_b and E_s are the Young's moduli of the bulk porous solid and its nonporous skeleton, respectively, and C_{GA} is a constant depending on the structural details of the backbone. Evaluating large quantities of data for rigid polymers, elastomers, metals and glasses Gibson and Ashby found C_{GA} to be approximately 1 for the majority of materials [101].

A class of materials, which is not in line with the Gibson-Ashby model but of particular importance for this work, are aero- and xerogels [53]. As was experimentally shown in ref [102] for this type of material the scaling of E_b with the bulk denisty ρ_b is given by

$$\frac{E_b}{E_0} = \left(\frac{\rho_b}{\rho_0}\right)^{\alpha}, \tag{2.9}$$

where α is a scaling exponent in the range of 2 to 4, while E_0 and ρ_0 are Young's modulus and density of a reference point, which does not necessarily correspond to the nonporous solid skeleton. The difference between the Gibson-Ashby model and aerogel like structures is the interconnectivity of the skeleton (compare Figure 2.1): within the Gibson-Ashby model it is assumed that the skeleton is fully interconnected in the form of straight-lined beams causing mechanical load to be evenly distributed throughout the porous structure. Contrary, the skeleton of aero- and xerogels exhibits distorted connections, which are more prone to bending than beams, and dead ends, which do not contribute to the mechanical stiffness of the porous solid at all. Notably, since the scaling exponent α is found empirically, Eq. 2.9 should only be applied in the bulk density range used for the determination of α.

2.2. Adsorption

2.2.1. Fundamentals and Terminology

An effect of particular relevance for porous solids is the phenomenon of adsorption describing the accumulation of atoms or molecules in the vicinity of a solid surface, when the solid is brought into contact with a fluid. The atoms or molecules adsorbed on the solid surface are denoted as *adsorbate*, while the atoms and molecules in fluid form (not adsorbed) are the *adsorptive*. The solid brought in contact with the fluid is the *adsorbent*. The reverse process of adsorption, i.e., a decrease of the amount adsorbed on the solid surface, is denoted as *desorption*. Depending on the nature of the adsorption process it is referred to as *physisorption* or *chemisorption*. Physisorption is exothermic, fully reversible and based on attractive dispersion forces or specific molecular interactions arising e.g. from polarization or dipoles. Chemisorption on the other hand describes adsorption involving the formation of chemical bounds between the adsorbate and the adsorbent. In this work adsorption is always considered to be physisorption. On a side note, adsorption has to be distinguished from *absorption*, where matter is incorporated by a solid or fluid without the possibility to define a clear phase boundary.

In the context of porous solids it is furthermore important to distinguish between *open* and *closed* porosity: if the porosity of a porous solid can be entered by a fluid it is open porosity in contrast to closed porosity, which is not accessible to the fluid. The attributes open and closed are connected to specific fluids, as a material's porosity may be open for one fluid but closed for another. This work always considers porosity to be open, if not explicitly stated otherwise.

The adsorption properties of a porous solid for a gas are characterized by the adsorption isotherm, i.e., the amount of adsorbate within the porous solid[1] N_a as a function of the relative gas pressure p/p_0 at thermodynamic equilibrium for given temperature T. Here p is the (partial) gas pressure and p_0 is the saturation pressure of the adsorptive at temperature T. Notably, experimental adsorption isotherms are commonly given as specific adsorption N_a/m_{sample}, where m_{sample} is the mass of sample investigated, which in turn is equal to the mass of its nonporous skeleton m_s. Furthermore, measurements of adsorption isotherms typically begin at the lowest possible partial pressure of the adsorptive and stepwise increase the relative gas pressure above the adsorbent up to the equilibrium gas pressure of $p/p_0 = 1$. Following the highest gas pressure the adsorption measurement may be complemented by a series of decreasing gas pressures steps. This leads to a two-part adsorption isotherm with an adsorption and a desorption branch. In particular the adsorption isotherms of mesoporous materials may exhibit hystereses between their adsorption and desorption branches. The classification of adsorption isotherms according to the IUPAC recommendations is shown in Figure 2.2.

[1] Generally one has to distinguish between absolute and excess amount of adsorbate, however, for all situations considered in this work both quantities are essentially identical. Compare ref [103].

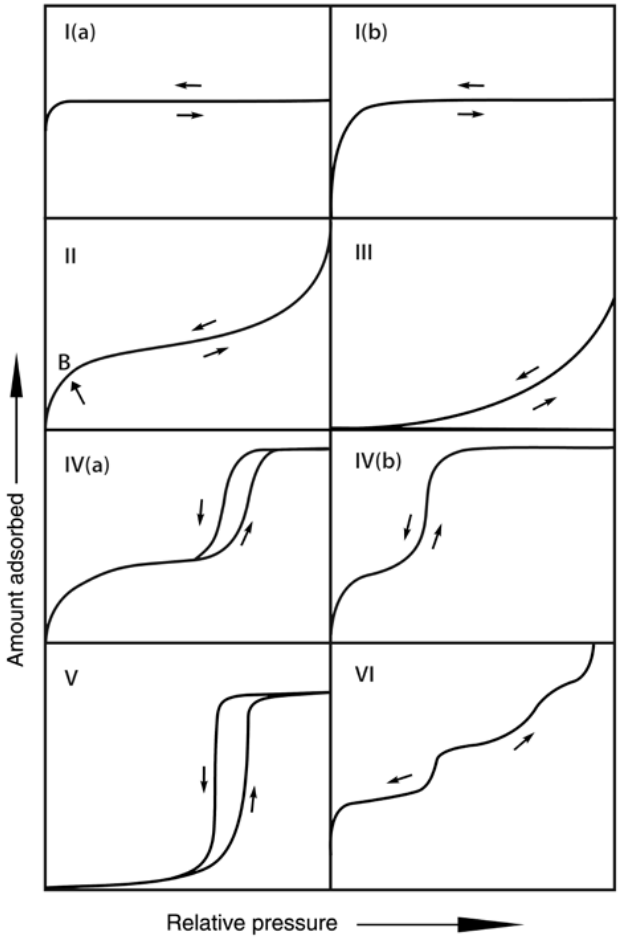

Figure 2.2.: IUPAC classification of adsorption isotherms [99] ©2015 IUPAC & De Gruyter. Adsorption isotherms of types I(a) and I(b) are associated with microporous materials, adsorption isotherms of types IV(a), IV(b) and V with mesoporous materials and adsorption isotherms of types II, III and VI with macroporous materials.

2.2.2. Micropores

Micropores are pores of less than 2 nm in size, which are further subdivided into super micropores (size between 0.7 and 2 nm) and ultramicropores (size below 0.7 nm) [98]. The definition of micropores as a separate class of pores is due to the fundamentally different adsorption isotherms of microporous materials when compared to meso- and macroporous ones: microporous materials usually exhibit type I adsorption isotherms (Figure 2.2) featuring pore filling at very low relative pressures [1]. The exceptional adsorption behavior of micropores results from short distances between pore walls, which are comparable to the effective range of the attractive dispersion forces between adsorptive and adsorbent. As a consequence the attractive potentials of different pore walls overlap within a micropore resulting in significantly enhanced attraction for the adsorptive [104] (compare Figure 2.3).

In this work, adsorption of gas molecules in micropores was described by nonlocal density functional theory (NLDFT), which was introduced for adsorption phenomena by Tarazona [105, 106]. A comprehensive review on NLDFT and its application in the context of adsorption was recently given in ref [107]. The general concept of NLDFT calculations is the derivation of the spatial adsorbate density distribution ρ_a within a pore for given fluid-fluid and solid-fluid interactions by numerical minimization of the grand potential Ω_a of the adsorbate:

$$\Omega_a\left[\rho_a\left(\boldsymbol{r}\right)\right] = F_{ideal}\left[\rho_a\left(\boldsymbol{r}\right)\right] + F_{excess}\left[\rho_a\left(\boldsymbol{r}\right)\right] + \int \rho_a\left(\boldsymbol{r}\right)\left(U_{ext}\left(\boldsymbol{r}\right) - \mu\right)\,\mathrm{d}\boldsymbol{r}. \quad (2.10)$$

Here F_{ideal} and F_{excess} are the free energy contributions of the adsorbate due to ideal gas behavior and fluid-fluid interaction, respectively, μ is the chemical potential and $\boldsymbol{r}$ is the position vector within the pore. With respect to adsorption measurements the chemical potential is typically calculated for the experimental conditions defined by relative pressure and temperature, $\mu = R_g T \cdot \ln(p/p_0)$, where R_g is the gas constant. The integral term in Eq. 2.10 describes the interaction of the adsorbate with an (external) mean field U_{ext} resulting from the presence of an adsorbent.

Typically fluid-fluid as well as solid-fluid interaction exhibit long ranged attraction and short ranged repulsion (compare Figure 2.3 and Appendix A). For the calculations performed in this work the attractive fluid-fluid interaction was modeled by the Weeks-Chandler-Andersen perturbation scheme [108] and the short ranged hard sphere repulsion by the RLST version [109] of Rosenfeld's fundamental measure theory [110]. In previous works this model for fluid-fluid interaction was validated against experimental data for liquid vapor equilibrium pressure and densities as well as surface tension of the unconfined fluid [111].
The quantitative description of the solid-fluid interaction requires a model for the geometry of the micropores. Since the microporous materials investigated in this work were nearly exclusively carbons, the micropores within NLDFT calculation were modeled as slits consisting of two parallel opposing surfaces. The external solid-fluid potential of a slit-shaped carbon micropore is the superposition of the Steele potentials U_{Steele} [112] of both walls:

$$U_{ext}\left(z\right) = U_{Steele}\left(z\right) + U_{Steele}\left(w_{cc} - z\right). \quad (2.11)$$

$$U_{Steele}\left(z\right) = 2\pi\rho_g\varepsilon_{sf}\sigma_{sf}^2\Delta\left[\frac{2}{5}\left(\frac{\sigma_{sf}}{z}\right)^{10} - \left(\frac{\sigma_{sf}}{z}\right)^{4} - \frac{\sigma_{sf}^4}{3\Delta\left(0.61\Delta + z\right)^3}\right]. \quad (2.12)$$

Here $w_{cc} = w + \sigma_{cc}$ is the distance between the centers of carbon atoms in opposing pore walls with $\sigma_{cc} = 0.34$ nm being the effective diameter of a carbon atom. The Steele potential describes solid-fluid interaction due to Van der Waals interaction and was derived for the adsorption on a plain graphite surface. Here

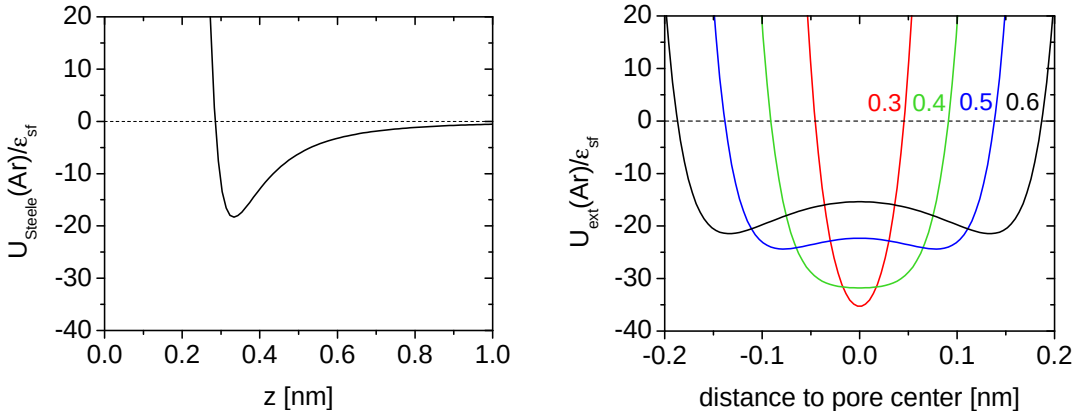

Figure 2.3.: Steele potential for Ar (left) and micropore potentials for Ar and pore widths of w equal to 0.3, 0.4, 0.5 and 0.6 nm (right).

ρ_g is the number density of graphite, Δ is the interlayer distance of graphite and ε_{sf} and σ_{sf} are parameters for range and depth of the Steele potential. Numerical values for the parameters of the Steele potential were taken from Ravikovitch et al. [113], where they were validated against experimental adsorption data on Sterling graphite. Figure 2.3 shows the Steel potential for the interaction with Ar atoms and the resulting external solid-fluid potentials for slit-shaped micropores of various widths. For numerical calculations solid-fluid interaction is typically cut-off for distances larger than $10\sigma_{sf}$, which is larger than any micropore.

A summary of the molecular models for the fluid and explicit parameters used for NLDFT calculations is given in the Appendix A.

From the results of NLDFT calculations, surface specific adsorption isotherms $N_{NLDFT}\left(p/p_0\right)$ for micropores of width w can be derived by spatial integration of the adsorbate density:

$$N_{NLDFT}\left(p/p_0, w\right) = \frac{1}{2N_A}\int_0^{w_{cc}} \rho_a\left(z, p/p_0, w\right)\,\mathrm{d}z, \tag{2.13}$$

where N_A is the Avogadro constant. Many microporous materials exhibit significant structural disorder, which requires a set of theoretical adsorption isotherms determined for various values of w. In this case the correlation of experimental and NLDFT adsorption isotherms is given by the integral adsorption equation (IAE) [114]:

$$\frac{N_a}{m_{sample}}\left(p/p_0\right) = \int_{w_{min}}^{w_{max}} N_{NLDFT}\left(p/p_0, w\right)\cdot S_{diff}\left(w\right)\,\mathrm{d}w. \tag{2.14}$$

Here N_a/m_{sample} is the specific experimental adsorption isotherm and S_{diff} is the specific differential pore area distribution, while w_{min} and w_{max} are the smallest and the largest pore width considered within NLDFT calculations. S_{diff} is directly related to the specific differential pore volume distribution V_{diff}, the spe-

cific cumulative pore area distribution S_{cum} and the specific cumulative pore volume distribution V_{cum} of the material investigated by

$$V_{diff}(w) = \frac{1}{2} S_{diff}(w) \cdot w, \tag{2.15}$$

$$S_{cum}(w) = \int_{w_{min}}^{w} S_{diff}(w')\ \mathrm{d}w', \tag{2.16}$$

$$V_{cum}(w) = \int_{w_{min}}^{w} V_{diff}(w')\ \mathrm{d}w'. \tag{2.17}$$

More advanced models, such as 2-dimensional DFT calculations [115] or quenched solid density functional theory [116], try to take into the structural or energetic heterogeneity of the walls; however, the numerical deviations to traditional NLDFT calculations are rather small in most cases. The limits for the application of DFT calculations to adsorption are adsorbates, which exhibit specific interactions with functional groups on the pore walls (the most prominent example being H_2O) or cannot be approximated by Van-der-Waals spheres.

2.2.3. Meso- and Macropores

In contrast to micropores, the size of meso- and macropores is significantly larger than the effective range of adsorbent-adsorptive interaction. Therefore gas adsorption in meso- and macropores is usually strongly dependent on the fluid-fluid interaction of the adsorptive, in particular once the surface area of the pore is fully covered by adsorbate. Mesoporous materials exhibit adsorption isotherms of type IV or V, while adsorption measurements on macroporous materials result in type II, III or VI adsorption isotherms (Figure 2.2). The distinction between the adsorption isotherms of meso- and macroporous materials arises from the experimental resolution of capillary condensation, which describes the spontaneous filling of the pore volume with adsorbate at a relative gas pressure below $p/p_0 = 1$. Capillary condensation separates the adsorption isotherm of mesoporous materials into two regimes: the film regime, where the pore wall is covered by an adsorbate film consisting of one or multiple layers of atoms/molecules, and the filled pore regime, where the entire pore volume is filled by adsorbate except for menisci at the adsorbate-adsorptive interface at the pore entrances. The adsorption isotherms of many mesoporous materials exhibit an adsorption hysteresis between adsorption and desorption branch, i.e., capillary condensation and its reversed process capillary evaporation occur at different relative pressures.

Generally, models for the adsorption in meso- and macropores are to be separated into classically models and molecular approaches involving computational and/or statistical methods. The essential difference between both types of models is that molecular approaches explicitly calculate the configuration of the adsorbed atoms/molecules within pores, while classical models assume properties of bulk liquid for the adsorbed phase. Therefore molecular approaches such as Grand

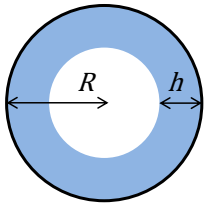

Figure 2.4.: Adsorbate film of thickness h in a cylindrical pore of radius R.

Canonical Monte Carlo (GCMC) simulations and density functional theory (DFT) calculations are considered to be superior for the description of adsorption, if the interaction for the investigated adsorbent-adsorptive combination can be described adequately within the framework of the respective approach [99]. However, the advantage of classical models is their analytical formulation, which is often more instructive than a computational method, in particular for the understanding of adsorption-induced stress in mesopores discussed in sections 2.3.2 and 2.3.3. In the following adsorption in meso- and macropores is therefore illustrated within the framework of the classical Derjaguin-Broekhoff-de Boer (DBdB) theory [117–119] for pores of cylindrical geometry. The deviations between DBdB theory and computational models become negligible for pore sizes exceeding about 6 nm [84, 120], since the adsorbate usually tends to liquid like properties for increasing pore size. From the perspective of modeling a distinction of meso- and macroporous is not required.

The foundation of the DBdB theory is the superposition of the adsorbate interaction with a plain adsorbent surface and the capillary effect arising from the curved adsorbate-adsorptive interface. For a cylindrical pore of radius R at thermodynamic equilibrium this approach leads to the following relation for the chemical potential in adsorptive and adsorbate:

$$\mu = R_g T \cdot \ln\left(p/p_0\right) = -V_L \left[\Pi\left(h\right) - \frac{\gamma_{lv}}{R-h}\right]. \tag{2.18}$$

Here R_g is the gas constant, V_L is the molar volume of the adsorptive in liquid form, Π is the disjoining pressure, γ_{lv} is the liquid-vapor surface tension of the adsorptive, R is the radius of the cylindrical pore and h is the thickness of the adsorbed layer (Figure 2.4).

The disjoining pressure Π is the pressure within the adsorbed film resulting from the adsorbate-adsorbent interaction, which is assumed to be independent of the pore geometry. Typically $\Pi(h)$ is determined from experimental data on a macroporous reference system with similar surface properties and known specific surface area. The respective procedure is exemplified in the Appendix B.

Solving Eq. 2.18 for the film thickness h results in the function $h(p/p_0)$ describing

the adsorption inside the cylindrical mesopore prior to capillary condensation. The specific adsorption isotherm of the cylindrical pore in film regime $N_{a,film}/m_{sample}$ is given by

$$\frac{N_{a,film}}{m_{sample}}\left(p/p_0\right) = \frac{S_{DBdB}}{2V_L} \cdot \frac{2Rh\left(p/p_0\right) - h\left(p/p_0\right)^2}{R}, \tag{2.19}$$

where $S_{DBdB} = 2\pi RL/m_{sample}$ is the specific surface area of the cylindrical pore of length L. Due the classical nature of DBdB theory the specific adsorption isotherm in the filled pore regime $N_{a,filled}/m_{sample}$ simply corresponds to the situation of a liquid filled pore:

$$\frac{N_{a,filled}}{m_{sample}} = \frac{S_{DBdB}}{2V_L} \cdot R = \text{const.} \tag{2.20}$$

The transitions between film and filled pore regime, i.e., capillary condensation and evaporation, take place at the film thicknesses h_c and h_e, respectively. Capillary evaporation occurs at the energetic equilibrium of a pore covered by a film of thickness h_e and a liquid filled pore, which is given the Derjaguin equation

$$R_g T \cdot \ln\left(p_e/p_0\right) = -2V_L\left[\frac{\gamma_{lv}}{R-h_e} + \frac{1}{\left(R-h_e\right)^2}\int_{h_e}^{R}\left(R-h'\right)\Pi\left(h'\right)\,\mathrm{d}h'\right]. \tag{2.21}$$

Here p_e denotes the gas pressure corresponding to h_e according to Eq. 2.18. Contrary to capillary evaporation, capillary condensation results from the spontaneous collapse of the film state, when the increasing concave curvature of the adsorbate film cannot be balanced anymore by the solid-fluid attraction. The critical film thickness for the stability of the film h_c is given by

$$\left.\frac{\mathrm{d}\Pi\left(h\right)}{\mathrm{d}h}\right|_{h=h_c} + \frac{\gamma_{lv}}{\left(R-h_c\right)^2} = 0. \tag{2.22}$$

Noteworthy, for attractive solid-fluid interaction the film thickness of capillary evaporation h_e is always smaller than the film thickness at capillary condensation h_c. Thus for the hysteresis region of the adsorption isotherm, where $h_e < h < h_c$, the adsorbate film is metastable with respect to the liquid filled pore.

2.3. Adsorption-Induced Deformation

Adsorption-induced deformation denotes structural changes of the adsorbent during the adsorption process and is an intrinsic part of the adsorption phenomenon, i.e., no adsorbent is entirely inert to the interaction with the adsorbate [44]. Since the volumetric strain of the porous solid caused by adsorption is below 1 % for most adsorbate-adsorbent combinations, the models described further below assume that (i) all deformations are elastic and Hook's law is applicable, (ii) the influence of deformation on adsorption is negligible, i.e., it is sufficient to model adsorption in rigid non-deformable pores (compare ref. [73]).

It should be noted that assumption (i) was recently challenged by Mouhat et al. [95], who predicted a reduction of the adsorbent's mechanical stiffness due to the adsorption process. However, various other studies analyzing experimental data on adsorption-induced deformation found no contradiction applying Hook's law and thus within this work assumption (i) is considered to be valid.

In general, the quantitative description of adsorption-induced deformation consists of two parts: a thermodynamic model for the stress within the adsorbate and a mechanical model based on the adsorbent structure to correlate the emerging stress to the adsorbent strain. However, as pointed out in ref [44] both models are coupled, since the geometry of the mechanical model includes the pore and therefore affects the configuration of the adsorbate and ultimately the stress imposed on the nonporous solid. Nevertheless, historically there are different concepts for the understanding of adsorption-induced stress, which are summarized in the following section 2.3.1. Explicit combinations of thermodynamically derived stresses and mechanical models suitable for the materials investigated in this work are discussed in sections 2.3.2 to 2.3.4.

2.3.1. Adsorption-Induced Stress in Nanopores

Within the last century several concepts were put forward to derive adsorption-induced stresses in nanoporous materials. In the following the most accepted and wide-spread models are presented. A more comprehensive overview was recently given in ref [44].

Bangham's Law

The concept nowadays known as Bangham's law stems from the work of Bangham and Fakhoury [51] and states that the adsorbent's strain ε is proportional to the reduction of its surface energy $\Delta\gamma_s$. The reduction of the adsorbent's surface due to the adsorption process in turn is given by the Gibbs adsorption equation:

$$\Delta\gamma_s(\mu) = \int_{-\infty}^{\mu} \frac{N_a(\mu')}{A_s}\,\mathrm{d}\mu'. \tag{2.23}$$

$$\Delta\gamma_s(h) = \int_0^h \Pi(h')\,\mathrm{d}h' - h\cdot\Pi(h). \tag{2.24}$$

While Eq. 2.23 is the general formulation of the Gibbs adsorption equation [3], Eq. 2.24 corresponds to the respective formulation within the framework of DBdB theory [79].

Since according to Eq. 2.23 the surface energy of the adsorbent reduces monotonically for progressing adsorption, Bangham's law predicts monotonic expansion of the adsorbent. The explicit correlation $\varepsilon(\Delta\gamma_s)$ depends on the detailed structure of the porous material considered. For rather simple structures such

as spheres or rods correlations of surface energy and strain are e.g. given in ref [121].

As was discussed by various authors (e.g. refs [97, 122, 123]), strictly speaking the change of the surface stress Δf_s is the thermodynamic quantity responsible for the adsorbent deformation instead of the change of surface energy $\Delta\gamma_s$. While these two quantities can be expected to be numerically very close for most adsorbate-adsorbent combinations, situations may occur, where Δf_s and $\Delta\gamma_s$ deviate significantly. This issue was recently investigated by Gor and Bernstein [97]. However, Gor and Bernstein concluded that significant deviations between surface energy and surface stress are most likely limited to adsorbate-adsorbent combinations, where site-specific adsorption or the arrangement of the adsorbed molecules are of particular importance, e.g., the adsorption of H_2O on hydroxylated α-quartz [98].

Capillary Pressure

The *capillary pressure*[2] p_{cap} denotes the pressure in adsorbate filled pores arising from the adsorbate-adsorptive interface at the pore entrance. Capillary pressure is independent of pore geometry and size and in the context of adsorption experiments typically given in terms of relative pressure p/p_0 by

$$p_{cap} = \frac{R_g T}{V_L} \ln\left(p/p_0\right). \tag{2.25}$$

Notably, capillary pressure is a classical concept assuming the adsorbate to exhibite the molar volume of free liquid V_L. With respect to the adsorption-induced deformation of mesoporous materials 2.25 was successfully applied in various studies to describe experimental data in the filled pore regime, e.g., refs [27, 28, 30]. As a consequence, the proportionality of experimental strain to the logarithm of relative pressure is considered a characteristic of adsorbate filled mesopores.

Adsorption Stress Model

The adsorption stress model was originally proposed by Ravikovitch and Neimark [70] and is based on the minimization of the grand potential of the adsorbate by deformation of the pore. Therefore it can be considered a more generalized approach to adsorption-induced deformation than the previously described concepts. Quantitatively, the adsorption stress σ_a inside a pore is calculated as the derivative of the grand potential of the adsorbate Ω_a with respect to the (absolute) pore volume V at constant temperature T and chemical potential μ [70]:

$$\sigma_a = -\left.\frac{\partial \Omega_a}{\partial V}\right|_{\mu,T}. \tag{2.26}$$

[2]The term *capillary pressure* is not explicitly defined in literature. Depending on the author the term on right hand side of Eq. 2.25 is denoted as capillary pressure, Laplace pressure or capillary approximation. In this work the term capillary pressure is used to create a clear distinction from the Laplace pressure arising from curved liquid-vapor interfaces.

The grand potential of the adsorbate Ω_a is given by the Gibbs equation [124]

$$\Omega_a\left(\mu, V, T\right) = \Omega\left(\mu_r, V, T\right) - \int_{\mu_r}^{\mu} N_a\left(\mu', V, T\right) \mathrm{d}\mu', \tag{2.27}$$

where $\Omega(\mu_r, V, T)$ denotes the reference state of chemical potential μ_r and N_a is the amount of adsorbate within the pore. Common reference states are the dry pore in an evacuated state ($\mu_r \to -\infty$) and the wet pore filled with liquid at saturation ($\mu_r = 0$). To provide quantitative expressions Eq. 2.27 has to be solved by an adsorption model appropriate to the adsorption process considered, e.g. Eq. 2.10 in case of NLDFT calculations.

Depending on the pore geometry considered (sphere [70], cylinder [79] or slit [75][3]) Eq. 2.26 is given by

$$\sigma_a = -\frac{1}{4\pi R^2} \left.\frac{\partial \Omega_a}{\partial R}\right|_{\mu,T} \qquad \text{for spherical pore,} \tag{2.28a}$$

$$\sigma_a = -\frac{1}{2\pi RL} \left.\frac{\partial \Omega_a}{\partial R}\right|_{\mu,T} \qquad \text{for cylindrical pore,} \tag{2.28b}$$

$$\sigma_a = -\frac{1}{A} \left.\frac{\partial \Omega_a}{\partial w}\right|_{\mu,T} \qquad \text{for slit-shaped pore.} \tag{2.28c}$$

Here R is the radius of a spherical or cylindrical pore, L is the length of the cylindrical pore, while w and A are width and cross-sectional area of a slit-shaped pore, respectively. As discussed in a reference related to this work [129], the adsorption stress model given by 2.26 implies isotropic stress within the pore, which is strictly speaking only valid for isotropic pore geometries such as spheres. For anisotropic pore geometries such as cylinders or slits on the other hand, anisotropic adsorption stress is to be expected. In this context it is important to note that Eq. 2.28b and 2.28c correspond to the stress arising normal to the walls of cylindrical and slit-shaped pores, respectively, while stress orientated parallel to the pore walls is not explicitly considered and potentially neglected. Ref [129] therefore introduced an extension of the adsorption stress model distinguishing between adsorption stress normal to the pore wall $\sigma_{a,\perp}$ and adsorption stress orientated tangential to the pore wall $\sigma_{a,\parallel}$. For the cylindrical pore this approach resulted in:

$$\sigma_{a,\perp} = -\left.\frac{\partial \Omega_a}{\partial V_{cyl}}\right|_{\mu,T,L} = -\frac{1}{2\pi RL} \left.\frac{\partial \Omega_a}{\partial R}\right|_{\mu,T}, \tag{2.29a}$$

$$\sigma_{a,\parallel} = -\left.\frac{\partial \Omega_a}{\partial V_{cyl}}\right|_{\mu,T,R} = -\frac{1}{\pi R^2} \left.\frac{\partial \Omega_a}{\partial L}\right|_{\mu,T} = -\frac{\Omega_a}{V_{cyl}}. \tag{2.29b}$$

[3] Eq. 2.28c is closely related to the so-called *solvation pressure* investigated by various authors, e.g., refs [71, 125–128], without the context of adsorption-induced deformation.

Here $V_{cyl} = \pi R^2 L$ is the volume of the cylindrical pore. The last equality in Eq. 2.29b follows from the fact that for $L \gg R$ the adsorbate configuration within the pore is independent of the pore length and thus $\partial\Omega_a/\partial L$ is simply Ω_a/L. While $\sigma_{a,\perp}$ from Eq. 2.29a is equal to σ_a from Eq. 2.28b, it was shown in ref [129] that $\sigma_{a,\parallel}$ is clearly different from σ_a thereby illustrating the anisotropy of the stress within the adsorbate.

Analogous expressions can easily be derived for the slit-shaped pore of volume $V_{slit} = w \cdot A$:

$$\sigma_{a,\perp} = -\left.\frac{\partial\Omega_a}{\partial V_{slit}}\right|_{\mu,T,A} = -\frac{1}{A}\left.\frac{\partial\Omega_a}{\partial w}\right|_{\mu,T}, \tag{2.30a}$$

$$\sigma_{a,\parallel} = -\left.\frac{\partial\Omega_a}{\partial V_{slit}}\right|_{\mu,T,w} = -\frac{1}{w}\left.\frac{\partial\Omega_a}{\partial A}\right|_{\mu,T} = -\frac{\Omega_a}{V_{slit}}. \tag{2.30b}$$

In the following Eq. 2.28 is referred to as *original* adsorption stress model, while Eq. 2.29 and 2.30 are denoted as *extended* adsorption stress model.

2.3.2. Cylindrical Meso- and Macropores

This section deals with adsorption-induced stresses and strains in cylindrical meso- and macropores assuming the idealized structure of a cylindrical tube. The cylindrical tube as shown in Figure 2.5 is defined by an inner radius R (pore radius), an outer radius R_{out}, the respective porosity $\phi = R^2/R_{out}^2$, the length L and the pore volume $V_{cyl} = \pi L R^2$.

As described in detail in a reference related to this work [129], the modeling of adsorption-induced stress in cylindrical mesopores is performed by the combination of the classical DBdB theory (Eq. 2.18 to 2.22) and the extended adsorption stress model (Eq. 2.29). This approach leads to the anisotropic adsorption stresses orientated normal and tangential to the cylindrical pore wall, i.e., $\sigma_{a,\perp}$ and $\sigma_{a,\parallel}$, respectively. Furthermore, both $\sigma_{a,\perp}$ and $\sigma_{a,\parallel}$ have to be separated for the regimes of the film and filled state due capillary condensation/evaporation (see section 2.2.3). In summary this leads to the following set of equations:

$$\sigma_{a,\perp,film}(h) = -\frac{\gamma_s}{R} + \frac{\Delta\gamma_s(h)}{R} - \gamma_{lv}\left[\frac{1}{R-h} - \frac{1}{R}\right], \tag{2.31a}$$

$$\sigma_{a,\parallel,film}(h) = -\frac{2\gamma_s}{R} + \frac{2\Delta\gamma_s(h)}{R} + \frac{h^2}{R^2}\left[\Pi(h) - \frac{\gamma_{lv}}{R-h}\right] - \frac{2}{R^2}\int_0^h h'\Pi(h')\,\mathrm{d}h', \tag{2.31b}$$

$$\sigma_{a,\perp,filled}(p/p_0) = -\frac{\gamma_{sl}}{R} + p_0 + p_{cap}(p/p_0), \tag{2.31c}$$

$$\sigma_{a,\parallel,filled}(p/p_0) = -\frac{2\gamma_{sl}}{R} + p_0 + p_{cap}(p/p_0). \tag{2.31d}$$

Here h is the thickness of the adsorbate film on the pore wall, γ_s is the surface energy of the evacuated solid forming the pore, $\Delta\gamma_s(h)$ is the change of the solid surface energy due to the adsorption process (Eq. 2.23), γ_{lv} is the liquid-vapor surface tension of the adsorbate in liquid form, Π is the disjoining pressure, γ_{sl} is the surface energy of the liquid covered solid, p_0 the saturation pressure of the adsorptive and p_{cap} the capillary pressure according to Eq. 2.25. In the film regime the correlation between h and p/p_0 is given by Eq. 2.18.

The adsorption stress in the film regime, i.e., $\sigma_{a,\perp,film}$ (Eq. 2.31a) and $\sigma_{a,\parallel,film}$ (2.31b), can be interpreted as follows: in the evacuated state the nonporous wall material of the tube is subject to stress due to its surface energy γ_s. This pre-stress is represented by the terms γ_s/R and $2\gamma_s/R$, in Eq. 2.31b and 2.31a, respectively. The fact, that surface energy related stress in the direction parallel to the wall is twice as large as normal to the pore wall, is a simple consequence of the cylindrical pore geometry (compare e.g. ref [121]). When the adsorption process sets in, the wall material's surface energy is reduced by $\Delta\gamma_s$, i.e. Bangham's law (section 2.3.1), resulting in the stresses $\Delta\gamma_s(h)/R$ (Eq. 2.31a) and $2\Delta\gamma_s(h)/R$ (Eq. 2.31b), which cause the material to expand with respect to its evacuated state. Again the factor of two between the different stress components follows from the cylindrical geometry of the pore. For the adsorption stress tangential to the pore walls, $\sigma_{a,\parallel,film}$ (Eq. 2.31b), all remaining terms are usually second order effects, which have quantitatively only minor impact. For the adsorption stress normal to the pore wall, $\sigma_{a,\perp,film}$ (Eq. 2.31a), on the other hand an additional significant stress contribution occurs, i.e., $\gamma_{lv}\,[1/(R-h)-1/R]$. This term is a Laplace stress arising from the curvature of the adsorbate film in the radial plane of the pore, which is always negative thereby contracting the pore.

In filled pore regime the pre-stress terms of $\sigma_{a,\perp,filled}$ (Eq. 2.31c) and $\sigma_{a,\parallel,filled}$ (Eq. 2.31d) are related to the surface energy of the liquid covered wall material γ_{sl} (in direct analogy to the prestress in the film regime) and the saturation pressure of the adsorptive p_0. Furthermore, the stresses normal and tangential to the pore wall are both directly proportional to capillary pressure p_{cap} (Eq. 2.25), which is fully in line with the concept of an isostatic capillary pressure.

Of particular importance for a consistent description of the adsorption stress by Eq. 2.31 is the correlation of the surface energy of dry and wet solid, γ_s and γ_{sl}, respectively. Here, the Frumkin-Derjaguin equation [130] adapted to the cylindrical pore geometry [129] is applied:

$$\gamma_s = \gamma_{sl} + \gamma_{lv} + \frac{1}{R}\int_0^R (R-h)\,\Pi\,(h)\,\mathrm{d}h. \tag{2.32}$$

The mechanical response of the cylindrical tube to the adsorption process follows

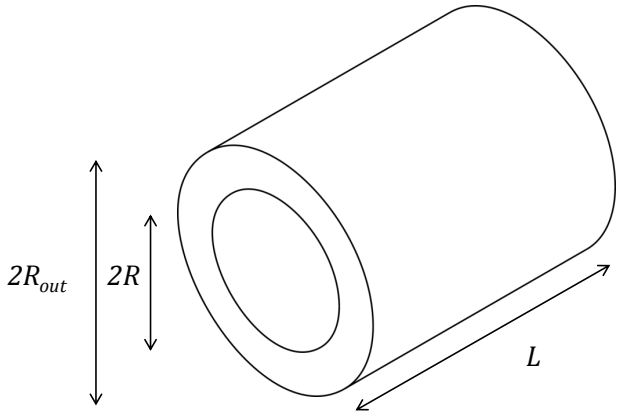

Figure 2.5.: Schematic of the cylindrical tube exhibiting the inner radius R, an outer radius R_{out} and length L. Reprinted with permission from ref [129]. Copyright 2017 American Chemical Society.

from the solution of the Lamé problem [129]:

$$\varepsilon_{a,\perp} = \frac{\Delta R_{out}}{R_{out}} = \frac{1}{E_s}\frac{\phi}{1-\phi}\left(2\sigma_{a,\perp} - \nu_s\sigma_{a,\parallel}\right), \tag{2.33a}$$

$$\varepsilon_{a,\parallel} = \frac{\Delta L}{L} = \frac{1}{E_s}\frac{\phi}{1-\phi}\left(\sigma_{a,\parallel} - 2\nu_s\sigma_{a,\perp}\right). \tag{2.33b}$$

Here $\varepsilon_{a,\perp}$ is the strain of the outer radius of the tube and $\varepsilon_{a,\parallel}$ is the strain of the tube length, while E_s and ν_s are the Young's modulus and Poisson's ratio of the nonporous solid forming the tube, respectively. Both E_s and ν_s are assumed to be constant isotropic properties.

2.3.3. Aero- and Xerogels

The disordered pore and backbone structure of aero- and xerogels (Figure 2.1) is significantly more complex than the cylindrical tube introduced in the previous section. Typically, aero- and xerogels materials consist of almost spherical particles forming a three-dimensional disordered open porous network. The pores defined by the particle network are usually in the range of meso- and/or macropores and irregular in terms of shape. In analogy to the cylindrical pore described in section 2.2.3 the adsorption isotherms of mesoporous aero- and xerogels (and thereby also the adsorption-induced strains) are to be separated in film and filled pore regime, whose transitions are given by capillary condensation and evaporation.

For low relative pressures the adsorbate forms an approximately uniform film on the particles of the aero-/xerogel [131]. In this part of the film regime the volumetric strain of the network (with respect to the evacuated state) corresponds to the volumetric expansion of the particles ε_{part}, which results from the reduction of their surface energy, i.e., Bangham's law [121]:

$$\varepsilon_{part} = \frac{\sigma_{part}}{K_{part}} = \frac{2\Delta\gamma_s}{K_{part}R_{part}}. \tag{2.34}$$

Here σ_{part} is the volumetric strain due to the change of the surface energy $\Delta\gamma_s$, while K_{part} and R_{part} are the bulk modulus and the radius of the spherical particles, respectively. If the particles are very small and/or significantly fused the adsorbate may no longer perceive individual particles but rather cylindrical rods. In this case the volumetric strain of the aero-/xerogel structure is better described by the axial strain of a cylindrical rod [121]:

$$\varepsilon_{rod} = \frac{1-\nu_{rod}}{1-2\nu_{rod}} \cdot \frac{\sigma_{rod}}{K_{rod}} = \frac{1-\nu_{rod}}{1-2\nu_{rod}} \cdot \frac{2\Delta\gamma_s}{K_{rod}R_{rod}}. \tag{2.35}$$

Here σ_{rod} is the axial strain on the cylindrical rod, while K_{rod}, R_{rod} and ν_{rod} are the bulk modulus, the radius and the Poisson's ratio of the rods, respectively.

As was shown by Scherer [55], Salazar [132] and Gommez [131], the adsorbate films of neighboring particles eventually merge with progressing adsorption and create a non-uniform adsorbate film exhibiting segments of convex and segments of concave curved liquid-vapor interface. In analogy to the cylindrical pore described in the previous section the different segments are subject to Laplace stress, whose extent depends on the local curvature of the film. As a consequence, the explicit formulation of the resulting Laplace stress within an aero-/xerogel would require for detailed structure and adsorption models in analogy to ref [132]. This represents a non-trivial task, which could not be accomplished within the scope of this work.

To obtain at least a rough estimate of the aero-/xerogel's strain due to the Laplace stress $\sigma_{Laplace}$ the cylindrical pore model from the previous section is used (compare Eq. 2.31a):

$$\sigma_{Laplace} = -\gamma_{lv}\left[\frac{1}{R-h} - \frac{1}{R}\right]. \tag{2.36}$$

Here γ_{lv} is the liquid-vapor surface tension of the adsorbate in liquid form, R is the radius of the cylindrical pore and h is the thickness of the adsorbate film within the pore. Since aero-/xerogels do not actually exhibit cylindrical pores, in this context R and h have to considered model parameters without clear physical representation. Their numerical values follow from modeling of the aero-/xerogel adsorption isotherm by DBdB theory for the cylindrical pore (section 2.2.3). Furthermore, it is assumed that deformation of the sol gel network due to the Laplace stress can be described by an average isotropic pressure on the whole aero-/xerogel network given by $\phi_{net} \cdot \sigma_{Laplace}$, where ϕ_{net} is the interparticle porosity of the aero-/xerogel network (compare ref [27]). The resistance of the porous solid to isotropic pressure is its bulk modulus K_b. This leads to Laplace stress induced strain $\varepsilon_{Laplace}$ of the aero-/xerogel

$$\varepsilon_{Laplace} = \frac{\phi_{net} \cdot \sigma_{Laplace}}{K_b} = -\frac{\phi_{net}}{K_b} \cdot \gamma_{lv} \left[\frac{1}{R-h} - \frac{1}{R} \right]. \tag{2.37}$$

Notably, due to the concave interface within the cylindrical mesopore $\varepsilon_{Laplace}$ is always negative.

In summary, the overall volumetric strain of the aero-/xerogel network in the film regime $\varepsilon_{net,film}$ is therefore given by the superposition of Eq. 2.34/2.35 and 2.37:

$$\varepsilon_{net,film} = \varepsilon_{part/rod} + \varepsilon_{Laplace}. \tag{2.38}$$

While above considerations are sufficient for a macroporous aero-/xerogel network, a mesoporous network will eventually exhibit a transition to the filled pore state via capillary condensation for increasing gas pressure. In the filled pore state the volumetric strain of the network $\varepsilon_{net,filled}$ (again with respect to the evacuated state) is described by

$$\varepsilon_{net,filled} = \Delta\varepsilon_{sl} + \frac{1}{K_b} \left[\phi_{net} \cdot p_{cap} - p \right]. \tag{2.39}$$

Here $\Delta\varepsilon_{sl}$ describes the strain of the aero-/xerogel network resulting from the expansion of the particles due to immersion in liquid. $\Delta\varepsilon_{sl}$ can be determined from Eq. 2.34 or 2.35 for spherical or strut like particles, respectively, by replacing $\Delta\gamma_s$ with the difference of surface energy between dry and wetted solid, $\gamma_s - \gamma_{sl}$ (Eq. 2.32). The second term of Eq. 2.39 can be understood as an average capillary pressure $\phi_{net} \cdot p_{cap}$ (compare ref [27]) and gas pressure p acting upon the entire porous solid of bulk modulus K_b.

2.3.4. Disordered Microporous Carbon

Historically, the first attempts to model adsorption-induced deformation of microporous carbon were based on Bangham's law (Eq. 2.23) [18, 19, 51]; recently this approach was also combined with Biot's theory of poromechanics [82]. However, a large number of experimental reports found microporous carbons to exhibit nonmonotonic deformation during gas adsorption (e.g. refs [4–6, 10, 18–21]): they contract for low stages of micropore filling and pass over to expansion with progressing adsorption. This characteristic behavior cannot be explained by Bangham's law, since Bangham's law does only predict monotonic expansion.[4] This apparent contradiction follows from the fact that Bangham's law considers adsorption on an individual plane solid surface - a situation fundamentally different from adsorption in a micropore, where solid-fluid potentials of different walls overlap (compare section 2.2.2).

[4]The nonmonotonic deformation of microporous carbons is also found for adsorbate-adsorbent combinations, for which according to Gor and Bernstein the approximation of Bangham's law should be valid. Therefore the findings of Gor and Bernstein cannot be considered a general explanation for the deformational behavior of microporous materials during gas adsorption.

The pore geometry commonly considered to be the most suitable choice for microporous carbons with respect to adsorption phenomena is the slit-shaped pore (e.g. refs [133–135]). Based on this pore geometry Lakhanpal and Flood qualitatively explained the contraction of microporous materials for low degrees of pore filling by an attractive bridging of opposing pore walls by the adsorbate [20]. Later it was shown by Ash et al. that an actual bridge of adsorbate between the walls is not necessary; the presence of the adsorbate between the plates is sufficient to induce pressure within the pore [136].

In 2006, a quantitative description of the stress induced onto micropores by the adsorption process was proposed by Ravikovitch and Neimark [70], who utilized the combination of the original adsorption stress model and NLDFT calculations. The authors interpreted the nonmonotonic deformation of a spherical micropore based on the molecular adsorbate-adsorbate and adsorbate-adsorbent interactions: for low degrees of micropore filling the adsorbates mediates the long-ranged attractive solid-fluid interaction (compare Figure 2.3) and the pore contracts, while with progressing adsorption the adsorbate density inside the micropore increases and eventually the short-ranged repulsive solid-fluid and fluid-fluid interactions translate into an expansion of the pore.

In 2008, Kowalczyk and co-workers applied the adsorption stress explicitly to slit-shaped carbon micropores utilizing Eq. 2.28c (original adsorption stress model) in combination with GCMC simulations [75]. This study found that adsorption stress in slit-shaped micropores is strongly dependent on the width of the pore due a simple geometric packing effect: if the pore width equals a multiple of the adsorbate's molecular/atomic diameter, the packing of the adsorbate inside the pore is very dense and the short-ranged repulsion of the interaction potentials causes expansive adsorption stress. However, if the ratio of pore width and adsorbate diameter is unfavorable, the packing of the adsorbate is rather loose and the attractive interaction dominates resulting in a contraction of the pore. Thus, Kowalczyk et al. concluded that the experimentally observed nonmonotonic deformation of microporous carbons during gas adsorption follows from the pore size distribution of the carbon, i.e., contracting and expanding pores are subsequently filled with adsorbate. With respect to the calculation of the adsorption stress σ_a, a volumetric averaging over the entire pore volume was therefore suggested [75]:

$$\bar{\sigma}_a = \frac{1}{V_{mic}} \int \sigma_a(w) \cdot V_{diff}(w)\, \mathrm{d}w. \tag{2.40}$$

Here V_{mic} is the specific micropore volume of the carbon matrix and V_{diff} (Eq. 2.15) is the differential specific micropore volume of pores with width w. The volumetric strain of the microporous carbon matrix ε_m was then correlated to its effective bulk modulus K_m:

$$\varepsilon_m = \frac{1}{K_m} \left[\phi_{mic} \cdot \bar{\sigma}_a - p \right]. \tag{2.41}$$

where ϕ_{mic} is the porosity of the microporous matrix and p is the external gas pressure. Eq. 2.41 can be interpreted as an effective internal stress $\phi_{mic} \cdot \sigma_a$ acting on the carbon matrix, which is simultaneously compressed by the external gas pressure p.

Due the shortcomings of the original adsorption stress regarding anisotropic pore geometries (see section 2.3.1) this work also applies the extended adsorption stress model to describe the strain of microporous materials. This approach has not been reported so far and requires a more complex model of the carbon matrix than used in the original adsorption stress model. The structural model used in this work is shown in Figure 2.6 and follows from the substructure of microporous carbons investigated in this work, i.e., carbon xerogels, as described in refs [137, 138]: the microporous matrix consist of (nonporous) nanometer sized graphitic domains denoted as *microcrystallites*, whose interspaces form micropore volume [138]. For the model, the microcrystallites are assumed to be cubic and connected edge wise, which has to be considered an approximation [137, 138]. With respect to modeling of adsorption and adsorption-induced stress it is furthermore assumed that the wedge-shaped interspaces between the microcrystallites can be reasonably approximated by a volumetric distribution of slit-shaped pores. The major advantage of the structure shown in Figure 2.6 compared to the approach of the original adsorption stress model is its capacity to separate the net strain of the microporous matrix ε_m into strain resulting from actual deformation of the nonporous solid skeleton, i.e., the cubic microcrystallites, and its rearrangement:

$$\varepsilon_m = \varepsilon_s + \phi_{mic} \cdot \varepsilon_\beta. \tag{2.42}$$

Here the strain ε_s describes isotropic volumetric changes of the cubic microcrystallites without changes to the cube arrangement, i.e., strain at constant angle β (compare Figure 2.6). On the contrary, the strain ε_β denotes the change of the pore volume at constant solid volume, i.e., strain of the matrix due to changes of the angle β.

To correlate ε_s and ε_β to the stresses predicted by the extended adsorption stress model for slit-shaped pores, $\sigma_{a,\perp}$ (Eq. 2.30a) and $\sigma_{a,\parallel}$ (Eq. 2.30b), the following assumptions are made: the stress $\sigma_{a,\parallel}$ acting tangential to the skeleton-pore interface affects the cubic microcrystallites on all sides effectively creating an isotropic stress σ_s within the solid. Due to the stress balance at thermodynamic equilibrium the transfer of $\sigma_{a,\parallel}$ onto the solid is then given by (compare [129]):

$$\sigma_s = \frac{\phi_{mic}}{1 - \phi_{mic}} \cdot \sigma_{a,\parallel}. \tag{2.43}$$

Additionally, the adsorption stress $\sigma_{a,\perp}$ orientated normal to the cube walls acts upon the solid leading to the effective strain of the cubic microcrystallites of

$$\varepsilon_s = \frac{\sigma_s - \sigma_{a,\perp}}{K_s} = \frac{1}{K_s}\left[\frac{\phi_{mic}}{1-\phi_{mic}} \cdot \sigma_{a,\parallel} - \sigma_{a,\perp}\right], \tag{2.44}$$

where K_s is the bulk modulus of the nonporous skeleton, i.e., the microcrystallites.

Changes of the angle β between cubes can only be induced by stress normal to the pore walls, i.e., $\sigma_{a,\perp}$. To quantify the resulting strain ε_β an effective bulk modulus K_β is introduced, that describes the resistance of the microcrystallite interconnection with respect to changes of β. Therefore ε_β is given by

$$\varepsilon_\beta = \frac{\sigma_{a,\perp}}{K_\beta}. \tag{2.45}$$

Inserting Eq. 2.43 to 2.45 in Eq. 2.42 results in

$$\varepsilon_m = \frac{\phi_{mic}}{1-\phi_{mic}} \cdot \frac{\sigma_{a,\parallel}}{K_s} + \left(\frac{\phi_{mic}}{K_\beta} - \frac{1}{K_s}\right)\sigma_{a,\perp}. \tag{2.46}$$

Eq. 2.46 reveals that the strain of the microporous matrix is the net result of two potentially opposing mechanism represented by the terms depending on $\sigma_{a,\parallel}$ and $\sigma_{a,\perp}$, respectively. The first term related to $\sigma_{a,\parallel}$ is always positive and describes the expansion of the nonporous solid skeleton in direct analogy to Bangham's law. On the other hand, the second term related to $\sigma_{a,\perp}$ corresponds to the adsorption stress model in its original formulation. Consequently, the strain contribution related to $\sigma_{a,\perp}$ may be positive or negative depending on the particular pore size (distribution) of the carbon.

To take into account the pore size distribution of the microporous carbon, the stresses $\sigma_{a,\parallel}$ and $\sigma_{a,\perp}$ can be averaged in the same way as for the original adsorption stress model:

$$\bar{\sigma}_{a,\perp} = \frac{1}{V_{mic}} \int \sigma_{a,\perp}(w) \cdot V_{diff}(w)\,\mathrm{d}w, \tag{2.47}$$

$$\bar{\sigma}_{a,\parallel} = \frac{1}{V_{mic}} \int \sigma_{a,\parallel}(w) \cdot V_{diff}(w)\,\mathrm{d}w. \tag{2.48}$$

In the limit of an incompressible skeleton ($K_s \to \infty$) Eq. 2.46 is reduced to $\varepsilon_m = \phi_{mic}/K_\beta \cdot \bar{\sigma}_{a,\perp}$, which is essentially the original adsorption stress model, since the gas pressure p is usually negligible compared to $\sigma_{a,\perp}$.

An aspect of particular relevance for the validation of the results derived by the extended adsorption stress model is the correlation of the mechanical parameters K_s and K_β to the effective bulk modulus of the microporous matrix K_m. Since the carbon microcrystallites in the considered model are fully interconnected, it is assumed that the carbon matrix can be described by the Gibson-Ashby model (Eq.

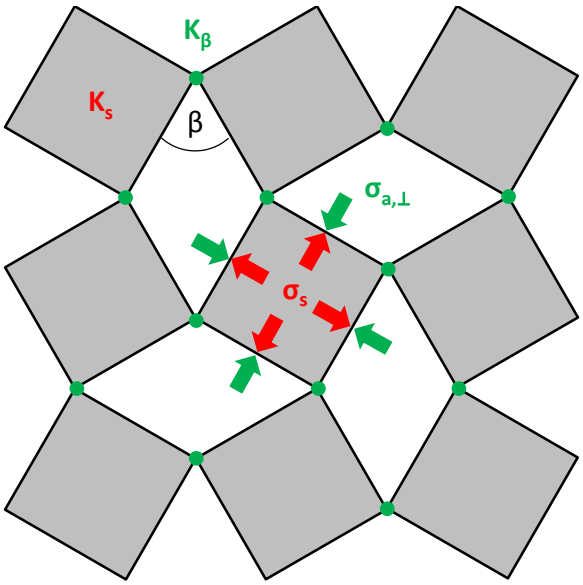

Figure 2.6.: Schematic of the microporous matrix for the extended adsorption stress model. K_s is the bulk modulus of the nonporous solid cubes and K_β represents the resistance of the cube network to changes of the angle β. The stresses σ_s and $\sigma_{a,\perp}$ result from gas adsorption within the pores.

2.8). If furthermore the Poisson's ratios of nonporous skeleton and microporous matrix do not deviate drastically, the following approximation holds:

$$K_m = K_s \cdot (1 - \phi_{mic})^2 . \tag{2.49}$$

3. Model Materials and Experimental Methods

This chapter summarizes the model materials investigated, the characterization techniques applied and the experimental technique used to study the effect of adsorption-induced deformation, i.e., in-situ dilatometry.

3.1. Model Materials

The model materials investigated in this work were chosen in order to cover adsorption-induced deformation of micro- and mesopores in ordered as well as in disordered systems; a classification of the applied model materials is shown in Figure 3.1. Typically ordered materials are considered better model materials due to their well defined structure, however, the vast majority of technically relevant nanoporous materials exhibits various degrees of structural disorder (one of the most prominent examples being microporous carbon). Therefore the comparison of adsorption-induced deformation effects in ordered and disordered materials is of interest in particular for application related follow-up work.

	ordered	disordered
microporous	zeolites	amorphous carbon (xerogel)
mesoporous	hierarchically structured porous silica	amorphous silica (aerogel)

Figure 3.1.: Classification of the model materials investigated with respect to the pore size regime most relevant for adsorption-induced deformation and the material's structural order.

Most investigations within the framework of this thesis focus on microporous materials, in particular on microporous carbons, because it was only recently that theoretical models successfully approached the issue of adsorption-induced deformation of micropores. Consequently, reliable experimental data of adsorption-induced deformation of microporous materials in combination with thorough sample characterization are considered a valuable foundation for validation and refinement of the proposed theoretical concepts. Since microporous materials may also contain mesopores, investigations of selected mesoporous silica complement the list of model materials analyzed. The purely mesoporous silica materials allow for studies of adsorption-induced deformation in mesopores independent of micropore deformation effects.

3.1.1. Carbon Xerogels

The synthetic amorphous carbons used in this work were derived from organic precursors prepared via the sol-gel process as described in ref [139] with some modifications with respect to educt ratios, gelation/aging period and drying [140]. For the preparation of the organic precursors the molar ratio R/C of resorcinol to catalyst was 5000 for all samples, while the mass ratio M of resorcinol and formaldehyde to the mass of the total starting solution was either 30 or 50 %. The gelation and aging period was 24 h at 85 °C for all samples. Subsequently, the samples were placed for at least 1 d in an excess of ethanol (bath volume roughly 10times larger than the sample volume) to exchange the aqueous phase within the gel pores by ethanol. Finally, the organic precursors were dried under ambient conditions in a fume cupboard and then pyrolized for 1 h in an Ar atmosphere at a temperature T_{pyr} of either 800 or 900 °C (heating rate 4 K/min).

The resulting carbon xerogels are amorphous non-graphitizable monolithic carbons [141] consisting of a disordered three-dimensional network of interconnected, approximately spherical particles, whose interspaces form meso- and/or macropores [142] (compare Figures 2.1 and 3.2). The particle size and the interparticle porosity depend on the synthesis parameters R/C and M, respectively, and can be varied over a large range [140, 143, 144]; in contrast the internal structure of the particles was found to be very similar for most R/C-M combinations [143, 145–147]. The particles are built up by small graphitic domains referred to as *microcrystallites* forming micropores in their interspaces (Figure 3.2) [142]. The arrangement of the microcrystallites is considered highly disordered, though some authors suggested a higher degree of order towards the surface of the particles [137]. At T_{pyr} between 800 and 900 °C the dimensions of the microcrystallites are about 3 nm lateral [142] and 1 nm perpendicular to the graphene layers [138]. The distance between graphene layers is about 0.4 nm [138] and therefore larger than the value of 0.3355 nm found for macroscopic graphite crystals [137]. The size of the micropores as evaluated from small angle X-ray scattering data is about 0.5 nm [138].

With respect to this work the advantages of carbon xerogels are the capabilities of

- producing monolithic samples without an additional binder phase, whose form can be adapted to the requirements of the in-situ dilatometry set-up.
- deliberately varying the parameters of the xerogel network, in particular the average diameters of particles and interparticle pores via the synthesis parameters.
- modifying the micropore structure of the carbon xerogels by after treatments, i.e., *activation* and *thermal annealing*, without significantly affecting the meso- and macropore structure.

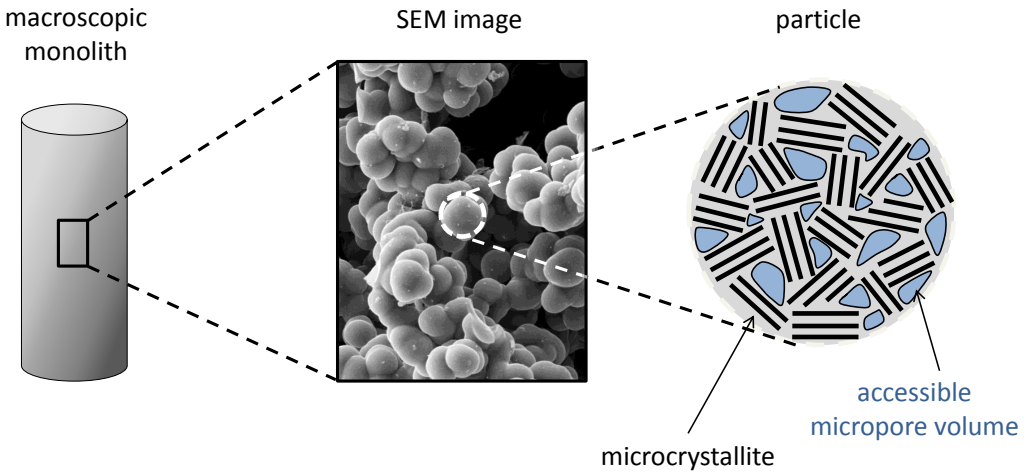

Figure 3.2.: Schematic of the different structural levels of carbons xerogels, i.e., (from left to right) the monolithic sample, the particle network as seen by scanning electron microscopy (SEM) and the internal particle structure according to refs [137, 142].

After Treatment: Activation

The activation of carbon xerogels does not differ from the activation of other amorphous carbons and was already described by various authors, e.g. refs [145, 147–149]. Generally, the term *activation* describes chemical or physical modifications of carbons increasing their accessible surface area. Chemical activation is typically carried out by hot acids, while thermal activation involves reactions with oxidizing gases (typically H_2O, CO_2 or air) at temperatures between 800 and 1100 °C [133]. In this work activation of carbon xerogels was performed for 2 h in a mixed Ar-CO_2 atmosphere at 850 °C. The underlying reaction is the Boudouard equilibrium [150]

$$C\,(s) + CO_2 \rightleftarrows 2CO\,(g)\,. \tag{3.1}$$

The reaction of carbon with CO_2 is endothermic and therefore requires continuous heating but simultaneously allows for more control of the process [133]. An important parameter of the activation process is the so-called *burn-off*, i.e., the relative mass loss of the carbon by the activation process. Depending on the degree of burn-off the structural change of the carbon is expected as follows [133]: the first step of activation is the removal of disordered carbon structures opening blocked pores and/or improving access to already existing pores. With progressing activation also the ordered carbon structures are affected by the activation process. This leads to a widening of the already existing pores and eventually to the creation of significantly larger pores by removal of walls between adjacent pores. In this work the burn-off was purposefully kept low (about 5 wt%) to prevent modifications of the carbon beyond the micropore scale.

A potential side effect of the activation process is the modification to the functional groups on the carbon surface. For the above described activation pro-

cedure X-ray photoelectron spectroscopy (XPS) measurements e.g. revealed that the amount of oxygen on a carbon xerogel surface increases from 2.0 to 3.1 at% for a burn-off of approximately 10 wt% [151, 152]. Changes to the carbon's functional groups may have tremendous effect on its adsorption properties with respect to polar adsorbate molecules such as H_2O, see e.g. refs [153–158]. However, for the adsorbates applied to carbons activated in this work, i.e., N_2 and CO_2, the impact was considered negligible.

After Treatment: Thermal Annealing

In the context of carbon xerogels the term *thermal annealing* commonly refers to the exposure of the carbon to temperatures exceeding 1000 °C in a non-oxidizing atmosphere [138, 159–161]. The thermal annealing can be performed directly during the pyrolysis or subsequent to pyrolysis as a separate after treatment. In either case, the thermal annealing has a significant impact on the properties of the microcrystallites and therefore also on the microporosity of the carbon: in the temperature range of 1000 to 1800 °C the lateral size of the microcrystallites increases from 3 to nearly 5 nm [159, 161] but remains constant for higher temperatures [161]. For temperatures exceeding 1500 °C also the size perpendicular to the graphene layers grows from 1 to about 1.5 nm at 2000 °C [138, 160]. In parallel the interlayer distance of the graphene layers decreases with increasing temperature [162]; this process is particular pronounced for temperatures above 1800 °C [138, 160], however, the interlayer distance of natural graphite is not reached. The accessibility of the microporosity between the microcrystallites decreases with the thermal annealing temperature [138, 160, 161, 163], although the total (partially closed) micropore volume and its average micropore size were found to increase along with the microcrystallites [138]. The progressing closure of micropores was interpreted by Dahn et al. by a "falling cards model" [163, 164], which assumes a successive alignment of graphene sheets with neighboring microcrystallites. On a side note, it is currently not clear whether the growth of the microcrystallites during the annealing process blocks the pore access entirely or just decreases it to the point, where the microporosity appears inaccessible for most fluids.

In this work thermal annealing was performed as an after treatment. Carbon xerogels were exposed to 1200, 1400, 1600 and 1800 °C, respectively, for 15 min under Ar atmosphere.

Denotation of Carbon Xerogel Samples

The labeling of the different carbon samples investigated in this work was chosen to reflect their synthesis parameters R/C, M and T_{pyr} as well as their potential after treatment, i.e., activation or thermal annealing. An overview over all prepared carbon xerogels is given in Table 3.1. To meet the requirements of the in-situ dilatometry setup described in section 3.3.3 all samples were prepared as cylindrical rods of 3 to 5 mm in diameter and 3 to 5 cm in length.

Table 3.1.: Carbon xerogels investigated in this work, their synthesis parameters and after treatments. E.g. the label *C5000/50/1200* denotes a carbon xerogel, whose organic precursor was synthesized for the parameters $R/C = 5000$ and $M = 50$. The sample was then pyrolized and thermally annealed at 1200 °C.

sample	R/C	M [%]	T_{pyr} [°C]	after treatment
C5000/30/800	5000	30	800	-
C5000/50/800	5000	50	800	-
C5000/50/900	5000	50	900	-
C5000/50/900A	5000	50	900	activation
C5000/50/1200	5000	50	1200	annealing 1200 °C
C5000/50/1400	5000	50	1400	annealing 1400 °C
C5000/50/1600	5000	50	1600	annealing 1600 °C
C5000/50/1800	5000	50	1800	annealing 1800 °C

The samples C5000/30/800 and C5000/50/800 were prepared by Timo Wildhage [165] and the organic precursors for the other carbon samples were prepared by Dr. Matthias Wiener.

3.1.2. Zeolites

Zeolites are microporous aluminosilicates exhibiting cage like micropore structures [2]. The zeolite samples investigated in this work were provided by *CWK Chemiewerk Bad Köstritz*: one zeolite of type LTA, KÖSTROLITH 4ABFK [166], and one zeolite of type FAU, KÖSTROLITH 13XBFK [167]. Both zeolites were produced from zeolite powder, metakaolin and lye, where metakaolin serves as a temporary binder for the zeolite powder, which is eventually also converted into zeolite [168, 169]. This procedure results in binderless monolithic zeolites; in contrast, most commercially available zeolites contain a non-zeolite binder phase. The lack of binder is of particular importance for this work, because it allows for an unambiguous attribution of the observed adsorption-induced deformation to the zeolite. Notably, this was not the case for previous studies on adsorption-induced deformation on zeolites including a clay binder phase [35, 36].

Both monolithic zeolite samples, KÖSTROLITH 4ABFK and 13XBFK, exhibit two levels of internal structure: a disordered macroporous network of polycrystalline zeolite and a well-ordered micropore structure within the individual zeolite crystals. Detailed investigations of the macropore structure are given in ref [170]. The micropore structure of both zeolite types is shown in Figure 3.3. The KÖSTROLITH 4ABFK exhibits a cubic structure with six circular entrances into the micropore, whose diameter is 0.41 nm [171]. The KÖSTROLITH 13XBFK on the other hand exhibits a roughly spherical pore shape with four circular entrances of 0.74 nm in diameter [171]. With respect to gas adsorption it is important to

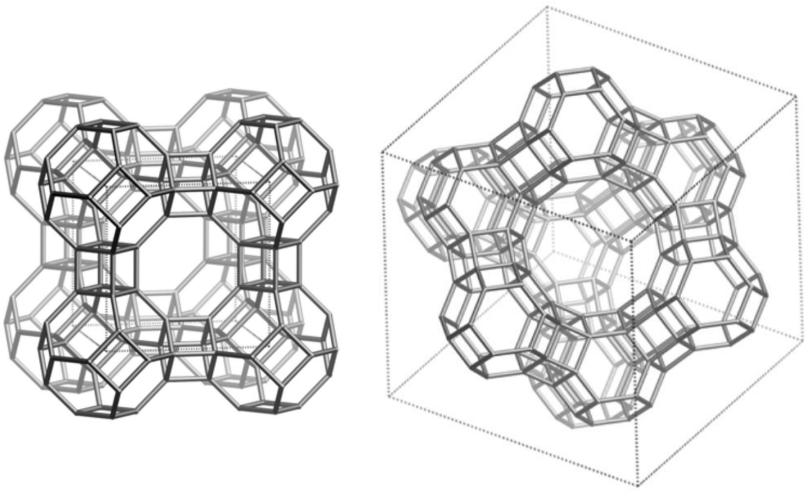

Figure 3.3.: Schematics of zeolite unit cells for LTA and FAU structures (KÖSTROLITH 4ABFK, LTA (left) and KÖSTROLITH 13XBFK, FAU (right) [171]).

note, that the above given dimensions correspond to distances from atom center to atom center. Therefore adsorbate molecules perceive smaller pore sizes and entrances due to the volume occupied by the nonporous solid phase. This effect can be seen e.g. from ref [70], where the adsorption of a FAU type zeolite was described under the assumption of spherical pores resulting in an accessible pore diameter of 0.6 nm instead of 0.74 nm.

Zeolites were included in this work, since their microporosity is highly ordered and well defined eliminating ambiguity about shape and size (distribution) of the micropores. The drawback of zeolites are the complex solid-fluid interactions within the micropores compared to carbons, which makes modeling of the adsorption process significantly more challenging (compare ref [70]).

3.1.3. Silica Aerogel

The silica aerogel investigated was produced by *Airglass* (Staffanstorp, Sweden) via a sol-gel process using tetramethoxysilane as precursor [172]. In analogy to carbon xerogels, silica aerogels are built up by disordered three-dimensional network of approximately spherical particles (compare Figures 2.1 and 3.2); however, in contrast to carbon xerogels, the particles itself are generally nonporous consisting of pure amorphous silica. The pore volume of the particle network is typically mesoporous only making silica aerogels a good model system for a disordered mesoporous solid. Since untreated silica aerogels tend to be so compliant that they undergo significant elastic or even plastic deformation during a gas adsorption process [27], the sample investigated in this work was sintered in order to increase its mechanical stiffness and thus prevent plastic effects. The sintering was performed at ambient atmosphere at a temperature of 1050 °C for approximately 13 min. During the sinter process the solid phase of the silica aerogel rearranges

in a viscous flow driven by the reduction of the local curvature of the silica phase [173]. This caused a reduction of the aerogel's specific surface area by 44 % and its total specific pore volume by 37 %; in parallel its density increased by 84 % and its Young's modulus by nearly 1200 %.[1] The drastic increase of silica aerogel's Young's modulus results from the increase of its bulk density (Eq. 2.9) and the reinforcement of the connections between particles.

Synthesis, sintering and pre-sintering characterization of the silica aerogel investigated in this work was performed by Dr. Gudrun Reichenauer. A sample of similar treatment was described in ref [57].

3.1.4. Hierarchical Structured Porous Silica

The hierarchical structured porous silica investigated in this work was provided by the group of Prof. Dr. Nicola Hüsing (Paris-Lodron University, Salzburg) within the scope of the project *Deformation of Hierarchical and Anisotropic Solids by Fluid Adsorption* (German Science Foundation, RE1148/10-1). The subsequent sintering was performed within the master thesis of Anna M. Waag [175].

Following the synthesis protocols given in refs [176, 177] a hierarchically structured porous silica sample was prepared by a sol-gel process, which utilizes a surfactant as a structural directing agent. When diluted in aqueous HCl, the surfactant molecules form cylindrical shaped micelles, which arrange in a hexagonal pattern. The surfactant-HCl solution is then mixed with a modified silane that forms a gel in between the cylindrical micelles. When gelation was completed, the sample was immersed into trimethylchlorosilane (TMCS) and subsequently dried under ambient conditions. TMCS covers the surface of the gel making it hydrophobic; this enables the gel to be dried at ambient conditions without structural damage by the capillary pressure of the solvent. The resulting hierarchical structured silica is a monolith (here with respect to the requirements of the in-situ dilatometry setup shaped as a cylinder), which exhibits two structural levels schematically illustrated in Figure 3.4. On the scale of macropores the material consists of a three-dimensional disordered strut network, where the individual struts are approximately of 500 nm in diameter and 2-3 µm in length [176]. Inside the struts well-defined and ordered cylindrical mesopores of approximately 7 nm in diameter are arranged on a hexagonal lattice [176].

The sample investigated in this work was furthermore calcined for 10 h at 500 °C in ambient atmosphere to remove the TMCS and residual surfactant. Since the calcination step is known to introduce microporosity into the silica phase, the sample was additionally subjected to sintering at 950 °C for 15 min under ambient atmosphere. As described in the previous section sintering of silica materials evens out structural inhomogeneities, i.e., in this case the microporosity.

[1] The silica aerogel in its untreated state exhibit a total specific pore volume of 5.18 cm^3/g, a density of 1.45 g/cm^3, a specific surface area of 683 m^2/g and a Young's modulus of 4.5 MPa [174].

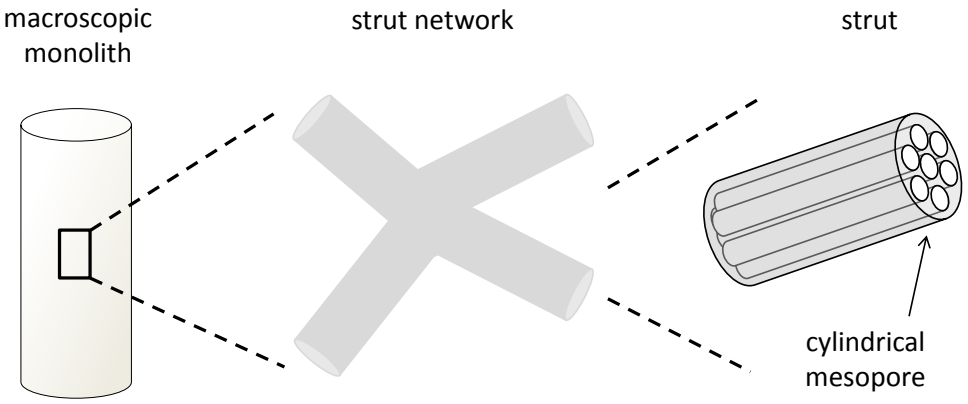

Figure 3.4.: Schematic of the hierarchically structured porous silica.

From the perspective of adsorption induced-deformation hierarchically structured porous silica was recently of particular interest, since it provides one of the rare cases, where adsorption-induced deformation can be investigated on the scale of monolithic samples (e.g. by in-situ dilatometry) as well as on the scale of the mesopore lattice (e.g. by in-situ small angle X-ray scattering) [178].

3.2. Characterization Techniques

The major goal of the material characterization performed in this work was to obtain the input parameters required for the theoretical models of adsorption-induced deformation or validate their respective output parameters.

3.2.1. Determination of Bulk Density

The (apparent) bulk density of a monolithic sample is given by

$$\rho_b = \frac{m_{sample}}{V_{sample}}, \tag{3.2}$$

where m_{sample} denotes the sample mass and V_{sample} the monolithic sample volume. Since porous solids tend to adsorb significant amounts of atmospheric gases (in particular H_2O), the determination of m_{sample} requires preliminary degassing under vacuum conditions. For meso- and macroporous materials a temperature of 110 °C is typically sufficient to remove adsorbed species within 1 d, while microporous samples exhibit higher adsorption potentials and are therefore degassed at temperatures up to 400 °C. After degassing is completed the sample has to be placed on a balance without anew adsorption. Since the process of degassing and weighing is also mandatory prior to each adsorption measurement, commercial sorption instruments possess a special degas station for this particular purpose. The design of the degas station used in this work and the work steps to obtain the mass of the degassed sample m_{sample} are described in [179].

For samples of well defined monolithic geometry the sample volume V_{sample} can simply be calculated from the sample dimensions measured by a caliper. Contrary, for ill defined monolithic geometry this approach to V_{sample} is often not possible. In such cases an alternative way to obtain ρ_b is Eq. 2.1, which requires knowledge of the total specific pore volume V_p and the density of the nonporous backbone ρ_s.

3.2.2. Gas Adsorption Measurements

Gas adsorption measurements for sample characterization were performed for the established adsorptive-temperature combination of N_2/77 K and CO_2/273 K. The combination of N_2/77 K is known for two disadvantages [180]: a) the N_2 molecule exhibits a small quadrupole moment, which may cause specific interactions with the adsorbent surface. b) at the cryogenic temperature of 77 K diffusion of gas molecules in (ultra)micropores may become extremely slow preventing reliable determination of equilibrium gas pressures. In such cases CO_2 adsorption at 273 K is often used as an alternative approach.

All adsorption isotherms presented in this work were recorded by a commercial volumetric adsorption instrument (ASAP2020, Micromeritics), which was also used as part of the in-situ dilatometry setup described in the following section. For details regarding the experimental setup and the measurement procedure see section 3.3. Notably, experimental adsorption isotherms are commonly given as specific adsorption N_a/m_{sample}, where N_a is the molar amount adsorbed and m_{sample} is the mass of sample investigated.

Although there is a large number of models for the evaluation of adsorption isotherms [3], many of them are only valid for particular pore sizes regimes or adsorbate-adsorbent combinations. The adsorption models suitable for the materials investigated in this work are briefly described in the following.

Gurvich Rule

The Gurvich rule was proposed by Gurvich [181] and assumes that the density of the adsorbate is equal to the one of unconfined bulk fluid. Based on this, the amount adsorbed $N_a\,(\text{plateau})$ at the plateaus of type IV and V adsorption isotherms at relative pressures close to saturation can be converted into the combined specific micro- and mesopore volume of the sample:

$$V_{Gurvich} = \frac{N_a\,(\text{plateau})}{m_{sample}} \cdot V_L = V_{mic} + V_{meso}. \tag{3.3}$$

Here V_L is the molar volume of the adsorbate as bulk liquid. As discussed in sections 2.2.2 and 2.2.3, the density of the adsorbate phase may deviate from bulk fluid in particular for micropores and mesopores smaller than 7 nm. As was shown by atomistic adsorption models, for N_2 adsorption in carbon micro- and mesopores

the relative deviation in density can be estimated be to on the order of percent [182].

BET Theory

The BET theory of Brunauer, Emmett und Teller [183] was developed to describe adsorption on a plain solid surface. According to BET theory the adsorption isotherm of a porous solid is given by

$$\frac{N_a}{m_{sample}}(p/p_0) = \frac{N_{mono}}{m_{sample}} \cdot \frac{C_{BET} \cdot p/p_0}{(1-p/p_0)\,(1-p/p_0+C_{BET} \cdot p/p_0)}. \tag{3.4}$$

Here N_{mono} is the (molar) amount of adsorbate forming an atomic/molecular layer on the adsorbent surface (the so-called *monolayer capacity*) and C_{BET} is an energetic parameter quantifying the strength of the solid-fluid attraction relative to the fluid-fluid attraction.

For the evaluation of adsorption isotherms the BET equation is transformed to a linearized counterpart

$$\frac{p/p_0}{N_a/m_{sample} \cdot (1-p/p_0)} = \frac{1}{C_{BET} \cdot N_{mono}/m_{sample}} + \frac{C_{BET}-1}{C_{BET} \cdot N_{mono}/m_{sample}} \cdot p/p_0. \tag{3.5}$$

Inserting experimental data, $N_a/m_{sample}\,(p/p_0)$, into Eq. 3.5, the parameters N_{mono}/m_{sample} and C_{BET} are obtained from slope and axis intercept of a line of best fit. The monolayer capacity N_{mono} in turn is connected to the specific surface area S_{BET} of the porous solid by

$$S_{BET} = \frac{N_{mono}}{m_{sample}} \cdot N_A \cdot A_a, \tag{3.6}$$

where N_A is the Avogadro constant and A_a the cross-sectional area of an atom/molecule adsorbed. For N_2 adsorption at 77 K a well-established value for A_a is 0.162 nm^2 [1].

Due to the assumptions made for its derivation the BET theory is only valid for meso- and macroporous solids and even for these the BET theory commonly matches experimental data only in the range of $0.05 < p/p_0 < 0.35$, i.e., only up to the completion of the monolayer [3]. There are recommendations to adapt the BET theory for the evaluation of adsorption isotherms of microporous materials [184], but despite these adaptations the resulting surface area S_{BET} does not represent a physically meaningful area of the microporous solid [99]. Consequently in this work the BET-theory was not applied to microporous materials.

t-plot Method

The t-plot method of Lippens and de Boer [185] utilizes the Gurvich rule (see Eq. 3.3) and reference isotherms to determine the so-called specific *external* surface

area S_{ext} of meso- and macropores (i.e. $S_{ext} = S_{meso} + S_{mac}$) as well as the specific micropore volume V_{mic} (t-plot) of the sample investigated:

$$\frac{N_a}{m_{sample}} (p/p_0) \cdot V_L = S_{ext} \cdot h (p/p_0) + V_{mic} (\text{t-plot}) . \tag{3.7}$$

Here V_L is the molar volume of the adsorbate as bulk liquid and $h (p/p_0)$ is the statistical thickness of the adsorbate film on the meso- and macropore surface area (prior to capillary condensation). $h (p/p_0)$ is usually determined empirically from an adsorption isotherm on a purely macroporous reference material, whose surface chemistry is assumed to be comparable with the sample investigated. Plotting the data from experimental adsorption isotherms according to 3.7 and performing a linear fit allows for the determination of S_{ext} and V_{mic} (t-plot) from slope and intercept of the fit, respectively.

In this work the t-plot method was exclusively applied to microporous carbons and respective reference isotherm was taken from the work of Magee [186]:

$$h (p/p_0) = 0.1\text{nm} \left[0.88 \cdot (p/p_0)^2 + 6.45 \cdot p/p_0 + 2.98 \right] . \tag{3.8}$$

Noteworthy, Eq. 3.8 is only valid in the range of 0.4 nm $< h <$ 0.7 nm.

Analysis by DFT and GCMC

The analysis of experimental adsorption isotherms by computational approaches such as density functional theory (DFT) and grand canonical Monte Carlo (GCMC) is usually based on the inversion of the integral adsorption equation (IAE). For the slit-shaped pore geometry the IAE can be formulated as (compare Eq. 2.14):

$$\frac{N_a}{m_{sample}} (p/p_0) = \int_{w_{min}}^{w_{max}} N_{kernel} (p/p_0, w) \cdot S_{diff} (w) \, \mathrm{d}w. \tag{3.9}$$

Here N_{kernel} is the so-called kernel of the computational model, i.e., a series of computationally determined surface specific adsorption isotherms for different pore sizes, and S_{diff} is the specific differential pore area distribution with respect to the pore width w; w_{min} and w_{max} are the smallest and the largest pore width within the kernel, respectively. S_{diff} is directly related to the specific differential pore volume distribution $V_{diff} (w)$, the specific cumulative pore area distribution S_{cum} and the specific cumulative pore volume distribution V_{cum} (Eq. 2.15, 2.16 and 2.17, respectively). Fitting of experimental adsorption isotherms requires the numerical deconvolution of the IAE typically performed by Tikhonov regularization [187]. It is important to note that the deconvolution of the IAE is an ill-posed problem from the mathematical point of view and therefore there is no unambiguous solution for S_{diff}.

In this work the above described approach was used to analyze the microporosity of carbon xerogels based on NLDFT calculations performed for N_2

adsorption at 77 K and CO_2 adsorption at 273 K. The respective kernels were created within the framework of this work [188] assuming slit-shaped pore geometry (see section 4.1). In this case, the specific micropore volume $V_{mic}\,(\mathrm{DFT})$, the specific micropore area $S_{mic}\,(\mathrm{DFT})$ and the average micropore width $\bar{w}$ can be derived from the specific differential pore area distribution S_{diff} by:

$$V_{mic}\,(\mathrm{DFT}) = \int_0^{2\,\mathrm{nm}} V_{diff}\,(w)\;\mathrm{d}w, \tag{3.10}$$

$$S_{mic}\,(\mathrm{DFT}) = \int_0^{2\,\mathrm{nm}} S_{diff}\,(w)\;\mathrm{d}w, \tag{3.11}$$

$$\bar{w} = \frac{2V_{mic}\,(\mathrm{DFT})}{S_{mic}\,(\mathrm{DFT})}. \tag{3.12}$$

Since micropore filling and monolayer formation in meso- and macropores may occur in the same relative pressure regime, the kernels included a set of slit-shaped mesopores. The fitting algorithm for the deconvolution of the IAE was taken from Ravikovitch et al. [113].

3.2.3. Sound Velocity Measurements

Sound velocity measurements were performed with a setup developed by Gross [189, 190]. The setup consists of an ultrasonic emitter connected to an ultrasonic pulse generator and an ultrasonic receiver connected to an oscilloscope. The sample is placed between emitter and receiver and the distance l_{sound} between them is measured by an indicator. The pulse generator simultaneously triggers the ultrasonic emitter and the recording of the oscilloscope. This way the runtime Δt of the ultrasonic pulse through sample can measured on the display of the oscilloscope. The emitted waves are longitudinal and of frequencies of 0.5 or 1.0 MHz depending on the settings of the setup. The longitudinal sound velocity v_{sound} of the sample is calculated by

$$v_{sound} = \frac{l_{sound}}{\Delta t}. \tag{3.13}$$

From the longitudinal sound velocity the linear modulus C_{11} of the sample is calculated by [191]

$$C_{11} = \rho_b \cdot v_{sound}^2, \tag{3.14}$$

which in turn can be transferred into Young's and bulk modulus of the porous solid for given bulk Poisson's ratio ν_b [100]:

$$E_b = \frac{(1-2\nu_b)\,(1+\nu_b)}{1-\nu_b} \cdot C_{11}, \tag{3.15}$$

$$K_b = \frac{1+\nu_b}{3\,(1-\nu_b)} \cdot C_{11}. \tag{3.16}$$

3.2.4. Scanning Electron Microscopy (SEM)

All microscopy images were made with the scanning electron microscope *Ultra Plus* by Carl-Zeiss NTS Gmbh. To obtain images a focused electron beam (acceleration voltage 1 to 30 keV) sweeps in a raster across the sample surface producing different types of signal including back scattered electrons, secondary electrons and characteristic X-rays. The signals used for image formation are backscattered electrons and secondary electrons, which are measured locally resolved for each beam position by respective detectors. Details on the instrument and the microscopic technique are given in refs [192, 193], respectively. Notably, microscopy images only represent a very small part of the sample investigated.

3.3. Gas Adsorption Measurements with in-situ Dilatometry

In order to experimentally access the adsorption-induced deformation of the model materials presented in section 3.1 this work utilized a dilatometer integrated into a commercial volumetric sorption instrument (ASAP2020, Micromeritics). The combined setup was developed by Wildhage and Balzer [10, 165, 194] based on a prototype of Reichenauer and Scherer [27] and allows for state-of-the-art adsorption measurements complemented by in-situ dilatometry. The experimental data obtained by this setup are the common adsorption isotherm $N_a/m_{sample}\,(p/p_0)$ and the dilatometric strain isotherm $\varepsilon_{dil}\,(p/p_0)$ of the sample, i.e., the linear strain of the sample investigated corresponding to its adsorption isotherm. For the measurements performed in this work the dilatometric part of the setup was subject to further modifications to improve the suppression of disruptive effects and ensure reproducible measurements at high strain resolutions. In the following the final version of the overall setup and the applied measurement procedures are described. Also, potential artifacts in the dilatometric signal and respective countermeasures are discussed.

3.3.1. Experimental Setup

The experimental setup consists of two parts: one is a commercial volumetric sorption instrument (ASAP2020, Micromeritics) and the other a self-designed dilatometer (Figure 3.5) replacing the original sample holder of the adsorption instrument. This way the functionality of the adsorption instrument could be fully preserved.

The core of the volumetric adsorption instrument is a vacuum chamber of calibrated volume called *manifold*, which is connected to a vacuum pump system, gas supply, and the sample holder [179, 195]. The manifold is equipped with a temperature sensor and three pressure gauges (Baratrons© by MKS suited for pressures ranging from $1.33{\cdot}10^{-6}$ to 0.133 MPa, $1.33{\cdot}10^{-8}$ to $1.33{\cdot}10^{-3}$ MPa and $1.33{\cdot}10^{-9}$ to $1.33{\cdot}10^{-4}$ MPa, respectively). The vacuum pump system consists of a molecular drag pump (TMH 071 P by Pfeiffer), a cold trap, a self-designed vacuum storage and a membrane pump (MVP 015-2 by Pfeiffer). The gas supply allows

for the use of N_2, Ar and CO_2; the purities of the gases were 5.0 for N_2, 5.0 for Ar and 4.5 for CO_2.

For the adsorption of condensable vapors such as H_2O the adsorption instrument was upgraded by a vapor option provided by the instrument manufacturer. The vapor option includes a temperature controlled reservoir for liquids (also connectable to the manifold) and a heating device for the manifold. The adsorption instrument was controlled by the original software provided by the manufacturer. In addition to the original setup of the sorption instrument, the signals of the pressure gauges and the states of the most important valves inside the manifold were separately recorded by a self-designed software also collecting the dilatometric data. The time-dependent pressure data allow for checking the thermodynamic equilibrium based on the conditions set in the adsorption instrument's software, while the valve states were utilized for parsing the dilatometric data.

The central parts of the dilatometer are a length sensor (LVDT PR 750-100 + LVC-2500 by Macrosensors) and a self-designed glass sample holder. A schematic of the dilatometric setup is shown in Figure 3.5. The length sensor consists of an electrical coil arrangement and a metal core, whose displacement within the coil arrangement is measured by the change of induced current [196]. The coil arrangement is mounted to the upper part of the sample holder, while the lower part of the sample holder containing the sample is placed in a tempering bath. Inside the sample holder the metal core is connected to a push rod placed on top of the sample. This way deformation of the sample is transferred onto the metal core by the push rod and measured by the length sensor. The push rod was made from a glass tube (outer diameter 5.3 mm, inner diameter approximately 3.5 mm) of nearly identical diameter as the sample holder thereby serving as a mechanical guide for the push rod. The gas transport from the sorption instrument to the sample is provided by a connected vertical channel through metal core and push rod.

Since the length sensor was found to be sensitive to temperature fluctuations in the lab, it was surrounded by a temperature controlled shield [194]. Due to various modifications made to the setup in this work, the temperature controlled shield was entirely redesigned; also the previously installed relay control of the length sensor [194] was removed, since it had no measureable impact on the data quality of the revised setup. The signal of the length sensor was measured by a multimeter (3457A by Hewlett-Packard) and recorded by a self-designed software, which also monitored the lab temperature and the temperature of the coil arrangement. For the latter a temperature sensor was directly attached on the surface of coil arrangement.

3.3.2. Measurement Procedure

For adsorption measurements with in-situ dilatometry the adsorption instrument and dilatometer ran parallel without direct connection to each other, i.e., the adsorption instrument determined the regular adsorption isotherm $N_a/m_{sample}\,(p/p_0)$,

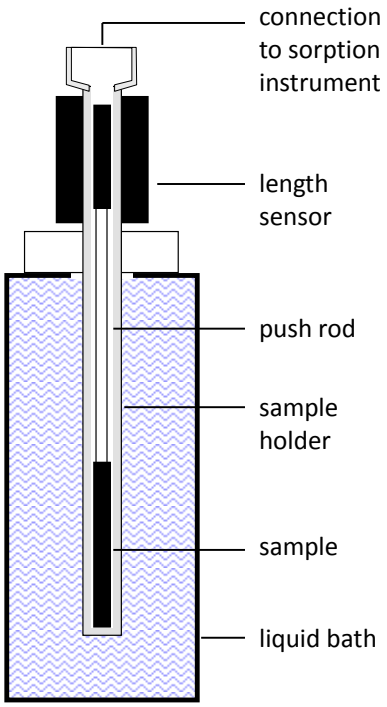

Figure 3.5.: Schematic of the dilatometric setup. Reprinted from ref [197] with permission from Elsevier.

while the dilatometer continuously monitored the length of the sample in parallel. The dilatometric strain isotherm $\varepsilon_{dil}\,(p/p_0)$ was determined after completion of the adsorption measurement by relating dilatometric and adsorption data. A detailed protocol for measurements is given in the following:

Prior to the measurement the sample is degassed in an original sample holder of the adsorption instrument and weighed as described in section 3.2. The length L_0 of the sample is measured by a caliper. Then the sample is moved into the dilatometric sample holder and again degassed. To check the degassing state of the sample, the vacuum system is disconnected from the manifold in regular intervals and the pressure increase inside the manifold still connected to the sample holder is measured. When the so determined pressure increase becomes indistinguishable from the leak rate of the manifold, i.e., approximately 10^{-7} mbar·l/s, the sample is considered fully degassed. This process requires typically 1 d. When the degassing is completed, the sample holder (still connected to the pumping system) is placed in the bath controlling the sample temperature during the measurement. The adsorption measurement is paused till sample and sample holder are thermally equilibrated with the bath, i.e., the dilatometric signal reaches a constant value. The bath for Ar and N_2 adsorption measurements was LN_2; a constant LN_2 level around the sample holder was maintained by the use of an isothermal jacket provided with the commercial adsorption instrument [195]. For CO_2 and H_2O

adsorption the bath was water mixed with a small amount of glycol connected to a liquid thermostat. The external temperature sensor of the thermostat was placed in the bath to ensure its constant temperature.

The measurement starts from the degassed, evacuated and thermally equilibrated state of the sample; at this point the reference length of the sample as seen by the dilatometric setup is l_0.[2] To obtain the different points of the adsorption isotherm the adsorption instrument doses defined amounts of gas into the sample holder. After each dosing step the change of the gas pressure over time inside the sample holder is monitored; when the pressure change drops below a previously set threshold value, the system is considered to be in thermal equilibrium and the current gas pressure and amount adsorbed are taken as equilibrium values. This procedure is repeated for each point of the adsorption isotherm till the equilibrium gas pressure reaches either the saturation pressure of the adsorptive or the technical pressure limit of the sorption instrument, i.e., 0.1 MPa. Afterwards the adsorption instrument may stepwise remove gas from the sample holder to determine the desorption branch of the adsorption isotherm. In parallel the dilatometer continuously measures the length l of the sample. When the measurement is completed, the values of $l\,(p/p_0)$ corresponding to the data points of the adsorption isotherm are determined by a simple automated evaluation routine via time stamps as well as separately recorded pressure transducer signals and valve stats. For each data point of the adsorption isotherm the length change $\Delta l\,(p/p_0) = l\,(p/p_0) - l_0$ is calculated, which finally results in the linear strain isotherm

$$\varepsilon_{dil}\,(p/p_0) = \frac{l\,(p/p_0) - l_0}{L_0} = \frac{\Delta l\,(p/p_0)}{L_0}. \tag{3.17}$$

Additional measurements accompanying each adsorption isotherm run are the determination of the so-called *free space* and potentially the saturation pressure of the adsorptive. The free space measurement is a mandatory procedure for each adsorption measurement calibrating the volume inside the sample holder accessible to the adsorptive, i.e., the volume not occupied by the nonporous skeleton of the sample. Details on free space measurements are given in refs [179, 195]. It is important to note that the degassed sample is exposed to He during the free space measurement, which in case of microporous materials may lead to He entrapment and therefore erroneous equilibrium gas pressures [198]. In this work free space measurements on microporous materials were therefore separated from actual adsorption measurements by an additional degassing step.

Furthermore, the saturation pressure of the adsorptive p_0 has to be known either from literature or from measurements during the adsorption instrument. In this work literature values of p_0 were used for CO_2 and H_2O adsorption measurements(1.4278 MPa for CO_2 at 243 K, 3.4852 MPa for CO_2 at 273 K,

[2]The dilatometric reference length of the sample l_0 differs from absolute length of the sample L_0, since the measurement range of the dilatometer is only about 2 mm.

7.2108 MPa for CO_2 at 303 K and 0.00317 MPa for H_2O at 298 K) [199], while for N_2 and Ar adsorption measurements p_0 was measured at regular intervals during the recording of the adsorption isotherms.

3.3.3. Dilatometric Artifacts, Countermeasures and Accuracy

Regarding the resolution of the dilatometric setup a general problem is the displacement of the sample during the measurement due to mechanical disturbances resulting in apparent sample strain. In the final version of the setup the only constrain for the sample is the push rod placed on top of it (weight of about 7 g), i.e., the sample is not additionally fixed. An explicit fixation of the sample inside the sample holder was rejected to avoid suppressing or redirecting the adsorption-induced deformation of the sample, which is typically volumetrically isotropic. Therefore the sample-push rod arrangement retained some inherent instability. The most persistent mechanical disturbances that had to be addressed were vibrations from the vacuum pumping system, in particular the membrane pumps, and shocks due to switches of the pneumatic valves inside the manifold. Respective countermeasures were twofold:

(i) to increase the mechanical stability of the sample position the push rod as well as the bottom of the sample holder were made as plain as possible. For this a coarse grained glass frit was placed in the lower end of the push rod and fused with the tube. Then the lower end of the push rod was cut by a diamond saw. Furthermore, a plain cut metal rod was pressed into the glass based sample holder during its production.

(ii) to reduce the occurrence of mechanical disturbances the membrane pumps were relocated from the instrument's chassis onto the floor below the instrument and a vacuum storage (approximately 30 l) was put in their place. Furthermore a new connecting part between adsorption instrument and sample holder was designed, which has a significantly enhanced capacity to absorb mechanical shocks originating from the adsorption instrument (a picture is shown in Appendix C).

Obviously, the impact of these modifications onto the mechanical stability of the sample also depend on its geometry, which in most cases was that of a cylindrical rod, whose ends had been cut by a diamond saw. Samples, which could not be provided in such a convenient shape, were smoothed to exhibit at least one plain surface to stand on. For all samples investigated in this work these countermeasures were sufficient to suppress the above described issues below the resolution limit of the overall setup given by other boundary conditions (see discussion on dilatometric resolution in the next paragraph). Nevertheless, singular jumps of the dilatometric signal with no apparent correlation to the instrument were observed occasionally. These events were attributed to shocks originating from outside the instrument and if significant simply corrected from the experimental data.

After the suppression of mechanical disturbances the resolution of the dilatometric setup had to be re-evaluated, since theoretically the resolution of a LVDT is only limited by electrical noise and the accuracy of the connected multimeter [196]. From preliminary measurements with N_2 at 77 K on a nonporous glass rod (Appendix D) the accumulated noise from electrical, mechanical and thermal influences at constant gas pressure was found to be ± 0.05 to ± 0.10 µm. Additionally, the preliminary measurements revealed a slight dependence of the dilatometric signal on the gas pressure inside the sample holder, which exceeded the background noise approximately by a factor of 2.5. However, with respect to the magnitude of commonly observed adsorption-induced deformations this apparent sample deformation is still quite small. For practical reasons the apparent sample deformation due to changes of pressure was therefore considered the accuracy limit of the dilatometric setup leading to a resolution of ± 0.25 µm. For typical sample lengths L_0 between 0.5 and 5 cm this resolution translates to an accuracy of ε_{lin} of $\pm\ 5{\cdot}10^{-5}$ to $\pm\ 5{\cdot}10^{-6}$.

4. Results

This section summarizes the results obtained by NLDFT calculations, sample characterization and in-situ dilatometry measurements, which collectively form the base for the discussion on adsorption-induced deformation in the next chapter.

4.1. Nonlocal Density Functional Theory

Based on the procedure outlined in section 2.2.2 and Appendix A NLDFT calculations were preformed for the adsorption in slit-shaped carbon micro- and mesopores employing the software presented in ref [116] adapted for a single component, i.e., the adsorbate. The adsorptives considered were N_2 at 77 K, Ar at 77 K and CO_2 at 243, 273 and 303 K. The respective solid-fluid and fluid-fluid interaction parameters are summarized in Table A.1. The range of pore width and relative pressure covered in each kernel is given Table 4.1. The focus of each kernel was the microporosity, while mesopores were only required for sample characterization (compare section 3.2.2) or adsorption references (Appendix B).

The NLDFT results relevant for the modeling of experimental adsorption and strain data are the theoretical adsorption isotherms $N_{NLDFT}\left(p/p_0, w\right)$ (Eq. 2.13) and the respective grand potential of the adsorbate $\Omega_a\left(p/p_0, w\right)$ (Eq. 2.10) with the pore width w as model parameter. Examples of theoretical micropore adsorption isotherms calculated for the adsorption of N_2 at 77 K and CO_2 at 273 K are shown in Figures 4.1a and b as molar adsorbate density $\rho_{mol} = 2/w \cdot N_{NLDFT}\left(p/p_0, w\right)$. The obtained adsorption isotherms are essentially identical to NLDFT calculations previously performed by Ravikovitch et al. [113] except for the inclusion of pore widths smaller than the nominal van der Waals diameter σ_{sf} of the adsorbate. As can be seen from Figures 4.1a and b the filling of micropores generally takes place at lower relative pressure the smaller the pore becomes. This trend is due to the increase of solid-fluid attraction for decreasing pore width (compare Figure 2.3), however, as will be discussed in more detail further below pores smaller than σ_{sf} are an exception to this rule. On a side note, micropore filling of N_2 at 77 K is predicted to occur in very distinct steps; for smaller micropores in a single step, for larger micropores in 2 to 3 consecutive steps (Figure 4.1a). This behavior is considered a computational artifact resulting from the combination of the cryogenic temperature of 77 K and the assumption of smooth walls, which in turn causes distinct layer formation of the adsorbate on the pore walls. In real carbon materials the pore walls are likely not entirely smooth and homogenous but exhibit some energetic and structural heterogeneity. Consequently, the sharp steps in the theoretical N_2 adsorption isotherms will be smeared in real carbon materials. This issue was already discussed in literature [180] and more recent

Table 4.1.: Range of pore width w and relative pressure range p/p_0 covered by the kernels for the different adsorbates at temperature T. The bracketed values in the pore width column denote the step width in the respective interval.

adsorbate	T [K]	w [nm]	p/p_0
Ar/N_2	77.4	0.2 to 2.0 (0.01) 2.0 to 8.0 (0.2) 40	10^{-11} to 0.98
CO_2	273.15	0.2 to 2.0 (0.01) 2.0 to 8.0 (0.2) 40	10^{-7} to 0.98
	243.15/303.15	0.2 to 2.0 (0.01)	10^{-7} to 0.1

adsorption models try to explicitly take into account the roughness of the pore walls [115, 116]. Contrary, the elevated temperature for CO_2 adsorption at 273 K disturbs the formation of distinct layers within the carbon micropores and thus the theoretical CO_2 adsorption isotherms exhibit no steps despite the assumption of ideal walls (Figure 4.1b).

The results from the NLDFT calculations, $N_{NLDFT}\left(p/p_0, w\right)$ and $\Omega_a\left(p/p_0, w\right)$, were used to derive the stress isotherms $\sigma_{a,\perp}\left(p/p_0, w\right)$ and $\sigma_{a,\parallel}\left(p/p_0, w\right)$ according to Eq. 2.30a and 2.30b, respectively. Examples for the calculated stress isotherms are given in Figures 4.1c to f, respectively, again for the adsorption of N_2 at 77 K and CO_2 at 273 K.

To begin with the more complex behavior of adsorption stress normal to the pore walls, $\sigma_{a,\perp}\left(p/p_0, w\right)$, is considered. Based on Figures 4.1c and d micropores can be classified into micropores, where $\sigma_{a,\perp}$ is always positive, micropores, where $\sigma_{a,\perp}$ is always negative and micropores, which are subject to negative adsorption stress for low relative pressure and switch to positive adsorption stress with progressing adsorption.[1] To understand the reason for this behavior, furthermore the filling pressure p_{fill} and the adsorbate mass density inside the carbon micropores $\rho_{mass} = \rho_{mol} \cdot m_{mol}$ are derived from the calculated adsorption isotherms. Here p_{fill} marks the inflection point of the theoretical adsorption isotherm. If the adsorption isotherm exhibits more than one inflection point, p_{fill} corresponds to the inflection point at the highest relative pressure. The relative filling pressure p_{fill}/p_0, the adsorption stress normal to the pore wall $\sigma_{a,\perp}$ and the adsorbate mass density ρ_{mass} are shown as a function of the pore width w for N_2 adsorption at 77 K and for CO_2 adsorption at 273 K in Figure 4.2. As can be seen from Figures 4.2c to f at saturation pressure both, $\sigma_{a,\perp}$ and ρ_{mass}, oscillate with respect to w illustrating

[1] Positive adsorption stress is directed towards to boundaries of the pore, while negative adsorption stress is directed towards the center of the pore.

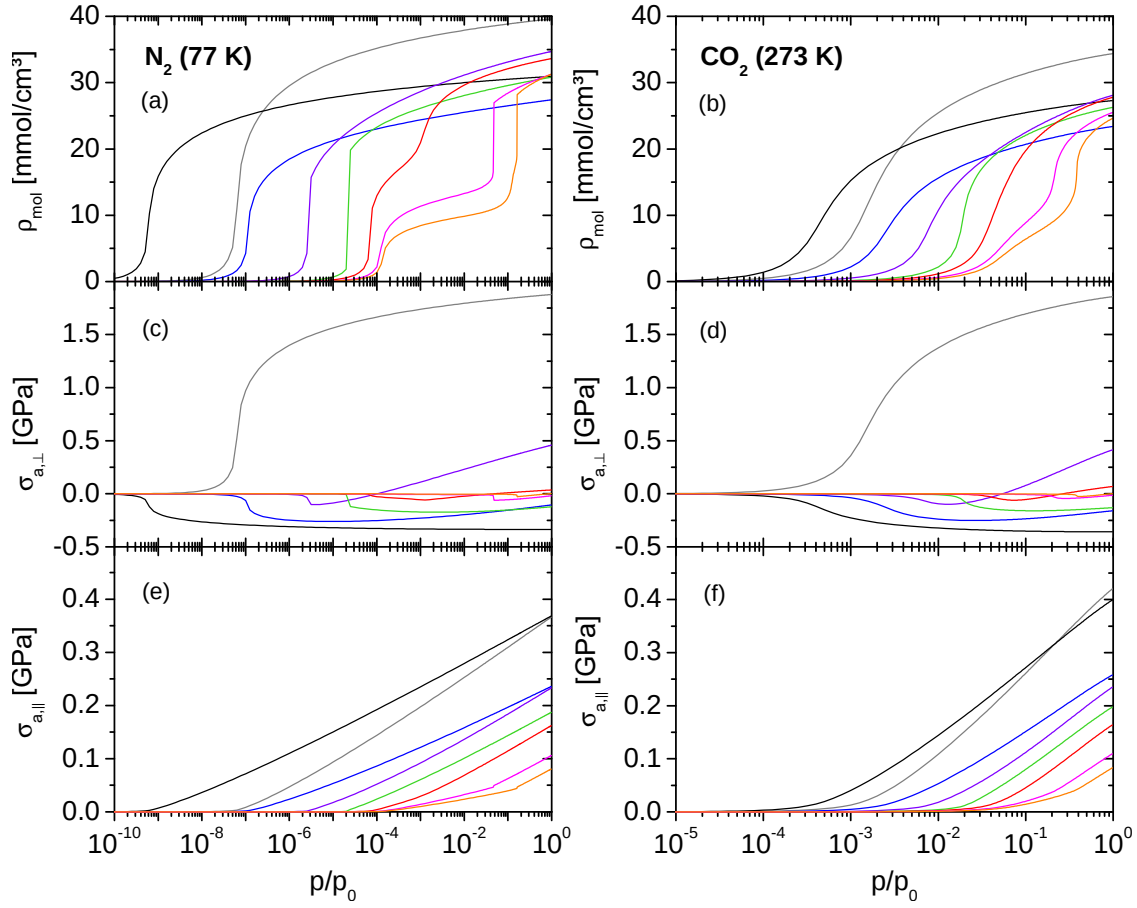

Figure 4.1.: Theoretical adsorption isotherms for N_2 at 77 K (a) and CO_2 at 273 K (b) given as molar volume ρ_{mol} and corresponding stresses normal and tangential to the pore walls, i.e., $\sigma_{a,\perp}$ (N_2 in (c) and CO_2 in (d)) and $\sigma_{a,\parallel}$ (N_2 in (e) and CO_2 in (f)), respectively. The pore widths within each plot are 0.4, 0.3, 0.5, 0.6, 0.8, 1, 1.5 and 2 nm (from left to right).

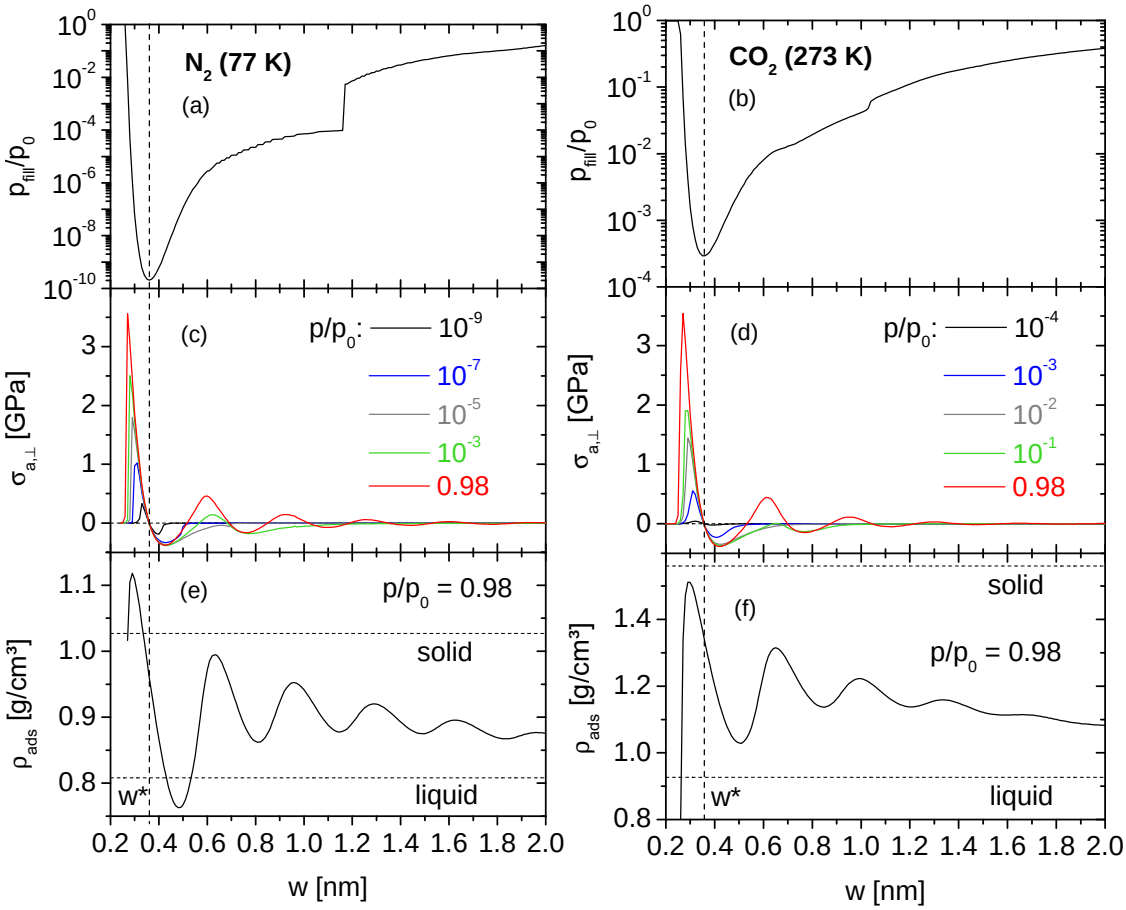

Figure 4.2.: Relative filling pressure p_{fill}/p_0 (a and b), normal adsorption stress $\sigma_{a,\perp}$ (c and d) and mass density ρ_{mass} (e and f) derived from NLDFT calculations for N_2 at 77 K and CO_2 at 273 K, respectively, as a function of pore width w. $\sigma_{a,\perp}$ is shown for different relative pressures p/p_0; ρ_{mass} is shown close to saturation complemented by the solid and liquid density of the adsorbate (solid N_2 at 21 K [200], liquid N_2 at 77 K [199], solid CO_2 at 194 K [200] and liquid CO_2 at 273 K [199]).

the geometric nature of $\sigma_{a,\perp}$ [75, 128]:[2] if the pore width is commensurate with the nominal van der Waals diameter of the adsorbate, the adsorbate density within the pore will be high and the short ranged repulsion of the solid-fluid and fluid-fluid interactions will cause positive adsorption stress normal to the pore walls. Contrary, if the pore width differs from integral multiples of the adsorbate diameter, the adsorbate density is reduced and the adsorbate mediates the long ranged solid-fluid attraction leading to negative adsorption stress normal to the pore walls.

An exceptional behavior is shown for the pore width w^* approximately equal to the nominal van der walls diameter σ_{sf} of the solid-fluid interaction. As can be seen from Figures 4.2a to d, pores of width w^* exhibit the lowest relative filling pressure of all pores, while they are at the same time free of adsorption stress normal to the pore walls. This result is interpreted in terms of w^* being the most comfortable pore size, which is geometrically and energetically ideal for the adsorbate. For $w < w^*$ the normal adsorption stress is extremely large and positive, which fits the picture of adsorbate molecules squeezing into pores smaller than their nominal diameter. A more detailed discussion on this effect is given in a reference related to this work [188].

In comparison to $\sigma_{a,\perp}$, the stress tangential to the pore walls, $\sigma_{a,\parallel}$, (Figures 4.1e and f) shows a rather clear pattern: once the pore is filled ($p/p_0 > p_{fill}/p_0$), $\sigma_{a,\parallel}$ increases with relative pressure in an approximately logarithmic fashion. Additionally, the slope of all stress isotherms is very similar and pores filling at lower relative pressure exhibit larger values for $\sigma_{a,\parallel}$. These observations are easily understood, when considering the definition of $\sigma_{a,\parallel}$ and the underlying grand potential (Eq. 2.27 and 2.30b):

$$\sigma_{a,\parallel} = -\frac{\Omega_a}{V_{slit}} \propto R_g T \int \rho_{mol} \, \mathrm{dln}\,(p/p_0)\,. \tag{4.1}$$

For $p/p_0 > p_{fill}/p_0$ the changes of the adsorbate density ρ_{mol} tend to become small and therefore $\sigma_{a,\parallel}$ is approximately proportional to $\ln(p/p_0)$. Furthermore, the slope of the stress isotherm $\partial\sigma_{a,\parallel}/\partial\ln(p/p_0)$ is proportional to ρ_{mol}, whose pore widths dependency is only moderate (compare Figures 4.2e and f).

The effect of temperature on the NLDFT results is exemplified in Figure 4.3 for CO_2 adsorption at 243, 273 and 303 K. For increasing temperature the adsorption isotherms are shifted to higher relative pressure due to the increased thermal energy of the adsorbate. This effect is independent of the pore width and also applies to the tangential stress in the micropores $\sigma_{a,\parallel}$. The dependence of the normal adsorption stress $\sigma_{a,\perp}$ on temperature varies for different pore widths. For pores smaller than w^*, $\sigma_{a,\perp}$ is again only shifted to higher relative pressure for increasing temperature, while for pores larger than w^* also the magnitude of $\sigma_{a,\perp}$ changes. As can be seen from the inset in Figure 4.3 the contraction for

[2] The oscillations of $\sigma_{a,\perp}$ and ρ_{mass} are slightly shifted with respect to one another; this observation was already discussed in ref [128].

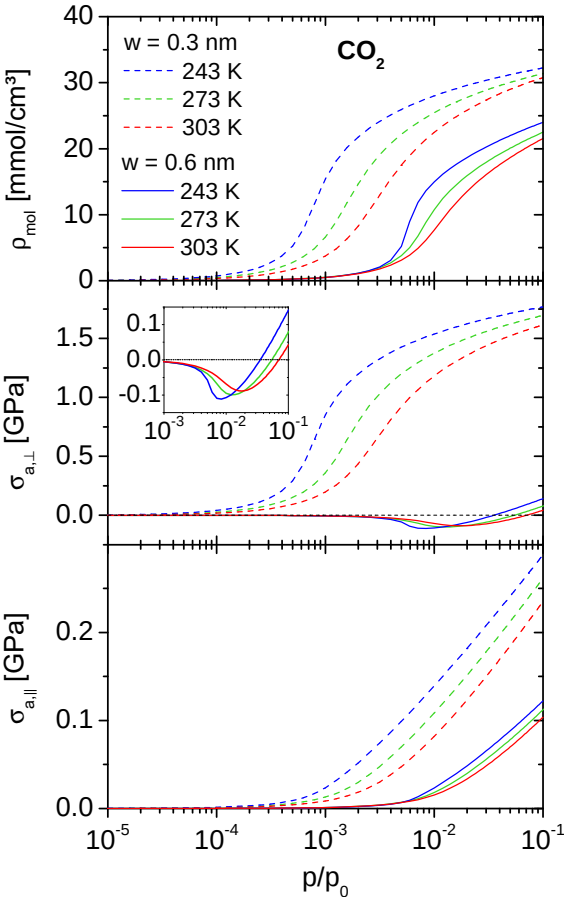

Figure 4.3.: Theoretical adsorption isotherms for CO_2 adsorption at 243, 273 and 303 K in slit-shaped pores of width 0.3 and 0.6 nm given as molar volume ρ_{mol} and corresponding stresses normal and tangential to the pore walls, i.e., $\sigma_{a,\perp}$ and $\sigma_{a,\parallel}$, respectively.

initial micropore filling and the expansion for progressing adsorption become more pronounced with decreasing temperature. These observations are in line with previous NLDFT calculations [128] and GCMC simulations [94] on the dependence of $\sigma_{a,\perp}$ on temperature.

4.2. Sample Characterization

This section summarizes the results of the characterization techniques described in section 3.2 applied to the model materials presented in section 3.1. The focus of the sample characterization is to provide all information necessary for the application and validation of the theoretical models on adsorption-induced deformation described in section 2.3.

4.2.1. SEM Images

SEM images of the carbon xerogels C5000/30/800 and C5000/50/800 are shown in Figures 4.4 and 4.5; the SEM images of the other carbon samples are virtually identical to the ones of C5000/50/800 and therefore not presented here. Images of the zeolites, the silica aerogel and the hierarchical structured silica are given in Figures 4.6, 4.7, 4.8 and 4.9, respectively. In all cases the resolution of the images was sufficiently good to relinquish sputter coating of the samples.

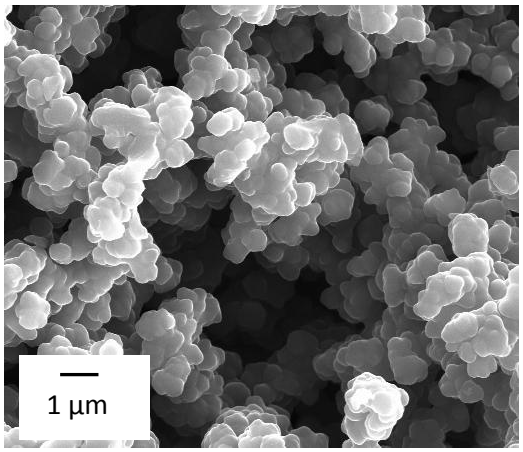

Figure 4.4.: SEM image of the carbon xerogel C5000/30/800. Reprinted from ref [197] with permission from Elsevier.

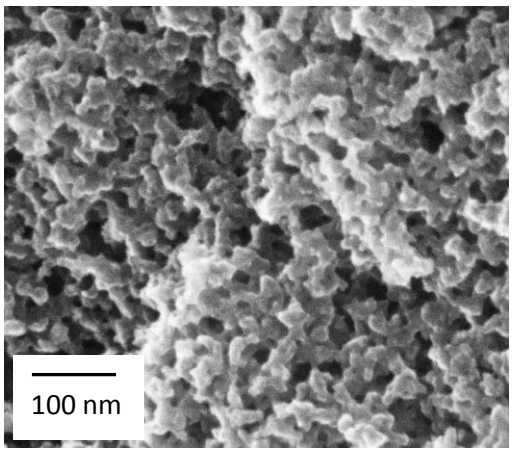

Figure 4.5.: SEM image of the carbon xerogel C5000/50/900, which is representative for all other micro-mesoporous carbon xerogels. Adapted with permission from ref [201]. Copyright 2015 American Chemical Society.

4.2.2. Monolithic Density and Sound Velocity Measurements

The densities of all monolithic samples were determined after degassing according to the procedure described in section 3.2.1 (Table 4.2). All carbon xerogels and the hierarchical structured silica were specifically prepared for in-situ dilatometry measurements as ideal cylinders and thus volume and density of the sample bodies could be precisely determined. The binderless zeolites supplied by *CWK Chemiewerk Bad Köstritz* were roughly spherical in shape allowing only for an

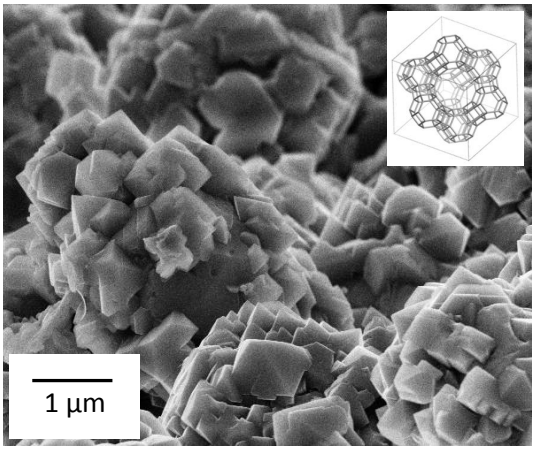

Figure 4.6.: SEM image of the Zeolite KÖSTROLITH 13XBFK. The inset shows the schematic of the zeolite's micropore structure.

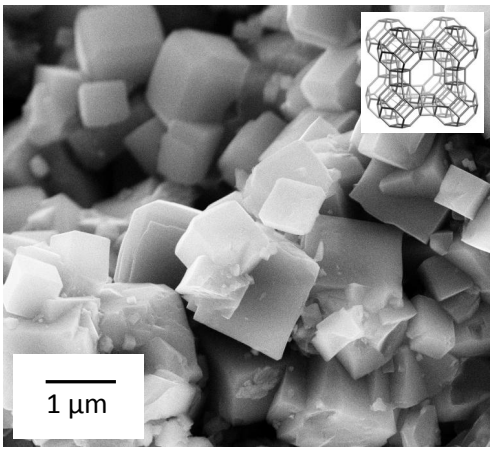

Figure 4.7.: SEM image of the sample Zeolite KÖSTROLITH 4ABFK. The inset shows the schematic of the zeolite's micropore structure.

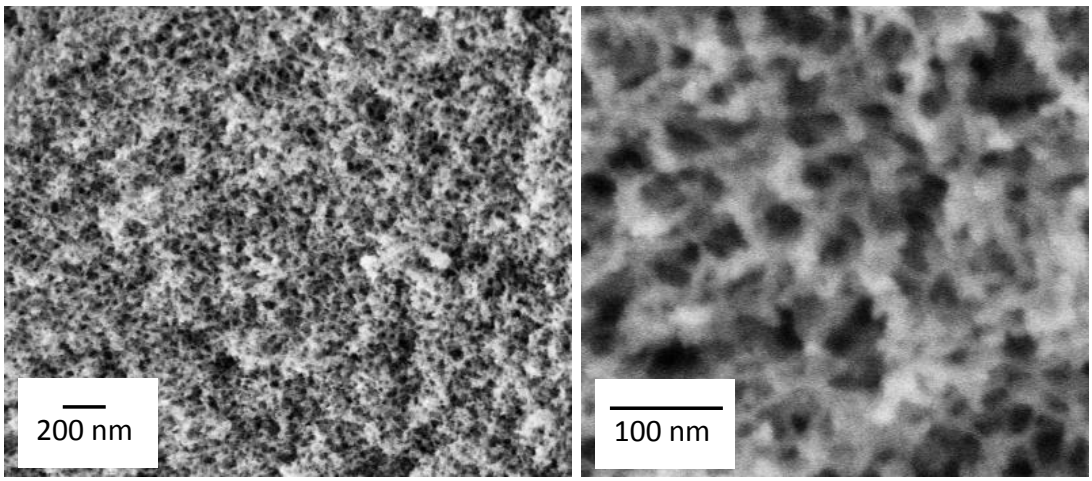

Figure 4.8.: SEM images of the silica aerogel. Due to the low electrical conductivity of amorphous silica the contrast of the image becomes significantly worse for increased magnification.

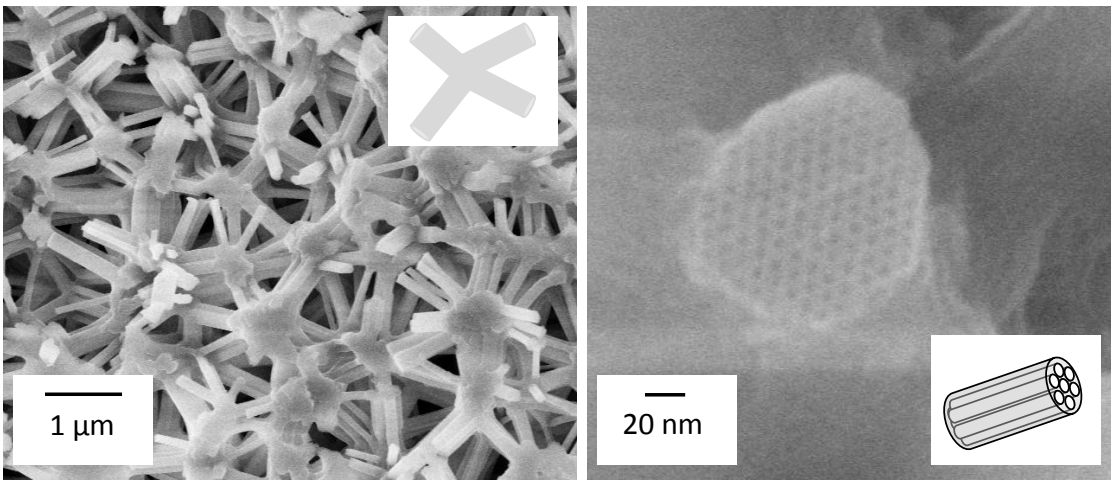

Figure 4.9.: SEM images of the hierarchical structured porous silica. The insets show schematics of the sample's structural entities. Adapted with permission from ref [129]. Copyright 2017 American Chemical Society.

approximate determination of the samples' densities. The silica aerogel sample resembled vaguely a cuboid but was too ill shaped for an external determination of the sample volume; for this sample the density was determined from Eq. 2.1 applying the total pore volume determined by the Gurvich rule from the N_2 adsorption isotherm (Table 4.3) and the density of nonporous sintered silica (2.1 $\pm$ 0.1) g/cm^3 as given in literature [202].

The sound velocities of all samples except the zeolites were determined by ultrasound runtime measurements as described in section 3.2.3. The obtained sound velocities range from 500 to 3000 m/s and consequently the ultrasonic wavelengths were on the order of several hundred microns, i.e., significantly larger than any structure within the samples. Therefore, the ultrasonic wave was not sensitive to the nanostructure of the samples but perceived the effective properties of the porous materials. Following Eq. 3.13 to 3.16 the sound velocity was used to determine the Young's modulus E_b and the bulk modulus K_b of the porous samples. For this the Poisson's ratio of the porous solids ν_b was not explicitly measured but rather assumed to be in the range of $\nu_b = 0.20 \pm 0.05$. This covers the vast majority of ν_b values reported in literature for porous glasses, aero- and xerogels [121, 203]. Due to the weak mathematical dependence of E_b and K_b on ν_b the resulting accuracy is still acceptable. The results are given in Table 4.2.

4.2.3. Gas Adsorption

Gas adsorption measurements for structural characterization (section 3.3.3) were performed with N_2 at 77 K and CO_2 at 273 K. N_2 at 77 K was chosen for all

Table 4.2.: Density ρ_b of the macroscopic monolithic samples and the respective results of sound velocity measurements, i.e., the longitudinal sound velocity v_{sound}, the Young's modulus E_b and the bulk modulus K_b. For the calculation of E_b and K_b a Poisson's ratio of $\nu_b = 0.20 \pm 0.05$ was assumed.

sample	ρ_b [g/cm^3]	v_{sound} [m/s]	E_b [MPa]	K_b [MPa]
C5000/30/800	0.292 ± 0.011	525.2 ± 2.6	72.5 ± 7.4	40.3 ± 5.8
C5000/50/800	0.741 ± 0.016	3052 ± 32	6210 ± 550	3450 ± 450
C5000/50/900	0.649 ± 0.011	2723 ± 33	4330 ± 380	2410 ± 310
C5000/50/900A	0.618 ± 0.011	2673 ± 32	3980 ± 350	2210 ± 280
C5000/50/1200	0.640 ± 0.011	2965 ± 46	5070 ± 460	2810 ± 370
C5000/50/1400	0.637 ± 0.011	2986 ± 12	5110 ± 410	2840 ± 350
C5000/50/1600	0.637 ± 0.011	3016 ± 31	5220 ± 430	2900 ± 370
C5000/50/1800	0.629 ± 0.010	3033 ± 20	5210 ± 430	2890 ± 360
Zeolite LTA	1.040 ± 0.077	-	-	-
Zeolite FAU	1.048 ± 0.044	-	-	-
silica aerogel	0.267 ± 0.009	493 ± 13	58.4 ± 6.6	32.4 ± 5.1
hierarchical structured porous silica	0.525 ± 0.029	2547 ± 91	3070 ± 420	1700 ± 310

carbon samples, the silica aerogel and the hierarchical structured silica due to their more or less pronounced mesopore structure. The carbon and zeolite samples were also subjected to CO_2 adsorption at 273 K to obtain further information on their microporosity.

The N_2 adsorption isotherms of the silica aerogel and the hierarchical structured silica were analyzed by Gurvich rule and BET theory for the total mesopore volume $V_{Gurvich}$, the specific mesopore surface area S_{BET} and the energetic parameter C_{BET}; additionally, the average mesopore diameter $d_{meso} = 4V_{Gurvich}/S_{BET}$ was calculated assuming cylindrical pore geometry (Eq. 2.3b). The respective results are summarized in Table 4.3.

The N_2 adsorption isotherms of the carbon samples were analyzed by the Gurvich rule and the t-plot method for the combined micro- and mesopore volume $V_{Gurvich}$, the micropore volume V_{mic} (t-plot) and the specific surface area of the carbon particles S_{ext}. From these results the specific mesopore volume $V_{meso} = V_{Gurvich} - V_{mic}$ (t-plot) and the average mesopore diameter $d_{meso} = 4V_{meso}/S_{ext}$ were calculated assuming cylindrical pore geometry (Eq. 2.3b). The results for the carbon based samples are given in Table 4.4.

To obtain further information on the (accessible) microporosity of the carbon samples their N_2 and CO_2 adsorption isotherms were analyzed by the integral

Table 4.3.: Structural parameters of mesoporous silica model materials obtained from N_2 adsorption isotherms by Gurvich rule and BET-Theory, i.e., the specific mesopore volume $V_{Gurvich}$, the specific surface area S_{BET} and the C_{BET} parameter. Additionally the average mesopore diameter d_{meso} is given.

sample	$V_{Gurvich}$ [cm^3/g]	S_{BET} [m^2/g]	C_{BET}	$\bar{d}_{meso}$ [nm]
silica aerogel	3.27 ± 0.12	380 ± 5	71 ± 2	34.4 ± 1.3
hierarchical structured porous silica	0.24 ± 0.01	203 ± 5	79 ± 2	4.7 ± 0.2

Table 4.4.: Structural parameters of carbon samples obtained from N_2 adsorption isotherms by Gurvich rule and t-plot method, i.e., the specific pore volumes $V_{Gurvich}$, V_{mic} (t-plot) and V_{meso} as well as the specific external surface area S_{ext}. Additionally, the mesopore volume and the average mesopore diameter d_{meso} are given.

sample	$V_{Gurvich}$ [cm^3/g]	S_{ext} [m^2/g]	V_{mic} (t-plot) [cm^3/g]	V_{meso} [cm^3/g]	$\bar{d}_{meso}$ [nm]
C5000/30/800	-	11 ± 1	0.25 ± 0.01	-	990 ± 140*
C5000/50/800	0.86 ± 0.01	205 ± 10	0.20 ± 0.01	0.66 ± 0.01	12.9 ± 0.7
C5000/50/900	1.09 ± 0.01	235 ± 10	0.23 ± 0.01	0.86 ± 0.01	14.7 ± 0.7
C5000/50/900A	1.14 ± 0.01	235 ± 10	0.26 ± 0.01	0.88 ± 0.01	15.0 ± 0.7
C5000/50/1200	1.05 ± 0.01	240 ± 10	0.17 ± 0.01	0.87 ± 0.01	14.6 ± 0.7
C5000/50/1400	0.98 ± 0.01	236 ± 10	0.11 ± 0.01	0.87 ± 0.01	14.7 ± 0.7
C5000/50/1600	0.90 ± 0.01	230 ± 10	0.05 ± 0.01	0.86 ± 0.01	14.8 ± 0.7
C5000/50/1800	0.89 ± 0.01	235 ± 10	0.02 ± 0.01	0.87 ± 0.01	14.8 ± 0.7

* This value was obtained by the macropore volume derived from bulk and particle density and is obviously in the range of macropores (Eq. 2.1).

adsorption equation (section 3.2.2) utilizing the results of the NLDFT calculations obtained within this work (section 4.1). As described in refs [113, 188] the analysis of neither N_2 nor CO_2 adsorption isotherm is sufficient to obtain the entire micropore size distribution of a carbon. Analysis of N_2 adsorption data is limited to pore widths larger than approximately 0.5 nm, while the analysis of CO_2 adsorption data is limited to pore widths smaller than approximately 1 nm. A solution to this problem is the combination of the pore size distributions obtained from N_2 and CO_2 adsorption data in the overlapping range of 0.5 nm $< w <$ 1 nm [188, 204]; this is illustrated in Figure 4.10 for the sample C5000/50/800. As was emphasized in refs [188, 197] the (partially very sharp) spikes of PSDs obtained by automated Tikhonov regularization should be not be overinterpreted as a detailed substructure of the carbon but considered artifacts of the applied algorithm. From the combined PSD the specific micropore volume V_{mic} (DFT) (Eq. 3.10), the

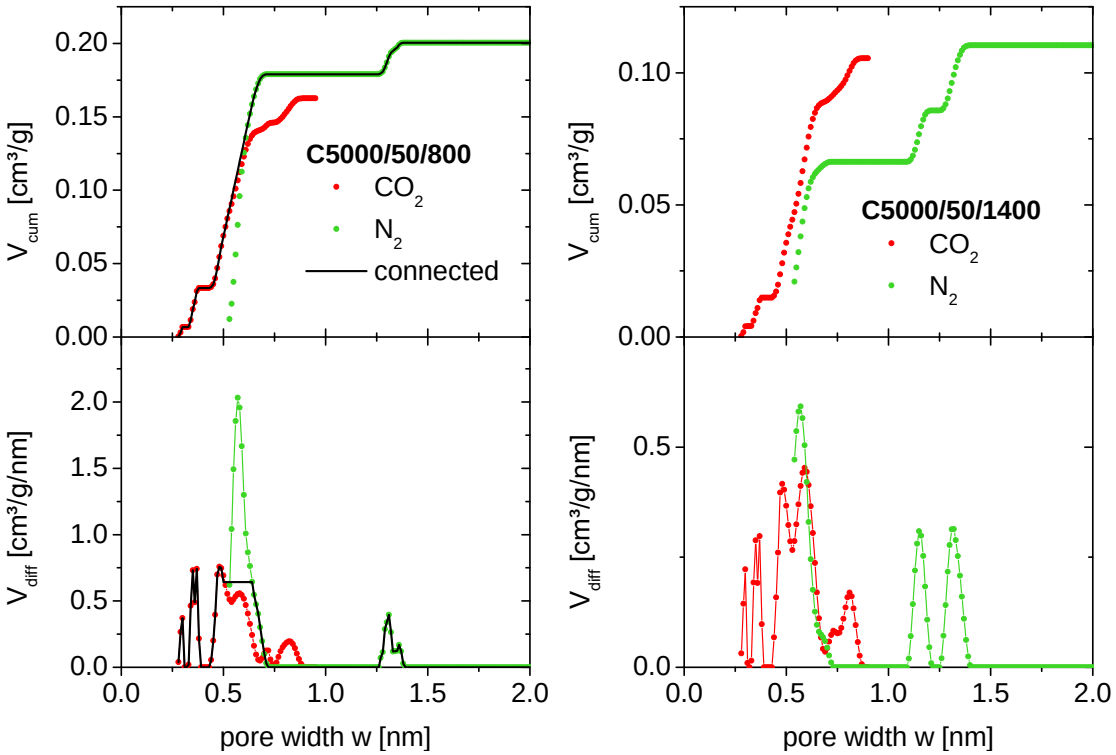

Figure 4.10.: PSDs evaluated from N_2 and CO_2 adsorption isotherms for the samples C5000/50/800 (left) and C5000/50/1400 (right). Additionally, for the sample C5000/50/800 a connected PSD is shown.

specific micropore area S_{mic} (DFT) (Eq. eq:SmicDFT) and the average micropore width $\bar{w}$ (Eq. 3.12) were determined; respective results are summarized in Table 4.5.

While this approach is feasible for carbon samples, which exhibit microporosity fully accessible for both N_2 and CO_2 [201], the microporosity in thermally annealed carbon samples may offer different accessibilities for N_2 and CO_2. For the samples investigated in this work, this effect was found for annealing temperatures exceeding 1200 °C. The apparent consequence is that for samples annealed above 1200 °C the cumulative PSDs derived from N_2 and CO_2 adsorption data no longer exhibit an intersection point (Figure 4.10). Therefore, for the carbon samples annealed at 1400, 1600 and 1800 °C separate N_2 and CO_2 micropore size distributions had to be determined. Unfortunately, the lack of an intersection point of the cumulative PSDs leaves room for some arbitrariness, how the information from N_2 and CO_2 data evaluation are to be combined. The procedure used in this work to obtain at least an estimate of the respective PSDs is described in the Appendix E.

Table 4.5.: Results of the NLDFT analysis of N_2 and CO_2 adsorption isotherms, i.e., the specific micropore volume V_{mic} (DFT), the specific micropore area S_{mic} (DFT) and the average pore width $\bar{w}$. For carbons annealed at temperatures of 1400, 1600 and 1800 °C N_2 and CO_2 access different fractions of the overall microporosity and thus results for N_2 and CO_2 differ.

sample	V_{mic} (DFT) N_2/CO_2 [cm^3/g]	S_{mic} (DFT) N_2/CO_2 [m^2/g]	$\bar{w}$ N_2/CO_2 [nm]
C5000/30/800	0.252	973	0.52
C5000/50/800	0.200	750	0.53
C5000/50/900	0.218	815	0.54
C5000/50/900A	0.256	945	0.59
C5000/50/1200	0.171	575	0.59
C5000/50/1400	0.110/0.134	306-337/433	0.65-0.72/0.62
C5000/50/1600	0.052/0.072	133-148/227	0.71-0.79/0.64
C5000/50/1800	0.026/0.033	71-76/102	0.69-0.74/0.65

4.2.4. Derived Structural Quantities

By combining the monolithic density ρ_b (Table 4.2) and the results obtained from the gas adsorption measurements (Table 4.3 to 4.5) additional structural parameters of the samples investigated were derived. For the carbon xerogels the following parameters were calculated (section 2.1): the density of the porous solid's skeleton $\rho_s(N_2) = 1/(1/\rho_b - V_{Gurvich})$ as perceived by N_2 molecules at 77 K, the density $\rho_{part} = 1/(1/\rho_b - V_{meso})$, the diameter $d_{part} = 6/(S_{ext} \cdot \rho_{part})$ and the porosity $\phi_{part} = V_{mic}(\mathrm{DFT}) \cdot \rho_{part}$ of the microporous particles within the xerogel as well as the porosity of the particle network $\phi_{net} = 1 - \rho_b/\rho_{part}$. All numerical results are given in Table 4.6.

For the mesoporous carbon samples not subjected to annealing $\rho_s(N_2)$ corresponds to the density of the carbon microcrystallites forming the particles and the obtained values are well in line with the results from He pycnometry $\rho_s(He)$ = (2.06 ± 0.06) g/cm^3 reported in literature [142]. In contrast, for the annealed samples $\rho_s(N_2)$ is lower than $\rho_s(He)$, since a fraction of the total pore volume is not accessible to N_2; this effect becomes more pronounced with increasing annealing temperature [132]. For the macroporous carbon xerogel, C5000/30/800, $\rho_s(N_2)$ could not be determined and for all consecutive calculations $\rho_s(He)$ was used instead. Furthermore, for the sample C5000/30/800 an average macropore diameter was calculated by $d_p = 4(1/\rho_b - 1/\rho_{part})/S_{ext}$ (Table 4.4).

For the silica aerogel, the parameters $d_{part} = 6/(S_{BET} \cdot \rho_{part})$ and ϕ_{net} were calculated in analogy to the carbon xerogels assuming the particle density to be equal to the density of nonporous silica, i.e., $\rho_{part} = \rho_{silica}$ = (2.1 ± 0.1) g/cm^3 [202]. Since the particles of the silica aerogel as seen by SEM (Figure 4.8)

Table 4.6.: Structural parameters of the carbon xerogels, i.e., the solid density of the nonporous solid skeleton $\rho_s\,(N_2)$ as perceived by N_2 molecules, the density ρ_{part}, the diameter d_{part} and the porosity ϕ_{part} of the microporous particles forming the xerogel network as well as the porosity of the particle network ϕ_{net}.

sample	$\rho_s\,(\mathrm{N_2})$ [g/cm^3]	ρ_{part} [g/cm^3]	d_{part} [nm]	ϕ_{part} N_2/CO_2 [%]	ϕ_{net} [%]
C5000/30/800	-	1.38 ± 0.05	395 ± 26	35 ± 2	79 ± 4
C5000/50/800	2.05 ± 0.13	1.45 ± 0.07	20.2 ± 0.7	29 ± 2	49 ± 3
C5000/50/900	2.21 ± 0.14	1.47 ± 0.06	17.3 ± 0.5	33 ± 2	56 ± 3
C5000/50/900A	2.11 ± 0.13	1.35 ± 0.06	18.8 ± 0.6	36 ± 2	54 ± 2
C5000/50/1200	1.91 ± 0.11	1.44 ± 0.06	17.4 ± 0.5	25 ± 2	56 ± 3
C5000/50/1400	1.68 ± 0.08	1.43 ± 0.06	17.8 ± 0.5	15/19 ± 2	55 ± 3
C5000/50/1600	1.49 ± 0.06	1.39 ± 0.06	18.8 ± 0.6	7/10 ± 1	54 ± 2
C5000/50/1800	1.44 ± 0.06	1.40 ± 0.06	18.3 ± 0.6	3/4.6 ± 1	55 ± 2

Table 4.7.: Structural parameters of the silica aerogel, i.e., the diameter of the network entities assuming spherical (d_{part}) or cylindrical (d_{rod}) geometry as well as the porosity of the sol gel network ϕ_{net}.

sample	d_{part} [nm]	d_{rod} [nm]	ϕ_{net} [%]
silica aerogel	7.5 ± 0.4	5.0 ± 0.2	87 ± 5

may be fused by the sintering process, the approximation of spherical particles may no longer be valid and instead the silica structure is better described by cylindrical rods. Therefore the structural characterization of the silica aerogel is complemented by the strut diameter $d_{rod} = 4/\left(S_{BET} \cdot \rho_{silica}\right)$ (Eq. 2.6b). All numerical results are given in Table 4.7.

The hierarchical structured silica was analyzed with respect to the density $\rho_{strut} = 1/\left(1/\rho_s + V_{Gurvich}\right)$ and the porosity $\phi_{strut} = 1 - \rho_{strut}/\rho_s$ of the struts forming the macroporous network as well as the lattice parameter $d_{latt} = d_{meso}\left(\pi/\left(2\sqrt{3}\phi_{strut}\right)\right)^{1/2}$ of the hexagonal mesopore lattice [178] and the porosity of the strut network $\phi_{net} = 1 - \rho_b/\rho_{strut}$. Again the density of the nonporous solid phase ρ_s was assumed to be equal to the literature value for sintered silica [202]. The obtained results are given in Table 4.8.

Table 4.8.: Structural parameters of the hierarchically structured silica, i.e., the density ρ_{strut} and the porosity ϕ_{strut} of the mesoporous struts, the constant of the hexagonal mesopore lattice d_{latt} and the porosity of the macroporous network ϕ_{net}.

sample	ρ_{strut} [g/cm^3]	ϕ_{strut} [%]	d_{latt} [nm]	ϕ_{net} [%]
hierarchical structured porous silica	1.40 ± 0.05	34 ± 2	7.8 ± 0.4	62 ± 4

4.3. in-situ Dilatometry

A major part of this work consists of comprehensive measurements of gas adsorption combined with in-situ dilatometry. Based on the structural properties of the samples different combination of analysis gas and temperature were applied, i.e., the purely mesoporous silica samples (silica aerogel and hierarchical structured silica) were only investigated during N_2 adsorption at 77 K, while for the microporous carbon xerogels in-situ dilatometry measurements were also performed for CO_2 adsorption at 273 K. The micro-mesoporous carbon sample C5000/50/800 was additionally investigated during the adsorption of Ar at 77 K and H_2O at 298 K. The microporous zeolites were only analyzed for CO_2 adsorption at 273 K. As described in section 3.3 each measurement consists of a common adsorption isotherm $N_a/m_{sample}\,(p/p_0)$ and a linear strain isotherm $\varepsilon_{dil}\,(p/p_0)$. For the sake of comparison (in particular of different adsorbates) all amounts adsorbed are given as specific liquid volume $N_a/m_{sample} \cdot V_L$.

In the following the different types of adsorption and strain isotherms obtained are described. To begin with, the mesoporous silica aerogel and hierarchical structured silica are considered; their combined N_2 adsorption and strain isotherms are shown in Figure 4.11 and 4.12, respectively. Both samples exhibit type IV(a) adsorption isotherms characteristic for mesoporous materials (compare Figure 2.2). However, due to the larger pore size and higher mesoporosity of the silica aerogel its adsorption hysteresis is a more pronounced and found at higher relative pressure. The higher mesoporosity of the silica aerogel also increases the overall adsorption by an order of magnitude compared to the hierarchical structured silica. Contrary to the qualitative similarity of their adsorption isotherms, the strain isotherms of silica aerogel and hierarchical structured silica appear significantly different. While the hierarchical structured silica shows essentially monotonic expansion with increasing relative pressure (except for the hysteresis regime), the silica aerogels expands only at very low relative pressure before switching to contraction for progressing adsorption and back to expansion, once it reaches the filled pore state. Also, the strain hysteresis and the local minima/maxima values of the strain isotherm are significantly more pronounced for the silica aerogel. Notably, each sample is qualitatively in line with strain isotherms reported in

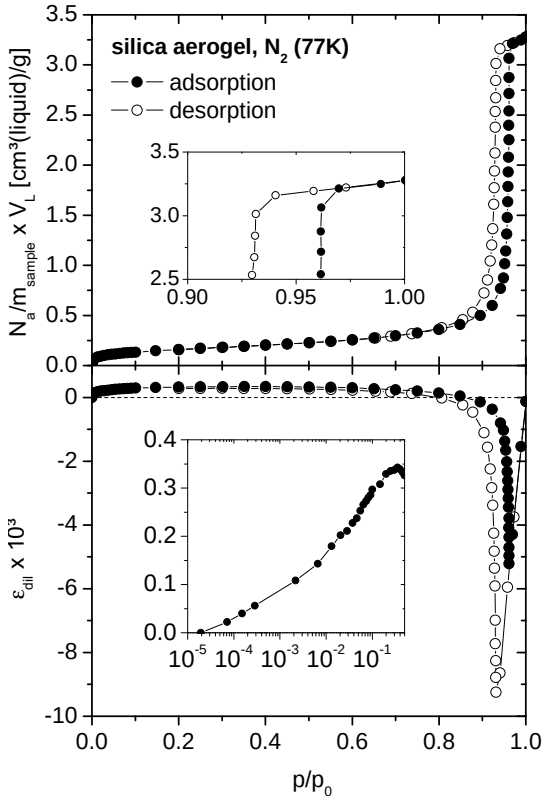

Figure 4.11.: Experimental N_2 adsorption and strain isotherm at 77 K for the silica aerogel. The inset in the upper panel shows a magnification of the adsorption isotherm's plateau regime and the inset in the lower panel shows a magnification of the sample's expansion at low relative pressure.

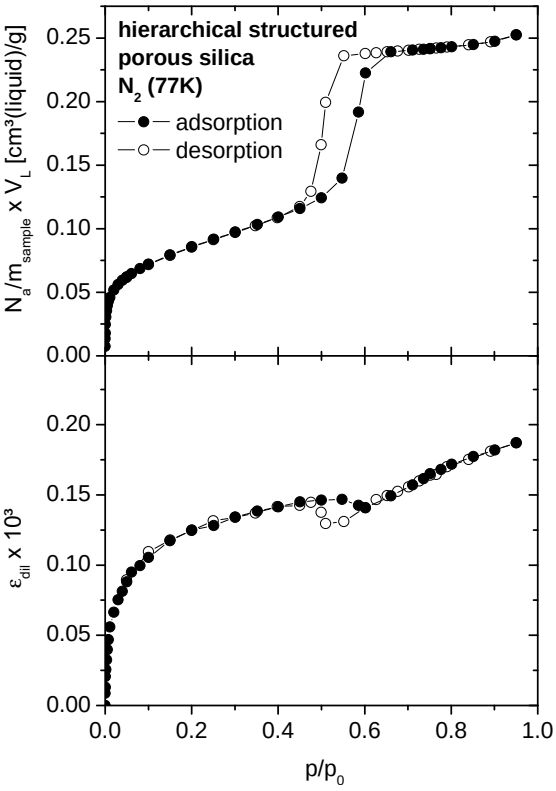

Figure 4.12.: Experimental N_2 adsorption and strain isotherm at 77 K for the hierarchical structured silica. Adapted with permission from ref [129]. Copyright 2017 American Chemical Society.

literature for comparable materials ([27] for silica aerogels and [25] for porous glass).

To illustrate adsorption and adsorption-induced deformation of carbon xerogels the adsorption and strain isotherms of the sample C5000/50/800 are shown for N_2 and Ar at 77 K in Figure 4.13, for CO_2 at 273 K in Figure 4.14 (left) and H_2O at 298 K in Figure 4.14 (right). A detailed discussion of these experimental data sets can be found in reference related to this work [201] and thus only the most important aspects are repeated here. To begin with, the N_2 and Ar isotherms of the carbon xerogel are considered. Due to the micro- and mesoporosity of the sample C5000/50/800 its N_2 (77 K) adsorption isotherm (Figure 4.13, left) is a combination of the IUPAC types I(a) and IV(a). In contrast, the Ar (77 K) adsorption isotherm of the sample exhibits no capillary condensation and correlated adsorption hysteresis; this effect is known in literature and attributed to the fact that the temperature of 77 K is below the triple point of Ar [205]. In the low relative pressure regime ($p/p_0 < 0.1$, see Figure 4.13, right) N_2 (77 K)

and Ar (77 K) adsorption isotherms of the sample C5000/50/800 run essentially parallel corresponding well to various other carbon materials found in literature (e.g. [180, 206]). The shift in relative pressure between N_2 and Ar adsorption results from the small quadrupole moment of the N_2 molecule, which slightly increases its interaction potential with carbon [207]. The strain isotherms for N_2 and Ar adsorption both show the nonmonotonic behavior reported for the combination of various microporous carbons and adsorbents (e.g. [5–7, 10, 18–21, 52, 208]: for initial adsorption the sample contracts till it reaches a strain minimum. For further progressing adsorption the contraction is regressing and the sample shifts over to monotonic expansion. In addition to that, the N_2 strain isotherm exhibits a small strain hysteresis in the range relative pressure range of the filled pore state (inset in Figure 4.13, right). However, the fact that Ar and N_2 strain isotherms are virtually identical, except for the above mentioned shift in relative pressure, suggests that the state of filled mesopores, which is only achieved in the N_2 experiment, is of minor importance for the strain in the considered sample.

The adsorption of CO_2 at 273 K (Figure 4.14) causes qualitatively the same strain isotherm as N_2 and Ar at 77 K, but the initial contraction is significantly smaller. As to be expected for micropore filling, the CO_2 adsorption and strain isotherms are fully reversible within the experimental accuracy. Notably, the experimental data sets for CO_2 are restricted to relative pressures below 0.03 due to the instruments limit in absolute pressure of 1 bar (compare section 3.3).

Finally, H_2O (298 K) adsorption on carbon (Figure 4.14, right) differs to some extent from the adsorption of the other adsorbates due to the weak interaction of the H_2O molecule with hydrophobic carbon surface [209]. The adsorption of H_2O molecules does not create a homogeneous film on the carbon as other adsorbates, but rather forms clusters around polar functional groups on the carbon surface, which eventually coalesce and fill adjacent micropores [210]. As a consequence, H_2O adsorption in carbon micropores shows quite different characteristics compared to the other adsorbates considered in this work including that the density of the H_2O phase within the micropores is significantly lower than free water (approximately 0.8 g/cm^3 [201, 211, 212]). As a side effect, capillary condensation in carbon mesopores is usually not observed without oversaturation of the sample [212]. The often observed hysteresis of carbon H_2O adsorption isotherms is therefore not related to mesopores but to the configuration of H_2O molecules within the micropores, which is predicted to change between ad- and desorption [213]. Despite the significant differences of H_2O adsorption in carbons when compared to other adsorptives, the corresponding H_2O strain isotherm of the carbon exhibits again the common nonmonotonic shape. However, quantitatively the minimum of the H_2O strain isotherm is deeper and the maximal expansion approaching saturation is lower than for the other adsorptives.

The adsorption and strain isotherms for the second type of microporous material investigated in this work, i.e., the zeolites Köstrolith 4ABFK (type LTA) and

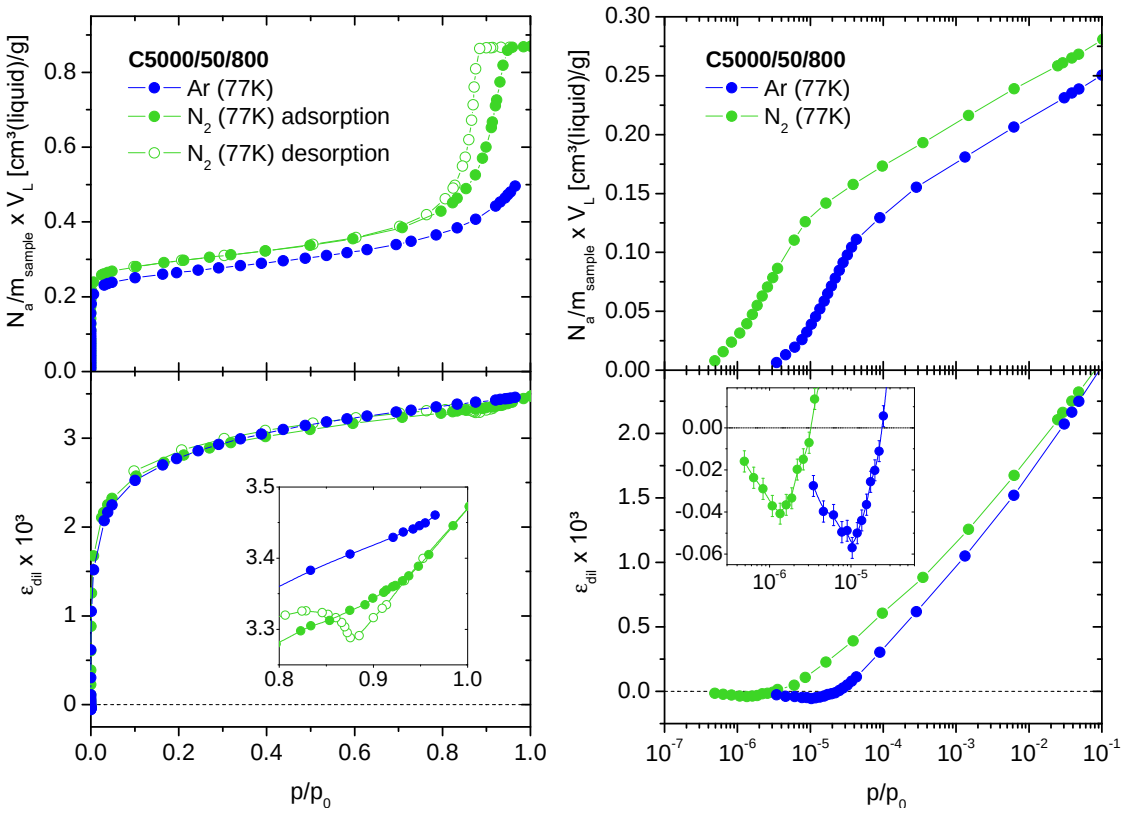

Figure 4.13.: Experimental N_2 and Ar adsorption and strain isotherms obtained for the sample C5000/50/800 at 77 K (on linear scale (left) and on half-logarithmic scale (right)). Closed symbols denote adsorption and open symbols denote desorption. The inset in the lower panel (left) is a magnification of the strain isotherm in the relative pressure regime of capillary condensation, while the inset in the lower panel (right) is a magnification of initial sample contraction at low relative pressure. Adapted with permission from ref [201]. Copyright 2015 American Chemical Society.

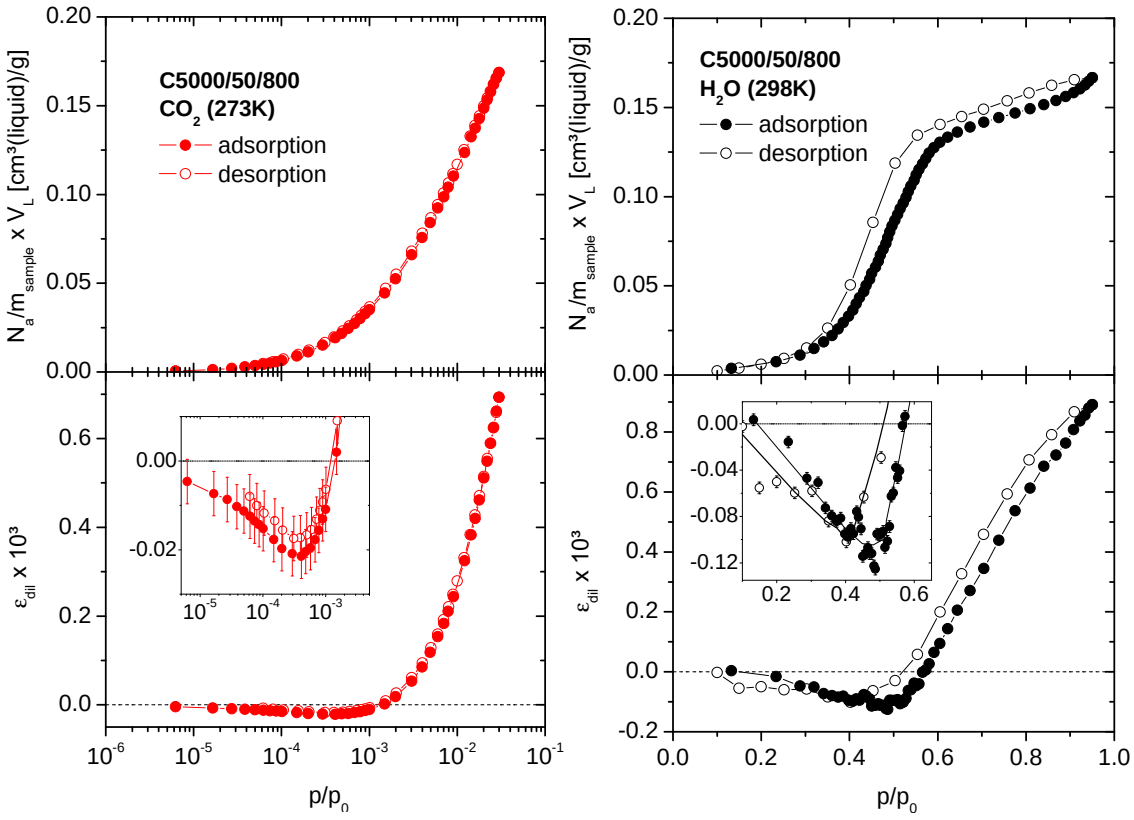

Figure 4.14.: Experimental CO_2 and H_2O adsorption and strain isotherms obtained for the sample C5000/50/800 at 273 and 298 K, respectively. Closed symbols denote adsorption and open symbols denote desorption. The adsorption isotherms are given in specific liquid volume. The insets in the lower panels show magnifications of initial sample contraction at low relative pressure. Adapted with permission from ref [201]. Copyright 2015 American Chemical Society.

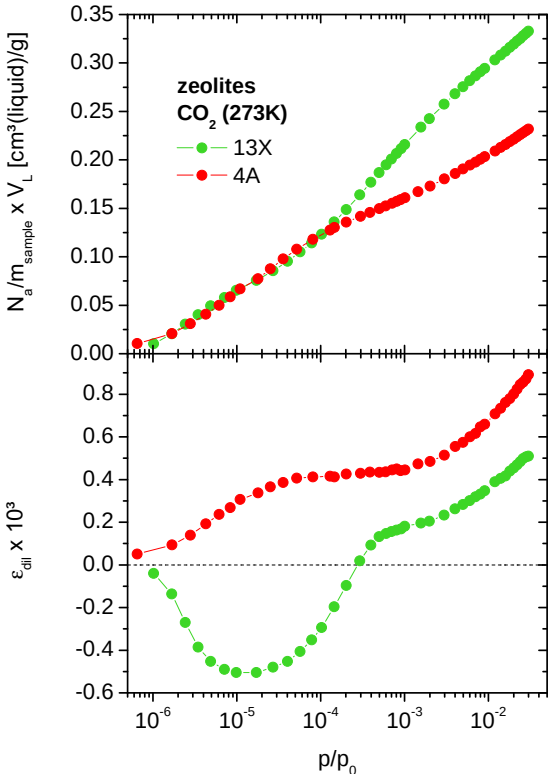

Figure 4.15.: Experimental CO_2 adsorption and strain isotherms obtained for the zeolite samples Köstrolith 4ABFK (type LTA) and 13XBFK (type FAU) at 273 K.

Köstrolith 13XBFK (type FAU), were obtained for CO_2 adsorption at 273 K and are shown in Figure 4.15.[3] In the relative pressure range $p/p_0 < 10^{-4}$ the adsorption isotherms for both zeolites are very similar showing approximately logarithmic dependence between N_a/m_{sample} and p/p_0. For relative pressures above 10^{-4} the adsorption of the zeolite 13XBFK is larger than for the zeolite 4ABFK and both adsorption isotherms drift apart. Contrary to the adsorption isotherms, the strain isotherms of both samples are qualitatively different. While the zeolite 13XBFK exhibits the common nonmonotonic strain isotherm reported in literature for zeolites during Kr and Xe adsorption [35–37], the strain isotherm of the zeolite 4ABFK shows monotonic expansion over the whole relative pressure range considered. This rather exceptional result is discussed in section 5.6.

[3] Analogous measurements for N_2 adsorption at 77 K were not possible, because at 77 K the microporosity of the zeolite 4A is not accessible to N_2.

5. Discussion

In this section the experimental results of adsorption measurements with in-situ dilatometry (section 4.3) are discussed in correlation with the theoretical models for adsorption-induced deformation (section 2.3). The outline of this section follows the structural features of the sample materials, i.e., micro- and mesoporosity as well as order and disorder (Figure 3.1). The final goal of each section is to identify the major deformation mechanisms relevant for the samples considered and (where possible) obtain a quantitative description of the dilatometric strain. For the latter, the structural parameters of each sample (section 4.2) and the NLDFT calculations (section 4.1) serve as input, while the typically unknown mechanical parameters of the samples are adapted and compared to reference values.

5.1. Hierarchical Structured Porous Silica - Ordered Mesoporosity

The approach for the description of the strain isotherm of the hierarchical structured porous silica (Figure 4.12) is a combination of the adsorption stress model for cylindrical mesopores, DBdB theory and the mechanical model of a cylindrical tube (section 2.3.2). The strategy applied in the following begins at modeling of the experimental adsorption isotherm of the hierarchical structured silica by DBdB theory. Based on the obtained DBdB model parameters, the stresses inside a cylindrical pore and the respective strains of a cylindrical tube are calculated. For a quantitative description of the sample's dilatometric strain isotherm furthermore a simple strut network model is introduced. The filled pore regime of the strain isotherm is then fitted to the overall model and predictions for film and hysteresis regime are derived. Finally, mechanical and structural parameters of the hierarchical structured silica are evaluated from strain data. A very detailed discussion of this procedure is given in a publication related to this work [129] and thus only the most important aspects are reproduced in this section.

The first step of describing the dilatometric strain isotherm of the hierarchical silica (N_2, 77 K) is the modeling of the respective experimental adsorption isotherm by DBdB theory assuming the cylindrical pore geometry (Eq. 2.18 to 2.22). The disjoining reference isotherm $\Pi(h)$ of a macroporous silica material with similar surface chemistry required for the modeling is given in Appendix B. Figure 5.1 shows the experimental adsorption isotherm and the result of the DBdB modeling. The structural parameters adapted in the theoretical model were the average mesopore diameter $d_{DBdB} = 4.7$ nm and the specific mesopore surface area $S_{DBdB} = 205$ m^2/g, which are both in good agreement with the results from other

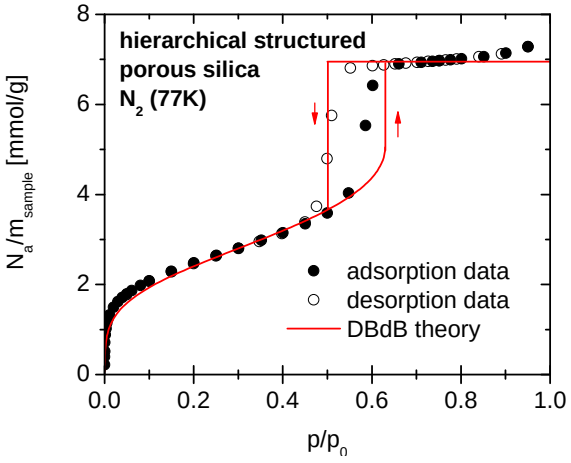

Figure 5.1.: Experimental adsorption isotherm (N_2, 77 K) of the hierarchical structured porous silica (closed symbols adsorption, open symbols desorption) and respective modeling by DBdB theory. Adapted with permission from ref [129]. Copyright 2017 American Chemical Society.

adsorption models, i.e., $S_{BET} = 203$ m^2/g and $\bar{d}_{meso} = 4.7$ nm (Table 4.3).

Employing the mesopore diameter d_{DBdB} and the respective reference isotherm $\Pi(h)$ (Appendix B) the stress isotherms $\sigma_{a,\perp}(p/p_0)$ and $\sigma_{a,\parallel}(p/p_0)$ were calculated according to Eq. 2.29 in film and filled pore regime, respectively (Figure 5.2); the offset of the strains was shifted to match the reference point, i.e., zero stress at vacuum conditions.

The radial stress $\sigma_{a,\perp}$ shown in Figure 5.2 corresponds to the adsorption stress of the Gor-Neimark model [79] and shows the approximately triangular hysteresis behavior also found in many experimental studies on the adsorption-induced deformation of mesoporous materials, e.g., refs [25, 28, 30]. Notably, the stress hysteresis is a direct consequence of the adsorption hysteresis. Comparing radial and axial stresses, the axial stress $\sigma_{a,\parallel}$ is found to be approximately twice as large as the radial one $\sigma_{a,\perp}$ in the film regime; this result is typical for Bangham stress dominated effects on cylindrical structures [121]. In the hysteresis regime the loop of the axial stress $\sigma_{a,\parallel}$ is reversed in comparison to the radial stress. Considering the definition of $\sigma_{a,\parallel}$ (Eq. 2.29b) the hysteresis of the axial stress follows directly of the hysteresis of the adsorbate's grand potential: at the relative pressure of capillary condensation $\sigma_{a,\parallel}$ exhibits an upward step, since the film state is metastable with respect to the filled pore state, while capillary evaporation is an equilibrium transition and consequently the axial stress exhibits no jump at this point. Lastly, in the film regime both stresses run parallel due to their dependence on the capillary pressure.

Inserting the stresses $\sigma_{a,\perp}(p/p_0)$ and $\sigma_{a,\parallel}(p/p_0)$ as shown in Figure 5.2 into Eq. 2.33 the corresponding theoretical strain isotherms $\varepsilon_{a,\perp}(p/p_0)$ and $\varepsilon_{a,\parallel}(p/p_0)$

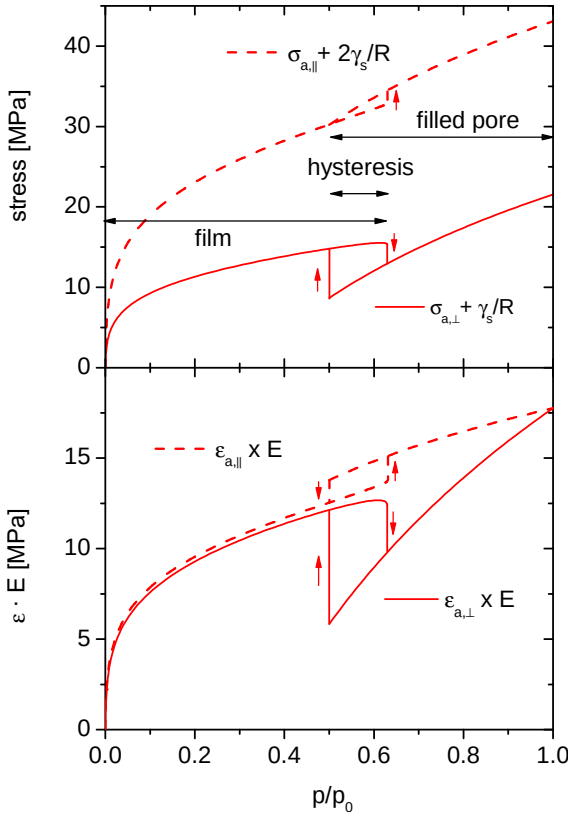

Figure 5.2.: Axial stress $\sigma_{a,\parallel}(p/p_0)$ and radial stress $\sigma_{a,\perp}(p/p_0)$ calculated according to Eq. 2.29 for a pore diameter $d_{DBdB} = 4.7$ nm (upper panel); corresponding axial strain $\varepsilon_{a,\parallel}(p/p_0)$ and radial strain $\varepsilon_{a,\perp}(p/p_0)$ calculated from the strains shown in the upper panel according to Eq. 2.33 multiplied by the Young's modulus of the nonporous solid backbone E. The Poisson's ratio ν applied to Eq. 2.33 was assumed to be 0.2 [129] (lower panel). The horizontal lines in the upper panel mark the different regimes of the adsorption process, i.e., the film regime, the hysteresis regime and the filled pore regime. Adapted with permission from ref [129]. Copyright 2017 American Chemical Society.

are obtained (Figure 5.2). Since the mechanical properties E and ν required for explicit calculations of $\varepsilon_{a,\perp}$ and $\varepsilon_{a,\parallel}$ are a priori unknown, the strain isotherms shown in Figure 5.2 are represented in terms of $\varepsilon \cdot E$, with E being a simple scaling factor for the strains. The impact of the Poisson's ratio ν on the strain isotherms is generally more complex (see solution of the Lamé problem in Eq. 2.33), however, because the nonporous solid phase of the hierarchically silica can be expected to be similar to other silica based materials, a reasonable estimate for the Poisson's ratio is $\nu = 0.20 \pm 0.05$ [121]. For this limited range of the Poisson's ratio the variation of the strain isotherms is only minor [129] and therefore the representative value of $\nu = 0.20$ was used for the lower plot in Figure 5.2.

The comparison of axial and radial strains predicted by the model shows that both strains are almost identical in the film state of the adsorption process. While this result may appear counterintuitive with respect the large difference of the underlying stresses in this state, it is a simple consequence of the cylindrical pore geometry and its response to axial and radial strain, respectively (Eq. 2.33). For the same reason axial and radial strains in the filled pore regime deviate significantly from one another, although the related stresses in both directions are proportional to the capillary pressure. Of particular importance are the shapes of the strain hystereses in both cases: while the radial strain exhibits the hysteresis commonly associated with mesoporous materials [25, 28, 30], i.e., within the hysteresis loop the filled pore state exhibits lower strain than in the film state, this behavior is reversed for the axial strain. The hysteresis of the axial strain isotherm follows from qualitative identical hysteresis of the underlying axial stress. In addition to that, the Poisson's effect causes a direct correlation of axial and radial strain hysteresis, i.e., the radial strain hysteresis is to some extent inversely imprinted on the axial strain hysteresis and vice versa. Since radial and axial strain hystereses show qualitatively opposing behavior, this way both strain hystereses become even more pronounced.

In the next step, the experimentally determined dilatometric strain isotherm $\varepsilon_{dil}\,(p/p_0)$ of the hierarchically silica (4.12) is compared to the theoretical model described above. For this, the macroporous strut network of the sample has to be taken into account. Here it is assumed that the strut network can be simplified by two perpendicular arranged struts as shown in Figure 5.3. In this case the dilatometric strain corresponds to a superposition of the struts' axial and radial strains, with the deformation of the individual struts being given by the cylindrical tube model. Quantitatively, this approach leads to

$$\varepsilon_{dil} = x \cdot \varepsilon_{a,\perp} + (1 - x) \cdot \varepsilon_{a,\parallel}, \qquad 0 \leq x \leq 1, \tag{5.1}$$

where the model parameter x is the relative contribution of the radial strain to the dilatometric strain of the macroscopic monolith sample and $(1 - x)$ the respective contribution of the axial strain.

For the quantitative data evaluation, at first the filled pore regime is considered,

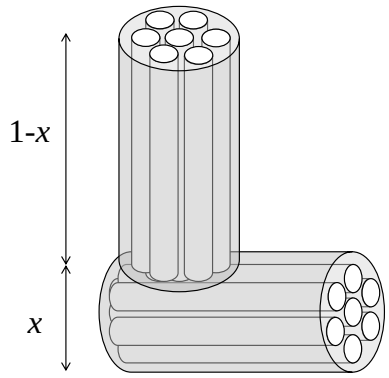

Figure 5.3.: Model of two perpendicular arranged struts as representation of the whole strut network. Reprinted with permission from ref [129]. Copyright 2017 American Chemical Society.

since here axial and radial strain (and therefore their superposition according to Eq. 5.1) are predicted to be directly proportional to the capillary pressure p_{cap} (Eq. 2.31c and 2.31d). As shown in Figure 5.4 the linear correlation $\varepsilon_{dil} \propto p_{cap}$ is indeed valid for the experimental data of the hierarchically silica considered in this work. By combining Eq. 2.29, 2.33 and 5.1 the slope $\partial\varepsilon_{dil}/\partial p_{cap}$ and the intercept $\varepsilon_{dil}\,(p_0)$ of the linear fit shown in Figure 5.4 can be written as

$$\varepsilon_{dil}\,(p_0) = \varepsilon_{a,\perp}\,(p_0) = \varepsilon_{a,\parallel}\,(p_0) = 2 \cdot \frac{1-\nu}{E} \cdot \frac{\phi}{1-\phi} \cdot \frac{\gamma_s - \gamma_{sl}}{R}, \tag{5.2}$$

$$\frac{\partial\varepsilon_{dil}}{\partial p_{cap}} = x \cdot \frac{2-\nu}{E} \cdot \frac{\phi}{1-\phi} + (1-x) \cdot \frac{1-2\nu}{E} \cdot \frac{\phi}{1-\phi}. \tag{5.3}$$

Notably, Eq. 5.2 neglects the impact of the saturation pressure p_0 on the sample strain implying $E \gg p_0$.

To obtain a description of the strain isotherm over the whole relative pressure range based on the stresses $\sigma_{a,\perp}$ and $\sigma_{a,\parallel}$ (Figure 5.2) Eq. 2.33 as well as Eq. 5.2 and 5.3 (solved for E and x, respectively) are inserted into Eq. 5.1 resulting in

$$\varepsilon_{dil} = 2\left(\frac{\partial\varepsilon_{dil}}{\partial p_{cap}} - \frac{1}{k}\right)\sigma_{a,\perp} + \left(\frac{2}{k} - \frac{\partial\varepsilon_{dil}}{\partial p_{cap}}\right)\sigma_{a,\parallel}, \tag{5.4}$$

$$k = \frac{2}{\varepsilon_{dil}\,(p_0)} \cdot \frac{\gamma_s - \gamma_{sl}}{R} = \frac{E}{1-\nu} \cdot \frac{1-\phi}{\phi}. \tag{5.5}$$

Here $\partial\varepsilon_{dil}/\partial p_{cap}$ and k are effective mechanical parameters of the sample investigated, which incorporate the sample properties E, ν, ϕ and x. On the other hand, the parameter k is also fully determined by the fit parameter $\varepsilon_{dil}\,(p_0) = \varepsilon_{dil}\,(p_{cap} = 0)$, the pore radius R and the surface energy change $\gamma_s - \gamma_{sl}$, which were already obtained by the fit shown in Figure 5.4 and the modeling of the adsorption isotherm by DBdB theory (Figure 5.1), respectively. Thus the

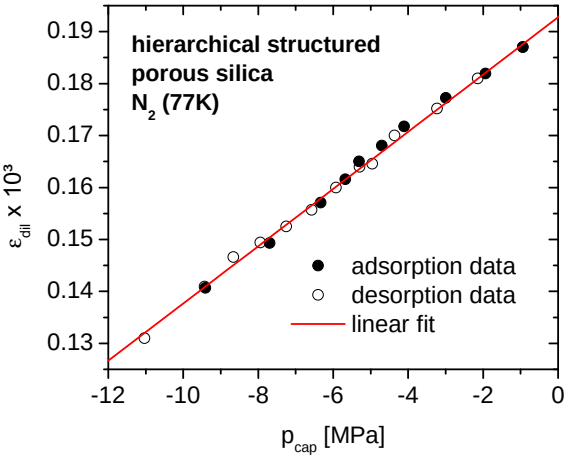

Figure 5.4.: Experimental strain of the hierarchical structured porous silica (Figure 4.12) in the filled pore regime plotted versus capillary pressure p_{cap} (Eq. 2.25) and fitted by a linear correlation [129]. The shown data corresponds to the plateau of the sample's adsorption isotherm (Figure 5.1) in the relative pressure range between 0.5 and 1. Adapted with permission from ref [129]. Copyright 2017 American Chemical Society.

dilatometric strain isotherm is given over the whole relative pressure range by Eq. 5.4 when combing the modeling of the adsorption isotherm (Figure 5.1), the stresses $\sigma_{a,\parallel}(p/p_0)$ and $\sigma_{a,\perp}(p/p_0)$ (Figure 5.2) and the fit of the strain in the filled pore regime (Figure 5.4).

The experimental strain isotherm and the result of Eq. 5.4 are compared in Figure 5.5 as a function of relative pressure and specific amount adsorbed, respectively. Here the surface energy change $\gamma_s - \gamma_{sl} = 50.6\ \mathrm{mJ/m^2}$ (Eq. 2.32), the pore radius $R = d_{DBdB}/2 = 2.35$ nm (Figure 5.1) and the fit parameters $\partial\varepsilon_{dil}/\partial p_{cap} = 5.51{\cdot}10^{-6}\ \mathrm{MPa^{-1}}$ and $\varepsilon_{dil}(p_0) = 1.93{\cdot}10^{-4}$ (Figure 5.4) were applied. Due to the inclusion of the fit parameters $\partial\varepsilon_{dil}/\partial p_{cap}$ and $\varepsilon_{dil}(p_0)$ into Eq. 5.4 the theoretical strain isotherm is in good agreement with the experiment for the filled pore regime. Consequently, film and hysteresis regime of the strain isotherms have to be considered for further validation of the applied approach. In the film regime, the theoretical model underestimates the dilatometric strain: starting from vacuum conditions, the discrepancy between model and experiment increases with relative pressure up to $p/p_0 \approx 0.2$. Here the quantitative deviations begin to recede leading to quantitative agreement of theoretical and dilatometric strain at the point of capillary condensation. Furthermore, the predicted shape of the strain hysteresis is qualitatively correct, i.e., within the strain loop the filled pore state exhibits lower strain than the film state.

Finally, explicit values for the Young's modulus E and the structural parameter x are derived. Inserting the surface energy change $\gamma_s - \gamma_{sl}$, the pore radius $R = d_{DBdB}/2$ and the fit parameters $\partial\varepsilon_{dil}/\partial p_{cap}$ and $\varepsilon_{dil}(p_0)$ as given above as well

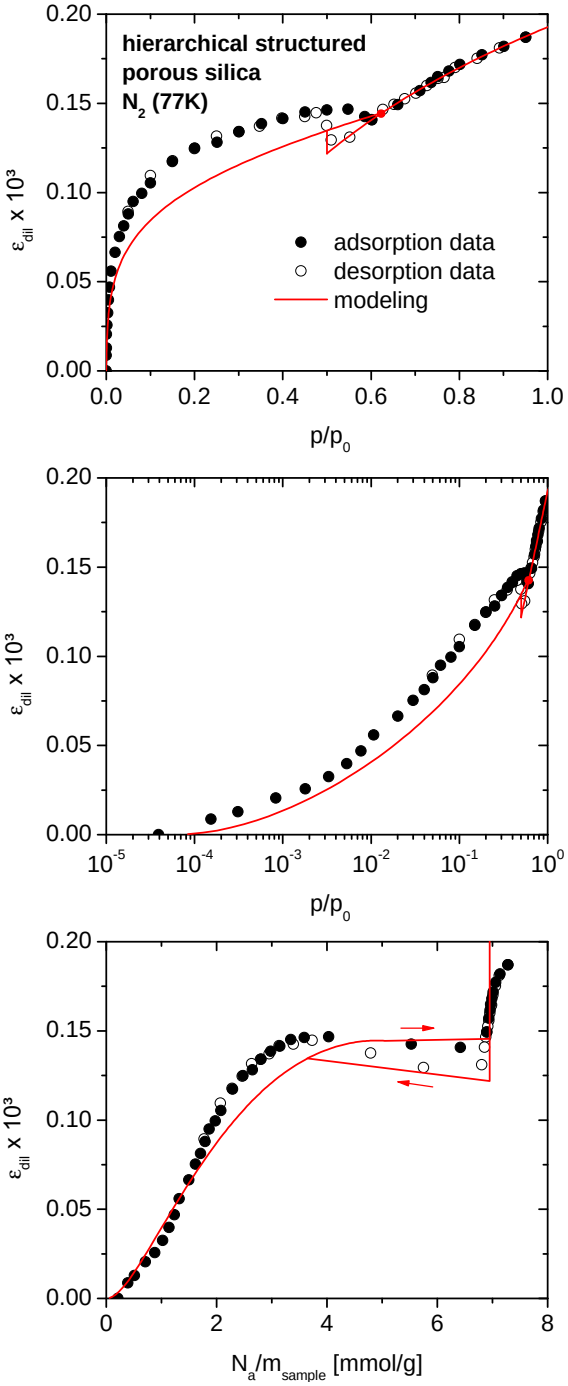

Figure 5.5.: Experimentally determined dilatometric strain data and respective theoretical predictions by Eq. 5.4 as a function of relative pressure on linear scale (upper panel), relative pressure on logarithmic scale (middle panel) and specific amount adsorbed (lower panel) [129]. Adapted with permission from ref [129]. Copyright 2017 American Chemical Society.

as the strut porosity $\phi = \phi_{strut} = 0.34 \pm 0.02$ (Table 4.8) and the Poisson's ratio $\nu = 0.20 \pm 0.05$ into Eq. 5.2 and 5.3 yields $E = (92 \pm 6)$ GPa and $x = 0.33 \pm 0.02$. According to Figure 5.3 the ratio $(1 - x)/x$ should be equal to the average ratio of strut length to strut diameter; from the SEM image of the sample shown Figure 4.9 one may estimate $(1 - x)/x$ in the range of 2 to 5. This corresponds to $x = 0.20$ to 0.33, which is in reasonable agreement with the result obtained from the model. The Young's modulus E on the other hand appears rather high when e.g. compared to the Young's modulus of fused silica (73 GPa [214]). An obvious interpretation of the high apparent Young's modulus is the model's neglect of deformation effects beyond the individual mesopore, i.e., in particular bending of struts within the macroporous strut network. Based on the structure seen on SEM images (Figure 4.9) it appears likely that the struts cannot deform entirely free, but are subject to mechanical confinement arising from their knot like connections. Such confinement could be capable of redirecting adsorption stimulated expansion into strut bending, which would only partially be detected by the dilatometric technique and therefore create the impression of increased mechanical stiffness.

Another potential source for deviations between model and experiment is the assumption of constant mechanical properties for the nonporous solid skeleton, i.e., E and ν. While the magnitude of the observed dilatometric strain suggests the validity of elastic deformation, both, increase as well as decrease of the adsorbent's mechanical stiffness due to adsorption were suggested [95, 215]. This effect should be particularly pronounced for microporous materials, but cannot be excluded for mesoporous samples.

In summary, the applied combination of advanced adsorption stress model, DBdB theory and mechanical model of a cylindrical tube is capable of describing adsorption-induced deformation of the hierarchically structured silica. The numerical values for the obtained mechanical and structural parameters (E and x, respectively) are in reasonable agreement with expectations. Although the model simplifies specific aspects of the sample structure such as the macroporous strut network, the major mechanisms of its adsorption-induced deformation are apparently well covered.

5.2. Silica Aerogel - Disordered Mesoporosity

For the discussion of the experimental strain isotherm obtained for the silica aerogel during N_2 adsorption at 77 K (Figure 4.11) the theoretical framework for adsorption-induced deformation of aero-/xerogel networks described in section 2.3.3 was applied. Since aero-/xerogel structures considered in this work are entirely disordered and isotropic, the correlation of the dilatometric (linear) strain ε_{dil} and the theoretical (volumetric) network strain ε_{net} is given by:

$$\varepsilon_{net} = (1 + \varepsilon_{dil})^3 \approx 3\varepsilon_{dil}. \tag{5.6}$$

The second equality in Eq. 5.6 is an approximation for $\varepsilon_{dil} \ll 1$, which is valid

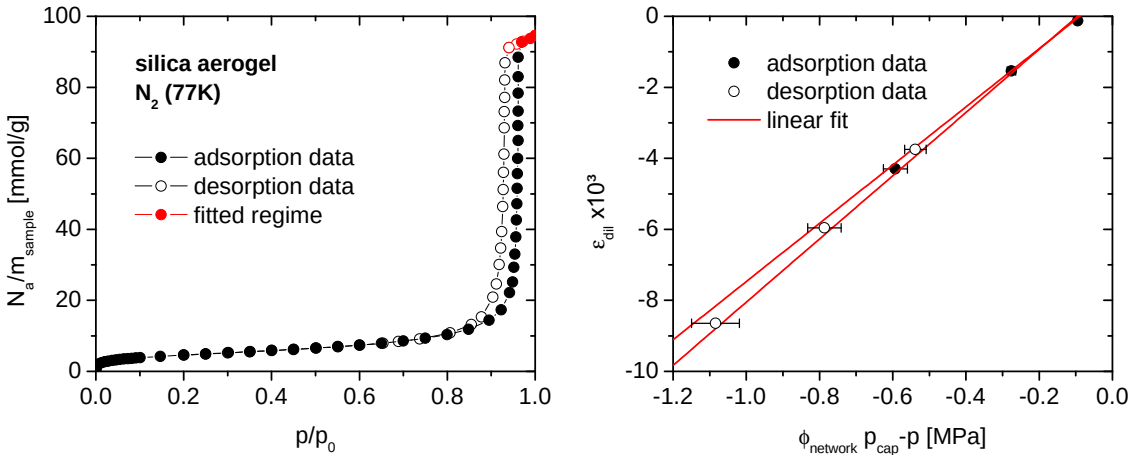

Figure 5.6.: Experimental adsorption isotherm of the silica aerogel (N_2, 77 K) (left) and respective dilatometric strain in the filled pore regime including linear fits according to Eq. 2.39 (right). Full symbols denote adsorption, open symbols denote desorption.

for all aero-/xerogel samples considered in this work.

In direct analogy to the deformation of the hierarchical structured silica discussed in the previous section, the strain isotherm of the silica aerogel has to be separated into film and filled pore regime (Eq. 2.38 and 2.39, respectively). Again, the state of filled pores is considered first, before the more complex film regime is analyzed. Thus, data evaluation begins at relative pressure > 0.9, where the type IV adsorption isotherm of the silica aerogel exhibits the plateau associated with the filled pore state.[1] Following Eq. 2.39 in this regime, the strain of the sample $\varepsilon_{net,filled}$ is predicted to be proportional to $(\phi_{net} \cdot p_{cap}\,(p/p_0) - p)^2$ with the proportionality factor being equal to the aerogel's inverse bulk modulus, i.e., $1/K_b$. Here ϕ_{net} is the porosity of the aerogel's network, p_{cap} is the capillary pressure (Eq. 2.25) and p is the gas pressure of the adsorptive. To verify this correlation Figure 5.6 shows a plot of ε_{dil} versus $(\phi_{net} \cdot p_{cap}\,(p/p_0) - p)$ and the most extreme linear fits possible within the error bars, which are dominated the accuracy of ϕ_{net} (Table 4.7). The slopes of the linear fits allow for the determination of the bulk modulus $K_b = (39.1 \pm 1.6)$ MPa. This value is higher than the one obtained from sound velocity measurements, i.e., (32.4 ± 5.1) MPa (Table 4.2), however, in the very limits of accuracy both values are still consistent.

An additional consistency check for Eq. 2.39 is the sample strain at saturation pressure $\varepsilon_{net}\,(p_0)$, which can be determined by extrapolation of the fit shown in Figure 5.6. According to the combination of Eq. 2.39 with Eq. 2.34 and 2.35,

[1] Due to the adsorption-induced strain the "plateau" of the silica aerogel's adsorption isotherm is not flat but exhibits some slope.

[2] In contrast to the hierarchically structured silica discussed in the previous section, the bulk modulus of the silica aerogel is so low that the impact of the adsorptive pressure p onto the aerogel strain cannot be neglected.

respectively, $\varepsilon_{net}(p_0)$ is given by

$$\varepsilon_{net}(p_0) = \frac{2(\gamma_s - \gamma_{sl})}{R_{part} K_{part}} - \frac{p_0}{K_b} \qquad \text{for spherical particles or} \tag{5.7a}$$

$$\varepsilon_{net}(p_0) = \frac{1-\nu_{rod}}{1-2\nu_{rod}} \cdot \frac{2(\gamma_s - \gamma_{sl})}{R_{rod} K_{rod}} - \frac{p_0}{K_b} \qquad \text{for cylindrical rods} \tag{5.7b}$$

depending on the geometry of the network forming entities. For quantitative evaluation of $\varepsilon_{net}(p_0)$ obtained from Figure 5.6 the bulk modulus of the network entities is calculated to be $K_{part} = (12 \pm 1)$ GPa or $K_{rod} = (25 \pm 6)$ GPa, respectively, assuming $\nu_{rod} = 0.20 \pm 0.05$ [121], $\gamma_s - \gamma_{sl} = 55$ mJ/m^2 (Eq. 2.32 with $R = \bar{d}_{meso}/2 = 17.2$ nm, Table 4.3), $p_0 = 0.1$ MPa [193], $K_b = (39.1 \pm 1.6)$ MPa as well as the radii $R_{part} = d_{part}/2 = 3.75$ nm and $R_{rod} = d_{rod}/2 = 2.5$ nm, respectively (Table 4.7).

For comparison, the bulk modulus of nonporous fused silica $K_{silica} = 39.9$ GPa is considered [214] showing that neither K_{part} nor K_{rod} reach the stiffness of fused silica. The relative deviations between the bulk moduli obtained from the model and the reference value favor the model of rod-shaped structural entities as would be expected for significantly sintered silica aerogel.

In the next step, the film regime of the strain isotherm is considered (Eq. 2.38). Here two strain contributions arise: a positive strain from the Bangham effect, $\varepsilon_{part/rod}$ (Eq. 2.34 and 2.35), and a negative strain due the Laplace stress arising from the curvature of the adsorbate-adsorptive interface, $\varepsilon_{Laplace}$ (Eq. 2.37). As was shown by Gommes et al. [131], initially the adsorbate forms a uniform and convex film on the entities forming the network. In this situation the Laplace pressure arising from the adsorbate film can be expected to be quantitatively negligible and thus the adsorption-induced strain of the silica aerogel is exclusively given by Bangham's law for spherical or cylindrical particles, respectively, i.e., $\varepsilon_{net,film} = \varepsilon_{part/rod} \propto \Delta\gamma_s$. Figure 5.7 shows a plot of the silica aerogel's strain isotherm ε_{dil} as a function of the surface energy change $\Delta\gamma_s$ (Eq. 2.23), which exhibits a significant linear range. The most extreme linear fits possible within error bars allow for estimating the upper relative pressure limit to $0.1 < p/p_0 < 0.35$, where the assumption of a convex adsorbate film on the structural entities is valid (compare Figure 5.7). For higher relative pressures, the Laplace strain becomes significant and the silica aerogel contracts. For comparison, the statistical monolayer formation of the silica aerogel according to BET theory is reached at $p/p_0 \approx 0.1$. This allows for the conclusion that the first layer of adsorbed N_2 molecules indeed forms a convex layer on the network forming entities, while the consecutive layers tend to the formation of concave liquid-vapor interface segments, which in turn cause negative Laplace stress within the network. From the slopes of the linear fits in Figure 5.7 again the bulk moduli for spherical particles $K_{part} = (14.7 \pm 3.0)$ GPa and cylindrical rods $K_{rod} = (30.5 \pm 8.9)$ GPa can be evaluated according to Eq. Eq. 2.34 and 2.35 assuming the same values for ν_{rod} as well as

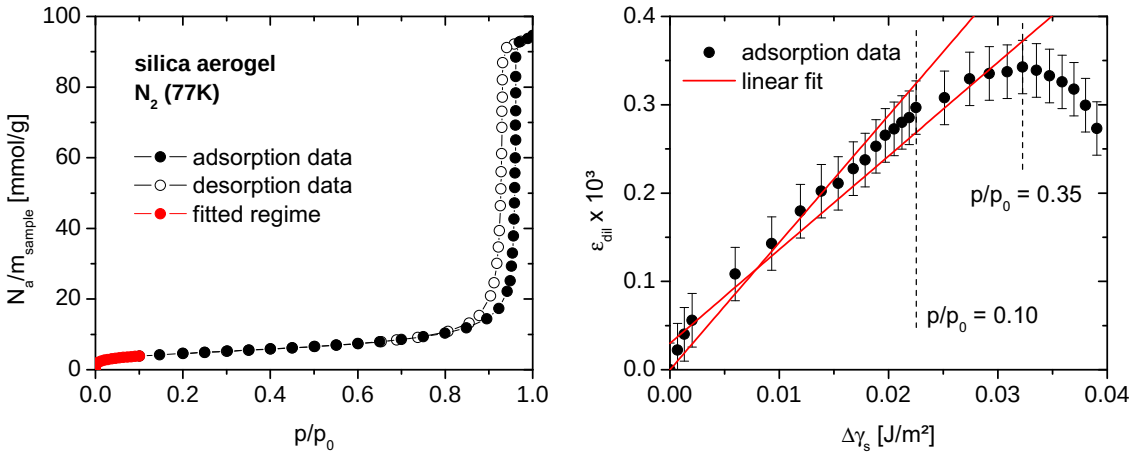

Figure 5.7.: Experimental adsorption isotherm of the silica aerogel (N_2, 77 K) (left) and its dilatometric strain for low relative pressures as a function of the change in surface energy $\Delta\gamma_s$ (Eq. 2.23) (right). The vertical lines in left plot indicate the relative pressure of the last data points still in line with the linear fits.

the radii R_{part} and R_{rod} as given above. The values for K_{part} and K_{rod} are slightly higher than the ones obtained from the filled pore regime but consistent within accuracy considerations.

To obtain a quantitative estimate of aero-/xerogels' strain due to Laplace pressure $\varepsilon_{Laplace}$, Eq. 2.37 was proposed assuming the adsorbate-adsorptive curvature as given by the DBdB model for adsorption in cylindrical pores (section 2.2.3). A preliminary step to the application of Eq. 2.37 is the modeling of the experimental adsorption isotherm of the silica aerogel by DBdB theory in analogy to the hierarchically structured silica. The experimental adsorption isotherm of the silica aerogel and the respective modeling by DBdB theory are shown in Figure 5.8 (upper panel). The focus of the modeling was to reproduce the slope of the adsorption isotherm in the film regime and the plateau-like filled pore regime. Since the shape of the pores within the aerogel network are only remotely cylindrical, the relative pressure of capillary condensation and evaporation were considered a less reliable foundation for the modeling. The resulting model parameters are the average mesopore diameter $d_{DBdB} = 33.2$ nm and the specific mesopore surface area $S_{DBdB} = 390$ m^2/g, which are both in good agreement with the results for $\bar{d}_{meso} = 34.4$ nm and $S_{BET} = 380$ m^2/g (Table 4.3). As can be seen from Figure 5.8 the DBdB model gives an approximate description of the experimental adsorption isotherm. Quantitative disagreement is found in particular for the hysteresis loop being predicted at slightly higher relative pressures than seen in the experiment.

To test Eq. 2.37 against the experimental data, the strain

$$\varepsilon_{Laplace} = 3\varepsilon_{dil} - \varepsilon_{part/rod} \tag{5.8}$$

is calculated from the dilatometric strain isotherm and the average fit for $\varepsilon_{part/rod}$

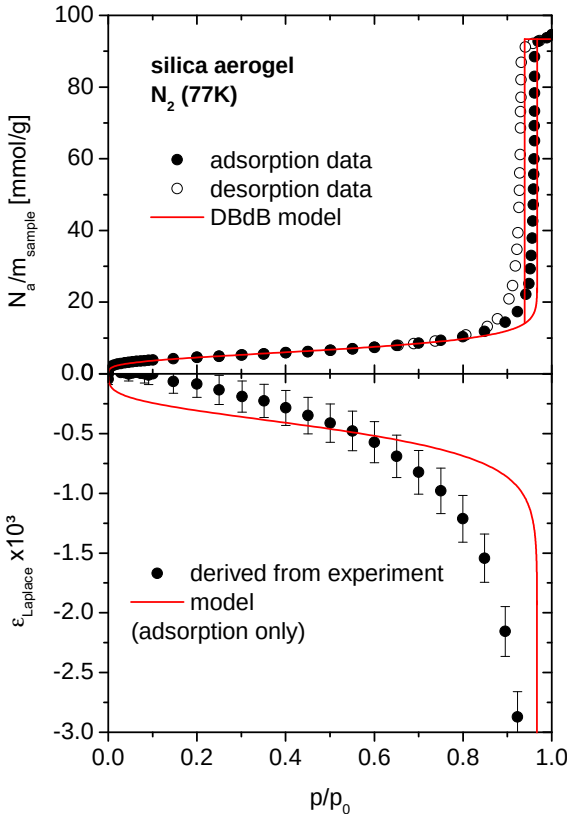

Figure 5.8.: Experimental adsorption isotherm of the silica aerogel (N_2, 77 K) and respective modeling by DBdB theory (upper panel). Volumetric strain $\varepsilon_{Laplace}$ due to curvature of the adsorbate derived from the dilatometric data of the silica aerogel (Eq. 5.8) and calculated by Eq. 2.37 (lower panel).

Table 5.1.: The bulk modulus of the silica aerogel K_b as obtained by sound velocity measurements and analysis of the strain isotherm as well as the bulk modulus of the nonporous silica phase K_{part}/K_{rod} derived from the strain isotherm. Literature values for nonporous amorphous silica K_{silica} are given for comparison.

approach	K_b [MPa]	K_{part}/K_{rod} [GPa]	K_{silica} [GPa]
sound velocity measurement	32.4 ± 5.1	-	-
strain isotherm (filled pore regime)	39.1 ± 1.6	12 ± 1/25 ± 6	-
strain isotherm (Bangham's law)	-	14.7 ± 3.0/30.5 ± 8.9	-
fused silica (literature)	-	-	39.9

as shown in Figure 5.7. In analogy to Eq. 2.37, Eq. 5.8 implies that the strain of the silica aerogel is superposition of the (negative) Laplace strain due to the curvature of the adsorbate-adsorptive interface and the (positive) strain of the nonporous network entities, i.e., Bangham's law. A comparison of $\varepsilon_{Laplace}$ derived via Eq. 5.8 and calculated according to Eq. 2.37 (assuming $\phi_{net} = 0.87$ (Table 4.7), $K_b = 39.1$ MPa and $R = d_{DBdB}/2 = 16.6$ nm) is shown in Figure 5.8 (lower panel). Notably, $\varepsilon_{Laplace}$ is very pronounced for the silica aerogel investigated, since the value of K_b is about three orders of magnitude lower than K_{part} or K_{rod}; in this regard, the silica aerogel differs significantly from the hierarchical structured porous silica in the previous section. As can be seen from Figure 5.8 the prediction of $\varepsilon_{Laplace}$ from the model can only be considered a rough estimate as it only captures the most general features of the actual process within the silica aerogel. The model overestimates the experimentally derived Laplace strain for $p/p_0 < 0.6$ and underestimates it for $p/p_0 > 0.6$ indicating that the average curvature of the adsorbate film in the aerogel network is smaller than in the cylindrical pore till $p/p_0 = 0.6$ and larger beyond that point.

In summary, the proposed theoretical framework for the adsorption-induced deformation of mesoporous and disordered aero-/xerogel networks gives reasonable results in the filled pore state and for low relative pressures, which is dominated by Bangham's law. Both regimes allow for the derivation of the bulk modulus of the nonporous silica phase, while the filled pore regime additionally contains information on the bulk modulus of the aerogel network. All obtained bulk moduli and their respective reference values are summarized in Table 5.1. As can be seen from Table 5.1 the value derived for K_b from in-situ dilatometry is in line with the result from sound velocity measurements. Furthermore, the nonporous silica phase within the aerogel (described by K_{part}/K_{rod}) is found to be more compliant than fused silica. Noteworthy, the impact of the Laplace stress on the aerogel network due to the curvature of the adsorbate film can only be roughly approximated.

5.3. Carbon Xerogel I - Disordered Microporosity

In this section adsorption and adsorption-induced deformation of the micro- and macroporous carbon xerogel (C5000/30/800) is discussed. Based on the aero-/xerogel model presented in section 2.3.3 and evaluated for a mesoporous silica aerogel in the previous section, it can be shown that adsorption-induced deformation related to the macroporosity of the sample C5000/30/800 can be neglected. Therefore the dilatometric strain measured for this sample is entirely correlated to its microporosity.

To evaluate the experimental strain isotherm of the carbon xerogel, the adsorption stress models for the microporous carbon matrix (section 2.3.4) are combined with the results of the NLDFT calculations presented in section 4.1, i.e., the theoretical adsorption isotherms $N_{NLDFT}\left(p/p_0, w\right)$ (Eq. 2.13), the adsorption stress normal to the pore walls $\sigma_{a,\perp}\left(p/p_0, w\right)$ (Eq. 2.30a) and the stress parallel to the pore walls $\sigma_{a,\parallel}\left(p/p_0, w\right)$ (Eq. 2.30b). Both, the common approach to the deformation of microporous carbons, i.e., the original adsorption stress model (Eq. 2.41), and the extended adsorption stress model proposed in this work (Eq. 2.46) were applied. While the original adsorption stress model considers the nonporous skeleton to be rigid and therefore attributes all deformation to the pore volume, the extended model explicitly takes into account the nonporous skeleton's mechanical response to adsorption. In either case, the model parameters are the micropore size distribution of the carbon and its mechanical properties, i.e., the moduli of the microporous phase K_m for the original and K_β and K_s for the extended adsorption stress model.

As explained in refs [188, 197], the most straight forward way to correlate the linear dilatometric strain ε_{dil} obtained for the sample C5000/30/800 to the volumetric strains predicted by the adsorption stress models, i.e., ε_m, is to assume $\varepsilon_m = 3\varepsilon_{dil}$. The implications of this assumption are: (i) the microporous particles within the xerogel network exhibit isotropic strain due to their inherent disorder, (ii) the xerogel network deforms in the same way as its constituting particles and (iii) all strains are significantly smaller than 1.

Since the pore size distribution (PSD) required for the modeling of the strain isotherm is directly connected to the adsorption isotherm of the carbon by the integral adsorption equation (IAE) (Eq. 2.14), the inclusion of the experimental adsorption isotherm into the modeling process is obvious. Two different approaches for the combined analysis of adsorption and dilatometric strain isotherm of microporous carbons were reported:[3]

(a) the modeling of adsorption and strain isotherm is performed separately. This approach is easier and gives better agreement with each set of data, since

[3]Earlier works applying the adsorption stress model to describe adsorption-induced deformation in microporous carbons [75, 80] modeled only the strain isotherm.

available computational procedures can be used for each fitting process. However, this strategy typically results in two different PSDs. This approach was applied in a reference related to this work [197] and justified there by the fact that the obtained PSDs were very similar.

(b) the modeling of adsorption and strain isotherm is performed simultaneously with one PSD. This approach cannot be performed by common computational fitting procedures and the agreement for both data sets is naturally worse than for separate fitting. However, it is a better check on the consistency of the applied theoretical framework and the "hand-made" modeling is often more instructional than the results from computational algorithms. The strategy for this case is to create a PSD from Gaussian profiles using the PSD obtained from the computational fitting of adsorption isotherm as a guideline and approximately maintain its cumulative specific micropore volume. This approach was used in another reference related to this work [188] and is the method applied in the following.

Given above considerations, the adsorption and dilatometric data of the sample C5000/30/800 for CO_2 at 273 K were modeled for both versions of the adsorption stress model according to approach (b). The experimental data for CO_2 adsorption is considered advantageous for the modeling process, because unlike N_2 or Ar adsorption at 77 K, CO_2 adsorption at 273 K allows resolving micropore filling for pore widths below 0.5 nm (compare section 4.2). The resulting theoretical adsorption and strain isotherms are shown in Figure 5.9 along with the experimental data. The respective PSDs are given in Figure 5.10. The bulk moduli for the microporous matrix are $K_m = (6.1 \pm 0.3)$ GPa for the original adsorption stress model (Eq. 2.41) as well as $K_\beta = (3.7 \pm 0.4)$ GPa and $K_s = (12.4 \pm 1.1)$ GPa for the extended adsorption stress model (Eq. 2.46). The accuracy of the moduli is dominated by the accuracy of the porosity of the microporous carbon matrix ϕ_{mic}, which is taken from the sample characterization results (Table 4.6).

In the following, both adsorption stress models are evaluated by comparing the applied PSDs. Furthermore, the modeling results shown in Figure 5.9 and 5.10 for CO_2 adsorption at 273 K are used to predict the sample's adsorption and strain isotherms for CO_2 adsorption at 243 and 303 K as well as for N_2 adsorption at 77 K. Afterwards all predictions are compared to respective experimental data. The derived mechanical properties of all carbon xerogels investigated in this work are discussed in section 5.5.3.

The comparison of theoretical modeling and experimental data (Figure 5.9) shows that both versions of the adsorption stress model are capable of describing the characteristic nonmonotonic deformation of the carbon sample, while the related PSDs simultaneously give a reasonable prediction of the adsorption isotherm. Systematic deviations between experiment and both theoretical approaches occur in the relative pressure region of $5{\cdot}10^{-6}$ to $5{\cdot}10^{-4}$: here the predicted amount adsorbed and the sample contraction are smaller than the respective experimental values. However, overall the quantitative agreement is rated as acceptable. From

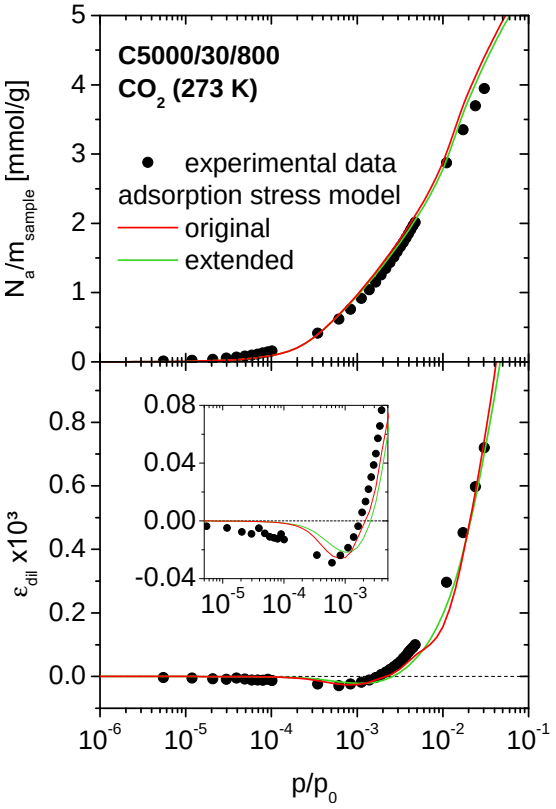

Figure 5.9.: Experimental adsorption and strain isotherms of the micro-macroporous carbon xerogel C5000/30/800 for CO_2 (273 K) and the respective modeling by the adsorption stress model in original and extended form.

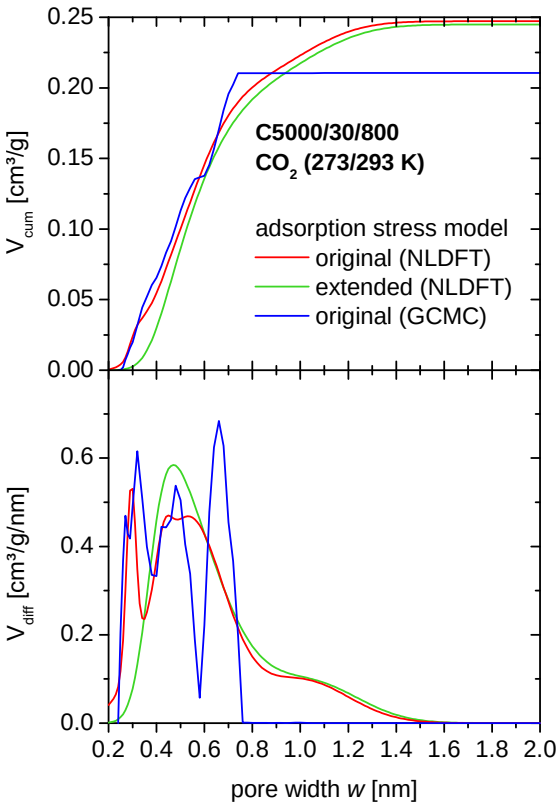

Figure 5.10.: Cumulative and differential pore volume distributions of the carbon xerogel C5000/30/800 evaluated from CO_2 data (273 K) by application of the original and the extended adsorption stress model and the results of NLDFT calculations. Additionally shown is the sample's PSD obtained by Kowalczyk et al. [197] from CO_2 data (293 K) applying the original adsorption stress model combined with GCMC simulations and an automated fitting procedure.

the applied PSDs (Figure 5.10) numerical values for specific micropore volume V_{mic} (DFT) (Eq. 3.10), specific surface area S_{mic} (DFT) (Eq. 3.11) and resulting average pore width $\bar{w}$ (Eq. 3.12) are derived and given in Table 5.2 along with the respective results obtained from common sample characterization via inversion of the IAE (Table 4.5). As can be seen from Table 5.2 the parameters of the differently obtained PSDs are rather close to one another. The key difference between original and extended adsorption stress model is found within the shapes of the applied PSDs (Figure 5.10): the PSD resulting from the application of the original adsorption stress model exhibits a sharp spike at a pore width of approximately 0.3 nm. This spike is essential for the original adsorption stress model in order to match the sample's expansion for increasing relative pressure, since only pores smaller than the molecular diameter of the adsorbate result in significant positive adsorption stress normal to the pore walls (compare Figures 4.1d and 4.2d). However, given the disordered micropore structure of carbon xerogels (Figure 3.2) this spike within the PSD seems unreasonable. Contrary to the original adsorption stress model, the extended adsorption stress model describes the sample's expansion by an expansion of the nonporous solid skeleton due to the adsorption stress parallel to the pore walls, which is found for pores of all widths (Figure 4.1f). This is illustrated in Figure 5.11, where the contributions of adsorption stress normal and parallel to the pore walls to the overall strain predicted are shown. As a consequence, the extended adsorption stress model does not require for large amounts of pores smaller than the molecular diameter of the adsorbate and the correlated PSD is very smooth.[4] Following this line of thought, the extended adsorption stress model can explain the nonmonotonic adsorption-induced deformation of microporous materials even for a monomodal PSD of slit-shaped pores. This directly challenges the conclusion of Kowalczyk and co-workers, who applied the original adsorption stress model to describe strain isotherms of carbons and attributed the characteristic nonmonotonic shape to the carbon's broad PSD [75].

Notably, the spike in the PSD of the original adsorption stress model at 0.3 nm is not limited to NLDFT calculations but also found for modeling based on GCMC simulations. This can be seen in Figure 5.10, which includes the sample's PSD determined by application of the original adsorption stress model on CO_2 strain data obtained at 293 K and evaluated by the combination of GCMC simulationss and an automated fitting algorithm [197]. The fact that the cumulative specific pore volume of the PSD from ref [197] is lower than the PSDs in this work results from the limitations of pore size analysis from CO_2 data at 293 K. Due to the elevated temperature, pores of width larger than 0.9 nm fill beyond the experimental pressure limit of 1 bar and thus cannot be resolved by theoretical analysis. Since the cumulative specific pore volume at 0.9 nm is approximately the same for all PSDs, the theoretical data evaluation can be considered consistent.

[4] On a side note, both PSDs obtained from simultaneous analysis of adsorption and strain isotherms are generally smoother than the PSD derived from the common adsorption analysis via inversion of the IAE (compare ref [197]).

Table 5.2.: Characteristics of the PSDs obtained for the micro-macroprous carbon xerogel C5000/30/800 from the common adsorption analysis via inversion of the IAE (data from Table 4.5) as well as the simultaneous analysis of adsorption and strain isotherms via original and extended adsorptions stress model, i.e., the specific micropore volume V_{mic} (DFT), the specific micropore area S_{mic} (DFT) and the average pore width $\bar{w}$.

approach	V_{mic} (DFT) N_2/CO_2 [cm^3/g]	S_{mic} (DFT) N_2/CO_2 [m^2/g]	$\bar{w}$ N_2/CO_2 [nm]
adsorption analysis (IAE)	0.252	973	0.52
original model	0.247	968	0.51
extended model	0.245	864	0.57

Further discussion on this effect is given in ref [197].

For further validation of both adsorption stress models, the PSDs and mechanical parameters obtained from the modeling of CO_2 adsorption and strain isotherms at 273 K are used to predict the same data sets at other temperatures. For this, experimental adsorption and strain isotherms of the sample C5000/30/800 are taken from ref [194], where CO_2 measurements on the very same sample were performed at 243 and 303 K. The respective experimental data sets and the corresponding theoretical predictions are shown in Figures 5.12.

As can be seen from Figure 5.12 both adsorption stress models predict the general trends correctly, i.e., for decreasing temperature the initial contraction increases and the expansion of the sample is shifted to higher relative pressures. However, as before quantitative deviations between experiment and theory occur in particular in the relative pressure region of the initial contraction and the correlated minimum. The extended adsorption stress model results in an overall better description of the minimum for CO_2 adsorption at 243 K in particular regarding its depth, while it significantly underestimates the initial contraction at 303 K. For the original adsorption stress model the situation is reversed: the contraction at 303 K is well described, while the contraction at 243 K is underestimated. Though no exhaustive explanation for these systematic shifts was found within this work, two issues of the modeling process should be kept in mind. For one, the temperature of 303 K is very close to critical temperature of CO_2 (304 K [200]) and therefore systematic deviations between real CO_2 and its Van der Waals model used in NLDFT calculations may occur (compare ref [216]). Second, the oscillating behavior of the original adsorption stress model for CO_2 adsorption at 243 K is a computational artifact resulting from the small number of theoretical adsorption isotherms contributing to positive adsorption stress (compare ref [188]).

In a last step, both adsorption stress models are applied to predict N_2 ad-

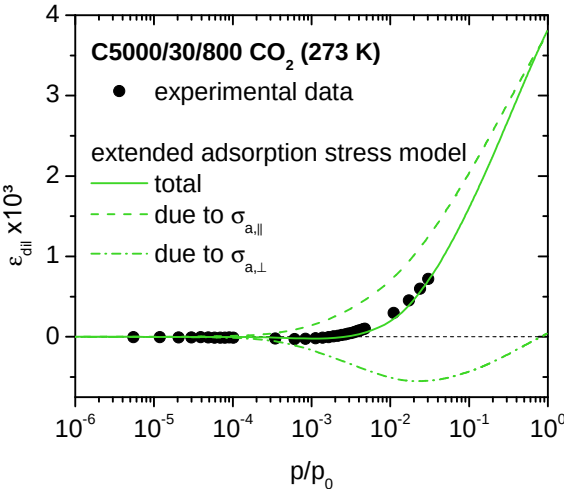

Figure 5.11.: Experimental strain isotherm of the micro-macroprous carbon xerogel C5000/30/800 for CO_2 (273 K) and the respective modeling by the extended adsorption stress model. In addition to the modeled overall strain of the sample also the contributions to the strain resulting from adsorption stress normal and tangential to the micropore walls are shown.

sorption and strain isotherms at 77 K for the sample C5000/30/800 again using the PSDs and mechanical parameters obtained from the modeling of CO_2 data at 273 K. Experimental data for N_2 at 77 K and respective predictions by the models are shown in Figure 5.13 on both, linear and logarithmic, pressure scales.[5] As can be seen from Figure 5.13, the qualitative features of adsorption and accompanying deformation are well captured by both models, however, quantitatively there are several deviations. The most obvious discrepancy between experiment and both models is that the predicted micropore filling begins at significantly lower relative pressures (see Figure 5.13(left)); only at relative pressures above approximately 10^{-5} theoretical and experimental adsorption isotherms agree quantitatively. This effect was already discussed in ref [188], where two major issues for N_2 adsorption in micropores at 77 K were identified: (i) the transport kinetics of N_2 molecules within carbon micropore at 77 K are potentially too slow to obtain reliable equilibrium pressures in the adsorption measurements. (ii) even small amounts of gases, which contaminate the sample, the sorption instrument or the adsorptive and are not adsorbed by the carbon at 77 K, such as H_2 or He, can lead to significantly higher apparent equilibrium pressures in the experiment. As a consequence, the relative pressure range below 10^{-5} is generally to be considered with great care when it comes to micropore adsorption of N_2 at 77 K [180].

With respect to the strain isotherms, the same shift as for the adsorption isotherms is found, i.e., the initial contraction of the sample is qualitatively

[5]The strain data obtained for the original adsorption stress was subjected to smoothing due to the finite number of theoretical isotherms within the applied kernel. This issue was already discussed in ref [188].

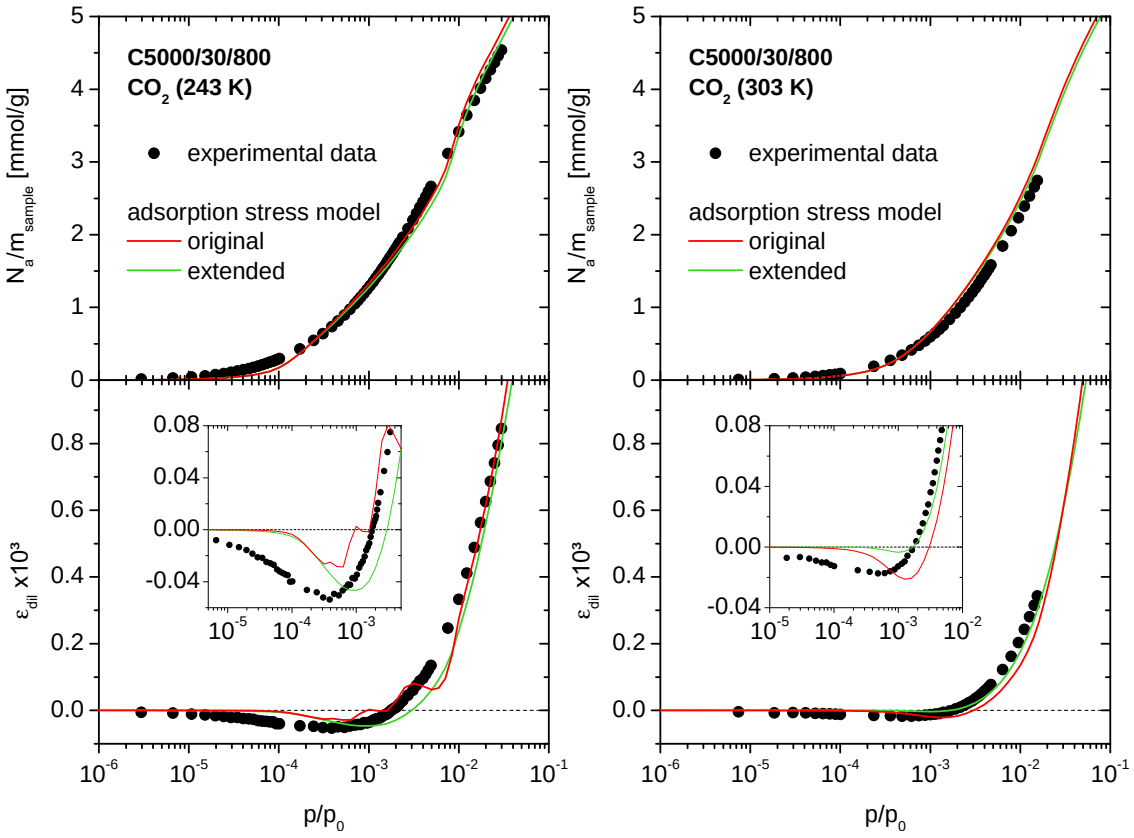

Figure 5.12.: Adsorption and strain isotherms of the micro-macroprous carbon xerogel C5000/30/800 for CO_2 at 243 K (left) and 303 K (right). Symbols represent the experimental data, while lines mark the predictions of the original and the extended adsorption stress model for adsorption-induced strain of the microporous carbon. For the modeling the same PSD and mechanical parameters are applied as in Figure 5.9.

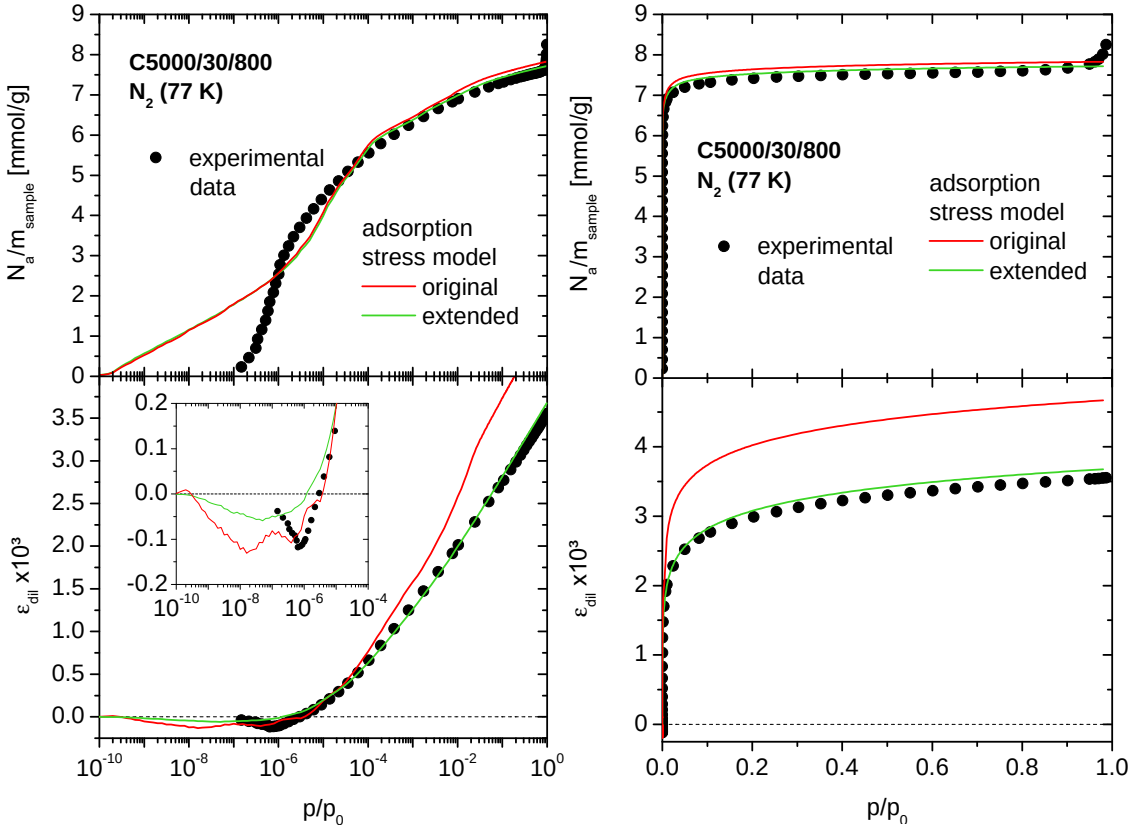

Figure 5.13.: Adsorption and strain isotherms of the micro-macroporous carbon xerogel C5000/30/800 for N_2 at 77 K on logarithmic (left) and linear scale pressure scale (right). Symbols represent the experimental data, while lines mark the predictions of the original and the extended adsorption stress model for adsorption-induced deformation of microporous carbon. For the modeling the same PSD and mechanical parameters are applied as in Figure 5.9.

correctly predicted by both theoretical models but it appears at significantly lower relative pressure than in the experiment. Regarding the quantitative extent of the initial sample contraction, the original adsorption stress model is in slightly better agreement with the experimental data than the extended model, however, for relative pressures beyond the critical range of $p/p_0 > 10^{-5}$ the extended adsorption stress model provides a significantly better description of the experimental data, since the original adsorption stress model considerably overestimates the samples expansion; this effect increases with relative pressure and becomes most pronounced at saturation pressure, where the relative deviation between original adsorption stress model and experiment reaches nearly 20 %. The major problem of the original adsorption stress model is its extreme sensitivity to the Van der Waals diameter of the adsorbate resulting from stress contributions of pores smaller than the nominal size of the adsorbate (compare Figures 4.2c and d and discussion in ref [188]). As such, switching from one adsorbate to another may have tremendous effects on the results of the original adsorption stress model, if the PSD is kept constant. To put this effect in perspective: the deviations seen in Figure 5.13 result from the difference of Van der Waals diameter between N_2 and CO_2, which is about 0.01 nm. When switching from CO_2 to Ar as done in ref [188] the difference of Van der Waals diameter is 0.02 nm and quantitative deviations between original adsorption stress model and experiment become even more pronounced. This rather fundamental issue of the original adsorption stress model is not limited to the slit-shaped micropore but is relevant to all anisotropic pore geometries, where the original adsorption stress neglects strain components. Contrary, the extended adsorption stress model suffers significantly less from pore width dependency of the normal component of the adsorption stress, since it requires no pores smaller than the nominal size of the adsorbate to model the sample's adsorption-induced deformation. As a consequence, the extended adsorption stress model is rated superior to the original one and is exclusively used for all further data evaluation in this work.

On a final note, another quite noteworthy result of the N_2 adsorption and strain data evaluation is that the strain of the microporous carbon continues in the relative pressure range $p/p_0 > 0.1$, where the corresponding adsorption isotherm exhibits essentially a plateau (Figure 5.13(right)). This effect is seen experimentally and also matches theoretical predictions. A descriptive explanation is the picture of an already filled micropore: adding only a few molecules into the pore is barely perceptible in terms of amount adsorbed, but with respect to the short-ranged repulsion of the fluid-fluid or solid-fluid potentials the energy change resulting from a slight decrease of the average intermolecular distance can be quite significant.

5.4. Carbon Xerogel II - Disordered Micro- and Mesoporosity

In this section the adsorption-induced deformation of the micro- and mesoporous carbon xerogel C5000/50/800 is investigated. As will be shown in detail below, for this sample the strain due to adsorption in the mesoporous network is small but not negligible compared to the strain of the microporous particles forming the network.

The strategy for the analysis of this data set is to start from the experimental N_2 adsorption isotherm and model it by DBdB theory for a cylindrical mesopore. From the DBdB isotherm the parameters are determined, which are required for the modeling of the network's adsorption-induced strain, i.e., strain related to Bangham's Law and Laplace stress. Then the experimental CO_2 (273 K) adsorption and strain isotherms are modeled by the extended adsorption stress model (compare section 5.3) complemented by the adsorption and strain effects related to the xerogel network (compare section 5.2). Based on the modeling of CO_2 data, predictions are made for the N_2 and Ar (77 K) strain and adsorption isotherms, which are compared to their experimental counterparts. In a last step, the implications of the obtained results for H_2O adsorption on the carbon xerogel are discussed. The mechanical parameters of the carbon xerogel C5000/50/800 derived from the modeling process are considered in section 5.5.3.

For the modeling of the experimental N_2 adsorption isotherm of the carbon xerogel C5000/50/800 via DBdB theory (Eq. 2.18 to 2.22) a suitable disjoining pressure isotherm $\Pi(h)$ for the adsorption of N_2 on carbon is required. In order to be consistent with the adsorption stress model applied in the subsequent steps, $\Pi(h)$ was derived from NLDFT calculations on a flat nonporous carbon surface; the respective adsorption and disjoining pressure isotherms are shown in the Appendix B. In analogy to the silica aerogel (section 5.2), the modeling of the experimental adsorption isotherm by DBdB theory focused on the reproduction of the slope in the film regime and the plateau in the filled pore regime. To take the microporosity of the carbon xerogel into account the total specific micropore volume $V_{mic}\,(\mathrm{DBdB})$ of the sample was introduced as an additional model parameter into Eq. 2.19 and 2.20 leading to

$$\frac{N_{a,film}}{m_{sample}}\left(p/p_0\right) = V_{mic}\,(\mathrm{DBdB}) + \frac{S_{DBdB}}{2V_L}\cdot\frac{2Rh\left(p/p_0\right) - h\left(p/p_0\right)^2}{R}, \tag{5.9}$$

$$\frac{N_{a,filled}}{m_{sample}} = V_{mic}\,(\mathrm{DBdB}) + \frac{S_{DBdB}}{2V_L}\cdot R = \mathrm{const.} \tag{5.10}$$

Here $N_a/m_{sample}\left(p/p_0\right)$ is the adsorption isotherm, S_{DBdB} is the specific surface area of the sample, V_L is molar volume of the adsorbate in liquid form, $h\left(p/p_0\right)$ is the thickness of adsorbate film given by Eq. 2.18 and R is the radius of the mesopores within the sample. As can be seen from Eq. 5.9 and 5.10, the impact of parameter $V_{mic}\,(\mathrm{DBdB})$ on the predicted adsorption isotherms is rather simple:

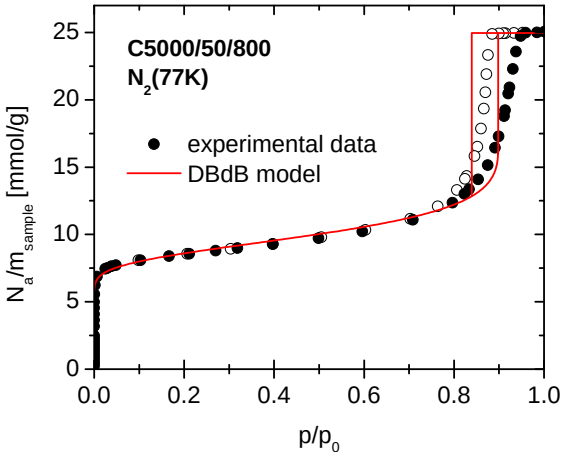

Figure 5.14.: Experimental adsorption isotherm of the micro- and mesoporous carbon xerogel C5000/50/800 for N_2 at 77 K and respective modeling by DBdB theory.

it just shifts the whole adsorption isotherm upwards by a constant value, i.e., micropore filling is not resolved in terms of relative pressure or pore size as e.g. done by the integral adsorption equation (IAE, Eq. 2.14).

The result of the DBdB modeling process including Eq. 5.9/5.10 is shown in Figure 5.14 giving an approximate description of the experimental data. As for the silica aerogel, the relative pressure of capillary condensation and evaporation are only approximately correct, since the xerogel network does not actually exhibit cylindrical pores as assumed in the DBdB model. The adjusted parameters are the specific surface area $S_{DBdB} = 190\ \mathrm{m^2/g}$, the pore diameter $d_{DBdB} = 2R = 14$ nm and the specific micropore volume $V_{mic}\,(\mathrm{DBdB}) = 0.20\ \mathrm{cm^3/g}$. All parameters applied are in good agreement with previous results from standard characterization (Table 4.4).

In the next step, the experimental CO_2 adsorption and strain isotherm of the carbon xerogel C5000/50/800 were modeled by the extended adsorption stress model complemented by the adsorption on the specific surface area S_{DBdB} and the related strain of the network particles due to Bangham's law. This approach is equivalent to the IAE (Eq. 2.14) complemented by the adsorption on the (external) particle surface for adsorption and a combination of the extended adsorption stress model (2.42 to 2.49) and Bangham's law (Eq. 2.23 and 2.34) for strain:

$$\begin{aligned}\frac{N_a}{m_{sample}}\,(p/p_0) = &\underbrace{\int_0^{2\ \mathrm{nm}} N_{NLDFT}\,(p/p_0, w)\cdot S_{diff}\,(w)\ \mathrm{d}w}_{\text{IAE}} \\ &+ \underbrace{\frac{N_{a,flat}}{A_s}\,(p/p_0)\cdot S_{DBdB}}_{\text{external surface area}},\end{aligned} \tag{5.11}$$

$$
\begin{aligned}
3\varepsilon_{dil} &= \varepsilon_m + \varepsilon_{part} \\
&= \underbrace{\frac{\phi_{mic}}{1-\phi_{mic}} \cdot \frac{\bar{\sigma}_{a,\parallel}}{K_s} + \left(\frac{\phi_{mic}}{K_\beta} - \frac{1}{K_s} \right) \bar{\sigma}_{a,\perp}}_{\varepsilon_m} + \underbrace{\frac{2\Delta\gamma_s}{R_{part} K_{part}}}_{\varepsilon_{part}}, \qquad (5.12a)
\end{aligned}
$$

$$
\Delta\gamma_s = \int_{-\infty}^{\mu} \frac{N_{a,flat}}{A_s} (\mu') \, \mathrm{d}\mu', \qquad (5.12b)
$$

$$
K_{part} = K_m = K_s \cdot (1 - \phi_{mic})^2 . \qquad (5.12c)
$$

Here $N_{NLDFT}(p/p_0, w)$ are the results of NLDFT calculations (Eq. 2.13) and S_{diff} is the differential surface area of pores of width w (Eq. 2.14). ε_{dil} is the dilatometric strain (Eq. 3.17), while ε_m and ε_{part} are the strains of the microporous matrix (Eq. 2.46) and the xerogel's network particles (Eq. 2.34), respectively. ϕ_{mic} is the porosity of the microporous carbon matrix (Table 4.6) and K_s and K_β are its mechanical moduli within the extended adsorption stress model (Eq. 2.46). $\bar{\sigma}_{a,\perp}$ and $\bar{\sigma}_{a,\parallel}$ are the volumetrically averaged stresses within the microporous carbon matrix according to Eq. 2.47 and 2.48, respectively. $\Delta\gamma_s$ is the change of the network particles' surface energy (Eq. 2.23), R_{part} is their average radius (Table 4.6) and K_{part} is their effective mechanical bulk modulus (Eq. 2.49). Furthermore, Eq. 5.11 and 5.12 utilize the surface specific adsorption $N_{a,flat}/A_s$ on a flat nonporous carbon surface, which was derived by NLDFT calculations (Appendix B). Notably, Eq. 5.11 and 5.12 neglect all effects related to the curvature of the adsorbate-adsorptive interface, i.e., capillary condensation/evaporation and Laplace strain, because the upper limit of relative pressure covered by the CO_2 experiment is below the relative pressure of CO_2 monolayer completion on the particles. Thus, no coherent adsorbate film is formed on the external surface of the particles and consequently no related adsorption or strain effects should arise (compare Figures 5.7 and 5.8 and respective discussion). On a side note, the difference between the description of adsorption by Eq. 5.9/5.10 and 5.11 is the focus of the investigated pressure regime: while Eq. 5.9/5.10 is aimed at the relative pressure regime of mesopore filling ($p/p_0 > 0.1$), where micropore filling is already completed, Eq. 5.11 focuses on the relative pressure regime of micropore filling and monolayer formation ($p/p_0 < 0.1$), where mesopore filling is of no significance.

The result of the simultaneous modeling of CO_2 adsorption and strain data according to Eq. 5.11 and 5.12, respectively, is shown in Figure 5.15 including an explicit separation of effects related to micropores and the xerogel's network particles, respectively. As can be seen from Figure 5.15 the contribution of the network particles to overall adsorption and strain is small. Furthermore, the agreement between model and experimental data is worse than for the sample micro-macroporous carbon xerogel investigated in the previous section but overall still acceptable. A major issue of the model was the reproduction of the initial

contraction minimum as seen in the experiment. All modeling attempts leading to an initial contraction minimum at the correct relative pressure failed to reproduce its depth and were typically not capable of describing the subsequent expansion. Thus, a modeling scenario with correct depth but wrong position of the initial contraction was favored.[6] The parameters adjusted for the modeling shown in Figure 5.15 are the mechanical moduli $K_s = (13.1 \pm 1.3)$ GPa and $K_\beta = (3.3 \pm 0.5)$ GPa and the PSD shown in Figure 5.16. The characteristics of the adjusted PSD are the specific micropore volume $V_{mic}\,(\mathrm{DFT}) = 0.197\ \mathrm{cm^3/g}$ (Eq. 3.10), the specific micropore area $S_{mic}\,(\mathrm{DFT}) = 686\ \mathrm{m^2/g}$ (Eq. 3.11) and the average micropore width $\bar{w} = 0.57$ nm (Eq. 3.12). The results for $V_{mic}\,(\mathrm{DFT})$, $S_{mic}\,(\mathrm{DFT})$ and $\bar{w}$ obtained for all carbon xerogels investigated in this work via the application of the extended adsorption stress model are summarized in Table 5.3. As for the micro-macroporous carbon xerogel, the PSD derived from the combined analysis of adsorption and strain isotherms is smoother than its counterpart obtained from the inversion of the IAE (compare Figures 4.10, 5.10 and E.1), though the above given characteristics are nearly identical.

Based on the modeling result for CO_2 data, predictions for adsorption and strain of the carbon xerogel C5000/50/800 are calculated for N_2 and Ar at 77 K. As for the modeling of CO_2 data, adsorption and strain are calculated as superpositions of micropore and xerogel network effects (Eq. 2.46 and Eq. 2.38/2.39, respectively), however, for N_2 adsorption now also the filled pore state is included, since capillary condensation occurs in the respective experiment:

$$\begin{aligned} 3\varepsilon_{dil} =& \varepsilon_m + \varepsilon_{net,film} = \varepsilon_m + \varepsilon_{part} + \varepsilon_{Laplace} \\ =& \underbrace{\frac{\phi_{mic}}{1-\phi_{mic}} \cdot \frac{\bar{\sigma}_{a,\parallel}}{K_s} + \left(\frac{\phi_{mic}}{K_\beta} - \frac{1}{K_s}\right)\bar{\sigma}_{a,\perp}}_{\varepsilon_m} \\ &+ \underbrace{\frac{2\Delta\gamma_s}{R_{part}K_{part}}}_{\varepsilon_{part}} \underbrace{- \gamma_{lv}\frac{\phi_{net}}{K_b}\left[\frac{1}{R-h} - \frac{1}{R}\right]}_{\varepsilon_{Laplace}} \quad \text{(film state)}, \end{aligned} \tag{5.13a}$$

[6] A hypothetical origin for the modeling issues could be that the solid-fluid interaction parameters used for NLDFT calculations were derived from adsorption measurements on graphite. However, the structure of the microcrystallites within the carbon xerogel (Figure 3.2 and respective description) differs to some extent from bulk graphite. In particular, CO_2 molecules may adsorb on functional groups and/or perpendicular to the orientation of the graphene layers leading to somewhat different interaction parameters than expected for bulk graphite.

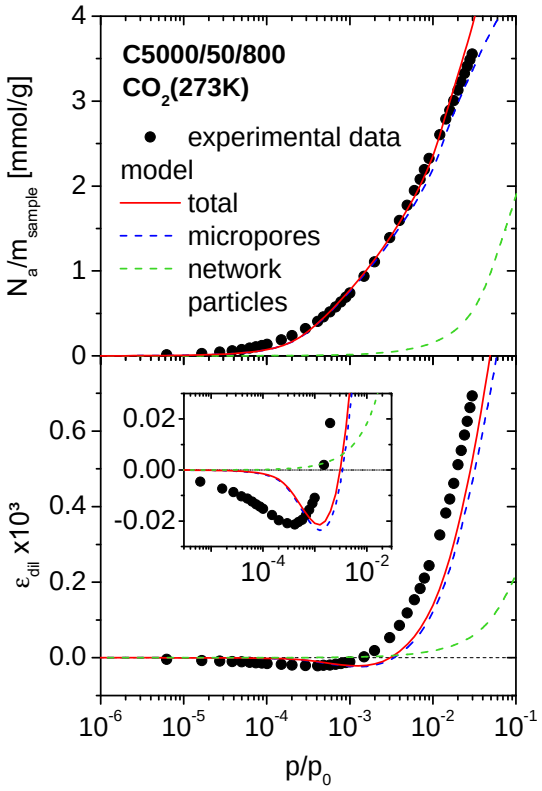

Figure 5.15.: Experimental adsorption and strain isotherms of the micro- and mesoporous carbon xerogel C5000/50/800 for CO_2 at 273 K and respective modeling by Eq. 5.11 and 5.12.

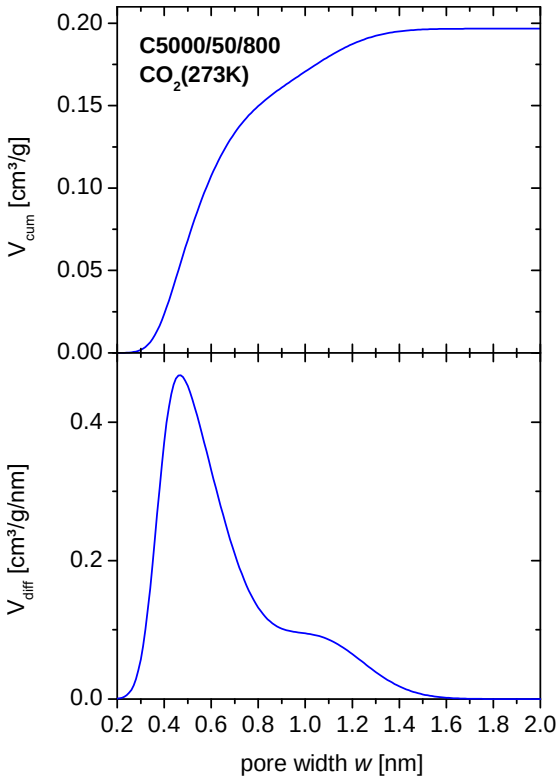

Figure 5.16.: Cumulative and differential pore volume distributions of the micro- and mesoporous carbon xerogel C5000/50/800 corresponding to modeling shown in Figure 5.15.

$$
\begin{aligned}
3\varepsilon_{dil} =& \varepsilon_m + \varepsilon_{net,filled} = \varepsilon_m + \Delta\varepsilon_{sl} + \varepsilon\left(p_{cap}\right) \\
=& \underbrace{\frac{\phi_{mic}}{1-\phi_{mic}} \cdot \frac{\bar{\sigma}_{a,\parallel}}{K_s} + \left(\frac{\phi_{mic}}{K_\beta} - \frac{1}{K_s}\right)\bar{\sigma}_{a,\perp}}_{\varepsilon_m} \\
&+ \underbrace{\frac{2\left(\gamma_s - \gamma_{sl}\right)}{R_{part}K_{part}}}_{\Delta\varepsilon_{sl}} + \underbrace{\frac{1}{K_b}\left[\phi_{net} \cdot p_{cap} - p\right]}_{\varepsilon(p_{cap})} \quad \text{(filled pore state)},
\end{aligned}
\tag{5.13b}
$$

In addition to the variables in Eq. 5.12, γ_{lv} is the liquid-vapor surface tension of the adsorbate, while ϕ_{net} is the porosity (Table 4.6) and K_b the bulk modulus (Table 4.2) of the xerogel's particle network. In contrast to the modeling of CO_2 or Ar strain (Eq. 5.12), the modeling of N_2 data (Eq. 5.13) includes the Laplace strain $\varepsilon_{Laplace}$ (Eq. 2.37) due to the curved adsorbate-vapor interface in the film regime (Eq. 5.13a). In the filled pore state (Eq. 5.13b), the strain of the microporous carbon matrix is furthermore complemented by strain related to the surface energy change between dry and wet carbon surface, $\gamma_s - \gamma_{sl}$, as well as to the capillary pressure $\varepsilon\left(p_{cap}\right)$ (Eq. 2.37). Here it is important to note that the Laplace strain $\varepsilon_{Laplace}$, as proposed by Eq. 2.37, does not give a good quantitative description of the xerogel network's respective strain, since the xerogel structure differs significantly from the cylindrical pore geometry assumed for Eq. 2.37 (compare Figure 5.8 and respective discussion). Fortunately, the bulk modulus K_b of the carbon xerogel C5000/50/800 considered in this section is so high (Table 4.2) that the Laplace strain $\varepsilon_{Laplace}$ has barely any impact on the overall strain. As such, the quantitative error resulting from the vague description of the Laplace strain by Eq. 2.37 is considered acceptable. Notably, the bulk modulus K_b of the carbon xerogel cannot be derived from the strain isotherm as was shown for the silica aerogel (Figure 5.6) due to the high contribution of micropore deformation in the filled pore regime; thus for the application of Eq. 5.13, K_b was taken from sound velocity measurements (Table 4.2).

The comparison of the experimental strain data and the respective predictions by Eq. 5.12/5.13 are shown for N_2 adsorption in Figures 5.17 to 5.19 and for Ar adsorption in Figures 5.20. The adsorption process in Figures 5.17 and 5.20 was predicted by 5.11; notably, the step-like adsorption seen in Figures 5.17 and 5.20 is a result of the smooth wall approximation of NLDFT calculations used to derive $N_{a,flat}/A_s$ (compare section 4.1). All Figures except Figure 5.19 include an explicit separation into micropore and network effects, i.e., adsorption on particles and in case of N_2 also mesopore filling. The Figures 5.17 and 5.20(left) focus on adsorption and strain in the low relative pressure regime of N_2 and Ar experiments; here the same general discrepancy between model and experiment already discussed in section 5.3 is observed, i.e., for relative pressure below 10^{-5} theoretical adsorption and strain are systematically shifted to lower relative pressure. Apart from this obvious issue, the initial contraction and subsequent expansion of the carbon xerogel are correctly described on a qualitative and for

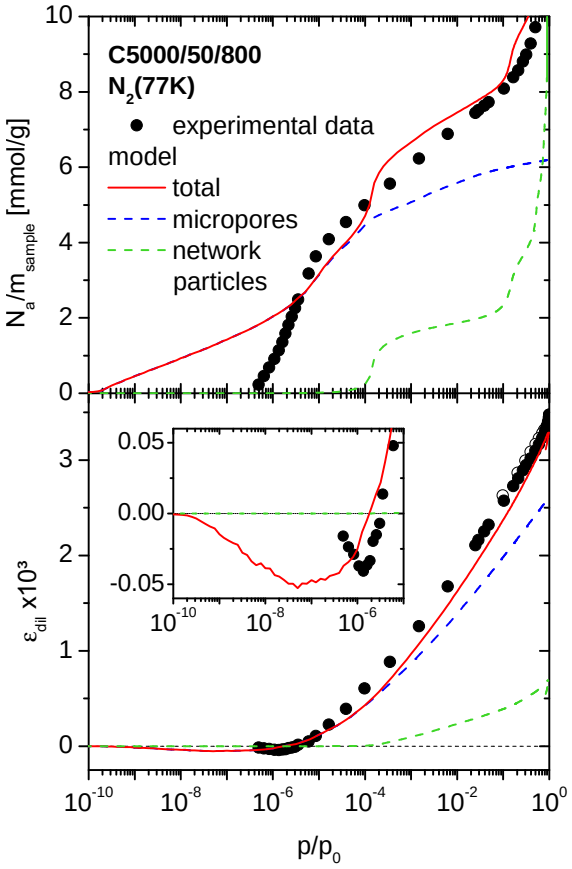

Figure 5.17.: Experimental adsorption and strain isotherms of the micro- and mesoporous carbon xerogel C5000/50/800 for N_2 at 77 K and respective modeling by respective modeling by Eq. 5.11 and 5.12.

relative pressures above 10^{-5} mostly also on a quantitative level. The contribution of particle related strain to the overall strain is clearly evident but significantly smaller than the strain of the microporous matrix within the particles. The same trend is found in Figures 5.18 and 5.20(right), where experimental data and model are shown on linear pressure scale emphasizing the adsorption process within the xerogel particle network.

Due to the dominance of micropore deformation and the high bulk modulus of the carbon xerogel the strain hysteresis typically associated with mesoporous materials is quite small; a zoom on the hysteresis of the N_2 strain isotherm is shown in Figure 5.19. Here the model correctly predicts the quality of the hysteresis slope, i.e., the strain in the filled pore state is lower than in the film state. However, quantitatively the theoretical hysteresis extends over a larger relative pressure range, which is a result of the DBdB modeling shown in Figure 5.14, and the predicted strain at saturation is slightly lower than in the experiment. Regarding the origin of the quantitative discrepancies at saturation pressure two major shortcomings of model have to be considered: (i) in the regime of the

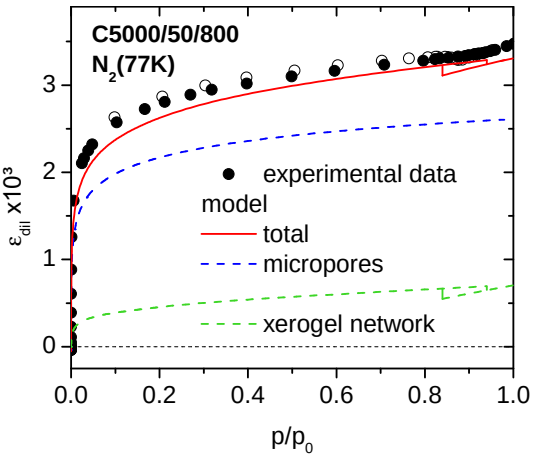

Figure 5.18.: Experimental strain isotherm of the micro- and mesoporous carbon xerogel C5000/50/800 for N_2 at 77 K and respective modeling by Eq. 5.12 shown on linear scale.

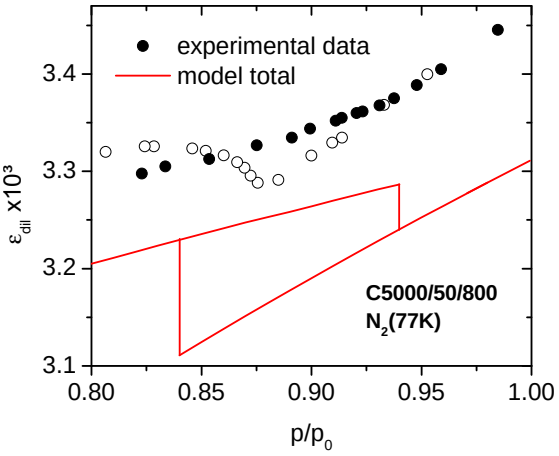

Figure 5.19.: Zoom of Figure 5.18 into the filled pore regime.

filled pore state, the quantitatively dominant micropore deformation is only an extrapolation based on the experimental CO_2 data at low relative pressure. Thus, minor changes of the model parameters obtained at low relative pressure will result in measurable changes for the sample strain close to saturation. (ii) the strain difference between film and filled pore state of the xerogel network is calculated based on the Frumkin-Derjaguin equation (Eq. 2.32), which here is given for the particular case of a cylindrical pore. As already emphasized earlier, the cylindrical pore model is only a coarse approximation for the actual pore structure of aero-/xerogel networks. Consequently, a quantitative exact prediction of the surface energy change from evacuated to N_2 covered carbon cannot be expected by the Frumkin-Derjaguin equation.

In contrast to N_2, neither the Ar adsorption nor the Ar strain isotherm exhibit capillary condensation and accompanying hysteresis (Figure 5.20), since at 77 K Ar generally cannot condense in pores larger than approximately 10 nm [205]. Thus adsorption and strain of the xerogel network are limited to the film state, where the strain isotherm follows from the strain of the microporous matrix within the particles and the strain of network particles due to Bangham's law. Due to the lack of capillary condensation the same modeling approach as for CO_2 (Eq. 5.11 and 5.12) is sufficient. Regarding the applied model, Figure 5.20 reveals that Eq. 5.11 overestimates the Ar adsorption within the xerogel network by roughly 10 %. Contrary, the overall strain of the sample is quite well described by Eq. 5.12.

In the last part of this section H_2O adsorption (298 K) of the micro- and mesoporous carbon xerogel C5000/50/800 and the respective strain are considered (Figure 4.14). H_2O adsorption in carbons occurs via cluster formation at

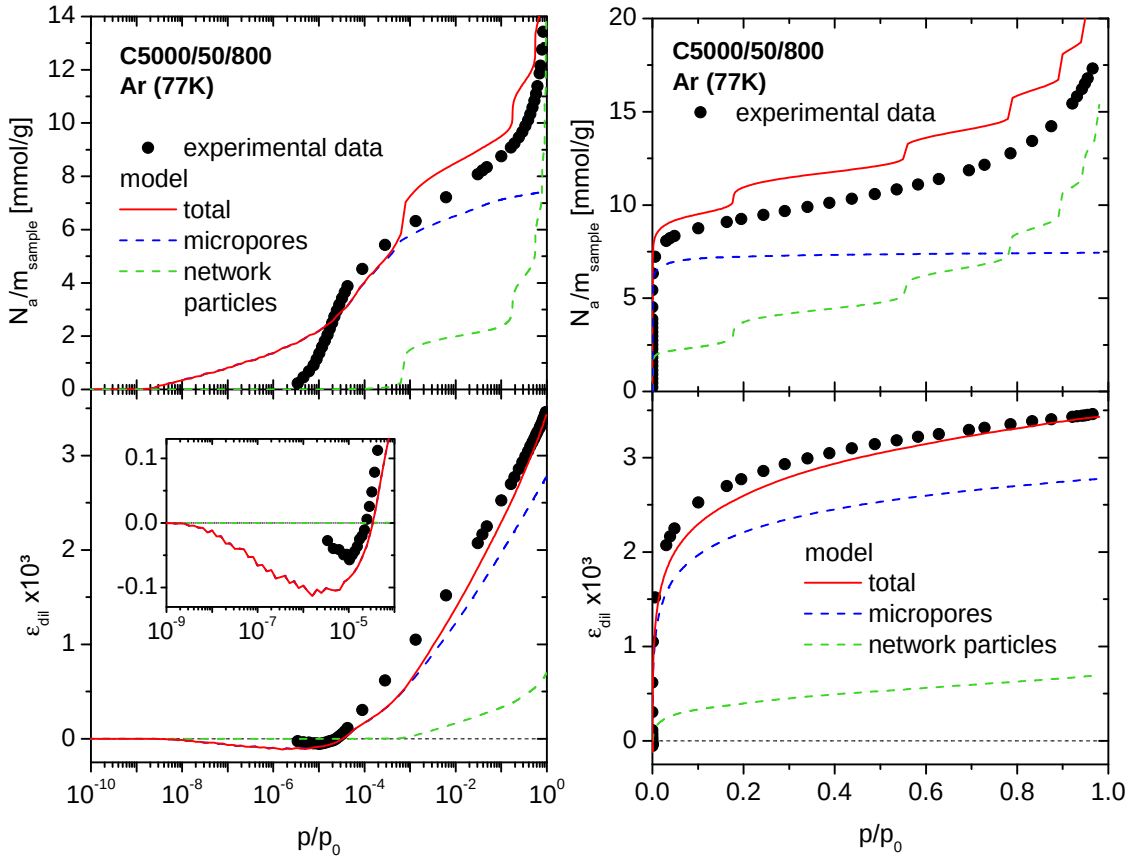

Figure 5.20.: Experimental adsorption and strain isotherms of the micro- and mesoporous carbon xerogel C5000/50/800 for *Ar* at 77 K and respective modeling by 5.11 and 5.12, shown on logarithmic (left) and linear pressure scale (right).

hydrophilic functional groups located within micropores and on the surface of the network particles [209, 210]. As a result the adsorption process is shifted to elevated relative pressures compared to the other adsorbates applied. The complex adsorption process of H_2O molecules on carbon cannot be described by the Van der Waals model of NLDFT preventing a quantitative analysis within the framework of this thesis. Nevertheless, some qualitative conclusions can be drawn from the available experimental data. As described in detail in ref [201], the mesopores of the carbon xerogel C5000/50/800 are too large to allow for a cluster induced capillary condensation prior to saturation pressure. Therefore, the adsorption of the sample is limited to micropore filling and potentially some cluster formation on the surface of the particles of the xerogel network; this situation bears some resemblance to the Ar experiment (Figure 5.20), where mesopore related effects are also only of minor importance.

When comparing the H_2O strain isotherm of the carbon xerogel 5000/50/800 (Figure 4.14) to the strain isotherms obtained for the adsorption of the other analysis gases (N_2, Ar, CO_2) (Figures 4.13 and 4.14) it can be seen that the shape of the strain isotherms in the regime of micropore filling is qualitatively identical for all adsorbates. This is also illustrated in Figure 5.21, which shows the dilatometric strain of the sample for all adsorbates as a function of the specific amount adsorbed. As a consequence, it can be assumed that cluster formation of H_2O causes the same stress mechanisms in the carbon as the other adsorbates, i.e., normal and tangential adsorption stress inside the slit-shaped micropores and potentially also stress on the xerogel's particles related to Bangham's law.[7] Quantitatively, the comparison of the different strain isotherms reveals that the initial contraction of the carbon xerogel during H_2O adsorption is about 2 to 6 times more pronounced than for the other adsorbates (Figure 5.21). Simultaneously, the expansion for increasing relative pressure is significantly less pronounced; for H_2O, the net strain of the carbon xerogel at saturation is nearly 4 times smaller than for N_2 or Ar. This leads to the conclusion that the expansive stresses, (i) adsorption stress tangential to micropore walls and (ii) stress on the particles due to Bangham's law, are weaker for H_2O adsorption than for the other adsorbates investigated. A potential explanation for this behavior is found in the density of the adsorbed H_2O phase, which is only about 0.8 g/cm^3 [201, 211, 212] and therefore significantly lower than the unconfined liquid state of H_2O (1.0 g/cm^3). With respect to adsorption-induced stresses, both expansive mechanisms (i) and (ii) are related to the adsorbate density as their magnitude depends on the energy density of the adsorbed phase: the adsorption stress parallel to the micropore walls (i) is related to the adsorbate density by Eq. 2.27 and 2.30b and the stress on the particles due to Bangham's law (ii) by Eq. 2.23. Contrary to the expansive stresses, the mostly contractive normal adsorption stress within the micropore

[7] It is still a matter of scientific debate, to which extent H_2O molecules adsorb in meso- and macropores [212, 217, 218]. Thus, it is currently not known, whether H_2O molecules adsorb to any significant amount on network particles within the investigated carbon xerogel. If significant H_2O adsorption occurs on the outside of the particles, a strain contribution from Bangham's law is expected, otherwise all strain results from micropore filling within the particles.

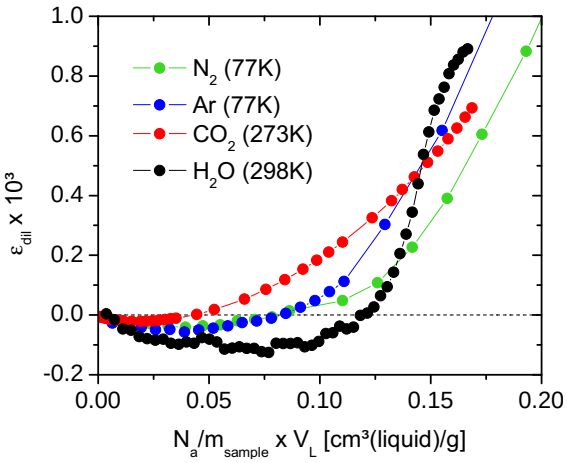

Figure 5.21.: Comparison of strain data obtained for the micro- and mesoporous carbon xerogel C5000/50/800 for different adsorbates as a function of the specific amount adsorbed.

(Eq. 2.30a) follows from the mediation of the attractive solid-fluid potentials of the opposing pore walls and is not hampered by a lower density of adsorbate molecules within the pore.

5.5. Carbon Xerogel III - Activation, Thermal Annealing and Mechanical Properties

In this section, the structural changes of carbon xerogels resulting from activation and thermal annealing are investigated by the combined analysis of adsorption and strain isotherms. The carbon xerogels used for this study are the micro- and mesoporous samples derived from the reference C5000/50/900 (activated sample C5000/50/900A, samples C5000/50/1200 to C5000/50/1800 annealed at the temperatures of 1200, 1400, 1600 and 1800 °C). The analysis gases applied were N_2 at 77 K and CO_2 at 273 K. For quantitative data analysis the same strategy as proposed in section 5.4 is applied, i.e., adsorption and strain effects resulting from micropores and the mesoporous xerogel network are superimposed (Eq. 5.9 to 5.13). In the last part of this section, the mechanical parameters derived from the modeling process are discussed for all carbon xerogels investigated.

5.5.1. Activation

The adsorption and strain isotherms of the micro- and mesoporous reference carbon xerogel C5000/50/900 and the respective activated sample C5000/50/900A (burn-off φ_{bo} = 4.0 wt%) are shown in Figure 5.22 for N_2 (77 K) and in Figure 5.23 for CO_2 (273 K). As can be seen from the N_2 adsorption isotherms of the samples (Figure 5.22) and the respective characterization (Tables 4.4 and 4.6), the applied activation affected only the micropore structure of the carbon xerogel, i.e., the properties of the mesoporous particle network (S_{ext}, V_{meso}, $\bar{d}_{meso}$ and ϕ_{net})

remained essentially constant. Notably, for increasing degrees of burn-off also changes to the mesopore structure are to be expected (see e.g. ref [147]). The comparison of the strain isotherms (lower panels in Figures 5.22 and 5.23) shows that the qualitative shape of strain isotherms is not affected by the activation. However, quantitatively the contraction of the activated sample at low relative pressures is significantly more pronounced and shifted to higher relative pressure when compared to the reference. Contrary, the maximum strain at N_2 saturation pressure and the strain hysteresis associated with mesopore filling remain nearly unchanged.[8]

To evaluate the changes induced by the activation process to the carbon xerogel's micropore structure, the experimental CO_2 adsorption and strain isotherms of activated and reference sample (Figure 5.23) were modeled in the direct analogy to the previous section 5.4. Eventually, also theoretical adsorption and strain isotherms were predicted for N_2 adsorption at 77 K and checked for consistency with respective experimental data. As for the micro- and mesoporous carbon xerogel considered in the previous section, the predictions for N_2 adsorption at 77 K were in reasonable agreement with the experimental data. The parameters derived from the modeling were again the bulk moduli of the microporous carbon matrix, K_s and K_β, (Eq. 2.46) as well as the PSD of the microporous phase. The PSDs of reference and activated sample are shown in Figure 5.24 and their numerical characteristics, $V_{mic}\,(\mathrm{DFT})$ (Eq. 3.10), the specific micropore area $S_{mic}\,(\mathrm{DFT})$ (Eq. 3.11) and the average micropore width $\bar{w}$ (Eq. 3.12) are given in Table 5.3. The values for the mechanical moduli of the carbon xerogels are summarized in Table 5.4 and discussed in section 5.5.3.

As can be seen from N_2 and CO_2 adsorption isotherms (upper panels of Figures 5.22 and 5.23) and the evaluated PSDs (Figure 5.24 and Table 5.3) of reference and activated carbon xerogel, the changes of the activation process to sample's micropore structure are twofold: (i) the overall specific micropore volume increases, (ii) the average micropore width increases. Effect (i) is a direct consequence of the burn-off $\varphi_{bo} = 4.0$ wt% leading to a theoretically expected increase of specific micropore volume of 0.028 cm^3/g (see Attachment F). This value is well in line with the change of specific micropore volume between the reference and the activated sample as seen by sample characterization (compare Table 4.4), i.e., the increase of the micropore volume by the activation process is well correlated to the removal of nonporous carbon within the sample's particles. For a more detailed understanding of effect (ii) the PSD in Figure 5.24 has to be considered.[9] Here it can be seen that the PSDs of activated and reference sample

[8] On a side note, activation of carbons is also considered a way to improve the access of gas molecules to microporosity. For the carbon xerogels considered, this effect was only found with respect to the equilibration time of the N_2 (77 K) adsorption measurement at low relative pressures, which became significantly shorter after the activation process. Furthermore, no evidence for inaccessible microporosity in the untreated carbon xerogel was found within error considerations.

[9] On a side note, the activation of a carbon reduces its overall mass and thus increases all its specific quantities such as specific surface area and specific pore volume regardless whether absolute changes

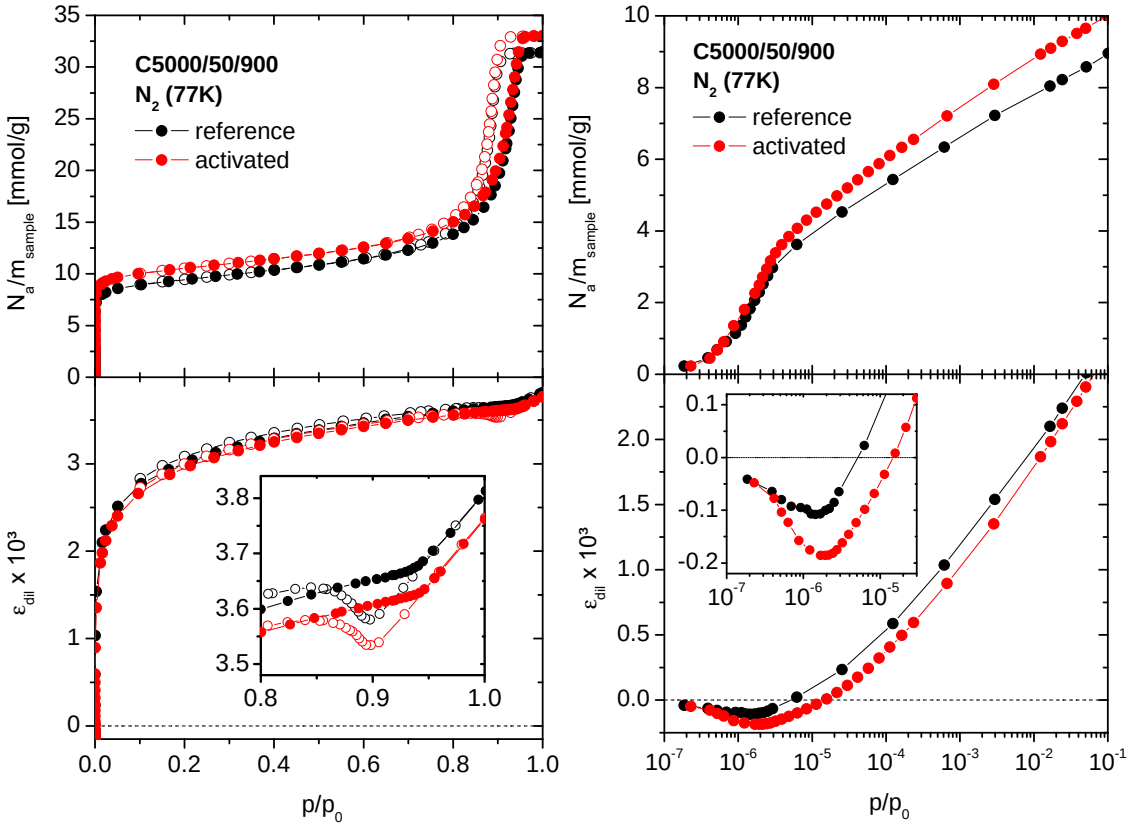

Figure 5.22.: Experimental adsorption and strain isotherms of the micro- and mesoporous activated carbon xerogel C5000/50/900A and its reference C5000/50/900 for N_2 at 77 K on linear (left) and logarithmic pressure scale (right). Full symbols denote adsorption, open symbols denote desorption. The inset (left) shows a magnification of the strain hysteresis associated with mesopore filling; the inset (right) shows a magnification of the samples' contraction at low relative pressure.

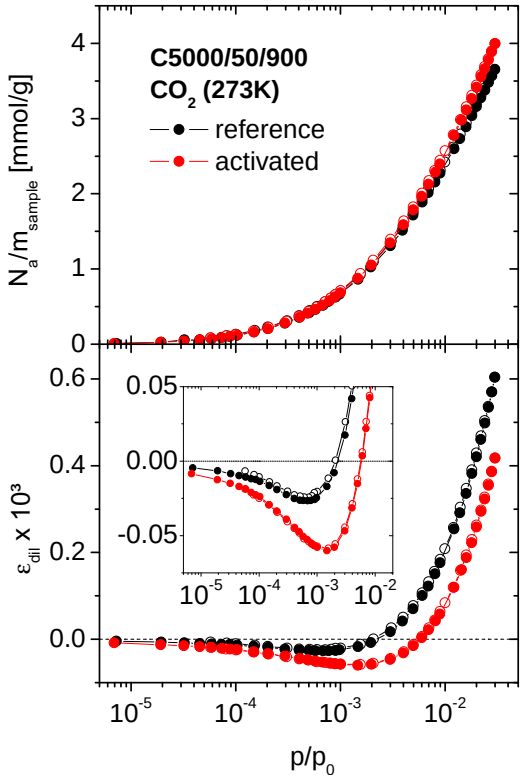

Figure 5.23.: Experimental adsorption and strain isotherms of the micro- and mesoporous activated carbon xerogel C5000/50/900A and its reference C5000/50/900 for CO_2 at 273 K shown on logarithmic scale. Full symbols denote adsorption, open symbols denote desorption. The inset shows a magnification of the samples' contraction at low relative pressure.

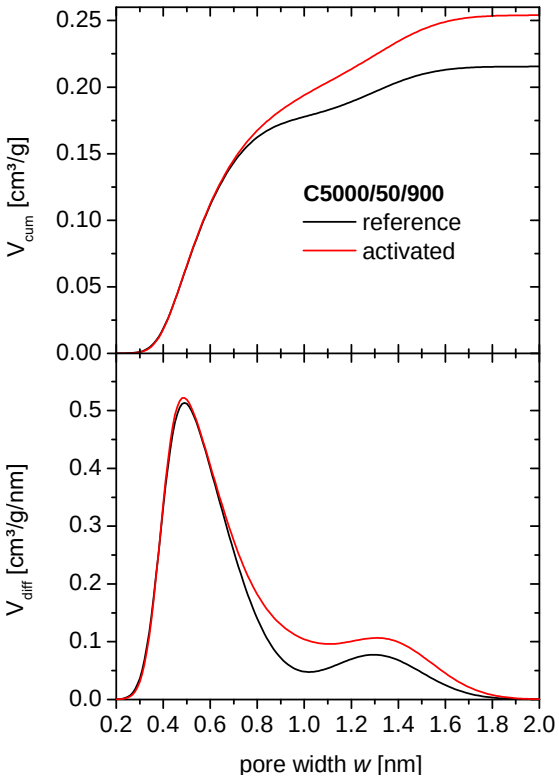

Figure 5.24.: Cumulative and differential pore volume distributions of the micro- and mesoporous activated carbon xerogel C5000/50/900A and its reference C5000/50/900 obtained from simultaneous modeling of the experimental CO_2 adsorption and strain isotherms shown in Figure 5.23.

deviate essentially only the range of pore widths > 0.7 nm, where the activation process increases the pore volume. Surprisingly, the pore volume of smaller pores is only remotely affected and thus the pore volume increase by activation results primarily from the creation of new pores rather than the widening of already existing pores. A potential interpretation of this finding is removal of disordered carbon patches within the matrix, which are more susceptible to the activation process than more ordered sections. A trivial consequence of this mechanism is the increase of the average pore width by activation.

In summary, the results of this section show that strain isotherms are quite sensitive even to minor changes in the micropore structure of carbons. Therefore the simultaneous analysis of adsorption and strain isotherm is a suitable tool to study the impact of structural modifications of microporous materials. The impact of activation on the carbon xerogel's mechanical properties is discussed in section 5.5.3.

5.5.2. Thermal Annealing

Thermal annealing induces structural changes to the carbon material, which are significantly more complex than the effects of activation. A major challenge for gas adsorption based analysis of annealed carbons is the diminishing accessibility of the carbon microporosity for gas molecules for increasing annealing temperature [138, 160]. This effect is attributed to the growth of the carbon microcrystallites, which restricts the interconnections between adjacent pores [164] (also compare Figure 5.25). As a consequence, adsorption measurements may detect only a fraction of the total microporosity of an annealed carbon and thus allow only for conclusions on the accessible pores [138]. As such, adsorption-induced deformation is only triggered in pores accessed by gas molecules. Notably, different analysis gases may exhibit different accessibility to the microporosity depending on molecular size and temperature of the adsorbate complicating a consistent data evaluation. Nevertheless, complementary to earlier works [138, 159, 160, 163, 164] an analysis of the annealing process by adsorption and adsorption-induced deformation was attempted.

The samples considered in this study were the micro- and mesoporous reference carbon xerogel C5000/50/900 and the derived samples C5000/50/1200 to C5000/50/1800 annealed at temperatures of 1200, 1400, 1600 and 1800 °C, respectively. As for the activation process, the applied analysis gases were N_2 at 77 K and CO_2 at 273 K. The respective adsorption and strain isotherms are shown in Figures 5.26 for N_2 and in Figure 5.27 for CO_2. The N_2 adsorption isotherms in Figure 5.26 and the derived structural parameters of the samples given in Tables 4.4, 4.5 and 4.6 demonstrate that the annealing process only affects

to the respective quantity occurred. In order to avoid misinterpretation of the actual structural modifications, surface area and pore volume should therefore be normalized to particle volume rather than sample mass when considering activation. However, for the case considered in this work the burn-off was so low, that this step is not required.

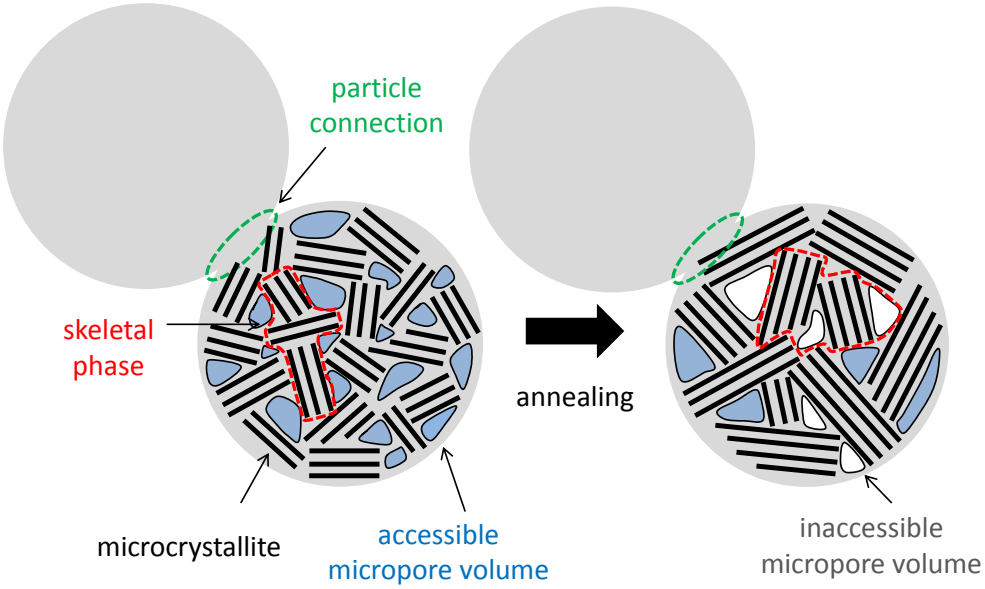

Figure 5.25.: Schematic illustrating the effect of annealing on the microporosity within network particles based on refs [138, 160, 164, 219]. Noteworthy, the skeletal phase of annealed samples as seen by gas adsorption includes inaccessible micropores. Additionally, the connection between particles is marked.

the microporosity of the carbon xerogels, while the mesoporous xerogel network is fully preserved. Furthermore, all adsorption isotherms clearly show the expected reduction of the accessible micropore volume to gas molecules with increasing annealing temperature.

The above described structural modifications of the carbon xerogels by thermal annealing allow already for some qualitative interpretation of the samples' strain isotherms (Figure 5.26 and 5.27): the most prominent feature of the strain isotherms is the significant reduction of the samples' strain with increasing annealing temperature. With respect to adsorption stress models (Eq. 2.41 and 2.46), this observation appears quite natural, since for a given PSD and mechanical moduli the strain of the microporous carbon matrix is expected to be correlated to its accessible porosity, which decreases for increasing annealing temperature (compare Figure 5.28). Furthermore, the samples' strain in the regime of micropore filling by N_2 (Figure 5.26) shows a systematical shift of the strain isotherms to higher relative pressure for increasing annealing temperature, while simultaneously the extent of the contraction becomes more pronounced. This indicates a change of the (accessible) pore structure towards larger micropores with annealing temperature, which was also found in the quantitative sample characterization (Table 4.5). However, the previous characterization also revealed that the accessible microporosity of the carbon xerogels annealed at 1400 °C and above differs for N_2 and CO_2, i.e., CO_2 at 273 K typically accesses a larger fraction of the total micropore volume than N_2 at 77 K. Thus, the trends found for

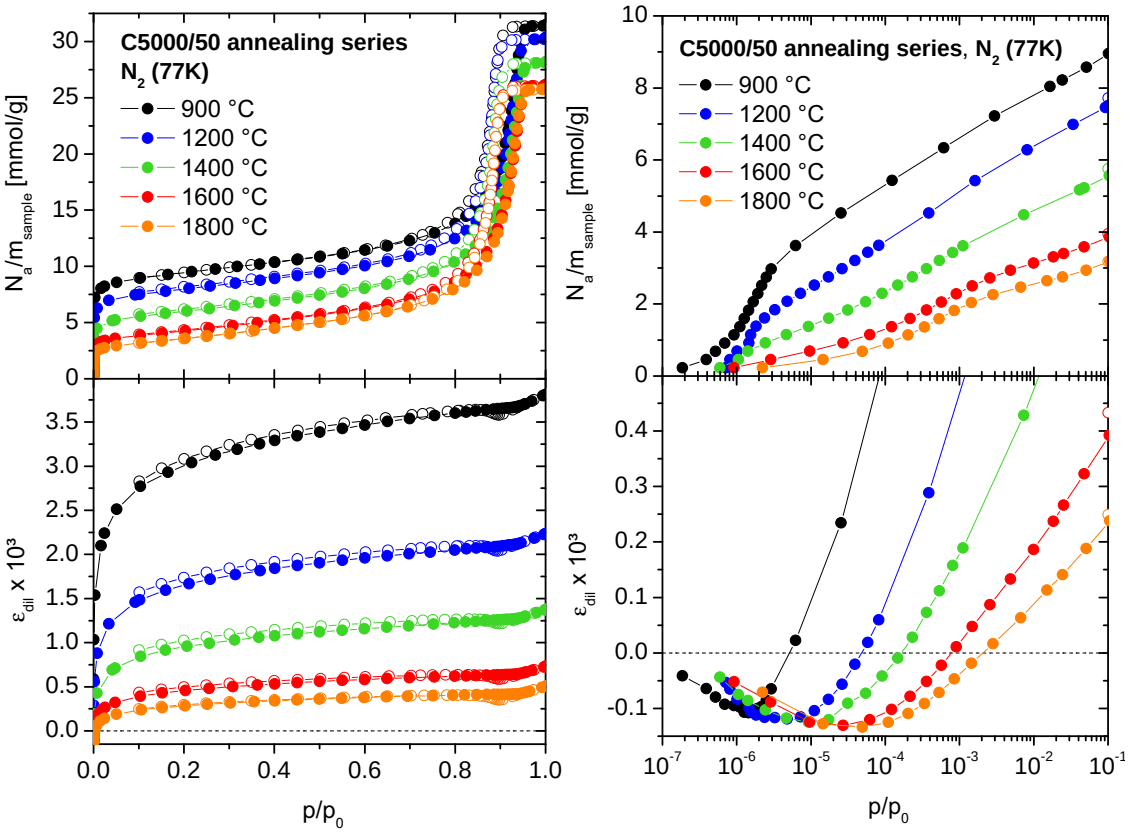

Figure 5.26.: Experimental adsorption and strain isotherms for the micro- and mesoporous reference carbon xerogel C5000/50/900 and the annealed samples C5000/50/1200, C5000/50/1400, C5000/50/1600 and C5000/50/1800 for N_2 at 77 K (left: linear pressure scale, right: logarithmic pressure scale). Full symbols denote adsorption, open symbols denote desorption.

micropore filling by N_2 are not necessarily reproduced in the CO_2 strain isotherms (Figure 5.27) due to the different accessibility of micropores for N_2 and CO_2. On the high relative pressure end of the N_2 strain isotherms, no significant difference is found for the hysteresis loops. This is due to the essentially identical structure of the mesoporous xerogel network for reference and annealed samples, which is the origin of adsorption and strain hystereses.

To obtain quantitative information beyond the qualitative picture given above, adsorption and strain isotherms of reference and annealed samples were analyzed according to the procedure applied in the previous sections 5.4 and 5.5.1. As before, this approach yields the carbon xerogels' PSDs (Figure 5.29) exhibiting the characteristic quantities V_{mic} (DFT) (Eq. 3.10), the specific micropore area S_{mic} (DFT) (Eq. 3.11) and the average micropore width $\bar{w}$ (Eq. 3.12) given in Table 5.3 as well as bulk moduli of the microporous carbon matrix, K_s and K_β, given in Table 5.4. Importantly, two significant differences to the modeling

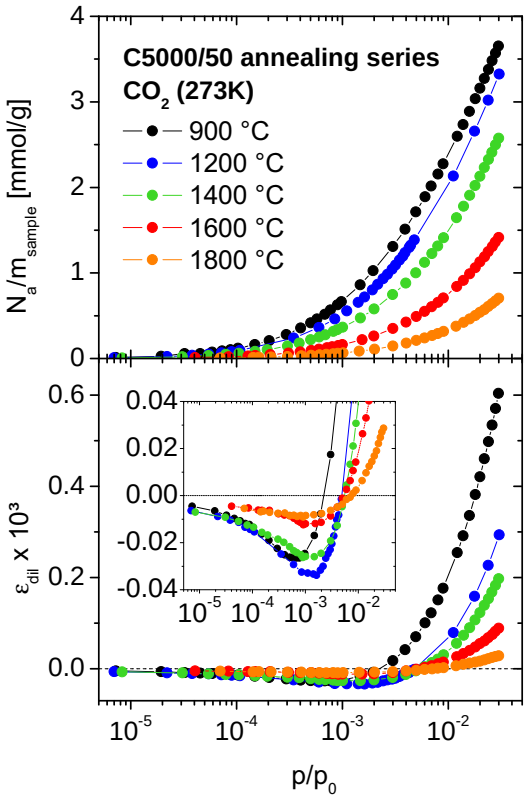

Figure 5.27.: Experimental adsorption and strain isotherms for the micro- and mesoporous reference carbon xerogel C5000/50/900 and the annealed samples C5000/50/1200, C5000/50/1400, C5000/50/1600 and C5000/50/1800 for CO_2 at 273 K. Data are shown on logarithmic scale. The inset shows a magnification of the samples' contraction at low relative pressure.

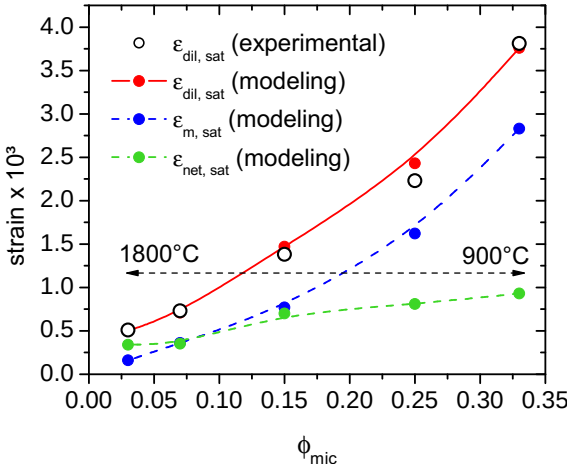

Figure 5.28.: Strain of the annealed carbon xerogels at N_2 saturation pressure $\varepsilon_{dil,sat}$ as determined experimentally by in-situ dilatometry as a function of the network particles' microporosity ϕ_{mic}. Complementary, the result of $\varepsilon_{dil,sat}$ from the modeling process (Eq. 5.13) and its contributions from micropores ($\varepsilon_{m,sat}$) and the xerogel network ($\varepsilon_{net,sat}$) are shown.

presented so far arise for the annealed carbon xerogels: (i) from the perspective of gas adsorption the skeletons of annealed carbon xerogels are no longer nonporous but contain inaccessible micropores. Thus, all properties for the "nonporous" skeleton derived from adsorption based sample characterization and modeling actually describe a porous carbon matrix (compare Figure 5.25). (ii) Due to the different accessibility of the annealed carbons for N_2 and CO_2, N_2 adsorption and strain isotherms can no longer be predicted from CO_2 data. Therefore N_2 and CO_2 data sets had to be evaluated independently resulting in two PSDs and two sets of mechanical parameters for each sample. This issue was relevant for all samples annealed at 1400 °C and above; for the carbon xerogel annealed at 1200 °C the difference in accessible micropore volume was minor and thus using only one set of model parameters was found to be sufficient for this sample. Noteworthy, the simultaneous modeling of the N_2 adsorption and strain data confirm the expected trend of reduced micropore related strain ε_m (Eq. 2.46) with increasing annealing temperature. This is illustrated in Figure 5.28, where experimental and theoretical strains of the carbon xerogels at saturation $\varepsilon_{dil,sat}$ are plotted as a function of the network particles' microporosity ϕ_{mic} (Table 4.6). Complementary, the strain contributions at saturation arising from the microporous matrix $\varepsilon_{m,sat}$ (Eq. 2.46 or 5.13, respectively) and the xerogel network $\varepsilon_{net,sat}$ (Eq. 2.39 or 5.13, respectively) are shown. From Figure 5.28 it can be seen that the strain contribution $\varepsilon_{m,sat}$ decreases significantly stronger for decreasing microporosity than $\varepsilon_{net,sat}$. Thus, for decreasing microporosity the relative contribution of $\varepsilon_{net,sat}$ to the overall sample strain increases. Comparing the characteristics of the PSDs obtained from the modeling of CO_2 data (Figure 5.27) the same trends as in section 4.2 are found: the accessible micropore volume and surface area decrease, but the average micropore size increases with the annealing temperature. The latter effect results from a disproportionate decrease of pore volume for widths below approximately 1 nm. With respect to carbon xerogels annealed at 1400 °C and above, the same results are found in the PSDs derived from N_2 and CO_2 data except for an overall decreased pore volume in case of N_2; therefore N_2 PSDs are not shown here. Noteworthy, the increase of average pore size is in line with previous studies on annealed carbon xerogels applying small angle X-ray scattering [138], where the total, i.e., accessible and inaccessible, microporosity was analyzed. This allows for the conclusion that accessible and inaccessible pore volume are subject to a quantitative similar increase of pore size.

In summary, the analysis of annealed carbon xerogels by simultaneous modeling of adsorption and strain isotherms reveals significant challenges for the method, since annealing may have tremendous effect on the pore accessibility. Nevertheless, the obtained results for the pore structure are qualitatively in line with expectations from adsorption analyses only. However, of particular interest are the mechanical parameters of the annealed carbon xerogels derived from strain data, which are analyzed in detail in the next section.

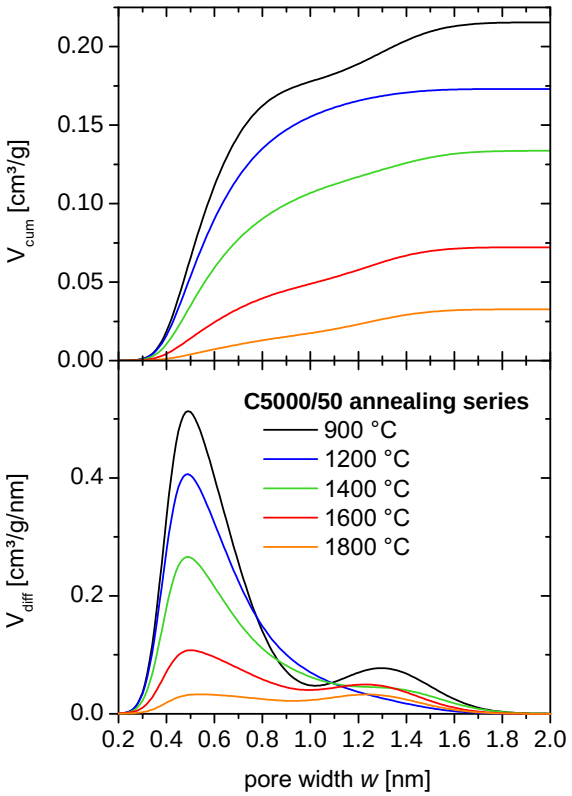

Figure 5.29.: Cumulative and differential pore volume distributions of the micro- and mesoporous reference carbon xerogel C5000/50/900 and the annealed samples C5000/50/1200, C5000/50/1400, C5000/50/1600 and C5000/50/1800 obtained from simultaneous modeling of the experimental CO2 adsorption and strain isotherms shown in Figure 5.27.

5.5.3. Mechanical Properties of Carbon Xerogels

In sections 5.3 to 5.5.2 adsorption and strain isotherms of different carbon xerogels were modeled by the combination of original or extended adsorption stress model (Eq. 2.41 and Eq. 2.46, respectively) and the integral adsorption equation (Eq. 2.14). This modeling process includes the adaptation of structural and mechanical characteristics of the underlying microporous carbon matrix, i.e., its PSD and the mechanical parameters K_m for the original adsorption stress model as well as K_s and K_β for the extended adsorption stress model, respectively. While the PSDs of the different carbon xerogels were already discussed, in the following the mechanical parameters obtained in the previous sections are considered: first on an individual base, then in comparison with reference values found in literature for similar microporous carbon based materials. The bulk moduli derived from the application of the extended adsorption stress model are summarized for all carbon xerogels in Table 5.4.

To begin with, the micro-macroporous carbon xerogel C5000/30/800 is consid-

Table 5.3.: Characteristic properties of the micropore size distributions obtained for all carbon xerogels from simultaneous modeling of the experimental adsorption and strain isotherms, i.e., the specific micropore volume V_{mic} (DFT), the specific micropore area S_{mic} (DFT) and the average micropore width $\bar{w}$. For carbons annealed at temperatures of 1400, 1600 and 1800 °C N_2 and CO_2 access different fractions of the overall microporosity and thus results for N_2 and CO_2 differ.

sample	V_{mic} (DFT) N_2/CO_2 [cm^3/g]	S_{mic} (DFT) N_2/CO_2 [m^2/g]	$\bar{w}$ N_2/CO_2 [nm]
C5000/30/800	0.245	864	0.57
C5000/50/800	0.197	686	0.57
C5000/50/900	0.215	717	0.60
C5000/50/900A	0.254	790	0.64
C5000/50/1200	0.173	593	0.58
C5000/50/1400	0.106/0.133	327/423	0.65/0.63
C5000/50/1600	0.050/0.072	151/207	0.66/0.70
C5000/50/1800	0.025/0.033	63/81	0.79/0.81

Table 5.4.: Mechanical moduli obtained for all carbon xerogels from simultaneous modeling of the experimental CO_2 adsorption and strain isotherms by the extended adsorption stress model, i.e., the bulk modulus of the nonporous carbon phase K_s, the effective pore modulus K_β and the resulting bulk modulus of the particles forming the xerogel network K_m. For carbons annealed at temperatures of 1400, 1600 and 1800 °C N_2 and CO_2 access different fractions of the overall microporosity and thus results for N_2 and CO_2 differ.

sample	K_s N_2/CO_2 [GPa]	K_β N_2/CO_2 [GPa]	K_m N_2/CO_2 [GPa]
C5000/30/800	12.4 ± 1.1	3.5 ± 0.4	5.2 ± 0.2
C5000/50/800	13.1 ± 1.3	3.3 ± 0.5	6.6 ± 0.3
C5000/50/900	13.8 ± 1.2	4.0 ± 0.5	6.2 ± 0.2
C5000/50/900A	14.6 ± 1.3	4.4 ± 0.5	6.0 ± 0.2
C5000/50/1200	16.0 ± 1.7	3.6 ± 0.6	9.0 ± 0.5
C5000/50/1400	15.9 ± 2.5/16.4 ± 2.1	2.1 ± 0.6/2.9 ± 0.6	11.5 ± 1.3/10.8 ± 0.9
C5000/50/1600	17.3 ± 1.7/17.2 ± 1.9	1.1 ± 0.3/1.6 ± 0.4	15.0 ± 2.0/14.0 ± 1.3
C5000/50/1800	17.0 ± 5.8/16.9 ± 3.8	0.5 ± 0.3/0.8 ± 0.3	16.0 ± 5.1/15.4 ± 3.1

ered, whose experimental isotherms were analyzed by both, original and extended, adsorption stress model (section 5.3). The original adsorption stress model yields the average bulk modulus of the microporous matrix $K_m = (6.1 \pm 0.3)$ GPa, which corresponds to the microporous particles of the carbon xerogel (Figure 3.2). The extended adsorption stress model on the other hand determines the parameters K_s and K_β allowing for a calculation of $K_m = (5.2 \pm 0.2)$ GPa via Eq. 2.49. Noteworthy, the bulk modulus K_s corresponds to the nonporous skeleton of the phase of the carbon xerogels, i.e., the carbon microcrystallites, while K_β describes the interconnection stiffness of the microcrystallites (compare Figures 2.6 und 5.25). Quantitatively, the values of K_m evaluated by the adsorption stress models are rather close giving no preference to either model. Due to the shortcomings of the original adsorption stress model (compare section 5.3) all other carbon xerogels were only evaluated by the extended adsorption stress model, whose results are considered in the following.

Comparing the particle bulk moduli K_m obtained for the different untreated carbon xerogels by the application of the extended adsorption stress model, an apparent difference between the micro-macroporous sample (C5000/30/800, $K_m = (5.2 \pm 0.2)$ GPa) and the micro-mesoporous samples (C5000/50/800, $K_m = (6.6 \pm 0.3)$ GPa and C5000/50/900, $K_m = (6.2 \pm 0.2)$ GPa, respectively) is observed. The slightly higher values of K_m for the micro-mesoporous carbon xerogels can be explained according to the Gibson-Ashby model (Eq. 2.8) by the higher particle density and respectively lower particle porosity ϕ_{part} of the mesoporous samples (Table 4.6), i.e., $K_m \propto (1 - \phi_{part})^2$. Noteworthy, as expected the parameters K_s and K_β are essentially constant within error bars for all untreated carbon xerogels (Table 5.4).

With respect to activation of the sample C5000/50/900 (section 5.5.1), the bulk moduli K_s, K_β and K_m remain approximately constant within error considerations (Table 5.4). These results suggest that the carbon material removed by the activation did not contribute significantly to the overall stiffness of the particle. This picture is well in line with the burn-off of highly disordered carbon segments described in section 5.5.1. Further support for the similar of values of K_m of reference and activated carbon xerogel is found in the also similar bulk moduli K_b of the monolithic samples (Table 4.2), since for given network properties K_m and K_b are expected to depend linearly onto one another (Eq. 2.8).

The most drastic changes of the carbon xerogels' mechanical properties are found for the annealing series (sample C5000/50/900 to 1800, section 5.5.2). Here the bulk modulus K_m of the particles within the xerogel network increases significantly with the annealing temperature from approximately 6 GPa at 900 °C to 16 GPa at 1800 °C, while bulk modulus of the skeletal phase K_s increases only moderately. Here it is important to note that the skeletal phase of the annealed carbon xerogels as seen by gas adsorption is not nonporous as for the untreated samples, but contains inaccessible microporosity (compare Figure 5.25). Thus the

bulk modulus of the actual nonporous carbon phase is expected to increase stronger than K_s. Furthermore, for annealing temperatures of 1400 °C and above N_2 and CO_2 exhibit different accessibility to the carbon xerogel's microporosity requiring for two different PSDs and two sets of mechanical parameters within the modeling process. However, the resulting values for K_m derived from N_2 and CO_2 data differ only slightly and are always consistent within error considerations (Table 5.4).

To explore whether the rather strong increase of the particles' mechanical stiffness K_m with annealing temperature can be validated by independent measurements, two other material properties and their dependence on the annealing temperature are considered: one is the monolithic bulk modulus K_b of the carbon xerogel samples, the other the thermal conductivity $\lambda_{thermal}$ of evacuated carbon xerogels. The monolithic bulk modulus K_b was determined for the annealed carbon xerogels investigated in this work via sound velocity measurements (Table 4.2). Since the porosity of the particle network remains essentially constant during the annealing temperature (Table 4.6), a direct correlation of bulk modulus K_b and particle modulus K_m is expected from structural models such as the Gibson-Ashby model (Eq. 2.8) or the empirical stiffness-density correlation by Gross (Eq. 2.9). From Figure 5.30, showing K_b and K_m as a function of the annealing temperature, it becomes obvious that this expectation is not met. While both mechanical moduli increase with annealing temperature, the respective dependences are clearly different: the particle modulus K_m exhibits an approximately linear dependency on the annealing temperature, whereas the bulk modulus K_b increases in particular in the temperature range between 900 and 1200 °C but is only remotely affected by higher temperatures. Notably, the same dependence of the bulk modulus K_b on the annealing temperature was found in other studies on carbon xerogels [161]. Assuming the applied model determines the particle stiffness K_m correctly, the correlations shown in Figure 5.30 suggest an inhomogeneous change of mechanical properties within the xerogel network preventing the increase of the particles' mechanical stiffness K_m to be fully transferred onto the stiffness of the bulk material K_b.

An indirect approach to the mechanical stiffness of the particles is found in the thermal conductivity $\lambda_{thermal}$ of annealed carbon xerogels. Here it is important to note that $\lambda_{thermal}$ of an evacuated carbon xerogel measured at elevated temperatures corresponds essentially to the thermal conductivity of the xerogel network itself, since contributions from gas transport within the network pores or radiation are negligible. Furthermore, a correlation of the xerogel network's thermal conductivity and its mechanical stiffness is expected [161, 219].[10] Thus, Figure 5.31 shows the particle modulus K_m as determined by the modeling process and the thermal conductivity $\lambda_{thermal}$ taken from ref [161] as a function of the annealing temperature. As can be seen from Figure 5.31 both, K_m and $\lambda_{thermal}$, increase linearly with the annealing temperature resulting in the correlation

[10] This statement is only valid, if no significant electronic contributions to the thermal conductivity arise as was shown for annealed carbon xerogels in ref [161].

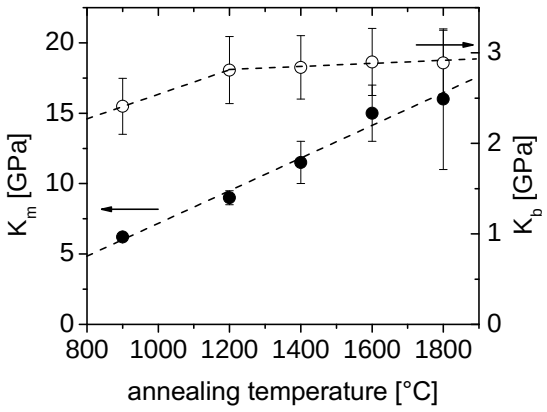

Figure 5.30.: The bulk moduli for the bulk carbon xerogel, K_b, (Table 4.2) and the microporous particles forming the network, K_m, (Table 5.4) as a function of the annealing temperature.

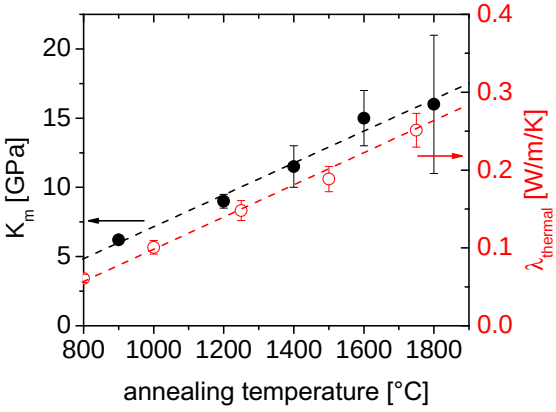

Figure 5.31.: The bulk moduli K_m for the microporous particles forming the network (Table 5.4) and the thermal conductivity $\lambda_{thermal}$ of evacuated carbon xerogels [161] as a function of the annealing temperature.

$\lambda_{thermal} \propto K_m$. At this point it is rather surprising that bulk modulus of the carbon particles K_m appears to be well correlated with the thermal conductivity $\lambda_{thermal}$ but not with bulk modulus K_b of the annealed carbon xerogel network.

Comparing the correlations of K_m, K_b and $\lambda_{thermal}$ with the annealing temperature, one may hypothesize that the connections between particles (compare Figure 5.25) do not exhibit the same structural changes during annealing as the particles themselves. However, to explain the findings presented in Figures 5.30 and 5.31, the particle connections have to be mechanical weaker than the bulk particles but should not exhibit reduced thermal conductivity. Unfortunately, no information about the properties of the particle connections and their dependence on annealing temperature are currently available and thus any further considerations remain purely speculative. Potential investigations to elucidate this issue would require for carbon xerogels with different particle interconnections, e.g., via a variation of the average particle diameter.

In the last part of this section the question is addressed, whether the absolute values of K_m obtained for the different carbon xerogels are reasonable. For comparison, two different references from literature are employed: (i) the bulk modulus of natural coal $K(coal) = 3.5$ GPa [61] and (ii) the bulk modulus of glassy carbon $K(glassy\ carbon) = 15$ GPa [220]. Natural coal and glassy carbon are microporous carbon-based materials of similar density as the particles within carbon xerogels (i.e. 1.3 to 1.5 g/cm^3), though obviously there are significant differences: natural coal usually exhibits some small amount ash and macropores in addition to its microporosity thereby increasing its overall mechanical compliance. Contrary, glassy carbon is extremely stiff, since the interconnection of the carbon phase within glassy carbon is so tight that its microporosity is entirely inaccessible

for gas molecules. Therefore, natural coal and glassy carbon can be considered extreme cases of microporous carbons. Comparing $K(coal)$ and $K(glassy\,carbon)$ with the values of K_m for untreated carbon xerogels, the results of the adsorption stress models suggest that the microporous particles within carbon xerogels are stiffer than coal but significantly more compliant than glassy carbon. With respect to the strong increase of K_m with thermal annealing, the bulk modulus of a carbon xerogel treated at 1800 °C ($K_m \approx 16$ GPa) is found to be very close to the one of glassy carbon. This result appears very reasonable, because both, glassy carbon and carbon xerogels thermally annealed at 1800 °C, exhibit little to no micropore volume accessible to gas molecules suggesting very tight interconnection of the nonporous carbon phase.

5.6. Zeolites - Ordered Microporosity

In the last section of the discussion, the experimental results obtained for the zeolites KÖSTROLITH 4ABFK and 13XBFK during CO_2 adsorption at 273 K (Figure 4.15) are compared with the qualitative understanding of micropore deformation obtained in the previous sections for microporous carbons. The major advantage of zeolites over microporous carbons is their high degree of order and thus monomodal PSD. As such, there is no ambiguity about pore size and structure causing the adsorption-induced deformation of the zeolite. The particular zeolite samples investigated in this work exhibit two structural levels, i.e., the level of the well-defined cage like micropores shown in Figure 3.3 and the level of the disordered macroporous network formed by subunits of pure zeolite shown in Figures 4.6 and 4.7. In direct analogy to carbon xerogels, the correlation of the (linear) dilatometric strain ε_{dil} with the theoretical predicted (volumetric) strain of the microporous matrix ε_m is thus given by the simple correlation $\varepsilon_m = 3\varepsilon_{dil}$, if $\varepsilon_{dil} \ll 1$.

To begin with, the experimental result for the zeolite 13XBFK (framework type FAU) is considered. The zeolite 13XBFK exhibits the typical nonmonotonic strain isotherm of microporous materials, which is quantitatively and qualitatively in line with previous in-situ dilatometry studies on FAU zeolites [35, 36] (see Figure 5.32). Noteworthy, these previous studies had no access to actual monolithic zeolites, but created virtual monoliths from zeolite powder and clay binder. This procedure raises the obvious question, whether the clay binder affects the strain isotherm of the artificial monolith compared to the pure zeolite phase. Since the dilatometric results obtained in this work on a binder-free zeolite monolith are well comparable to the binder-zeolite composite (Figure 5.32), it can be concluded that clay binder did not change the characteristic shape of the strain isotherm.

To describe the nonmonotonic shape of the strain isotherm for FAU zeolites, Ravikovitch and Neimark proposed the original adsorption stress model [70], which was later adapted for microporous carbon [75]. However, in contrast to carbons the geometry of the micropores within FAU zeolites can be approximated by a sphere

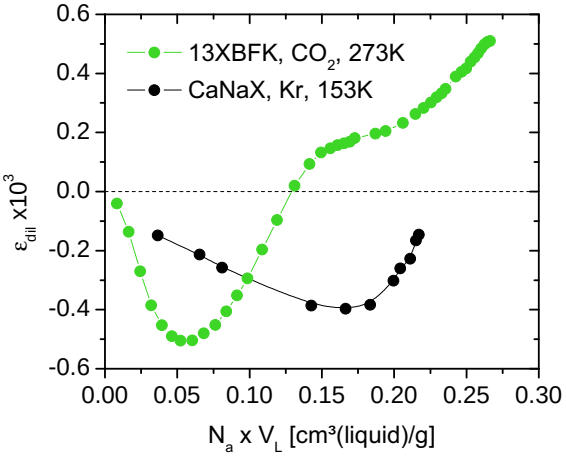

Figure 5.32.: Experimental dilatometric strain of the binderless zeolite 13XBFK during CO_2 adsorption at 273 K (this work) and a FAU zeolite-binder composite during Kr adsorption at 153 K [35].

and thus the extensions of the adsorption stress model described in section 2.3.1 are not required for the modeling process. As a consequence, the theoretical description of the zeolite strain by Ravikovitch and Neimark correctly took into account both stress mechanisms typical for micropores, i.e., the mediation of the pore wall potentials by the adsorbate and the reduction of the interfacial energy between pore and adsorbate. As shown for adsorption in slit-shaped micropores (section 4.1), the stress normal to the pore wall can be positive or negative depending on the ratio of pore size to molecular size of the adsorbate resulting in pore expansion or contraction, respectively, while the stress tangential to the pore walls is always positive and thus causes expansion. For the modeling of Xe and Kr adsorption of FAU zeolites Ravikovitch and Neimark found a spherical pore of 0.6 nm in diameter to be most appropriate, while the Van der Waals diameters of Xe, Kr and CO_2 (applied in this work) are all approximately 0.35 nm [70, 113]. Thus, the adsorption of these gases results in a loose packing of adsorbate atoms/molecules within the micropores of the FAU zeolite, which in turn causes the contraction of the pore, before the expansive interfacial energy change overtakes the contraction mechanism for progressing adsorption. In conclusion, the description of the strain isotherms of FAU zeolites and microporous carbon xerogels is the same on the qualitative level, though quantitative data evaluation would require additional NLDFT calculations adapted to the zeolite under investigation.

In the second part of this section the strain isotherms of the LTA zeolite 4ABFK is considered. Here it is important to note that previous studies on the deformation of LTA zeolites during the adsorption of Kr in the temperature range of 153 to 198 K showed once again the characteristic contraction-expansion strain isotherm [37]. On the other hand, the dilatometric strain isotherm of the zeolite 4ABFK obtained in this work for CO_2 adsorption at 273 K exhibits monotonic expansion only. A respective comparison is shown in Figure 5.33. Noteworthy,

the zeolite 4ABFK was found to exhibit no detectable N_2 adsorption at 77 K and consequently no related deformation.

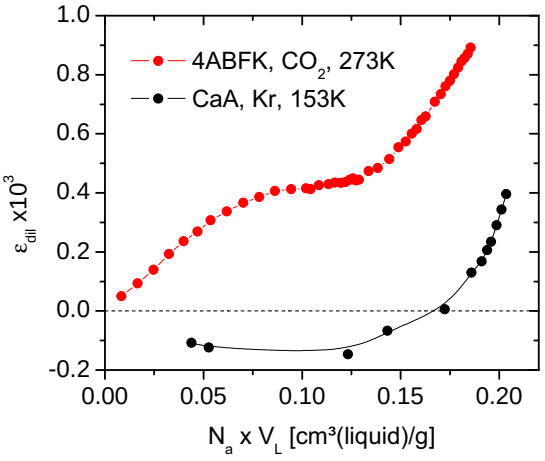

Figure 5.33.: Experimental dilatometric strain of the binderless zeolite 4ABFK during CO_2 adsorption at 273 K (this work) and a LTA zeolite-binder composite during Kr adsorption at 153 K [37].

To explain these apparently inconsistent results, two effects have to be taken into consideration:

(i) the micropore structure of the LTA zeolite differs from the one of the FAU zeolite in shape and size, i.e., in particular the effective diameter of the ring-shaped connections between the cubic pores is less than 0.4 nm and therefore of similar size as the effective Van der Waals diameters of Kr (0.36 nm, [70]), CO_2 (0.35 nm, [113]) or N_2 (0.36 nm, [113]).

(ii) the temperature of the adsorption measurement affects both, adsorption and strain isotherm. As already discussed in section 5.3, with increasing temperature adsorption and strain isotherms are shifted to higher relative pressure and the initial contraction of the strain isotherm is reduced. Furthermore, at the cryogenic temperature of 77 K the transport between micropores is hampered due to the low kinetic energy of the gas atoms/particles.

Following above considerations, the combination of a micropore size similar to the adsorbing gas molecules and the cryogenic temperature of 77 K provides a very intuitive explanation, why a monolithic piece of the zeolite 4ABFK did not exhibit adsorption in the N_2 experiment, i.e., due to diffusive limitations. Contrary, the results from ref [37] suggest that for temperatures above 150 K Kr can fully access the zeolite's microporosity and the corresponding strain isotherm is qualitatively identical to the strain isotherms of FAU zeolites or microporous carbons. This situation falls in line with the understanding of adsorption-induced deformation as described before.

The particular case of CO_2 adsorption at 273 K on the zeolite 4ABFK, however, requires some more interpretation. For one, NLDFT calculations for slit-shaped carbon micropores revealed that a monomodal PSD can result in monotonically increasing adsorption stress and consequently monotonic expansion, if the width of the pore is smaller than the van der Waals diameter of the adsorbate (section 4.1). In such cases, the adsorbed molecule does not mediate the long-ranged attraction of the pore wall potentials but their short-ranged repulsion. Given that the diameter of the pore entrances of the LTA zeolites is smaller than 0.4 nm it may indeed be smaller than the adsorbing CO_2 molecule depending on its orientation within the pore. Simultaneously, the pore entrance has to be larger than a Kr atom, since otherwise Kr adsorption would qualitatively result in the same strain isotherm as CO_2 adsorption. In this scenario, the monotonic expansion of the zeolite 4ABFK during CO_2 adsorption is the consequence of a very fine tuned sieving effect by the zeolite's pore entrances.

Another approach to the shape of the monotonic strain isotherm of the zeolite 4ABFK follows from the temperature dependence of adsorption-induced deformation. As was demonstrated experimentally for microporous carbons [6, 194], the initial contraction found in the strain isotherm reduces for increasing temperature to the point where it is barely [194] or not even at all detectable [6]. This effect is qualitatively in line with NLDFT calculations for slit-shape micropores shown in section 4.1, though a complete removal of the negative adsorption was not found in the temperature range considered there. However, the adsorption-induced strain of the LTA zeolite structure could be more sensitive to temperature than slit-shaped pores. To validate this explanation, temperature dependent measurements of adsorption-induced deformation would be required for the zeolite 4ABFK-CO2 combination.

6. Conclusions

The work at hand combines the results from in-situ dilatometry measurements during the adsorption process with currently available models for adsorption-induced deformation of nanoporous materials. The model materials investigated were a hierarchical structured silica, a silica aerogel, carbon xerogels and zeolites of type FAU as well as LTA, respectively. All of the model materials exhibited characteristic strain isotherms similar to previous studies reported in literature for comparable materials. The only exception in this regard is the LTA zeolite.

Based on comprehensive material characterization, theoretical models of adsorption-induced deformation were applied to the obtained experimental data. In summary this led to the following conclusions for the different model materials:

Hierarchical structured porous silica. The adsorption-induced deformation of the hierarchical structured silica is dominated by its well defined cylindrical mesopores, while its macropores have little to no impact on the obtained strains. The net strain of this sample at saturation is the smallest measured in this work and one of the smallest found in literature due to its sintering at 950 °C. The application of the extended adsorptions stress model results in a consistent description of adsorption and strain isotherm: prior to capillary condensation, i.e., in the film regime of the adsorption isotherm, the strain of the sample can be understood as a competition between positive strain induced by a progressive reduction of the solid surface energy (Bangham's law) and negative strain due to the concave liquid-vapor interface within the pore (Laplace strain). Since the former effect is quantitatively dominant for the considered adsorption of N_2 at 77 K, the sample is expanding for increasing relative pressure. After capillary condensation, when the mesopores are essentially completely filled with adsorbate, the pore structure within the sample is subjected to capillary pressure. The evaluated structural and mechanical properties of the sample are well in line with independent measurements and results reported in literature. On a side note, the proposed extension of the original adsorption stress model by Ravikovitch and Neimark was shown to be of considerable importance to obtain reasonable values for the model parameters.

Silica aerogel. In contrast to the hierarchical structured silica, the silica aerogel exhibits mesopores of ill-defined shape. However, the structural disorder does not change the fundamental mechanisms of the adsorption-induced deformation found for well-defined cylindrical pores within the hierarchical structured silica, i.e., Bangham's law and Laplace strain in the film regime of the adsorption isotherm as well as capillary pressure in the filled pore regime. However, the combination of the

particulate structure and the low density of the silica aerogel drastically changes the weighing of the different strain contributions enhancing the impact of Laplace and capillary pressure by several orders of magnitude. As a consequence, the silica aerogel exhibits the most extreme strain values of all samples considered. Notably, an increase of the sample's density would attenuate the extreme strain values potentially resulting in a similar strain isotherm as observed for the hierarchical structured silica.
The models proposed for the evaluation of the silica aerogel's strain isotherm give a qualitatively and mostly also quantitatively correct description of the material's adsorption-induced deformation. Bulk moduli for the nonporous silica particles and the macroscopic silica monolith were obtained from the filled pore regime and their respective values are well within the expectations derived sound velocity measurements. The bulk modulus of the nonporous silica particles is furthermore supported by the application of Bangham's law in the low relative pressure regime of the strain isotherm. The impact of the Laplace stress resulting from the curved adsorbate film within the aerogel structure is only qualitatively described by the approximation of the cylindrical pore model, while quantitatively significant deviations are observed.

Carbon xerogels. The strain isotherm of a carbon xerogel is a superposition of the adsorption-induced deformation of the particle network as found for the silica aerogel and the strain of the microporous matrix within the particles. The extent of each effect varies between samples depending on the respective structural details: if the particle network of the carbon xerogel is macroporous, the only significant strain contribution arises from the microporous matrix. For mesoporous carbon xerogels on the other hand, the network deformation was found to be relevant, however, for the particular species investigated in this work the respective contribution to the strain isotherms was smaller than the impact of the microporous matrix. Noteworthy, this result is directly related to the rather high bulk moduli of the carbon xerogel considered, i.e., for carbon xerogels of similar density as the silica aerogel strain related to mesopores would be a major contribution to the strain isotherm.
The evaluation of carbon xerogel strain isotherms clearly shows that both, the original as well as the extended adsorption stress model, are capable of describing the characteristic nonmonotonic strain isotherm of microporous materials. However, the extension of the adsorption stress model for pore anisotropy results in an overall more consistent data description than the original version applied in literature. The obtained pore size distributions and mechanical moduli for the carbon xerogels are well within expectations from previous studies and independent measurements.
Both after treatments applied to the carbon xerogels, i.e., activation and annealing, have clearly visible impact on the strain isotherms compared to their respective reference samples due changes of the microporous matrix within the particles. The quantitative analysis of the strain isotherms results again in reasonable predictions for structural and mechanical properties of the modified samples,

though in particular the annealing process creates significant challenges for the data evaluation process due to limitations of the micropore accessibility.

FAU and LTA zeolites. The strain isotherm of the FAU zeolite exhibits the same shape as the strain isotherms of carbon xerogels and other microporous materials, i.e., the characteristic contraction for initial pore filling, which crosses-over to expansion for progressing adsorption. The LTA zeolite on the other hand, exhibits a strain isotherm rarely seen for microporous materials: the LTA zeolite expands monotonously for increasing relative and amount adsorbed, respectively. While no quantitative description of this observation was available, qualitative explanations can be found within the pore size and temperature dependence of adsorption-induced micropore deformation.

Finally, some general conclusions can be to be drawn when considering the work at hand on the whole. In analogy to the introduction, these conclusions can be classified into theoretical and experimental advances as well as technical implications:

Theoretical advances. With respect to theoretical understanding of adsorption-induced deformation the major contribution of this work is the extension of the adsorption stress model originally proposed by Ravikovitch and Neimark for anisotropic pore geometries, i.e., the cylindrical pore and the slit-shaped pore. For both pore geometries, the extended adsorption stress model adds a qualitatively new level to the theory, which can be considered as an unification of the original adsorption stress model and Bangham's law.
Another noteworthy result is the finding that the adsorption-induced strain of materials exhibiting clearly distinguishable structural levels may be described by a superposition of models appropriate to the respective structures.

Experimental advances. The most valuable experimental accomplishment of this work is the in-situ dilatometry setup in its final form. The applied revisions improved the quality of strain measurements for materials exhibiting only very small deformations at potentially very low (relative) pressures. In combination with the vapor option of the connected adsorption instrument the overall setup can handle a respectable range of adsorbate-temperature combinations including the current standards for gas adsorption measurements, i.e., N_2 adsorption at 77 K, Ar adsorption at 87 K and CO_2 adsorption at 273 K.
Furthermore, the combination of the in-situ dilatometry setup and theoretical models proved to be a useful tool for structural and mechanical characterization of materials as was exemplified for the activation and thermal annealing of carbon xerogels. Notably, this approach allows for mechanical characterization on the level of the material's pores, which is a regime that is challenging to access otherwise.

Technical implications. With respect to this work's technical implications two fields come to mind: adsorption-driven actuation and electrical energy storage

via electrosorption. Regarding the development of actuators, the results of this work show that adsorption-induced stress generally increases for decreasing pore size, e.g., micropores exhibit larger stress than mesopores. However, the same trend is not necessarily true for the resulting adsorption-induced strains, which also depend on the effective resistance of the porous material to the applied stress. Apart from the mechanical stiffness of the nonporous skeleton forming the porous material, the porosity of the material is a major parameter for the extent of adsorption-induced strain. However, a material may exhibit an overall large porosity, but only a fraction of its pore volume comprises pores, which exhibit significant adsorption-induced stress. It can also be hypothesized that beyond purely structural dependencies of adsorption-induced deformation, modifications of a material's surface chemistry may result in enhanced or reduced interaction potentials for specific adsorptives thereby allowing for more control of the adsorbent's strain.
Another field related to gas adsorption and therefore gas adsorption-induced deformation is electrical energy storage via electrosorption, since the applied electrodes are often nanoporous to increase the surface area accessible to the electrolyte. Obviously, the Coulomb interaction potentials of ions and charged pore walls differ from gas adsorption, which is dominated by dispersion forces, but the strain inducing mechanisms should be generally similar in both cases. Thus a transfer of the results obtained in this work to electrosorption may be very helpful to understand the deformation of electrodes.

7. Appendix

A. Molecular Models of NLDFT Calculations

This section summarizes the molecular models for the fluid as applied in NLDFT calculations (see also a reference related to this work [188]). With respect to Eq. 2.10 explicit expressions for the free energy contributions of the adsorbate due to ideal gas behavior, F_{ideal}, and fluid-fluid interaction, F_{excess}, are required:

$$F_{ideal}\left[\rho_a\left(\boldsymbol{r}\right)\right] = k_B T \int \mathrm{d}\boldsymbol{r}\rho_a\left(\boldsymbol{r}\right)\left[\ln\left(\Lambda^3\left(\boldsymbol{r}\right)-1\right)\right], \tag{A.1}$$

$$F_{excess}\left[\rho_a\left(\boldsymbol{r}\right)\right] = F_{att}\left[\rho_a\left(\boldsymbol{r}\right)\right] + F_{HS}\left[\rho_a\left(\boldsymbol{r}\right)\right]. \tag{A.2}$$

Here k_B is the Boltzmann constant and Λ is the thermal de Broglie wavelength of an adsorbate molecule. The excess free energy F_{excess} of the fluid phase is separated into fluid-fluid attraction F_{att} and hard sphere repulsion F_{HS} contributions.

The fluid-fluid attraction F_{att} is modeled by the interaction potential ϕ_{att} according to the Weeks-Chandler-Andersen perturbation scheme [108]:

$$F_{att}\left[\rho_a\left(\boldsymbol{r}\right)\right] = \frac{1}{2}\iint \mathrm{d}\boldsymbol{r}\mathrm{d}\boldsymbol{r}'\rho_a\left(\boldsymbol{r}\right)\rho_a\left(\boldsymbol{r}'\right)\phi_{att}\left(\left|\boldsymbol{r}-\boldsymbol{r}'\right|\right), \tag{A.3}$$

$$\phi_{att}\left(r\right) = \begin{cases} -\varepsilon_{ff} & r < r_m = 2^{1/6}\sigma_{ff} \\ 4\varepsilon_{ff}\left[\left(\frac{\sigma_{ff}}{r}\right)^{12} - \left(\frac{\sigma_{ff}}{r}\right)^{6}\right] & r_m < r < r_c \\ 0 & r > r_c \end{cases} \tag{A.4}$$

Here ε_{ff} and σ_{ff} are parameters for depth and range of the interaction potential, respectively. r_m describes the minimum of the potential and r_c is the cutoff distance of the fluid-fluid interaction. In a previous work ε_{ff} and σ_{ff} were adapted to correctly describe physical properties of the unconfined fluid, e.g., liquid surface tension and liquid-vapor equilibrium [111] (Table A.1). The cutoff distance for fluid-fluid interaction was set to $5\sigma_{ff}$.

For the hard sphere repulsion free energy F_{HS}, the RLST version [109] of the fundamental measure theory of Rosenfeld [110] is employed:

$$\begin{aligned} F_{HS}\left[\rho_a\left(\boldsymbol{r}\right)\right] = \frac{1}{k_B T}\int \mathrm{d}\boldsymbol{r}\Bigg(&-n_0\ln\left(1-n_3\right) + \frac{n_1 n_2 - \boldsymbol{n_{V1}}\cdot\boldsymbol{n_{V1}}}{1-n_3} \\ &+\frac{n_2^3}{24\pi\left(1-n_3\right)^2}\left(1-3\xi^2+2\xi^3\right)\Bigg) \end{aligned} \tag{A.5}$$

Table A.1.: Summary of parameters applied in NLDFT calculations for the adsorption of N_2, Ar and CO_2. Here ε_{ff} and σ_{ff} are the parameters of the attractive fluid-fluid potential, d_{HS} is the molecular hard sphere diameter, ε_{sf} and σ_{sf} are the parameters of the solid-fluid potential [113, 216], T is the temperature and m_{mol} is the molar weight of the adsorbate[200].

adsorbate	ε_{ff}/k_B [K]	σ_{ff} [nm]	d_{HS} [nm]	ε_{sf}/k_B [K]	σ_{sf} [nm]	T [K]	m_{mol} [g/mol]
N_2	94.45	0.3575	0.3575	53.22	0.3494	77.4	28.013
Ar	118.05	0.3305	0.339	55.0	0.335	77.4	39.948
CO_2	235.9	0.3454	0.3495	81.5	0.343	273.15	44.01
	258.81		0.35547			243.15	
	215.49		0.34179			303.15	

$$n^{(\alpha)}(\boldsymbol{r}) = \int \boldsymbol{r}' \rho_a(\boldsymbol{r}')\, \omega^{(\alpha)}(\boldsymbol{r} - \boldsymbol{r}') \tag{A.6}$$

$$\begin{aligned}
&\omega^{(0)}(r) = \frac{\delta(R_{HS} - r)}{4\pi R_{HS}^2},\ \omega^{(1)}(r) = \frac{\delta(R_{HS} - r)}{4\pi R_{HS}},\\
&\omega^{(2)}(r) = \delta(R_{HS} - r),\ \omega^{(3)}(r) = \Theta(R_{HS} - r),\\
&\boldsymbol{\omega^{(V1)}}(\boldsymbol{r}) = \frac{\boldsymbol{r}}{r}\delta(R_{HS} - r),\ \boldsymbol{\omega^{(V2)}}(\boldsymbol{r}) = \frac{\boldsymbol{r}}{r}\frac{\delta(R_{HS} - r)}{4\pi R_{HS}}.
\end{aligned} \tag{A.7}$$

Here, $n^{(\alpha)}(\boldsymbol{r})$ are weighted densities derived by utilizing the scalar weighting functions $\omega^{(\alpha)}$ and the vectorial weighting functions $\boldsymbol{\omega^{(\alpha)}}$; additionally, $\xi = |\boldsymbol{n_{V2}}/n_2|$. In Eq. A.7 $\delta(r)$ is the Dirac delta function, $\Theta(r)$ is the Heaviside function and $R_{HS} = d_{HS}/2$ is the hard sphere radius of the adsorbate molecule with d_{HS} being the respective hard sphere diameter.

All parameters for NLDFT calculations were taken from Ravikovitch et al. [113] except for CO_2 adsorption at 243 and 303 K, where minor modifications to the fluid-fluid interaction parameters were made following the suggestions of ref [216] (Table A.1).

B. Disjoining Pressure Reference Isotherms

The application of DBdB theory (section 2.2.3) and the calculation of surface energy change (Eq. 5.11 and 5.12) require for explicit expressions of the disjoining pressure and reference isotherms, respectively. In this work reference isotherms were determined for N_2 adsorption on silica (77 K), N_2 adsorption on carbon (77 K), Ar adsorption on carbon (77 K) and CO_2 adsorption on carbon

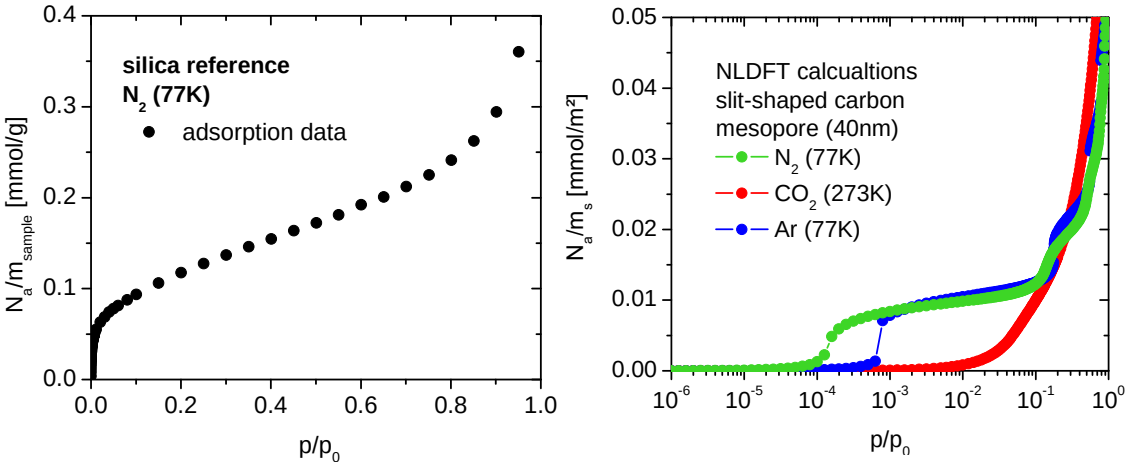

Figure B.1.: Experimental reference isotherms for the adsorption of N_2 (77 K) on silica (left) and theoretical reference isotherms derived by NLDFT calculations for a 40 nm wide slit-shaped carbon micropore and the adsorption of N_2 (77 K), Ar (77 K) and CO_2 (273 K) (right).

(273 K) (Figure B.1). The silica reference isotherm was determined on a purely macroporous silica sintered at 1000 °C exhibiting a specific surface area of $S = 9.9\ \mathrm{m^2/g}$; details on the preparation and characterization of the silica reference sample are given in a publication related to this work [129]. The carbon reference isotherms were determined by NLDFT calculations on a slit-shaped mesopore of 40 nm width, which was shown by Ravikovitch et al. to be sufficiently large to represent a flat surface [113]. Notably, NLDFT calculations yield surface specific adsorption N_a/A_s (compare section 2.2.2) in contrast to experiments, where the mass specific adsorption N_a/m_{sample} is determined. The step like adsorption of N_2 and Ar at 77 K on carbon (see Figure B.1) is a consequence of the smooth wall approximation of NLDFT calculations (see discussion in section 4.1).

From the reference isotherms shown in Figure B.1 explicit expressions for the disjoining pressure $\Pi(h)$ (Eq. 2.18) were derived for the adsorption of N_2 (77 K) on silica and carbon. Under the assumptions of liquid like density for the adsorbate ($V_L(N_2, 77K) = 34.66\ \mathrm{cm^3/mol}$ [79]) and very large pores ($R \to \infty$) the disjoining pressure as a function of relative pressure is given by (Eq. 2.18)

$$\Pi(p/p_0) = -\frac{R_g T}{V_L} \cdot \ln(p/p_0)\,. \tag{B.1}$$

Furthermore, the thickness of the adsorbate film h can be derived from the reference isotherms as

$$h(p/p_0) = \frac{V_L}{S} \cdot \frac{N_a}{m_{sample}}(p/p_0) \quad \text{or} \tag{B.2a}$$

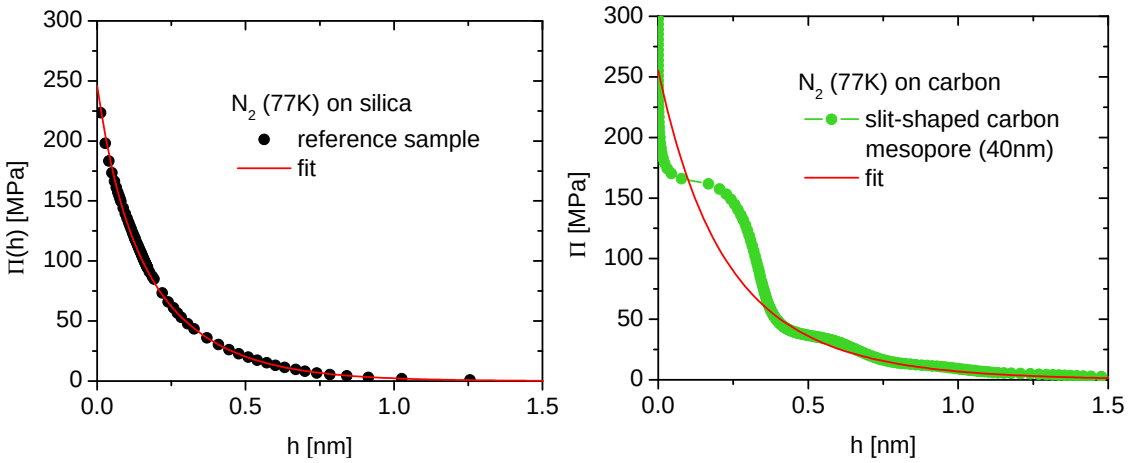

Figure B.2.: Plots of the disjoining pressure Π (Eq. B.1) as a function of the adsorbate film thickness h (Eq. B.2) for N_2 adsorption (77 K) on silica (left) and carbon (right) as well as respective fitting by Eq. B.3.

Table B.1.: Parameters of the disjoining pressure $\Pi(h)$ as described by Eq. B.3 for the adsorption of N_2 (77 K) on silica and carbon.

adsorbent	Π_1 [MPa]	λ_1 [nm]	Π_1 [MPa]	λ_2 [nm]
silica	178	0.23	68	0.073
carbon	155	0.32	100	0.15

$$h\,(p/p_0) = V_L \cdot \frac{N_a}{A_S}\,(p/p_0)\,. \tag{B.2b}$$

Together Eq. B.1 and B.2 allow for plotting $\Pi(h)$ (Figure B.2), which is then approximated by an analytical function such as [90]

$$\Pi\,(h) = \Pi_1\,\exp\,(-h/\lambda_1) + \Pi_2\,\exp\,(-h/\lambda_2)\,, \tag{B.3}$$

where Π_1, Π_2, λ_1 and λ_2 are fitting parameters. The fitting parameters obtained for N_2 adsorption on silica and carbon are summarized in Table B.1.

C. Connection between ASAP2020 and Dilatometer

Figure C.1 shows the connection between the commercial sorption instrument (ASAP2020) and the dilatometric setup designed within the framework of this thesis. The dilatometric side of the connection is a commercial *Ultra-Torr* adapter (*Swagelock*), while the other end is a specifically designed connector to meet the requirements of the sorption instrument. In between another adapter (*Swagelock*) and a copper tube were applied. The copper tube was bent to act like a spring

dampening mechanical shocks originating from the sorption instrument.

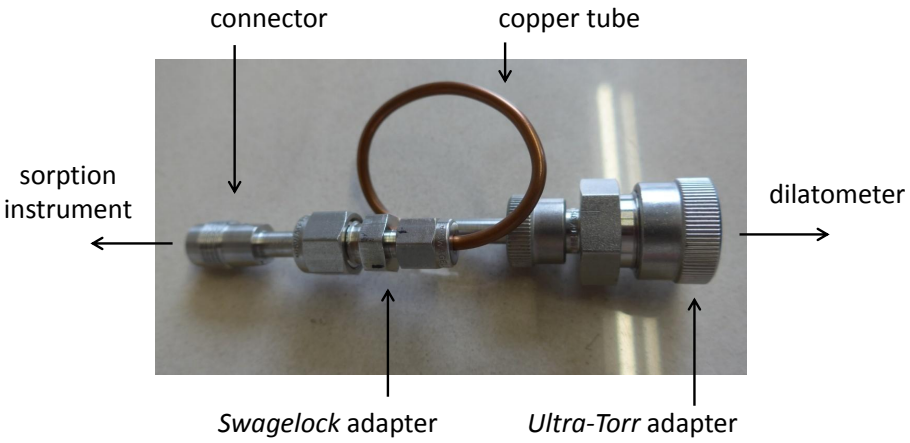

Figure C.1.: Connection between the commercial sorption instrument (ASAP2020) and the dilatometric setup.

D. in-situ Dilatometry Measurement on a Glass Rod

The in-situ dilatometry measurement on a nonporous glass rod ($L_0 \approx 4$ cm) for N_2 (77 K) revealed an approximately linear decrease of the dilatometric signal with the gas pressure inside the sample holder (Figure D.1). This strain exceeds the background noise approximately by a factor of 2.5. The origin of this effect is not fully understood; a potential explanation would be that the gas pressure expands the sample holder and compresses the push rod as well as the glass rod thereby causing a mixture of actual and apparent contraction of the sample. Thus, it may be possible to correct numerically for the pressure dependence of the dilatometric signal, but given the magnitude of the commonly observed adsorption-induced deformation this apparent deformation is quite small. For practical considerations, the strain shown in D.1 was therefore not explicitly corrected but rather incorporated into the accuracy of the overall setup.

E. PSDs from N2 and CO2 Adsorption for Annealed Carbon Xerogels

As described in section 4.2, the determination of the complete micropore size distribution of carbon xerogels annealed at 1400, 1600 and 1800 °C cannot be performed the same way as for the other carbon xerogels, because N_2 and CO_2 molecules access different fractions of the annealed samples' total micropore volume. Due to this issue the cumulative specific pore volume distributions derived for these samples from N_2 (77 K) and CO_2 (273 K) adsorption isotherms via

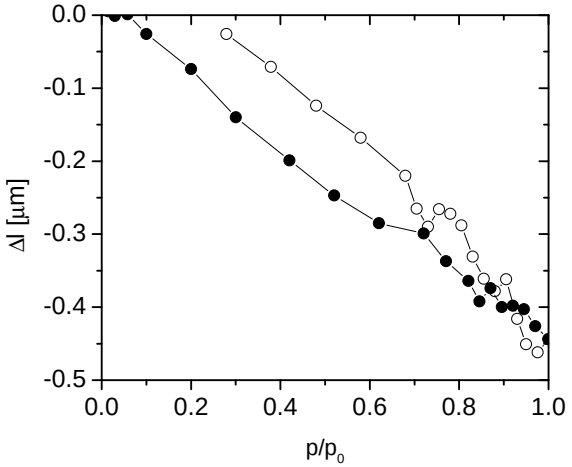

Figure D.1.: in-situ dilatometry measurement for N_2 adsorption at 77 K on a nonporous glass rod. The sample strain is given in absolute values.

NLDFT analysis do not exhibit an intersection point (compare Figure 4.10) and thus a direct connection of both PSDs is not possible.

In order to obtain information about the annealed carbons' micropore pore size distribution despite the above mentioned problem, assumptions had to be made regarding the accessibility for CO_2 and N_2 molecules. The procedures are illustrated in Figure E.1 for the carbon xerogel C5000/50/800:

For CO_2: the cumulative PSD determined from the CO_2 adsorption isotherm is considered valid for CO_2 molecules up to a pore width of 0.7 nm. For pore widths above 0.7 nm the cumulative PSD determined from N_2 adsorption is shifted upwards till it connects with the cumulative PSD derived from CO_2 adsorption. This implies that the accessibility for CO_2 molecules is the same as for N_2 molecules for pores larger than 0.7 nm. The connected cumulative PSD is differentiated with respect to the pore width to obtain the specific differential PSD.

For N_2: the cumulative PSD determined from the N_2 adsorption isotherm is considered valid for N_2 molecules above a pore width of 0.7 nm. Below a pore width of 0.7 nm the cumulative PSD accessible to N_2 has to be derived from the cumulative PSD derived from CO_2 adsorption. This procedure bears significant arbitrariness and thus two extreme scenarios are considered here:

(i) the cumulative PSD derived from the CO_2 adsorption isotherm is shifted downwards till it connects with cumulative PSD derived from the N_2 adsorption isotherm.

(ii) the cumulative PSD derived from the CO_2 adsorption isotherm is scaled downwards by a constant factor till connects with cumulative PSD derived from the N_2 adsorption isotherm.

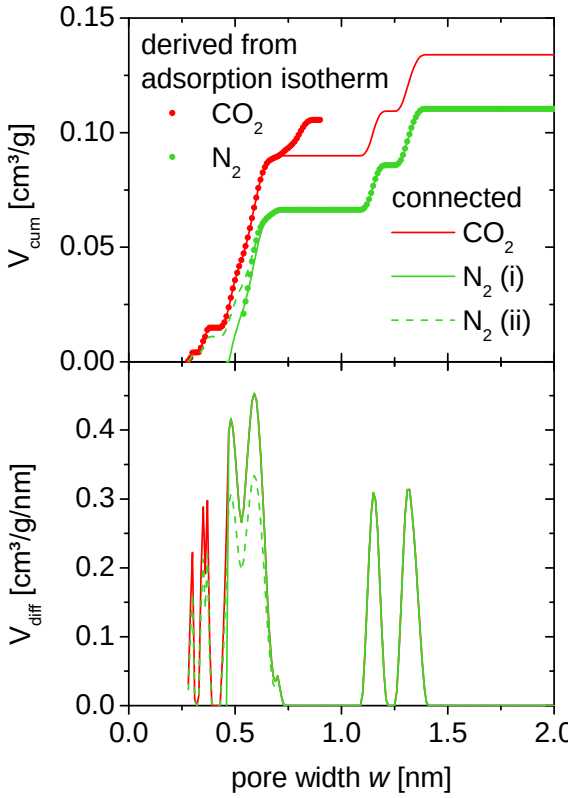

Figure E.1.: Cumulative and differential PSDs, V_{cum} and V_{diff}, respectively, accessible to N_2 (77 K) and CO_2 (273 K) for the annealed carbon xerogel C5000/50/1400.

As for CO_2, the connected cumulative PSDs are differentiated with respect to the pore width to obtain the specific differential PSDs. Notably, the intersection of the connected cumulative PSD with the pore width axis derived by these approaches and thus the smallest pore width accessible to N_2 molecules varies significantly. As a consequence of this approach, the characteristics quantities of the PSD accessible to N_2 molecules, i.e., V_{mic} (DFT), S_{mic} (DFT) and $\bar{w}$, exhibit a range rather than a single value (compare Table 4.5).

F. Estimate for Increase of Micropore Volume by Activation

To estimate the increase of a carbon xerogel's specific micropore volume ΔV_{mic} by activation, first the density ρ_{part} of the particles forming the carbon xerogel prior to activation is considered:

$$\rho_{part} = \frac{1}{V_{mic} + 1/\rho_s} = \frac{m_s}{V_{part}}. \tag{F.1}$$

Here V_{mic} is the carbon xerogel's specific micropore volume prior to activation, ρ_s is the density of the nonporous skeleton, m_s is the mass of the nonporous skeleton and V_{part} is the (absolute) volume of the particles.

The activation causes a relative mass loss φ_{bo} within the carbon particles leading to a new density of the carbon particles:

$$\rho'_{part} = \frac{1}{V'_{mic} + 1/\rho_s} = \frac{m'_s}{V_{part}} = \frac{(1-\varphi_{bo})\, m_s}{V_{part}} = (1-\varphi_{bo}) \cdot \rho_{part}. \tag{F.2}$$

The second equality in Eq. F.2 implies that the volume of the particle is conserved during activation, i.e., all burn-off takes place inside the particles and creates new micropore volume.

Combining Eq. F.1 and F.2 the change of specific micropore volume by activation is given by

$$\Delta V_{mic} = V'_{mic} - V_{mic} = \frac{\varphi_{bo}}{1-\varphi_{bo}} \cdot \frac{1}{\rho_{part}}. \tag{F.3}$$

Notably, if the experimentally detected change of micropore volume is equal to the result of Eq. F.3, it can be assumed that indeed all burn-off took place inside the particles. If Eq. F.3 overestimates the change of micropore volume, it is likely that the activation process changed the volume of the particles, e.g., by specific burn-off at the particles' surface. In this case an increased specific external surface area is expected. Finally, if Eq. F.3 underestimates the change of micropore volume, it is likely that the carbon xerogel contained micropore volume inaccessible prior to activation.

Acknowledgements

There are numerous people, who supported me directly or indirectly while I worked on this thesis. I am grateful to all of them.

In chronological order and without any claim to be exhaustive:

- Prof. Dr. Vladimir Dyakonov (Würzburg University) and Dr. Gudrun Reichenauer (Bavarian Center for Applied Energy Research) for giving me the opportunity to work on the topic of adsorption-induced deformation.
- The *Nanomaterials* group of the Bavarian Center for Applied Energy Research. Special thanks go out to my supervisor Dr. Gudrun Reichenauer, my former masterstudent Anna M. Waag as well as my colleagues Stephan Braxmeier and Dr. Matthias Wiener.
- Prof. Dr. Alexander V. Neimark and his group for a very instructional research stay at Rutgers University and continuous support afterwards. Special thanks go out to Dr. Richard T. Cimino for numerous discussions on scientific and technical aspects of DFT calculations.
- Prof. Dr. Gennady Y .Gor (New Jersey Institue of Technology) for continous collaboration including many fruitful discussions on the theory of adsorption and adsorption-induced deformation.
- Prof. Dr. Oskar Paris and his group (Montanuniversity Leoben) for detailed insight into the field of small angle X-ray scattering and constructive discussions on experimental aspects of measuring adsorption-induced deformation.
- Prof. Dr. Nicola Hüsing and her group (Salzburg University) for insight into the art of creating ordered nanoporous materials. Special thanks go out to her PhD students Christos Triantafillidis and Florian Putz for providing the hierarchical structured porous silica investigated within the framework of this thesis.
- Dr. Piotr Kowalczyk (Murdoch University) for fruitful discussions on the theory of adsorption-induced deformation.
- Chemiewerke Bad Köstritz for providing the binderless zeolite samples investigated in this thesis.
- Last but not least, my family and friends, who provided support, when I needed it most.

Furthermore, financial support is acknowledged from the German Academic Exchange Service (DAAD) as well as an international program funded by the Austrian Science Foundation (FWF, Project I 1605-N20) and the German Science Foundation (DFG, Project RE 1148/10-1) within the framework of the DACH agreement.

Symbols and Abbrevations

Latin Symbols

A	cross-sectional area of a slit-shaped pore
A_a	cross-sectional area of an adsorbed molecule
A_s	surface area of the porous solid's skeleton
C_{11}	linear elastic modulus
C_{BET}	C-Parameter of BET theory
C_{GA}	C-Parameter of Gibson-Ashby model
d_{HS}	hard sphere diameter of the adsorbate molecule
d_{latt}	mesopore lattice constant of hierarchical structured silica
d_p	diameter of cylindrical or spherical pore
d_{part}	diameter of spherical particle
d_{rod}	diameter of cylindrical rod
d_{strut}	diameter of mesoporous cylindrical strut in the hierarchical structured
E	Young's modulus
E_0	reference Young's modulus in aerogel scaling law
E_b	Young's modulus of the porous solid
E_s	Young's modulus of the porous solid's skeleton
F_{att}	free energy of the attractive interaction of adsorbate molecules
F_{excess}	free energy contribution due to molecular interaction of the adsorbate
F_{HS}	free energy of the hard sphere interaction of adsorbate molecules
F_{ideal}	free energy of the ideal gas
Δf_s	change of solid surface stress
h	adsorbate film thickness
h_c	critical adsorbate film thickness for capillary condensation
h_e	critical adsorbate film thickness for capillary evaporation
K	bulk modulus
k	effective bulk modulus of the cylindrical tube model
K_b	bulk modulus of the porous solid
k_B	Boltzmann constant
K_β	bulk modulus describing the resistance to changes of the pore shape
K_m	effective bulk modulus of the microporous carbon matrix
K_{part}	bulk modulus of the spherical particles in aero-/xerogel structures
K_{rod}	bulk modulus of rod-like particles in aero-/xerogel structures
K_s	bulk modulus of the porous solid's skeleton
K_{silica}	bulk modulus of nonporous amorphous silica
L	length of cylindrical pore/tube
l	length of sample as seen by the dilatometric setup
L_0	absolute length of sample in in-situ dilatometry measurement
l_0	reference length of sample as seen by the dilatometric setup
l_{sound}	distance between ultrasonic emitter and receiver
m_{mol}	molar mass of the adsorbate
m_s	mass of the porous solid's skeleton
m_{sample}	mass of monolithic sample
N_a	molar amount adsorbed

n_α	weighted densities of the applied fundamental measure theory
$N_{a,flat}$	molar amount adsorbed on a flat surface
N_A	Avogadro constant
N_{mono}	(molar) monolayer capacity of the BET theory
N_{NLDFT}	molar surface specific adsorption isotherm from NLDFT calculations
N_{kernel}	theoretically derived molar surface specific adsorption isotherm
p	gas pressure
p_0	gas saturation pressure
p/p_0	relative gas pressure
p_c	gas pressure of capillary condensation
p_{cap}	capillary pressure
p_e	gas pressure of capillary evaporation
p_{fill}	filling pressure of pores
R	pore radius of cylindrical pore
r_c	cutoff distance of the fluid-fluid interaction potential
R_g	gas constant
R_{HS}	hard sphere radius of the adsorbate molecule
r_m	minimum distance of the fluid-fluid interaction potential
R_{out}	outer radius of cylindrical tube
R_{part}	radius of spherical particle
R_{rod}	radius of cylindrical rod
$\boldsymbol{r}$	position vector within micropore
S	specific surface area of the porous solid
S_{BET}	specific surface area derived from BET theory
S_{cum}	specific cumulative surface area distribution
S_{DBdB}	specific surface area derived from DBdB theory
S_{diff}	specific differential surface area distribution
S_{ext}	specific external surface area of the t-plot method
S_{mac}	specific surface area of macropores
S_{meso}	specific surface area of mesopores
S_{mic}	specific surface area of micropores
T	temperature
Δt	runtime of ultrasonic pulse in sound velocity measurement
U_{ext}	external solid-fluid potential for NLDFT calculations
U_{Steele}	Steele potential
V	(absolute) pore volume
V_b	specific bulk volume of porous solid
V_{cum}	specific cumulative pore volume distribution
V_{cyl}	(absolute) volume of cylindrical pore
V_{diff}	specific differential pore volume distribution
$V_{Gurvich}$	specific pore volume according to the Gurvich rule
V_L	molar volume of the adsorbate in liquid phase
V_{mac}	specific macropore volume
V_{meso}	specific mesopore volume
V_{mic}	specific micropore volume
V_p	specific pore volume
V_{part}	absolute particle volume within carbon xerogel
V_s	specific volume of the nonporous solid skeleton
V_{sample}	geometric volume of a monolithic sample
V_{slit}	volume of a slit-shaped pore
v_{sound}	sound velocity
w	width of a sit-shaped pore
$\bar{w}$	average width of sit-shaped pores

w_{cc}	width of a slit-shaped carbon pore within NLDFT calculations
w_{max}	largest pore width within a kernel of sit-shaped pores
w_{min}	smallest pore width within a kernel of sit-shaped pores
x	parameter for the description of strain data of the hierarchical
z	Cartesian coordinate

Greek Symbols

α	exponent in aerogel scaling law
β	angle within the microporous carbon model
γ_{lv}	liquid-vapor surface energy
γ_{sl}	solid-liquid surface energy
γ_s	surface energy of the dry solid
$\Delta\gamma_s$	reduction of the solid surface energy by adsorption
Δ	interlayer distance of the Steele potential
ε	strain
$\varepsilon_{a,\perp}$	strain due to adsorption stress normal to the pore wall
$\varepsilon_{a,\parallel}$	strain due to adsorption stress parallel to the pore wall
ε_β	strain of the microporous matrix at constant skeleton volume
ε_{dil}	strain isotherm measured by in-situ dilatometry
ε_{ff}	fluid-fluid interaction parameter
$\varepsilon_{Laplace}$	strain due to Laplace stress
ε_m	strain of the microporous carbon matrix
ε_{net}	strain of a meso- or macroporous aero-/xerogel network
ε_{part}	strain of spherical particles within an aero-/xerogel network
ε_{rod}	strain of rod-like particles within an aero-/xerogel network
ε_s	strain of the nonporous skeleton
ε_{sf}	solid-fluid interaction parameter
Λ	thermal de Broglie wavelength of an adsorbate molecule
λ_1, λ_2	parameters of disjoining pressure fit
$\lambda_{thermal}$	thermal conductivity of the porous solid in the evacuated state
μ	chemical potential
μ_r	chemical potential of reference state
ν	Poisson's ratio
ν_b	Poisson's ratio of the porous solid
ν_{rod}	Poisson's ratio of rod-like particles within an aero-/xerogel network
ν_s	Poisson's ratio of the porous solid's skeleton
Π	disjoining pressure
Π_1, Π_2	parameters of disjoining pressure fit
ρ_0	reference density in aerogel scaling law
ρ_a	number density of the adsorbate
ρ_b	bulk density of the porous solid
ρ_g	number density of graphite in the Steele potential
ρ_{mass}	mass density of the adsorbate
ρ_{mol}	molar density of the adsorbate
ρ_{part}	density of a spherical particle
ρ_{rod}	density of a cylindrical rod
ρ_s	density of the porous solid's skeleton
ρ_{silica}	density of the nonporous amorphous silica
ρ_{strut}	density of the struts within the hierarchical structured silica
σ	stress
σ_a	adsorption stress

$\bar{\sigma}_a$	volumetrically averaged adsorption stress
$\sigma_{a,\perp}$	adsorption stress normal to the pore wall
$\bar{\sigma}_{a,\perp}$	volumetrically averaged adsorption stress normal to the pore wall
$\sigma_{a,\parallel}$	adsorption stress tangential to the pore wall
$\bar{\sigma}_{a,\parallel}$	volumetrically averaged adsorption stress tangential to the pore wall
σ_{cc}	effective diameter of a carbon atom within graphite
σ_{ff}	Van der Waals diameter of fluid-fluid interaction
$\sigma_{Laplace}$	Laplace stress due to curved adsorbate-adsorptive interface
σ_{part}	stress on spherical particles within an aero-/xerogel structure
σ_{rod}	stress on rod-like particles within an aero-/xerogel structure
σ_s	stress on the nonporous skeleton
σ_{sf}	Van der Waals diameter of solid-fluid interaction (Steele potential)
ϕ	porosity
ϕ_{att}	attractive potential of fluid-fluid interaction
φ_{bo}	carbon burn-off during activation
ϕ_{mic}	porosity of a microporous matrix
ϕ_{net}	interparticle porosity of an aero-/xerogel network
ϕ_{part}	intraparticle porosity of an aero-/xerogel network
ϕ_{strut}	porosity struts within a hierarchical structured porous silica
Ω_a	grand potential of the adsorbed phase
$\omega^{(\alpha)}$	weighing functions of the fundamental measure theory

Abbrevations

DBdB	Derjaguin-Broekhoff-de Boer
DFT	density functional theory
IAE	integral adsorption equation
IUPAC	International Union of Pure and Applied Chemistry
GCMC	grand canonical Monte Carlo
NLDFT	nonlocal density functional theory
PSD	pore size distribution
SEM	scanning electron microscopy

References

[1] S.J. Gregg and K.S.W. Sing. *Adsorption, Surface Area and Porosity*. 2nd. Academic Press, 1982.

[2] W. Kast. *Adsorption aus der Gasphase*. Weinheim: VCH Verlagsgesellschaft, 1988.

[3] F. Rouquerol, J. Rouquerol, and K. Sing. *Adsorption by Powders and Porous Solids. Principles, Methodology and Applications*. London: Academic Press, 1999.

[4] K. Kamegawa and H. Yoshida. "Preparation and characterization of swelling porous carbon beads". In: *Carbon* 35.5 (1997), pp. 631–639.

[5] A. A. Fomkin, N. I. Regent, and V. A. Sinitsyn. "Adsorption deformation in the microporous carbon adsorbent - benzene system and porous structure of adsorbents". In: *Russian Chemical Bulletin* 49.6 (2000), pp. 1012–1016.

[6] V. Y. Yakovlev, A. A. Fomkin, and A. V. Tvardovski. "Adsorption and deformation phenomena at the interaction of CO2 and a microporous carbon adsorbent". In: *Journal of Colloid and Interface Science* 268.1 (2003), pp. 33–36.

[7] V. Y. Yakovlev, A. A. Fomkin, and A. V. Tvardovski. "Adsorption and deformation phenomena at interaction of N2 and microporous carbon adsorbent". In: *Journal of Colloid and Interface Science* 280.2 (2004), pp. 305–308.

[8] A. V. Shkolin et al. "A technique for measuring an adsorption-induced deformation". In: *Instruments and Experimental Techniques* 51.1 (2008), pp. 150–155.

[9] A. V. Shkolin and A. A. Fomkin. "Deformation of AUK Microporous Carbon Adsorbent Induced by Methane Adsorption". In: *Colloid Journal* 71.1 (2009), pp. 119–124.

[10] C. Balzer et al. "Deformation of Porous Carbons upon Adsorption". In: *Langmuir* 27.6 (2011), pp. 2553–2560.

[11] A. V. Shkolin, A. A. Fomkin, and V. A. Sinitsyn. "Adsorption-Induced Deformation of AUK Microporous Carbon Adsorbent in Adsorption of n-Pentane". In: *Protection of Metals and Physical Chemistry of Surfaces* 47.5 (2011), pp. 555–561.

[12] A. V. Shkolin and A. A. Fomkin. "Adsorption deformation of AUK microporous carbon adsorbent at adsorption of n-heptane". In: *Protection of Metals and Physical Chemistry of Surfaces* 49.4 (2013), pp. 373–378.

[13] S. V. Potapov, A. V. Shkolin, and A. A. Fomkin. "Deformation of AUK microporous carbon adsorbent induced by krypton adsorption". In: *Colloid Journal* 76.3 (2014), pp. 351–357.

[14] A. V. Shkolin, S. V. Potapov, and A. A. Fomkin. "Deformation of AUK microporous carbon adsorbent induced by xenon adsorption". In: *Colloid Journal* 77.6 (2015), pp. 812–820.

[15] A. V. Shkolin et al. "Experimental study and numerical modeling: Methane adsorption in microporous carbon adsorbent over the subcritical and supercritical temperature regions". In: *Protection of Metals and Physical Chemistry of Surfaces* 52.6 (2016), pp. 955–963.

[16] F.T. Meehan. "The Expansion of Charcoal on Sorption of Carbon Dioxide". In: *Proceedings of the Royal Society of London. Series A* 115.770 (1927), pp. 199–207.

[17] D. H. Bangham and N. Fakhoury. "The Swelling of Charcoal. Part I - Preliminary Experiments with Water Vapour, Carbon Dioxide, Ammonia, and Sulphur Dioxide". In: *Proceedings of the Royal Society of London, Series A* 130.812 (1930), pp. 81–89.

[18] R. S. Haines and R. McIntosh. "Length Change of Carbon Rods Caused by Adsorption of Vapors". In: *Journal of Chemical Physics* 15.1 (1947), pp. 28–38.

[19] E. O. Wiig and A. J. Juhola. "The Adsorption of Water Vapor on Activated Charcoal". In: *Journal of American Chemical Society* 71.2 (1949), pp. 561–568.

[20] M. L. Lakhanpal and E. A. Flood. “Stresses and Strains in Adsorbate-Adsorbent Systems: IV. Contractions of Activated Carbon on Adsorption of Gases and Vapors at Low Initial Pressures”. In: *Canadian Journal of Chemistry* 35.8 (1957), pp. 887–899.

[21] J.R. Dacey and M.J.B. Evans. “Volume Changes in Saran Charcoal Caused by the Adsoption of Water, Methanol and Benzene Vapours”. In: *Carbon* 9.5 (1971), pp. 579–585.

[22] S. Mazumder, A. Karnik, and K. H. Wolf. “Swelling of coal in response to CO2 sequestration for ECBM and its effect on fracture permeability”. In: *Spe Journal* 11.3 (2006), pp. 390–398.

[23] S. Mazumder and K. H. Wolf. “Differential swelling and permeability change of coal in response to CO2 injection for ECBM”. In: *International Journal of Coal Geology* 74.2 (2008), pp. 123–138.

[24] R. Pini et al. “Role of adsorption and swelling on the dynamics of gas injection in coal”. In: *Journal of Geophysical Research* 114 (2009), B04203–B04216.

[25] C. H. Amberg and R. McIntosh. “A Study of Adsorption Hysteresis by Means of Length Changes of a Rod of Porous Glass”. In: *Canadian Journal of Chemistry* 30.12 (1952), pp. 1012–1032.

[26] D. J. C. Yates. “The Expansion of Porous Silica Glass Produced by the Adsorption of Non-Polar Gases at Liquid Air Temperatures”. In: *Transactions of the British Ceramic Society* 54 (1955), pp. 272–299.

[27] G. Reichenauer and G. W. Scherer. “Nitrogen adsorption in compliant materials”. In: *Journal of Non-Crystalline Solids* 277.2-3 (2000), pp. 162–172.

[28] K. P. Mogilnikov and M. R. Baklanov. “Determination of Young's modulus of porous low-k films by ellipsometric porosimetry”. In: *Electrochemical and Solid State Letters* 5.12 (2002), F29–F31.

[29] T. Herman, J. Day, and J. Beamish. “Deformation of silica aerogel during fluid adsorption”. In: *Physical Review B* 73.9 (2006), p. 094127.

[30] G. Günther et al. “Novel Insights into Nanopore Deformation Caused by Capillary Condensation”. In: *Physical Review Letters* 101.8 (2008), p. 086104.

[31] J. Prass et al. “Capillarity-driven deformation of ordered nanoporous silica”. In: *Applied Physics Letters* 95.8 (2009), p. 083121.

[32] M. Schoen et al. “Pore-lattice deformations in ordered mesoporous matrices: experimental studies and theoretical analysis”. In: *Physical Chemistry Chemical Physics* 12.37 (2010), pp. 11267–11279.

[33] K. Schappert and R. Pelster. “Unexpected Sorption-Induced Deformation of Nanoporous Glass: Evidence for Spatial Rearrangement of Adsorbed Argon”. In: *Langmuir* 30.46 (2014), pp. 14004–14013.

[34] V. F. Kononyuk, A. I. Sarakhov, and M. M. Dubinin. “Change in Linear Dimensions of Granules of Synthetic Zeolites with Adsorption of Water Vapors”. In: *Bulletin of the Academy of Sciences of the USSR, Division of chemical science* 21.8 (1972), pp. 1637–1642.

[35] B. P. Bering et al. “Alteration of Zeolite Granule Dimensions under Krypton Adsorption”. In: *Russian Chemical Bulletin* 26.11 (1977), pp. 2258–2261.

[36] O. K. Krasilnikova, A. I. Sarakhov, and M. M. Dubinin. “Alteration of the Linear Dimensions of NaX Zeolite Granules under Krypton Adsorption”. In: *Russian Chemical Bulletin* 26.7 (1977), pp. 1359–1363.

[37] B. P. Bering, O. K. Krasilnikova, and V. V. Serpinskii. “Deformation of Zeolite CaA Granule during Krypton Adsorption”. In: *Bulletin of the Academy of Sciences of the Ussr Division of Chemical Science* 27.12 (1978), pp. 2515–2517.

[38] A. V. Tvardovski et al. “Investigation of Cation-Substituted Vermiculite Deformation Upon Water Vapor Sorption”. In: *Journal of Colloid and Interface Science* 164.1 (1994), pp. 114–118.

[39] G. Dolino, D. Bellet, and C. Faivre. “Adsorption strains in porous silicon”. In: *Physical Review B* 54.24 (1996), pp. 17919–17929.

[40] G. Y. Gor et al. “Elastic response of mesoporous silicon to capillary pressures in the pores”. In: *Applied Physics Letters* 106.26 (2015), p. 261901.

[41] A. Grosman, J. Puibasset, and E. Rolley. “Adsorption-induced strain of a nanoscale silicon honeycomb”. In: *EPL* 109.5 (2015), p. 56002.

[42] G. Alberti, S. Murcia-Mascaros, and R. Vivani. "Pillared derivatives of gamma-zirconium phosphate containing nonrigid alkyl chain pillars". In: *Journal of the American Chemical Society* 120.36 (1998), pp. 9291–9295.

[43] S. Krause et al. "A pressure-amplifying framework material with negative gas adsorption transitions". In: *Nature* 532.7599 (2016), pp. 348–352.

[44] G. Y. Gor, P. Huber, and N. Bernstein. "Adsorption-Induced Deformation of Nanoporous Materials - a Review". In: *Applied Physics Reviews* 4 (2017), p. 011303.

[45] F.J.W. Whipple. "The Theory of the Hair Hygrometer". In: *Proceedings of the Physical Society of London* 34.1 (1921), pp. i–v.

[46] D. H. Bangham and N. Fakhoury. "The Expansion of Charcoal accompanying Sorption of Gases and Vapours". In: *Nature* 122 (1928), pp. 681–682.

[47] D. H. Bangham, N. Fakhoury, and A.F. Mohamed. "The Swelling of Charcoal. Part II - Some Factors Controlling the Expansion Caused by Water, Benzene and Pyridine Vapours". In: *Proceedings of the Royal Society of London. Series A* 134.834 (1932), pp. 162–183.

[48] D. H. Bangham, N. Fakhoury, and A. F. Mohamed. "The Swelling of Charcoal. Part III - Experiments with the Lower Alcohols". In: *Proceedings of the Royal Society of London. Series A* 147.860 (1934), pp. 152–175.

[49] D. H. Bangham. "The Swelling of Charcoal. Part IV - Stoichiometric Relations for the Lower Alcohols". In: *Proceedings of the Royal Society of London. Series A* 147.860 (1934), pp. 175–188.

[50] D. H. Bangham and R.I. Razouk. "The Swelling of Charcoal. Part V - The Saturation and Immersion Expansions and the Heat of Wetting". In: *Proceedings of the Royal Society of London. Series A* 166.927 (1938), pp. 572–586.

[51] D. H. Bangham and N. Fakhoury. "The Translational Motion of Molecules in the Adsorbed Phase on Solids". In: *Journal of the Chemical Society (Resumed)* (1931), pp. 1324–1333.

[52] E. A. Flood and R. D. Heyding. "Stresses and Strains in Adsorbent Adsorbate Systems". In: *Canadian Journal of Chemistry* 32.7 (1954), pp. 660–682.

[53] M. A. Aegerter, N. Leventis, and M. M. Koebel, eds. *Aerogels Handbook*. New York: Springer Science+Business Media, 2011.

[54] G. W. Scherer. "Characterization of Aerogels". In: *Advances in Colloid and Interface Science* 76-77 (1998), pp. 321–339.

[55] G. W. Scherer. "Adsorption in Aerogel Networks". In: *Journal of Non-Crystalline Solids* 225 (1998), pp. 192–199.

[56] G. Reichenauer and G. W. Scherer. "Extracting the pore size distribution of compliant materials from nitrogen adsorption". In: *Colloids and Surfaces a-Physicochemical and Engineering Aspects* 187 (2001), pp. 41–50.

[57] G. Reichenauer and G. W. Scherer. "Nitrogen Sorption in Aerogels". In: *Journal of Non-Crystalline Solids* 285.1-3 (2001), pp. 167–174.

[58] J. L. C. Rowsell and O. M. Yaghi. "Metal-organic frameworks: a new class of porous materials". In: *Microporous and Mesoporous Materials* 73.1-2 (2004), pp. 3–14.

[59] G. Ferey and C. Serre. "Large breathing effects in three-dimensional porous hybrid matter: facts, analyses, rules and consequences". In: *Chemical Society Reviews* 38.5 (2009), pp. 1380–1399.

[60] "Underground Geological Storage". In: *IPCC Special Report on Carbon Dioxide Capture and Storage*. Ed. by B. Metz et al. Cambridge University Press, 2005.

[61] S. Wong et al. "Enhanced coalbed methane and CO2 storage in anthracitic coals-Micro-pilot test at South Qinshui, Shanxi, China". In: *International Journal of Greenhouse Gas Control* 1.2 (2007), pp. 215–222.

[62] M. Boudot, H. Elletro, and D. Grosso. "Converting Water Adsorption and Capillary Condensation in Usable Forces with Simple Porous Inorganic Thin Films". In: *ACS Nano* 10 (2016), pp. 10031–10040.

[63] C. Ganser et al. “Cantilever bending based on humidity-actuated mesoporous silica/silicon bilayers”. In: *Beilstein Journal Of Nanotechnology* 7 (2016), pp. 637–644.

[64] D. Van Opdenbosch et al. “Moisture-Driven Ceramic Bilayer Actuators from a Biotemplating Approach”. In: *Advanced Materials* 28.26 (2016), pp. 5235–5240.

[65] G. Reichenauer et al. “In-situ monitoring of the deformation of nanopores due to capillary forces upon vapor sorption”. In: *BENSC Experimental Reports 2008*. Ed. by A. Rödig, A. Brandt, and H.A. Graf. Berlin Neutron Scattering Center, 2009, p. 216.

[66] C. T. Kresge et al. “Ordered Mesoporous Molecular-Sieves Synthesized by a Liquid-Crystal Template Mechanism”. In: *Nature* 359.6397 (1992), pp. 710–712.

[67] D. Y. Zhao et al. “Triblock copolymer syntheses of mesoporous silica with periodic 50 to 300 angstrom pores”. In: *Science* 279.5350 (1998), pp. 548–552.

[68] J. Prass et al. “Apparent lattice expansion in ordered nanoporous silica during capillary condensation of fluids”. In: *Journal of Applied Crystallography* 45 (2012), pp. 798–806.

[69] T. S. Jakubov and D. E. Mainwaring. “Adsorption-induced dimensional changes of solids”. In: *Physical Chemistry Chemical Physics* 4.22 (2002), pp. 5678–5682.

[70] P. I. Ravikovitch and A. V. Neimark. “Density functional theory model of adsorption deformation”. In: *Langmuir* 22.26 (2006), pp. 10864–10868.

[71] E. A. Ustinov and D. D. Do. “Effect of adsorption deformation on thermodynamic characteristics of a fluid in slit pores at sub-critical conditions”. In: *Carbon* 44.13 (2006), pp. 2652–2663.

[72] A. I. Rusanov and F. M. Kuni. “On the theory of the mechanochemical sorption-striction phenomenon in nanoporous bodies with dispersion forces”. In: *Russian Journal of General Chemistry* 77.3 (2007), pp. 371–392.

[73] D. D. Do, D. Nicholson, and H. D. Do. “Effects of Adsorbent Deformation on the Adsorption of Gases in Slitlike Graphitic Pores: A Computer Simulation Study”. In: *Journal of Physical Chemistry C* 112.36 (2008), pp. 14075–14089.

[74] A. Grosman and C. Ortega. “Influence of elastic deformation of porous materials in adsorption-desorption process: A thermodynamic approach”. In: *Physical Review B* 78.8 (2008), p. 085433.

[75] P. Kowalczyk, A. Ciach, and A. V. Neimark. “Adsorption-Induced Deformation of Microporous Carbons: Pore Size Distribution Effect”. In: *Langmuir* 24.13 (2008), pp. 6603–6608.

[76] G. Günther and M. Schoen. “Sorption strains and their consequences for capillary condensation in nanoconfinement”. In: *Molecular Simulation* 35.1-2 (2009), pp. 138–150.

[77] G. Günther and M. Schoen. “Sorption strain as a packing phenomenon”. In: *Physical Chemistry Chemical Physics* 11.40 (2009), pp. 9082–9092.

[78] S. H. Mushrif and A. D. Rey. “An integrated model for adsorption-induced strain in microporous solids”. In: *Chemical Engineering Science* 64.22 (2009), pp. 4744–4753.

[79] G. Y. Gor and A. V. Neimark. “Adsorption-Induced Deformation of Mesoporous Solids”. In: *Langmuir* 26.16 (2010), pp. 13021–13027.

[80] P. Kowalczyk et al. “Carbon Dioxide Adsorption-Induced Deformation of Microporous Carbons”. In: *Journal of Physical Chemistry C* 114 (2010), pp. 5126–5133.

[81] A. V. Neimark et al. “Stress-Based Model for the Breathing of Metal-Organic Frameworks”. In: *Journal of Physical Chemistry Letters* 1.1 (2010), pp. 445–449.

[82] M. Vandamme et al. “Adsorption and strain: The CO2-induced swelling of coal”. In: *Journal of the Mechanics and Physics of Solids* 58.10 (2010), pp. 1489–1505.

[83] J. Weissmüller, H. L. Duan, and D. Farkas. “Deformation of solids with nanoscale pores by the action of capillary forces”. In: *Acta Materialia* 58.1 (2010), pp. 1–13.

[84] G. Y. Gor and A. V. Neimark. “Adsorption-Induced Deformation of Mesoporous Solids: Macroscopic Approach and Density Functional Theory”. In: *Langmuir* 27.11 (2011), pp. 6926–6931.

[85] Y. Long et al. “Pressure enhancement in carbon nanopores: a major confinement effect”. In: *Physical Chemistry Chemical Physics* 13.38 (2011), pp. 17163–17170.

[86] M. Schoen and G. Günther. “Capillary condensation in deformable mesopores: wetting versus nanomechanics”. In: *Molecular Physics* 109.1 (2011), pp. 83–95.

[87] L. Brochard et al. “Adsorption-Induced Deformation of Microporous Materials: Coal Swelling Induced by CO2-CH4 Competitive Adsorption”. In: *Langmuir* 28.5 (2012), pp. 2659–2670.

[88] L. Brochard, M. Vandamme, and R. J. M. Pellenq. “Poromechanics of microporous media”. In: *Journal of the Mechanics and Physics of Solids* 60.4 (2012), pp. 606–622.

[89] P. Kowalczyk et al. “Methane-Induced Deformation of Porous Carbons: From Normal to High-Pressure Operating Conditions”. In: *Journal of Physical Chemistry C* 116.2 (2012), pp. 1740–1747.

[90] G. Y. Gor et al. “Adsorption of n-pentane on mesoporous silica and adsorbent deformation”. In: *Langmuir* 29.27 (2013), pp. 8601–8608.

[91] Y. Long et al. “High pressure effect in nanoporous carbon materials: Effects of pore geometry”. In: *Colloids and Surfaces A: Physicochemical and Engineering Aspects* 437 (2013), pp. 33–41.

[92] Y. Long et al. “On the molecular origin of high-pressure effects in nanoconfinement: The role of surface chemistry and roughness”. In: *Journal of Chemical Physics* 139.14 (2013), p. 144701.

[93] B. Coasne, Y. Long, and K. E. Gubbins. “Pressure effects in confined nanophases”. In: *Molecular Simulation* 40.7-9 (2014), pp. 721–730.

[94] P. Kowalczyk et al. “Effects of Critical Fluctuations on Adsorption-Induced Deformation of Microporous Carbons”. In: *Journal of Physical Chemistry C* 119.11 (2015), pp. 6111–6120.

[95] F. Mouhat et al. “Softening upon Adsorption in Microporous Materials: A Counterintuitive Mechanical Response”. In: *Journal of Physical Chemistry Letters* 6.21 (2015), pp. 4265–4269.

[96] R. Diao et al. “Monte Carlo Simulation of Adsorption-Induced Deformation in Finite Graphitic Slit Pores”. In: *Journal of Physical Chemistry C* 120.51 (2016), pp. 29272–29282.

[97] G. Y. Gor and N. Bernstein. “Revisiting Bangham’s Law of Adsorption-Induced Deformation: Changes of Surface Energy and Surface Stress”. In: *Physical Chemistry Chemical Physics* 18 (2016), pp. 9788–9798.

[98] G. Y. Gor and N. Bernstein. “Adsorption-Induced Surface Stresses of the Water/Quartz Interface: Ab Initio Molecular Dynamics Study”. In: *Langmuir* 32.21 (2016), pp. 5259–5266.

[99] M. Thommes et al. “Physisorption of gases, with special reference to the evaluation of surface area and pore size distribution (IUPAC Technical Report)”. In: *Pure and Applied Chemistry* 87.9-10 (2015), pp. 1051–1069.

[100] T.M. Atanackovic and A. Guran. *Theory Of Elasticity For Scientists and Engineers*. Bosten: Birkhäuser, 2000.

[101] L. J. Gibson and M. F. Ashby. *Cellular solids - Structure and properties*. 2nd. Cambridge: Cambridge University Press, 1999.

[102] J. Gross and J. Fricke. “Scaling of elastic properties in highly porous nanostructured aerogels”. In: *Nanostructured Materials* 6.5-8 (1995), pp. 905–908.

[103] A. L. Myers and P. A. Monson. “Adsorption in porous materials at high pressure: Theory and experiment”. In: *Langmuir* 18.26 (2002), pp. 10261–10273.

[104] D. H. Everett and J. C. Powl. “Adsorption in Slit-Like and Cylindrical Micropores in Henry's Law Region. A Model for the Microporosity of Carbons”. In: *Journal of the Chemical Society-Faraday Transactions I* 72 (1976), pp. 619–636.

[105] P. Tarazona. “Free-energy density functional for hard spheres”. In: *Physical Review A* 31.4 (1985), pp. 2672–2679.

[106] P. Tarazona, M.B. Marconi, and R. Evans. “Phase Equilibria of Fluids Interfaces and Confined Fluids Non-Local Versus Local Density Functionals”. In: *Molecular Physics* 60.3 (1987), pp. 573–595.

[107] J. Landers, G. Y. Gor, and A. V. Neimark. “Density functional theory methods for characterization of porous materials”. In: *Colloids and Surfaces A: Physicochemical and Engineering Aspects* 437 (2013), pp. 3–32.

[108] J. D. Weeks, D. Chandler, and H. C. Andersen. “Role of Repulsive Forces in Determining Equilibrium Structure of Simple Liquids”. In: *Journal of Chemical Physics* 54.12 (1971), pp. 5237–5247.

[109] Y. Rosenfeld et al. “Fundamental-measure free-energy density functional for hard spheres: Dimensional crossover and freezing”. In: *Physical Review E* 55.4 (1997), pp. 4245–4263.

[110] Y. Rosenfeld. “Free-Energy Model for the Inhomogeneous Hard-Sphere Fluid Mixture and Density-Functional Theory of Freezing”. In: *Physical Review Letters* 63.9 (1989), pp. 980–983.

[111] P. I. Ravikovitch, A. Vishnyakov, and A. V. Neimark. “Density functional theories and molecular simulations of adsorption and phase transitions in nanopores”. In: *Physical Review E* 64.1 (2001).

[112] W. A. Steele. *The Interactions of Gases with Solid Surfaces*. Oxford: Pergamon, 1974.

[113] P. I. Ravikovitch et al. “Unified approach to pore size characterization of microporous carbonaceous materials from N2, Ar, and CO2 adsorption isotherms”. In: *Langmuir* 16.5 (2000), pp. 2311–2320.

[114] N. A. Seaton, J. P. R. B. Walton, and N. Quirke. “A New Analysis Method for the Determination of the Pore-Size Distribution of Porous Carbons from Nitrogen Adsorption Measurements”. In: *Carbon* 27.6 (1989), pp. 853–861.

[115] J. Jagiello and J. P. Olivier. “2D-NLDFT adsorption models for carbon slit-shaped pores with surface energetical heterogeneity and geometrical corrugation”. In: *Carbon* 55 (2013), pp. 70–80.

[116] A. V. Neimark et al. “Quenched solid density functional theory and pore size analysis of micro-mesoporous carbons”. In: *Carbon* 47.7 (2009), pp. 1617–1628.

[117] B. V. Derjaguin. “A theory of capillary condensation in the pores of sorbents and of other capillary phenomena taking into account the disjoining action of polymolecular liquid films”. In: *Acta physicochimica URSS* 12 (1940), pp. 181–200.

[118] J. C. P. Broekhoff and J. H. De Boer. “Studies on Pore Systems in Catalysts. IX. Calculation of Pore Distributions from Adsorption Branch of Nitrogen Sorption Isotherms in Case of Open Cylindrical Pores. A. Fundamental Equations”. In: *Journal of Catalysis* 9.1 (1967), pp. 8–14.

[119] J. C. P. Broekhoff and J. H. De Boer. “Studies on Pore Systems in Catalysts. X. Calculations of Pore Distributions from Adsorption Branch of Nitrogen Sorption Isotherms in Case of Open Cylindrical Pores. B. Applications”. In: *Journal of Catalysis* 9.1 (1967), pp. 15–27.

[120] P. Ravikovitch and A. Neimark. “Calculations of Pore Size Distributions in Nanoporous Materials from Adsorption and Desorption Isotherms”. In: *Studies in Surface Science & Catalysis* 129 (2000), pp. 597–606.

[121] G. W. Scherer. “Dilatation of Porous Glass”. In: *Journal of the American Ceramic Society* 69.6 (1986), pp. 473–480.

[122] A. I. Rusanov. “Surface Thermodynamics Revisited”. In: *Surface Science Reports* 58.5-8 (2005), pp. 111–239.

[123] D. Kramer and J. Weissmüller. “A note on surface stress and surface tension and their interrelation via Shuttleworth's equation and the Lippmann equation”. In: *Surface Science* 601.14 (2007), pp. 3042–3051.

[124] T. L Hill. “Theory of Physical Adsorption”. In: *Advances in Catalysis* 4 (1952), pp. 211–258.

[125] J. E. Lane and T. H. Spurling. “Monte Carlo Simulation of the Effects of Adsorption on Interparticle Forces”. In: *Australian Journal of Chemistry* 33.2 (1980), pp. 231–239.

[126] I. K. Snook and W. Van Megen. “Solvation Forces in Simple Dense Fluids. I”. In: *Journal of Chemical Physics* 72.5 (1980), pp. 2907–2913.

[127] R. Evans and U. M. B. Marconi. “Phase-Equilibria and Solvation Forces for Fluids Confined between Parallel Walls”. In: *Journal of Chemical Physics* 86.12 (1987), pp. 7138–7148.

[128] P. B. Balbuena, D. Berry, and K. E. Gubbins. “Solvation Pressures for Simple Fluids in Micropores”. In: *Journal of Physical Chemistry* 97.4 (1993), pp. 937–943.

[129] C. Balzer et al. “Adsorption-Induced Deformation of Hierarchically Structured Mesoporous Silica - Effect of Local Anisotropy”. In: *Langmuir* 33 (2017), pp. 5592–5602.

[130] B. V. Derjaguin, N. V. Churaev, and E. A. Muller. *Surface Forces*. New York: Springer Science+Business Media, 1987.

[131] C. J. Gommes, P. I. Ravikovitch, and A. V. Neimark. "Positive curvature effects and interparticle capillary condensation during nitrogen adsorption in particulate porous materials". In: *Journal of Colloid and Interface Science* 314.2 (2007), pp. 415–421.

[132] R. Salazar and L. D. Gelb. "An investigation of the effects of the structure of gel materials on their adsorptive properties using a simple lattice-gas model". In: *Molecular Physics* 102.9-10 (2004), pp. 1015–1030.

[133] R. C. Bansal, J.-B. Donnet, and F. Stoeckli. *Active Carbon*. New York and Basel: Marcel Dekker, 1988.

[134] J. Pikunic, C. M. Lastoskie, and K. E. Gubbins. "Adsorption from the Gas Phase". In: *Handbook of Porous Solids - Volume 1*. Ed. by F. Schueth, K. S. W. Sing, and J. Weitkamp. Weinheim: Wiley-VCH, 2002.

[135] S. H. Madani et al. "Pore size distributions derived from adsorption isotherms, immersion calorimetry, and isosteric heats: A comparative study". In: *Carbon* 96 (2016), pp. 1106–1113.

[136] S. G. Ash, D. H. Everett, and C. Radke. "Thermodynamics of Effects of Adsorption on Interparticle Forces". In: *Journal of the Chemical Society-Faraday Transactions II* 69.8 (1973), pp. 1256–1277.

[137] K. Kinoshita. *Carbon - Electrochemical and Physicochemical Properties*. Hoboken: Wiley-Interscience, 1988.

[138] M. Wiener and G. Reichenauer. "Microstructure of porous carbons derived from phenolic resin - Impact of annealing at temperatures up to 2000°C analyzed by complementary characterization methods". In: *Microporous and Mesoporous Materials* 203 (2015), pp. 116–122.

[139] R. W. Pekala and F. M. Kong. "A Synthetic Route to Organic Aerogels - Mechanism, Structure, and Properties". In: *Journal de Physique Colloques* 50.C-4 (1989), pp. C433–C440.

[140] M. Wiener et al. "Accelerating the synthesis of carbon aerogel precursors". In: *Journal of Non-Crystalline Solids* 350 (2004), pp. 126–130.

[141] E. Fitzer et al. *Terminology for the description of carbon as a solid*. Tech. rep. Deutsche Keramische Gesellschaft - Arbeitskreis Kohlenstoff, 1998.

[142] R. W. Pekala and C. T. Alviso. "Carbon Aerogels And Xerogels". In: *Materials Research Society Symposium* 270 (1992), pp. 3–14.

[143] R. Saliger et al. "Carbon aerogels from dilute catalysis of resorcinol with formaldehyde". In: *Journal of Non-Crystalline Solids* 221.2-3 (1997), pp. 144–150.

[144] R. Brandt and J. Fricke. "Acetic-acid-catalyzed and subcritically dried carbon aerogels with a nanometer-sized structure and a wide density range". In: *Journal of Non-Crystalline Solids* 350 (2004), pp. 131–135.

[145] H. Proebstle, M. Wiener, and J. Fricke. "Carbon aerogels for electrochemical double layer capacitors". In: *Journal of Porous Materials* 10.4 (2003), pp. 213–222.

[146] V. Lorrmann et al. "Electrochemical double-layer charging of ultramicroporous synthetic carbons in aqueous electrolytes". In: *Electrochimica Acta* 86 (2012), pp. 232–240.

[147] M. Zeller et al. "Relationship Between Structural Properties and Electrochemical Characteristics of Monolithic Carbon Xerogel-Based Electrochemical Double-Layer Electrodes in Aqueous and Organic Electrolytes". In: *Advanced Energy Materials* 2.5 (2012), pp. 598–605.

[148] R. Saliger et al. "High surface area carbon aerogels for supercapacitors". In: *Journal of Non-Crystalline Solids* 225.1 (1998), pp. 81–85.

[149] H. Proebstle, R. Saliger, and J. Fricke. "Electrochemical investigation of carbon aerogels and their activated derivatives". In: *Characterization of Porous Solids V* 128 (2000), pp. 371–379.

[150] C. E. Mortimer. *Chemie - Das Basiswissen der Chemie*. 5th. Stuttgart; New York: Georg Thieme Verlag, 1987.

[151] S. Braxmeier. "Benetzungs- und Infiltrationsverhalten hochporöser Kohlenstoffe". diploma thesis. Julius-Maximilians-Universität Würzburg, 2005.

[152] H. P. Ebert et al. *LWSNet - Netzwerk zur Überwindung grundlegender Probleme bei der Entwicklung hocheffizienter Latentwärmespeicher auf Basis anorganischer Speichermaterialien*. Tech. rep. BMBF - Vorhaben 03SF0307A-G. 2008.

[153] K. Laszlo. "Characterization and adsorption properties of polymer-based microporous carbons with different surface chemistry". In: *Microporous and Mesoporous Materials* 80.1-3 (2005), pp. 205–211.

[154] K. Laszlo et al. "Influence of Surface Chemistry on the SAXS response of Polymer-Based Activated Carbon". In: *Langmuir* 21 (2005), pp. 8443–8451.

[155] K. Laszlo and E. Geissler. "Surface chemistry and contrast-modified SAXS in polymer-based activated carbons". In: *Carbon* 44.12 (2006), pp. 2437–2444.

[156] K. Laszlo, O. Czakkel, and E. Geissler. "Wetting and non-wetting fluids in surface-functionalised activated carbons". In: *Colloid and Polymer Science* 286.1 (2008), pp. 59–65.

[157] K. Laszlo, C. Rochas, and E. Geissler. "Water vapour adsorption and contrast-modified SAXS in microporous polymer-based carbons of different surface chemistry". In: *Adsorption* 14.4-5 (2008), pp. 447–455.

[158] K. Laszlo et al. "Water vapour adsorption in highly porous carbons as seen by small and wide angle X-ray scattering". In: *Carbon* 48.4 (2010), pp. 1038–1048.

[159] G. A. M. Reynolds et al. "The Effects of External Conditions on the Internal Structure of Carbon Aerogels". In: *Journal of Non-Crystalline Solids* 188.1-2 (1995), pp. 27–33.

[160] Y. Hanzawa et al. "Structural changes in carbon aerogels with high temperature treatment". In: *Carbon* 40.4 (2002), pp. 575–581.

[161] M. Wiener et al. "Thermal conductivity of carbon aerogels as a function of pyrolysis temperature". In: *International Journal of Thermophysics* 27.6 (2006), pp. 1826–1843.

[162] A. Oberlin. "Landmarks for graphitization". In: *Tanso* 224 (2006), pp. 281–298.

[163] E. R. Buiel, A. E. George, and J. R. Dahn. "Model of micropore closure in hard carbon prepared from sucrose". In: *Carbon* 37.9 (1999), pp. 1399–1407.

[164] J. R. Dahn, W. Xing, and Y. Gao. "The "falling cards model" for the structure of microporous carbons". In: *Carbon* 35.6 (1997), pp. 825–830.

[165] T. Wildhage. "Längenänderung mikroporöser Kohlenstoffe bei Adsorption". diploma thesis. Julius-Maximilians-Universität Würzburg, 2009.

[166] *Molecular Sieve KÖSTROLITH®4ABFK, datasheet*. 2012.

[167] *Molecular Sieve KÖSTROLITH®13XBFK, datasheet*. 2012.

[168] A. Brandt et al. *Adsorptionsmittelgranulat und Verfahren zu dessen Herstellung (EP2249 961B1)*. 2010.

[169] K. Schumann et al. "Bindemittelfreie zeolithische Molekularsiebe der Typen LTA und FAU". In: *Chemie Ingenieur Technik* 83.12 (2011), pp. 2237–2243.

[170] K. Schumann et al. "Investigation on the pore structure of binderless zeolite 13x shapes". In: *Microporous and Mesoporous Materials* 154 (2012), pp. 119–123.

[171] C. Baerlocher and L.B. McCusker. *Database of Zeolite Structures (http://www.iza-structure.org/databases/, retrieved January 2017)*.

[172] S. Henning. "Large-Scale Production of Airglass". In: *Aerogels*. Ed. by J. Fricke. Berlin Heidelberg New York Tokyo: Springer-Verlag, 1985, pp. 38–41.

[173] R. K. Iler. *The Chemistry Of Silica*. New York Chichester Brisbane Toronto: John Wiley & Sons, 1979.

[174] G. Reichenauer. *personal correspondance*. 2017.

[175] A. M. Waag. "Sorptionsbedingte Deformation nanoporöser, hierarchisch strukturierter Materialien". master thesis. Julius-Maximilians-Universität Würzburg, 2015.

[176] D. Brandhuber et al. “Glycol-modified silanes in the synthesis of mesoscopically organized silica monoliths with hierarchical porosity”. In: *Chemistry of Materials* 17.16 (2005), pp. 4262–4271.

[177] D. Brandhuber et al. “Cellular mesoscopically organized silica monoliths with tailored surface chemistry by one-step drying/extraction/surface modification processes”. In: *Journal of Materials Chemistry* 15.18 (2005), pp. 1801–1806.

[178] C. Balzer et al. “Relationship Between Pore Structure and Sorption-Induced Deformation in Hierarchical Silica-Based Monoliths”. In: *Zeitschrift für Physikalische Chemie* 229.7-8 (2015).

[179] *ASAP 2020 Operator's Manual V3.01*. Norcross, GA USA: Micromeritics Instrument Corporation, 2006.

[180] M. Thommes, K. A. Cychosz, and A. V. Neimark. “Advanced Physical Adsorption Characterization of Nanoporous Carbons”. In: *Novel Carbon Adsorbents*. Ed. by J. M. D. Tascon. Elsevier Ltd, 2012.

[181] L.G. Gurvich. “Physio-Chemical Attractive Force”. In: *Journal of the Russian Physical Chemistry Society* 47 (1915), pp. 805–827.

[182] G. Y. Gor et al. “Quenched solid density functional theory method for characterization of mesoporous carbons by nitrogen adsorption”. In: *Carbon* 50.4 (2012), pp. 1583–1590.

[183] S. Brunauer, P. H. Emmett, and E. Teller. “Adsorption of Gases in Multimolecular Layers”. In: *Journal of the American Chemical Society* 60.2 (1938), pp. 309–319.

[184] J. Rouquerol, P. Llewellyn, and F. Rouquerol. “Is the BET equation applicable to microporous adsorbents?” In: *Studies in Surface Science and Catalysis*. Ed. by P. Llewellyn et al. Amsterdam and Oxford: Elsevier, 2007, pp. 49–56.

[185] B. C. Lippens and J. H. de Boer. “Studies on Pore Systems in Catalysts V. The t method”. In: *Journal of Catalysis* 4.3 (1965), pp. 319–23.

[186] R. W. Magee. “Evaluation of the external surface area of carbon black by nitrogen adsorption”. In: *Rubber Chemistry and Technology* 68 (1994), pp. 590–600.

[187] A. N. Tikhonov. “Regularization of Incorrectly Posed Problems”. In: *Doklady Akademii nauk SSSR* 153 (1963), pp. 49–52.

[188] C. Balzer et al. “Deformation of Microporous Carbons during N2, Ar, and CO2 Adsorption: Insight from the Density Functional Theory”. In: *Langmuir* 32.32 (2016), pp. 8265–8274.

[189] J. Gross. “Mechanische Eigenschaften von Aerogelen”. diploma thesis. Julius-Maximilians-Universität Würzburg, 1987.

[190] J. Gross. “Die Schallgeschwindigkeit von Aerogelen und ihre Variation mit Dichte, Gasdruck und elastischer Vorspannung”. PhD thesis. Julius-Maximilians-Universität Würzburg, 1992.

[191] C. Kittel. *Introduction to Solid State Physics*. Wiley & Sons, 1995.

[192] *Betriebsanleitung ULTRA Plus*. Oberkochen, Germany: Carl Zeiss NTS, 2008.

[193] J. I. Goldstein et al. *Scanning Electron Microscopy And X-ray Microanalysis*. 3rd. New York: Springer Science+Business Media, 2003.

[194] C. Balzer. “Hochaufgelöste Messung adsorptionsinduzierter Längenänderung an porösen Kohlenstoffen”. diploma thesis. Julius-Maximilians-Universität Würzburg, 2010.

[195] Paul A. Webb and Clyde Orr. *Analytical methods in fine particle technology*. Norcross, GA USA: Micromeritics Instrument Corporation, 1997.

[196] *LVDT basics, Technical Bulletin 0103*. 2003.

[197] P. Kowalczyk et al. “Using in-situ Adsorption Dilatometry for Assessment of Micropore Size Distribution in Monolithic Carbons”. In: *Carbon* 103 (2016), pp. 263–272.

[198] J. Silvestre-Albero et al. “High-Resolution N2 Adsorption Isotherms at 77.4 K: Critical Effect of the He Used During Calibration”. In: *The Journal of Physical Chemistry C* 117.33 (2013), pp. 16885–16889.

[199] E.W. Lemmon, M.O. McLinden, and D.G. Friend. *Thermophysical Properties of Fluid Systems*. Nist Chemistry WebBook Database Number 69. Gaithersburg, MD: National Institute of Standards and Technology, (retrieved March 9, 2015).

[200] R. Weast. *CRC Handbook of Chemistry and Physics*. Boca Raton, FL, USA: CRC Press, 1983.

[201] C. Balzer et al. "Deformation of Microporous Carbon during Adsorption of Nitrogen, Argon, Carbon Dioxide, and Water Studied by in Situ Dilatometry". In: *Langmuir* 31.45 (2015), pp. 12512–12519.

[202] T. Woignier and J. Phalippou. "Skeletal Density of Silica Aerogels". In: *Journal of Non-Crystalline Solids* 93.1 (1987), pp. 17–21.

[203] J. Gross, G. Reichenauer, and J. Fricke. "Mechanical-Properties of SiO2 Aerogels". In: *Journal of Physics D - Applied Physics* 21.9 (1988), pp. 1447–1451.

[204] Y. W. Zhu et al. "Carbon-Based Supercapacitors Produced by Activation of Graphene". In: *Science* 332.6037 (2011), pp. 1537–1541.

[205] M. Thommes, R. Kohn, and M. Fröba. "Sorption and pore condensation behavior of pure fluids in mesoporous MCM-48 silica, MCM-41 silica, SBA-15 silica and controlled-pore glass at temperatures above and below the bulk triple point". In: *Applied Surface Science* 196.1-4 (2002), pp. 239–249.

[206] E. A. Ustinova and D. D. Do. "Adsorption of N2, Ar, acetone, chloroform and acetone-chloroform mixture on carbon black in the framework of molecular layer structure theory (MLST)". In: *Carbon* 43.12 (2005), pp. 2463–2473.

[207] M. Thommes. "Physical Adsorption Characterization of Nanoporous Materials". In: *Chemie Ingenieur Technik* 82.7 (2010), pp. 1059–1073.

[208] F. M. Farhan et al. "Stresses and Strains in Adsorbent-Adsorbate Systems. VI". In: *Canadian Journal of Chemistry* 45.6 (1967), pp. 589–593.

[209] A. Toth and K. Laszlo. "Water Adsorption by Carbons. Hydrophobicity and Hydrophilicity". In: *Novel Carbon Adsorbents*. Ed. by J. M. D. Tascon. Elsevier Ltd, 2012.

[210] M. M. Dubinin. "Water-Vapor Adsorption and the Microporous Structures of Carbonaceous Adsorbents". In: *Carbon* 18.5 (1980), pp. 355–364.

[211] T. Iiyama, M. Ruike, and K. Kaneko. "Structural mechanism of water adsorption in hydrophobic micropores from in situ small angle X-ray scattering". In: *Chemical Physics Letters* 331.5-6 (2000), pp. 359–364.

[212] M. Thommes et al. "Combining Nitrogen, Argon, and Water Adsorption for Advanced Characterization of Ordered Mesoporous Carbons (CMKs) and Periodic Mesoporous Organosilicas (PMOs)". In: *Langmuir* 29.48 (2013), pp. 14893–14902.

[213] T. Ohba and K. Kaneko. "Kinetically Forbidden Transformations of Water Molecular Assemblies in Hydrophobic Micropores". In: *Langmuir* 27.12 (2011), pp. 7609–7613.

[214] W. M. Haynes. *CRC Handbook of Chemistry and Physics*. London: Taylor & Francis, 2015.

[215] B. Coasne et al. "Enhanced mechanical strength of zeolites by adsorption of guest molecules". In: *Physical Chemistry Chemical Physics* 13.45 (2011), pp. 20096–20099.

[216] A. Vishnyakov, P. I. Ravikovitch, and A. V. Neimark. "Molecular level models for CO2 sorption in nanopores". In: *Langmuir* 15.25 (1999), pp. 8736–8742.

[217] T. Horikawa et al. "A new adsorption-desorption model for water adsorption in porous carbons". In: *Carbon* 49 (2011), pp. 416–424.

[218] M. Thommes et al. "Assessing surface chemistry and pore structure of active carbons by a combination of physisorption (H2O, Ar, N2, CO2), XPS and TPD-MS". In: *Adsorption* 17 (2011), pp. 653–661.

[219] M. Wiener. "Synthese und Charakterisierung Sol-Gel-basierter Kohlenstoff-Materialien für die Hochtemperatur-Wärmedämmung". PhD thesis. Julius-Maximilians-Universität Würzburg, 2009.

[220] C. Garion. "Mechanical Properties for Reliability Analysis of Structures in Glassy Carbon". In: *World Journal of Mechanics* 4 (2014), pp. 79–89.